



University of HUDDERSFIELD

University of Huddersfield Repository

Hamza, Esam

Analysis of Friction Stir Welding Using Tools with Different Pin Profiles

Original Citation

Hamza, Esam (2018) Analysis of Friction Stir Welding Using Tools with Different Pin Profiles. Doctoral thesis, University of Huddersfield.

This version is available at <http://eprints.hud.ac.uk/id/eprint/35101/>

The University Repository is a digital collection of the research output of the University, available on Open Access. Copyright and Moral Rights for the items on this site are retained by the individual author and/or other copyright owners. Users may access full items free of charge; copies of full text items generally can be reproduced, displayed or performed and given to third parties in any format or medium for personal research or study, educational or not-for-profit purposes without prior permission or charge, provided:

- The authors, title and full bibliographic details is credited in any copy;
- A hyperlink and/or URL is included for the original metadata page; and
- The content is not changed in any way.

For more information, including our policy and submission procedure, please contact the Repository Team at: E.mailbox@hud.ac.uk.

<http://eprints.hud.ac.uk/>

THERMAL ANALYSIS OF FRICTION STIR WELDING USING TOOLS WITH DIFFERENT PIN PROFILES

A THESIS SUBMITTED IN PARTIAL FULFILMENT OF THE REQUIREMENTS FOR THE
DEGREE OF DOCTOR OF PHILOSOPHY AT THE UNIVERSITY OF HUDDERSFIELD

By

Esam Hamza

School of Computing and Engineering

University of Huddersfield

UK

December 2018

In the memory of my beloved father Mr. Mohamed Hamza

ABSTRACT

Welding is an important process in manufacturing and fabrication where improving the weld quality and reducing the cost are the main targets. In view of that, extensive research is still being carried out to improve efficiency of the existing welding processes and developing alternative welding techniques. One such technique is friction stir welding which has the capability to produce high strength joints particularly for the materials that cannot be welded by the conventional welding processes. Controlling the FSW process parameters to improve the quality of welded joint is still a subject of active research. Controlling the welding thermal cycle through the geometrical and operational parameters may lead to produce sound weldments where defects can be avoided. Various studies have been carried out considering the various tool pin profiles to improve the mechanical strength of welded joint, but the influences of the pin profiles on the thermal characterisations have been rarely reported. Besides, the experimental work has often showed that it is cost and time consuming particularly when the effect of geometrical variables is investigated.

The present work focuses on the employment of modeling approaches to simulate the thermal field within the weldments which allow quantification of the thermal behaviour corresponding to the different proposed tool pins. A three – dimensional transient model has been developed to simulate the physical model of friction stir welding. It has then been employed to carry out the investigations under various geometrical and operational parameters. An analytical approach has been integrally used to develop novel mathematical equations that calculate the heat generation for all cases of welding tools to be studied. Then, to accomplish the CFD simulations of the cases under consideration, the heat generated amount has been applied to the pin and shoulder surfaces as a heat flux which represents the process heat input.

Both qualitative and quantitative analysis has been carried out for the temperature distribution within specimens welded by FSW using tools with different polygonal pins. In order to cover a wide range of geometrical and operational conditions, the numerical simulations have been conducted for various shoulder diameters, pin diameters, pin heights, material thicknesses, rotational speeds and axial loads. The attained results have given a clear picture of the transient and the spatial temperature behaviour as well as the effect of presence of the polygonal pin on the thermal field.

In the same way, a detailed CFD based investigation has been carried out on the thermal field for those FSW processes using tools with eccentric polygonal pins and tapered eccentric polygonal pins covering the same range of the geometrical and operational parameters. Furthermore, the current study made use of the peak temperature values for various cases under investigation in order to develop a semi-empirical correlation, which predict the maximum temperature in the weldments for various welding conditions. The developed prediction models of the peak temperature have shown a good accuracy particularly no single study has considered a wide range of investigations on the FSW thermal field which would be beneficial in selection of the welding parameters. Lastly, the advanced CFD modeling technique and the novel mathematical equations of heat generation being incorporated in this study have made it possible to spatially and transiently mapping of the thermal field even on the small scale of variations which led to a better understanding of the physical behaviour.

DECLARATION

- The author of this thesis (including any appendices and/or schedules to this thesis) owns any copyright in it (the “Copyright”) and he has given The University of Huddersfield the right to use such copyright for any administrative, promotional, educational and/or teaching purposes.
- Copies of this thesis, either in full or in extracts, may be made only in accordance with the regulations of the University Library. Details of these regulations may be obtained from the Librarian. This page must form part of any such copies made.
- The ownership of any patents, designs, trademarks and any and all other intellectual property rights except for the Copyright (the “Intellectual Property Rights”) and any reproductions of copyright works, for example graphs and tables (“Reproductions”), which may be described in this thesis, may not be owned by the author and may be owned by third parties. Such Intellectual Property Rights and Reproductions cannot and must not be made available for use without the prior written permission of the owner(s) of the relevant Intellectual Property Rights and/or Reproductions.

Declaration of Publications Arising from this Thesis

“A review of using Computational Fluid Dynamic in simulating of Friction Stir Welding and Parametric studies”

Hamza, E. 11th International Symposium on FSW (11ISFSW) 2016: TWI Ltd, Cambridge, UK.

Contribution of the candidate: I wrote this paper with no input or editorial changes from others. This paper forms the basis of the introduction in chapter 1 and some parts of my literature review in chapter 2.

“Computational Fluid Dynamics based Transient Thermal Analysis of Friction Stir Welding”

Hamza, E. Asim, T. and Mishra, R. 6th International and 43rd National Conference on Fluid Mechanics and Fluid Power (FMFP-2016). December 2016: Allahabad, India

Contribution of the candidate: I carried out all the research and wrote the first draft of this paper. I had editorial changes from my co-authors. The only part of research presented in this paper is the approach used to mimic the movement of the welding tool which appears in chapter 3. It has been indicated where this approach has been mentioned in chapter 3.

ACKNOWLEDGEMENTS

Foremost with limitless gratitude, I would like to express my deep thankfulness to almighty Allah who has given me the courage, strength, ability and knowledge to undertake and complete this work. Secondly, I would like to acknowledge my deepest gratitude to my parents for teaching me the moral values and for their emotional and financial support throughout my whole life. No words could satisfy my sincere love for them as I always knew that they trusted me and wished the best for me.

I would like to say a very big thank you to my supervisors Prof. Rakesh Mishra and Dr. Taimoor Asim for their supervision, helpful advice and continuous guidance which made this work a reality. I would also like to thank my colleagues in the Energy, Emission and Environment Research group at Huddersfield University for their help during PhD journey.

I would specially like to thank my lovely wife Enas Abudher and my children Anas, Diyaa Edden, Mohamed and Ahmed for their patience, extreme support and the countless sacrifices throughout my PhD journey, without their help I would not be able to achieve this.

Last but not least, I should mention my special gratitude to my brothers, sisters, relatives and friends for their continuous support and encouragement while I have been away from home.

Contents

ABSTARCT	III
DECLARATION	V
DECLARATION OF PUBLICATIONS ARISING FROM THIS THESIS	VI
ACKNOWLEDGEMENTS	VII
CONTENTS	VIII
LIST OF FIGURES	XIII
LIST OF TABLES	XXV
NOMENCLATURE	XXVI
GREEK SYMBOLS	XXVIII
SUBSCRIPTS	XXIX
ACRONYM	XXX
CHAPTER 1:INTRODUCTION	31
1.1 SOLID-STATE WELDING.....	32
1.2 FRICTION WELDING	32
1.3 FRICTION STIR WELDING	34
1.3.1 Definitions.....	36
1.3.2 Advantages and limitations.....	37
1.3.3 Applications of friction stir welding	38
1.3.4 Process parameters.....	39
1.4 HEAT GENERATION IN FRICTION STIR WELDING.....	42
1.4.1 Contact condition	43
1.4.2 Heat generation from friction.....	43
1.4.3 Heat dissipation.....	44
1.5 METAL FLOW IN FRICTION STIR WELDING	46
1.6 MODELLING OF FRICTION STIR WELDING	49
1.7 MOTIVATION.....	49
1.8 RESEARCH AIMS.....	51
1.9 STRUCTURE OF THE THESIS	51

CHAPTER 2:LITERATURE REVIEW	54
2.1 CFD MODELLING OF FRICTION STIR WELDING	55
2.1.1 Summary of Literature regarding CFD Modelling of friction stir welding	66
2.2 FRICTION STIR WELDING USING TOOLS WITH POLYGONAL PINS	66
2.2.1 Summary of Literature regarding Friction Stir Welding using tool with polygonal pins	70
2.3 FRICTION STIR WELDING USING TOOL WITH ECCENTRIC POLYGONAL PINS	70
2.3.1 Summary of Literature regarding Friction Stir Welding using tool with Eccentric polygonal pins	74
2.4 FRICTION STIR WELDING USING TOOL WITH TAPERED ECCENTRIC POLYGONAL PINS	75
2.4.1 Summary of literature regarding Friction Stir Welding using tool with Tapered Eccentric polygonal pins	82
2.5 SCOPE OF RESEARCH	82
2.6 SPECIFIC RESEARCH OBJECTIVES	83
CHAPTER 3:CFD MODELLING OF FRICTION STIR WELDING	85
3.1 THE GOVERNING EQUATIONS	86
3.2 PRE-PROCESSING	87
3.2.1 Model Regions and Geometry	87
3.2.2 Meshing of the Computational Domain.....	88
3.2.3 Dynamic Mesh	90
3.3 SOLVER EXECUTION	93
3.3.1 Selection of the Physical Models	93
3.3.2 Solidification / Melting Model.....	94
3.3.3 Material Properties.....	95
3.3.4 Boundary Conditions	96
3.3.5 Solver Setting and Convergence Criteria.....	97
3.4 MESH INDEPENDENCE TEST	98
3.5 TIME STEP INDEPENDENCE TEST.....	98
3.6 BENCHMARK TESTS	101
CHAPTER 4:... THERMAL CHARACTERISATION OF FRICTION STIR WELDING USING TOOL WITH POLYGONAL PINS	105

4.1	ANALYTICAL MODELING OF HEAT GENERATION FROM A TOOL WITH CONCENTRIC PIN	106
4.2	HEAT GENERATION FROM A TOOL WITH CONCENTRIC HEPTAGONAL PIN.....	106
4.2.1	Heat Generation from Shoulder Base	107
4.2.2	Heat Generation from Pin Side Surfaces	107
4.2.3	Heat Generation from the Pin Tip.....	109
4.2.4	Total Heat Generation from the Tool with Concentric Heptagonal Pin	110
4.3	THERMAL ANALYSIS OF FSW WHEN USING CONCENTRIC POLYGONAL PINS.....	114
4.3.1	Effects of Geometrical Parameters on the Thermal field of FSW	116
4.3.1.1	Effects of Shoulder Diameter on the Thermal field of FSW	117
4.3.1.2	Effects of Pin Diameter on the Thermal Field of FSW	122
4.3.1.3	Effects of Pin Height on the Thermal Field of FSW	128
4.3.1.4	Effects of the Workpiece Thickness on the Thermal Field of FSW	133
4.3.2	Effects of Rotational Speed on the Thermal Field of FSW	138
4.3.3	Effects of Axial Load on the Thermal Field of FSW.....	143
4.4	PREDICTION MODEL OF THE PEAK TEMPERATURE.....	148
4.5	SUMMARY OF THE THERMAL ANALYSIS CONDUCTED ON THE FSW USING TOOLS WITH CONCENTRIC POLYGONAL PINS	149
CHAPTER 5:... THERMAL CHARACTERISATION OF FRICTION STIR WELDING USING TOOL WITH ECCENTRIC PINS.....		151
5.1	ANALYTICAL MODELING OF HEAT GENERATION FROM A TOOL WITH ECCENTRIC PIN	152
5.2	HEAT GENERATION FROM A TOOL WITH ECCENTRIC HEPTAGONAL PIN	153
5.2.1	Heat Generation from Shoulder Base	153
5.2.2	Heat Generation from Pin Side Surfaces	154
5.2.3	Heat Generation from the Pin Tip.....	155
5.2.4	Total Heat Generation from the Tool with Eccentric Heptagonal Pin.....	156
5.3	THERMAL FIELD ANALYSIS OF FSW WHEN USING ECCENTRIC POLYGONAL PINS	159
5.3.1	Effects of Geometrical Parameters on the Thermal Field of FSW	160
5.3.1.1	Effect of Pin Eccentricity on the Thermal Field of FSW.....	160
5.3.1.2	Effect of Shoulder Diameter on the Thermal Field of FSW	165
5.3.1.3	Effect of pin diameter on the Thermal Field of FSW	171

5.3.1.4	The effect of pin Height on the Thermal Field of FSW	177
5.3.1.5	The effect of the workpiece thickness on the Thermal Field of FSW	181
5.3.2	The effect of rotational speed on the Thermal Field of FSW	185
5.3.3	The effect of axial load on the Thermal Field of FSW	190
5.4	PREDICTION MODEL OF THE PEAK TEMPERATURE.....	194
5.5	SUMMARY OF THE THERMAL ANALYSIS CONDUCTED ON THE FSW USING TOOLS WITH ECCENTRIC POLYGONAL PINS.....	196
CHAPTER 6:... THERMAL CHARACTERISATION OF FRICTION STIR WELDING USING TOOL WITH TAPERED PINS.....		198
6.1	ANALYTICAL MODELING OF HEAT GENERATION FOR A TOOL WITH TAPERED PIN	199
6.2	HEAT GENERATION FROM A TOOL WITH TAPERED ECCENTRIC HEPTAGONAL PIN.....	200
6.2.1	Heat Generation from Shoulder Base	200
6.2.2	Heat Generation from Pin Side Surfaces	201
6.2.3	Heat Generation from the Pin Tip.....	202
6.2.4	Total Heat Generation from the Tool with Tapered Eccentric Heptagonal Pin	203
6.3	THERMAL FIELD ANALYSIS OF FSW WHEN USING TAPERED ECCENTRIC POLYGONAL PINS	208
6.3.1	Effects of Geometrical Parameters on the Thermal Field of FSW	211
6.3.1.1	Effect of Pin Tapering on the Thermal Field of FSW	211
6.3.1.2	Effect of pin Eccentricity on the Thermal Field of FSW.....	217
6.3.1.3	Effect of Shoulder Diameter on the Thermal Field of FSW	222
6.3.1.4	Effect of pin diameter on the Thermal Field of FSW	228
6.3.1.5	The effect of pin Height on the Thermal Field of FSW.....	232
6.3.1.6	The effect of the workpiece thickness on the Thermal Field of FSW	237
6.3.2	The effect of rotational speed on the Thermal Field of FSW	241
6.3.3	The effect of axial load on the Thermal Field of FSW	247
6.4	PREDICTION MODEL OF THE PEAK TEMPERATURE IN THE EXISTENCE OF PIN TAPER ANGLE.....	252
6.5	SUMMARY OF THE THERMAL ANALYSIS CONDUCTED ON THE FSW USING TOOLS WITH TAPERED ECCENTRIC POLYGONAL PINS	253
CHAPTER 7:CONCLUSIONS		255
7.1	RESEARCH PROBLEM SYNOPSIS	256

7.2 RESEARCH AIMS AND MAJOR ACHIEVEMENTS	256
7.3 THESIS CONCLUSIONS.....	260
7.4 THESIS CONTRIBUTIONS	264
7.5 RECOMMENDATIONS FOR FUTURE WORK	266
REFERENCES.....	268
APPENDIX A:.....	276
APPENDIX B:.....	279
PUBLICATIONS	295

List of Figures

FIGURE 1.1 ROTARY FRICTION WELDING[3].....	33
FIGURE 1.2 DIRECT – DRIVE ROTARY FRICTION WELDING[4].....	33
FIGURE 1.3 INERTIA – DRIVE ROTARY FRICTION WELDING[4].....	34
FIGURE 1.4 LINEAR AND ORBITAL FRICTION WELDING[5]	34
FIGURE 1.5 FRICTION STIR WELDING IN A BUTT JOINT[6]	35
FIGURE 1.6 TILT ANGLE [7].....	36
FIGURE 1.7 FRICTION STIR WELDING ZONE [8]	37
FIGURE 1.8 DIFFERENT APPLICATIONS OF FRICTION STIR WELDING [5, 12].....	39
FIGURE 1.9 FSW WITH A TOOL CONSISTS A CONICAL SHOULDER AND A THREADED PROBE [13]	40
FIGURE 1.10 SHOULDER SHAPES AND FEATURES[14]	41
FIGURE 1.11 SOME OF TOOL PIN PROFILES[17].....	42
FIGURE 1.12 THERMAL ASPECTS OF FSW [6].....	44
FIGURE 1.13 MECHANISMS OF HEAT GENERATION AND DISSIPATION IN FSW [6]	45
FIGURE 1.14 HEAT TRANSFER PROCESSES OCCURRING DURING FSW [6].....	46
FIGURE 1.15 METAL FLOW PATTERNS AND METALLURGICAL PROCESSING ZONES DEVELOPED IN FSW [6].....	47
FIGURE 1.16(A, B, C, D) THE MATERIAL TRANSPORT IN THE SHOULDER/WORKPIECE INTERFACE REGION AND IN THE TOOL PIN/WORKPIECE INTERFACE REGION INTERFACE [1]	48
FIGURE 1.17 INCOMPRESSIBLE FLOW FIELDS IN FSW [1]	48
FIGURE 2.1 DESCRIPTION OF THE DIFFERENT REGIONS USED FOR THE MODELS [24]	55
FIGURE 2.2 PEAK TEMPERATURE AGAINST TRANSITIONAL AND ROTATIONAL SPEEDS [24]	56
FIGURE 2.3 THE WELDING MODEL [25]	57
FIGURE 2.4 SOLUTION DOMAIN AND THE BOUNDARIES[31]	58
FIGURE 2.5 MODEL’S GEOMETRY [32]	59
FIGURE 2.6 SCHEMATIC DRAWING OF THE THREE-DIMENSIONAL FLOW DOMAIN [33]	60
FIGURE 2.7 OVERVIEW OF THE SOLID AND FLUID REGIONS IN THE MODEL [34].....	61
FIGURE 2.8 SCHEMATIC DRAWING OF THE COMPUTATIONAL MODEL [35].....	61
FIGURE 2.9 SCHEMATIC SKETCH OF FSW SYSTEM AND BOUNDARY CONDITIONS [29]	62
FIGURE 2.10 A SCHEMATIC VIEW OF THE MODEL [39].....	64
FIGURE 2.11 SCHEMATIC OF FSW PLATE [41]	65

FIGURE 2.12 FSW TOOLS WITH DIFFERENT PIN PROFILES AND SHOULDER/PIN DIAMETER RATIOS [44].....	68
FIGURE 2.13 THE EFFECT OF THE TOOL PIN ECCENTRICITY ON THE PEAK TEMPERATURE FOR (A) AA1050-H12, (B) AA5754-H24 AT DIFFERENT WELDING SPEEDS [57].....	73
FIGURE 2.14 MODES OF TOOL OFFSET [58]	74
FIGURE 2.15 DIFFERENT PROFILES OF TAPERED TOOL PINS [60].....	75
FIGURE 2.16 DIFFERENT TOOL PINS GEOMETRIES [45]	77
FIGURE 2.17 TEMPERATURE CONTOURS: A) STRAIGHT PIN, B) TAPERED PIN [35]	78
FIGURE 2.18 VARIOUS TAPERED POLYGONAL PINS [65]	79
FIGURE 2.19 ESTIMATED VALUES OF MAXIMUM SHEAR STRESS [16].....	80
FIGURE 2.20 STEADY STATE- TEMPERATURE CONTOURS FOR SIX DIFFERENT CONDITIONS [67]	81
FIGURE 3.1 THE MAIN REGIONS IN THE COMPUTATION DOMAIN	87
FIGURE 3.2 TMAZ DETAILS	88
FIGURE 3.3 MESHING OF THE COMPUTATION DOMAIN	89
FIGURE 3.4 SMOOTHING PROCESS	91
FIGURE 3.5 REMESHING PROCESS	92
FIGURE 3.6 CALCULATION FLOW CHART.....	101
FIGURE 3.7 LOCATIONS OF MONITORING POINTS RELATED TO THE TOOL AND WORKPIECE DIMENSIONS.....	102
FIGURE 3.8(A) CALCULATED AND MEASURED TEMPERATURES AT POINT 1 (B) THE DIFFERENCE BETWEEN CALCULATED AND MEASURED TEMPERATURES AT POINT 1.....	103
FIGURE 3.9(A) CALCULATED AND MEASURED TEMPERATURES AT POINT 2 (B) THE DIFFERENCE BETWEEN CALCULATED AND MEASURED TEMPERATURES AT POINT 2.....	103
FIGURE 3.10(A) CALCULATED AND MEASURED TEMPERATURES AT POINT 3 (B) THE DIFFERENCE BETWEEN CALCULATED AND MEASURED TEMPERATURES AT POINT 3.....	103
FIGURE 3.11(A) CALCULATED AND MEASURED TEMPERATURES AT POINT 4 (B) THE DIFFERENCE BETWEEN CALCULATED AND MEASURED TEMPERATURES AT POINT 4.....	104
FIGURE 4.1 TOOLS WITH DIFFERENT PIN PROFILES (A) HEPTAGON, (B) OCTAGON, (C) NONAGON.	106
FIGURE 4.2 SHOULDER EFFECTIVE AREA AND THE INFINITESIMAL SEGMENT AREA FOR THE TOOL WITH HEPTAGONAL PIN PROFILE	107
4.3 MAIN TRIGONOMETRIC DIMENSIONS OF HEPTAGON AND THE INFINITESIMAL SEGMENT AREA OF EACH SIDE	108

4.4 SCHEMATIC OF THE HEPTAGONAL PIN TIP	110
FIGURE 4.5 HEAT GENERATION VARIATIONS W.R.T THE NUMBER OF SIDES OF A CONCENTRIC POLYGON TOOL	113
FIGURE 4.6 LOCAL MAXIMUM TEMPERATURE AT FOUR DIFFERENT POINTS	115
FIGURE 4.7 TEMPERATURE DISTRIBUTION VERTICAL PLANE AT DIFFERENT TIME STEPS CALCULATED FOR SHOULDER DIAMETERS OF 26MM AND 50MM	118
FIGURE 4.8 STATIC TEMPERATURE CONTOURS FOR DIFFERENT SHOULDER DIAMETERS A=26MM, B=34MM, C=42MM, D=50MM.	119
FIGURE 4.9 MAX. GLOBAL PEAK TEMPERATURE FOR DIFFERENT SHOULDER RADIUS (13MM, 17MM, 21MM, 25MM)	120
FIGURE 4.10 FLOW VELOCITY FIELD FOR DIFFERENT SHOULDER DIAMETERS A=26MM, B=50MM	120
FIGURE 4.11 MAX. LOCAL TEMPERATURE FOR DIFFERENT SHOULDER RADIUS AT DIFFERENT LOCATIONS	121
FIGURE 4.12 TIME – DEPENDENT VARIATION OF THE GLOBAL MAXIMUM SHEAR STRESS FOR DIFFERENT SHOULDER DIAMETERS	122
FIGURE 4.13 TEMPERATURE DISTRIBUTION FOR THE WELD CENTRE LINED VERTICAL PLANE AT DIFFERENT TIME STEPS CALCULATED FOR PIN DIAMETERS 6MM AND 12MM.....	123
FIGURE 4.14 STATIC TEMPERATURE CONTOURS FOR DIFFERENT PIN DIAMETERS A=6MM, B=12MM, C=18MM, D=24MM.....	124
FIGURE 4.15 LIQUID FRACTION CONTOURS FOR DIFFERENT PIN DIAMETERS (A) 3MM, (B) 6MM	125
FIGURE 4.16 MAX. GLOBAL TEMPERATURE FOR DIFFERENT SHOULDER RADIUS	126
FIGURE 4.17 MAX. LOCAL TEMPERATURE FOR DIFFERENT PIN RADIUS AT DIFFERENT LOCATIONS	126
FIGURE 4.18 FLOW VELOCITY FIELD FOR DIFFERENT PIN DIAMETERS AT UNDERNEATH THE SHOULDER AND THE PIN	127
FIGURE 4.19 A COMPARISON BETWEEN THE SHEAR STRESS VALUES WHEN USING A) DIFFERENT PIN SIZES AND B) DIFFERENT SHOULDER SIZES	128
FIGURE 4.20 TEMPERATURE DISTRIBUTION FOR THE VERTICAL PLANE AT DIFFERENT TIME STEPS CALCULATED FOR PIN HEIGHTS 9MM AND 12MM	129
FIGURE 4.21 STATIC TEMPERATURE CONTOURS FOR DIFFERENT PIN HEIGHTS A=9MM, B=10MM, C=11MM, D=12MM	130

FIGURE 4.22 MAX. GLOBAL TEMPERATURE FOR DIFFERENT PIN HEIGHT	131
FIGURE 4.23 LOCAL TEMPERATURE FOR DIFFERENT PIN HEIGHT AT DIFFERENT LOCATIONS ..	131
FIGURE 4.24 FLOW VELOCITY FIELD FOR DIFFERENT PIN HEIGHTS AT UNDERNEATH THE SHOULDER AND THE PIN	132
FIGURE 4.25 A COMPARISON BETWEEN THE TIME DEPENDENT MAXIMUM SHEAR STRESS FOR DIFFERENT GEOMETRICAL PARAMETERS: (A) VARIANT PIN HEIGHT (B) VARIANT PIN DIAMETER (C) VARIANT SHOULDER DIAMETER	133
FIGURE 4.26 TEMPERATURE DISTRIBUTION FOR THE VERTICAL PLANE AT DIFFERENT TIME STEPS CALCULATED FOR WORKPIECE THICKNESS 18.7MM AND 12.7MM	134
FIGURE 4.27 STATIC TEMPERATURE CONTOURS FOR DIFFERENT WORKPIECE THICKNESS A=12.7MM, B=14.7MM, C=16.7MM, D=18.7MM.	135
FIGURE 4.28 MAX. GLOBAL TEMPERATURE FOR DIFFERENT WORKPIECE THICKNESS.....	136
FIGURE 4.29 LOCAL PEAK TEMPERATURE FOR DIFFERENT WORKPIECE THICKNESS AT DIFFERENT LOCATIONS	136
FIGURE 4.30 FLOW VELOCITY FIELD FOR DIFFERENT WORKPIECE THICKNESS AT UNDERNEATH THE SHOULDER AND THE PIN	137
FIGURE 4.31 A COMPARISON BETWEEN THE TIME DEPENDENT MAXIMUM SHEAR STRESS FOR VARIANT WORKPIECE THICKNESS AGAINST TOOL GEOMETRICAL PARAMETERS: (A) VARIANT WORKPIECE THICKNESS (B)VARIANT PIN HEIGHT (C) VARIANT PIN DIAMETER (D) VARIANT SHOULDER DIAMETER	138
FIGURE 4.32 STATIC TEMPERATURE CONTOURS FOR DIFFERENT ROTATIONAL SPEED A=237R.P.M, B=437R.P.M, C=637R.P.M, D=837R.P.M.	139
FIGURE 4.33 LIQUID FRACTION CONTOURS CORRESPONDING TO THE TEMPERATURE RISING AT DIFFERENT TIMES FOR $\omega =837$ R.P.M	140
FIGURE 4.34 MAX. GLOBAL TEMPERATURE FOR DIFFERENT ROTATIONAL SPEEDS.....	141
FIGURE 4.35 MAX. LOCAL TEMPERATURE FOR DIFFERENT ROTATIONAL SPEEDS AT DIFFERENT LOCATIONS	141
FIGURE 4.36 FLOW VELOCITY FIELD FOR DIFFERENT ROTATIONAL SPEED AT UNDERNEATH THE SHOULDER AND THE PIN	142
FIGURE 4.37 VARIATION OF THE GLOBAL MAXIMUM SHEAR STRESS ALONG THE PROCESS TIME FOR DIFFERENT ROTATIONAL SPEEDS	143
FIGURE 4.38 STATIC TEMPERATURE CONTOURS FOR DIFFERENT AXIAL LOAD A=9.7MPA, B=11.2MPA, C=12.7MPA, D=14.2MPA.	144

FIGURE 4.39 LIQUID FRACTION VARIATION CORRESPONDING TO THE TEMPERATURE RISING AT DIFFERENT TIMES FOR AXIAL LOAD = 14.2MPA	145
FIGURE 4.40 MAX. GLOBAL TEMPERATURE FOR DIFFERENT LOADS.....	146
FIGURE 4.41 MAX. LOCAL TEMPERATURE FOR DIFFERENT LOADS AT DIFFERENT LOCATIONS	146
FIGURE 4.42 FLOW VELOCITY FIELD FOR DIFFERENT AXIAL LOADS AT UNDERNEATH THE SHOULDER AND THE PIN	147
FIGURE 4.43 TIME DEPENDENT VARIATION OF THE MAXIMUM SHEAR STRESS FOR DIFFERENT AXIAL LOADS	147
FIGURE 4.44 PREDICTION MODEL OF T_{MAX}	149
FIGURE 5.1 TOOLS WITH ECCENTRIC PINS (A) HEPTAGON, (B) OCTAGON, (C) NONAGON	152
FIGURE 5.2 THE PIN ECCENTRICITY (A) ECCENTRIC HEPTAGON, (B) ECCENTRIC OCTAGON, (C) ECCENTRIC NONAGON	153
FIGURE 5.3 SCHEMATIC DRAWING OF A TOOL WITH ECCENTRIC POLYGONAL PIN	153
FIGURE 5.4 SCHEMATIC DRAWING OF THE FRICTIONAL ZONE AND THE INFINITESIMAL AREAS RELATED TO THE ECCENTRIC HEPTAGONAL PIN SIDE.....	154
FIGURE 5.5 SCHEMATIC DRAWING OF THE FRICTIONAL ZONE AND THE INFINITESIMAL AREAS RELATED TO THE ECCENTRIC HEPTAGONAL PIN TIP.....	155
FIGURE 5.6 HEAT GENERATION VALUES WITH NO. OF POLYGON FACES FOR DIFFERENT ECCENTRIC DISTANCES	159
FIGURE 5.7 TEMPERATURE DISTRIBUTION FOR THE VERTICAL PLANE AT DIFFERENT TIME STEPS CALCULATED FOR PIN ECCENTRICITIES OF 0MM AND 0.9MM.....	161
FIGURE 5.8 STATIC TEMPERATURE CONTOURS FOR DIFFERENT PIN ECCENTRICITIES $A=0MM$, $B=0.3MM$, $C=0.6MM$, $D=0.9MM$	162
FIGURE 5.9 GLOBAL PEAK TEMPERATURE FOR DIFFERENT PIN ECCENTRICITIES	163
FIGURE 5.10 MAX. LOCAL TEMPERATURE FOR DIFFERENT ECCENTRICITIES AT DIFFERENT LOCATIONS	163
FIGURE 5.11 PATHS OF THE HYPOTHETICAL POINT “O” PRODUCED BY TOOLS WITH ECCENTRICITY OF 0 AND 0.9MM.....	164
FIGURE 5.12 FLOW VELOCITY FIELD FOR DIFFERENT ECCENTRICITIES $A=0MM$, $B=0.9MM$	164
FIGURE 5.13 VARIATION OF THE GLOBAL MAXIMUM SHEAR STRESS ALONG THE PROCESS TIME FOR DIFFERENT ECCENTRICITES	165

FIGURE 5.14 TEMPERATURE DISTRIBUTION FOR THE VERTICAL PLANE AT DIFFERENT TIME STEPS CALCULATED FOR SHOULDER DIAMETERS 26MM AND 50MM IN THE EXISTENCE OF ECCENTRICITY	166
FIGURE 5.15 COMPARISON BETWEEN THE TEMPERATURE DISTRIBUTION WHEN WELDING WITH PIN ECCENTRICITY AND WITH OUT AND FOR VARIED SHOULDER SIZES	167
FIGURE 5.16 STATIC TEMPERATURE CONTOURS FOR DIFFERENT SHOULDER DIAMETERS A=26MM, B=34MM,C=42MM, D=50MM UNDER THE EFFECT OF ECCENTRICITY	168
FIGURE 5.17 GLOBAL PEAK TEMPERATURE FOR DIFFERENT SHOULDER RADIUSSES WITH ECCENTRICITY AND WITHOUT	169
FIGURE 5.18 FLOW VELOCITY FIELD FOR DIFFERENT SHOULDER DIAMETERS IN EXISTENCE OF THE ECCENTRICITY A=26MM, B=50MM.....	169
FIGURE 5.19 LOCAL PEAK TEMPERATURE FOR DIFFERENT SHOULDER RADIUSSES WITH ECCENTRICITY AND WITHOUT AT DIFFERENT LOCATION	170
FIGURE 5.20 A COMPARISON BETWEEN THE LOCAL PEAK TEMPERATURES FOR DIFFERENT SHOULDER RADIUSSES WITH ECCENTRICITY AND WITHOUT AT DIFFERENT LOCATIONS.....	170
FIGURE 5.21 A COMPARISON BETWEEN THE SHEAR STRESS VALUES WHEN USING DIFFERENT SHOULDERS AND PIN ECCENTRICITIES	171
FIGURE 5.22 TEMPERATURE DISTRIBUTION FOR THE WELD CENTRE LINED VERTICAL PLANE AT DIFFERENT TIME STEPS CALCULATED FOR PIN DIAMETERS 6MM AND 12MM IN THE EXISTENCE OF ECCENTRICITY	172
FIGURE 5.23 COMPARISON BETWEEN THE TEMPERATURE DISTRIBUTION WHEN WELDING WITH PIN ECCENTRICITY AND WITHOUT AND FOR VARIED PIN SIZES	173
FIGURE 5.24 STATIC TEMPERATURE CONTOURS FOR DIFFERENT PIN DIAMETERS A=6MM, B=12MM, C=18MM, D=24MM IN THE EXISTENCE OF ECCENTRICITY	174
FIGURE 5.25 GLOBAL PEAK TEMPERATURE FOR DIFFERENT PIN RADIUSSES WITH ECCENTRICITY AND WITHOUT.....	174
FIGURE 5.26 LOCAL PEAK TEMPERATURE FOR DIFFERENT PIN RADIUSSES WITH ECCENTRICITY AND WITHOUT AT DIFFERENT LOCATIONS	175
FIGURE 5.27 A COMPARISON BETWEEN THE LOCAL PEAK TEMPERATURES FOR DIFFERENT PIN RADIUSSES WITH ECCENTRICITY AND WITHOUT AT DIFFERENT LOCATIONS	175
FIGURE 5.28 FLOW VELOCITY FIELD FOR DIFFERENT PIN DIAMETERS AT UNDERNEATH THE PIN IN EXISTENCE OF THE ECCENTRICITY.....	176

FIGURE 5.29 A COMPARISON BETWEEN THE SHEAR STRESS VALUES WHEN USING DIFFERENT PIN SIZES AND PIN ECCENTRICITIES	176
FIGURE 5.30 TEMPERATURE DISTRIBUTION FOR THE WELD CENTRE LINED VERTICAL PLANE AT DIFFERENT TIME STEPS CALCULATED FOR PIN HEIGHTS OF 9MM AND 12MM IN THE EXISTENCE OF ECCENTRICITY	177
FIGURE 5.31 COMPARISON BETWEEN THE TEMPERATURE DISTRIBUTION WHEN WELDING WITH PIN ECCENTRICITY AND WITHOUT AND FOR VARIED PIN HEIGHTS.....	178
FIGURE 5.32 STATIC TEMPERATURE CONTOURS FOR DIFFERENT PIN HEIGHTS $A=9\text{MM}$, $B=10\text{MM}$, $C=11\text{MM}$, $D=12\text{MM}$ IN THE EXISTANCE OF ECCENTRICITY	178
FIGURE 5.33 GLOBAL PEAK TEMPERATURE FOR DIFFERENT PIN HEIGHTS WITH ECCENTRICITY AND WITHOUT.....	179
FIGURE 5.34 LOCAL PEAK TEMPERATURE FOR DIFFERENT PIN HEIGHTS WITH AND WITHOUT ECCENTRICITY AT DIFFERENT LOCATIONS.....	179
FIGURE 5.35 A COMPARISON BETWEEN THE LOCAL PEAK TEMPERATURES FOR DIFFERENT PIN HEIGHTS WITH AND WITHOUT ECCENTRICITY AT DIFFERENT LOCATIONS	180
FIGURE 5.36 A COMPARISON BETWEEN THE SHEAR STRESS VALUES WHEN USING DIFFERENT PIN HEIGHTS AND PIN ECCENTRICITIES	180
FIGURE 5.37 TEMPERATURE DISTRIBUTION FOR THE VERTICAL PLANE AT DIFFERENT TIME STEPS CALCULATED FOR WORKPIECE THICKNESS 18.7MM AND 12.7MM IN THE EXISTENCE OF ECCENTRICITY	181
FIGURE 5.38 COMPARISON BETWEEN THE TEMPERATURE DISTRIBUTION WHEN WELDING WITH AND WITHOUT PIN ECCENTRICITY AND FOR VARIED WORKPIECE THICKNESSES.....	182
FIGURE 5.39 FLOW VELOCITY FIELD FOR DIFFERENT WORKPIECE THICKNESS AT UNDERNEATH THE PIN IN EXISTENCE OF ECCENTRICITY	182
FIGURE 5.40 STATIC TEMPERATURE CONTOURS FOR DIFFERENT WORKPIECE THICKNESS $A=12.7\text{MM}$, $B=14.7\text{MM}$, $C=16.7\text{MM}$, $D=18.7\text{MM}$ IN THE EXISTENCE OF ECCENTRICITY	183
FIGURE 5.41 GLOBAL PEAK TEMPERATURE FOR DIFFERENT WORKPIECE THICKNESS WITH AND WITHOUT ECCENTRICITY.....	183
FIGURE 5.42 LOCAL PEAK TEMPERATURE FOR DIFFERENT WORKPIECE THICKNESSES WITH AND WITHOUT ECCENTRICITY AT DIFFERENT LOCATIONS	184
FIGURE 5.43 A COMPARISON BETWEEN THE LOCAL PEAK TEMPERATURES FOR DIFFERENT WORKPIECE THICKNESSES WITH AND WITHOUT ECCENTRICITY AT DIFFERENT LOCATIONS	184

FIGURE 5.44 A COMPARISON BETWEEN THE MAXIMUM SHEAR STRESS VALUES WHEN USING DIFFERENT WORKPIECE THICKNESSES AND PIN ECCENTRICITIES	185
FIGURE 5.45 STATIC TEMPERATURE CONTOURS FOR DIFFERENT ROTATIONAL SPEED A=237R.P.M, B=437R.P.M, C=637R.P.M, D=837R.P.M IN THE EXISTENCE OF ECCENTRICITY.	186
FIGURE 5.46 COMPARISON BETWEEN THE TEMPERATURE DISTRIBUTION WHEN WELDING WITH AND WITHOUT PIN ECCENTRICITY AT HIGH ROTATIONAL SPEED.	187
FIGURE 5.47 COMPARISON BETWEEN THE EVOLUTION IN THE LIQUID FRACTION WHEN WELDING WITH AND WITHOUT PIN ECCENTRICITY AT HIGH ROTATIONAL SPEED.	188
FIGURE 5.48 GLOBAL PEAK TEMPERATURE FOR DIFFERENT ROTATIONAL SPEEDS WITH AND WITHOUT ECCENTRICITY	189
FIGURE 5.49 LOCAL PEAK TEMPERATURE FOR DIFFERENT ROTATIONAL SPEEDS WITH AND WITHOUT ECCENTRICITY AT DIFFERENT LOCATIONS	189
FIGURE 5.50 A COMPARISON BETWEEN THE LOCAL PEAK TEMPERATURES FOR DIFFERENT ROTATIONAL SPEEDS WITH AND WITHOUT ECCENTRICITY AT DIFFERENT LOCATIONS	189
FIGURE 5.51 A COMPARISON BETWEEN THE MAXIMUM SHEAR STRESS VALUES WHEN USING DIFFERENT ROTATIONAL SPEEDS AND PIN ECCENTRICITIES	190
FIGURE 5.52 TEMPERATURE DISTRIBUTION FOR THE VERTICAL PLANE AT DIFFERENT TIME STEPS CALCULATED FOR AXIAL LOADS 9.7MPa AND 12.7 MPa IN THE EXISTENCE OF ECCENTRICITY	191
FIGURE 5.53 STATIC TEMPERATURE CONTOURS FOR DIFFERENT AXIAL LOAD A=9.7MPa, B=11.2MPa, C=12.7MPa, D=14.2MPa IN THE EXISTENCE OF ECCENTRICITIES	192
FIGURE 5.54 GLOBAL PEAK TEMPERATURE FOR DIFFERENT AXIAL LOADS WITH AND WITHOUT ECCENTRICITY	193
FIGURE 5.55 LOCAL PEAK TEMPERATURE FOR DIFFERENT AXIAL LOADS WITH AND WITHOUT ECCENTRICITY AT DIFFERENT LOCATIONS	193
FIGURE 5.56 A COMPARISON BETWEEN THE LOCAL PEAK TEMPERATURES FOR DIFFERENT AXIAL LOADS WITH AND WITHOUT ECCENTRICITY AT DIFFERENT LOCATIONS	193
FIGURE 5.57 A COMPARISON BETWEEN THE MAXIMUM SHEAR STRESS VALUES WHEN USING DIFFERENT AXIAL LOADS AND PIN ECCENTRICITIES	194
FIGURE 5.58 PREDICTION MODEL OF T_{MAX} IN EXISTENCE OF ECCENTRICITY	196
FIGURE 6.1 TOOLS WITH TAPERED AND ECCENTRIC PINS (A) HEPTAGON, (B) OCTAGON, (C) NONAGON.....	199

FIGURE 6.2 SCHEMATIC DRAWING OF A TOOL WITH TAPERED ECCENTRIC POLYGONAL PIN	200
FIGURE 6.3 SCHEMATIC DRAWING OF THE FRICTIONAL ZONE AND THE INFINITESIMAL AREAS RELATED TO THE TAPERED ECCENTRIC HEPTAGONAL PIN SIDE	201
FIGURE 6.4 HEAT GENERATION VALUES WITH NO. OF POLYGON FACES FOR DIFFERENT TAPERING ANGLES AND ECCENTRIC DISTANCES	208
FIGURE 6.5 TEMPERATURE DISTRIBUTION FOR THE VERTICAL PLANE AT DIFFERENT TIME STEPS CALCULATED FOR PIN TAPER ANGLES OF $\Gamma=0^\circ$ AND $\Gamma=21^\circ$ AND $E=0.9\text{MM}$	212
FIGURE 6.6 TEMPERATURE DISTRIBUTION FOR THE VERTICAL PLANE AT DIFFERENT TIME STEPS CALCULATED FOR PIN TAPER ANGLES OF $\Gamma=0^\circ$ AND $\Gamma=21^\circ$ AND $E=0\text{MM}$	213
FIGURE 6.7 STATIC TEMPERATURE CONTOURS FOR DIFFERENT PIN TAPER ANGLE $A=\Gamma=0^\circ$, $B=$ $\Gamma=7^\circ$, $C=\Gamma=14^\circ$, $D=\Gamma=21^\circ$	214
FIGURE 6.8 GLOBAL PEAK TEMPERATURE FOR DIFFERENT PIN TAPER ANGLES	215
FIGURE 6.9 MAX. LOCAL TEMPERATURE FOR DIFFERENT TAPER ANGLES AT DIFFERENT LOCATIONS	215
FIGURE 6.10 A COMPARISON BETWEEN THE FLOW FIELD UNDER THE PIN WITH AND WITHOUT TAPER ANGLES	216
FIGURE 6.11 VARIATION OF THE GLOBAL MAXIMUM SHEAR STRESS ALONG THE PROCESS TIME FOR DIFFERENT TAPER ANGLES	217
FIGURE 6.12 TEMPERATURE DISTRIBUTION FOR THE VERTICAL PLANE AT DIFFERENT TIME STEPS CALCULATED AT THE SAME TAPER ANGLE FOR PIN ECCENTRICITIES OF 0MM AND 0.9MM	218
FIGURE 6.13 STATIC TEMPERATURE CONTOURS FOR DIFFERENT PIN ECCENTRICITIES $A=0\text{MM}$, $B=0.3\text{MM}$, $C=0.6\text{MM}$, $D=0.9\text{MM}$ IN THE EXISTENCE OF TAPER ANGLE	219
FIGURE 6.14 GLOBAL PEAK TEMPERATURE FOR DIFFERENT PIN ECCENTRICITIES WHEN $\Gamma=0^\circ$ AND $\Gamma=21^\circ$	220
FIGURE 6.15 LOCAL PEAK TEMPERATURE FOR DIFFERENT PIN ECCENTRICITIES WHEN $\Gamma=0^\circ$ AND $\Gamma=21^\circ$	220
FIGURE 6.16 A COMPARISON BETWEEN THE LOCAL PEAK TEMPERATURES FOR DIFFERENT PIN ECCENTRICITIES WITH TAPER ANGLE AND WITHOUT AT DIFFERENT LOCATIONS.....	221
FIGURE 6.17 A COMPARISON BETWEEN THE SHEAR STRESS VALUES WHEN USING PIN ECCENTRICITIES AND PIN TAPER ANGLES	222
FIGURE 6.18 TEMPERATURE DISTRIBUTION FOR THE VERTICAL PLANE AT DIFFERENT TIME STEPS CALCULATED FOR SHOULDER DIAMETERS 26MM AND 50MM IN THE EXISTENCE OF TAPER ANGLE AND ECCENTRICITY	223

FIGURE 6.19 COMPARISON BETWEEN THE TEMPERATURE DISTRIBUTION WHEN WELDING WITH PIN TAPER ANGLE AND WITHOUT WHEN $R_s=13\text{MM}$ AND $R_s=25\text{MM}$	224
FIGURE 6.20 STATIC TEMPERATURE CONTOURS FOR DIFFERENT SHOULDER DIAMETERS $A=26\text{MM}$, $B=34\text{MM}$, $C=42\text{MM}$, $D=50\text{MM}$ UNDER THE EFFECT OF PIN TAPER ANGLE AND ECCENTRICITY	225
FIGURE 6.21 GLOBAL PEAK TEMPERATURE FOR DIFFERENT SHOULDER RADIUSES WITH TAPER ANGLE AND WITHOUT	225
FIGURE 6.22 LOCAL PEAK TEMPERATURE FOR DIFFERENT SHOULDER RADIUSES WITH TAPER ANGLE AND WITHOUT AT DIFFERENT LOCATION	226
FIGURE 6.23 A COMPARISON BETWEEN THE LOCAL PEAK TEMPERATURES FOR DIFFERENT SHOULDER RADIUSES WITH TAPER ANGLE AND WITHOUT AT DIFFERENT LOCATIONS	226
FIGURE 6.24 FLOW VELOCITY FIELD FOR DIFFERENT SHOULDER DIAMETERS IN EXISTENCE OF THE TAPER ANGLE $A=26\text{MM}$, $B=50\text{MM}$	227
FIGURE 6.25 A COMPARISON BETWEEN THE SHEAR STRESS VALUES WHEN USING DIFFERENT SHOULDERS AND PIN TAPER ANGLES	227
FIGURE 6.26 TEMPERATURE DISTRIBUTION FOR THE WELD CENTRE LINED VERTICAL PLANE AT DIFFERENT TIME STEPS CALCULATED FOR PIN TOP DIAMETERS 12MM AND 24MM IN THE EXISTENCE OF PIN TAPER ANGLE AND ECCENTRICITY	228
FIGURE 6.27 COMPARISON BETWEEN THE TEMPERATURE DISTRIBUTION WHEN WELDING WITH PIN TAPER ANGLE AND WITHOUT FOR $R_{PT}=6\text{MM}$ AND $R_{PT}=12\text{MM}$	229
FIGURE 6.28 STATIC TEMPERATURE CONTOURS FOR DIFFERENT PIN TOP BASE DIAMETERS $A=12\text{MM}$, $B=18\text{MM}$, $C=24\text{MM}$ IN THE EXISTENCE OF PIN TAPER ANGLE AND ECCENTRICITY	230
FIGURE 6.29 GLOBAL PEAK TEMPERATURE FOR DIFFERENT PIN TOP BASE RADIUSES WITH TAPER ANGLE AND WITHOUT	230
FIGURE 6.30 LOCAL PEAK TEMPERATURE FOR DIFFERENT PIN RADIUSES WITH TAPER ANGLE AND WITHOUT AT DIFFERENT LOCATION	231
FIGURE 6.31 COMPARISON BETWEEN THE LOCAL PEAK TEMPERATURES FOR DIFFERENT PIN RADIUSES WITH TAPER ANGLE AND WITHOUT AT DIFFERENT LOCATIONS	231
FIGURE 6.32 A COMPARISON BETWEEN THE SHEAR STRESS VALUES WHEN USING DIFFERENT PIN SIZES AND PIN TAPER ANGLES	232

FIGURE 6.33 TEMPERATURE DISTRIBUTION FOR THE WELD CENTRE LINED VERTICAL PLANE AT DIFFERENT TIME STEPS CALCULATED FOR PIN HEIGHTS OF 9MM AND 12MM IN THE EXISTENCE OF PIN TAPER ANGLE AND ECCENTRICITY.....	233
FIGURE 6.34 COMPARISON BETWEEN THE TEMPERATURE DISTRIBUTION WHEN WELDING WITH PIN TAPER ANGLE AND WITHOUT AND FOR $H_p=9\text{MM}$ AND $H_p=12\text{MM}$	234
FIGURE 6.35 STATIC TEMPERATURE CONTOURS FOR DIFFERENT PIN HEIGHTS $A=9\text{MM}$, $B=10\text{MM}$, $C=11\text{MM}$, $D=12\text{MM}$ IN THE EXISTENCE OF PIN TAPER ANGLE AND ECCENTRICITY.....	234
FIGURE 6.36 GLOBAL PEAK TEMPERATURE FOR DIFFERENT PIN HEIGHTS WITH PIN TAPER ANGLE AND WITHOUT.....	235
FIGURE 6.37 LOCAL PEAK TEMPERATURE FOR DIFFERENT PIN HEIGHTS WITH AND WITHOUT PIN TAPER ANGLE AT DIFFERENT LOCATIONS.....	236
FIGURE 6.38 A COMPARISON BETWEEN THE LOCAL PEAK TEMPERATURES FOR DIFFERENT PIN HEIGHTS WITH AND WITHOUT PIN TAPER ANGLE AT DIFFERENT LOCATIONS.....	236
FIGURE 6.39 A COMPARISON BETWEEN THE SHEAR STRESS VALUES WHEN USING DIFFERENT PIN HEIGHTS AND PIN TAPER ANGLES.....	237
FIGURE 6.40 TEMPERATURE DISTRIBUTION FOR THE VERTICAL PLANE AT DIFFERENT TIME STEPS CALCULATED FOR WORKPIECE THICKNESS 18.7MM AND 12.7MM IN THE EXISTENCE OF PIN TAPER ANGLE AND ECCENTRICITY.....	238
FIGURE 6.41 COMPARISON BETWEEN THE TEMPERATURE DISTRIBUTION WHEN WELDING WITH AND WITHOUT PIN TAPER ANGLE FOR VARIED WORKPIECE THICKNESSES.....	238
FIGURE 6.42 STATIC TEMPERATURE CONTOURS FOR DIFFERENT WORKPIECE THICKNESS $A=12.7\text{MM}$, $B=14.7\text{MM}$, $C=16.7\text{MM}$, $D=18.7\text{MM}$ IN THE EXISTENCE OF PIN TAPER ANGLE AND ECCENTRICITY.....	239
FIGURE 6.43 GLOBAL PEAK TEMPERATURE FOR DIFFERENT WORKPIECE THICKNESS WITH AND WITHOUT PIN TAPER ANGLE.....	240
FIGURE 6.44 LOCAL PEAK TEMPERATURE FOR DIFFERENT WORKPIECE THICKNESSES WITH AND WITHOUT TAPER ANGLE AT DIFFERENT LOCATIONS.....	240
FIGURE 6.45 A COMPARISON BETWEEN THE LOCAL PEAK TEMPERATURES FOR DIFFERENT WORKPIECE THICKNESSES WITH AND WITHOUT TAPER ANGLE AT DIFFERENT LOCATIONS.....	240
FIGURE 6.46 A COMPARISON BETWEEN THE MAXIMUM SHEAR STRESS VALUES WHEN USING DIFFERENT WORKPIECE THICKNESSES AND PIN TAPER ANGLES.....	241

FIGURE 6.47 STATIC TEMPERATURE CONTOURS FOR DIFFERENT ROTATIONAL SPEED A=237R.P.M, B=437R.P.M, C=637R.P.M, D=837R.P.M IN THE EXISTENCE OF PIN TAPER ANGLE AND ECCENTRICITY.	242
FIGURE 6.48 COMPARISON BETWEEN THE TEMPERATURE DISTRIBUTION WHEN WELDING WITH AND WITHOUT PIN TAPER ANGLE AT HIGH ROTATIONAL SPEED.	243
FIGURE 6.49 COMPARISON BETWEEN THE EVOLUTION IN THE LIQUID FRACTION WHEN WELDING WITH AND WITHOUT PIN TAPER ANGLE AT HIGH ROTATIONAL SPEED.	244
FIGURE 6.50 GLOBAL PEAK TEMPERATURE FOR DIFFERENT ROTATIONAL SPEEDS WITH AND WITHOUT TAPER ANGLE	245
FIGURE 6.51 LOCAL PEAK TEMPERATURE FOR DIFFERENT ROTATIONAL SPEEDS WITH AND WITHOUT TAPER ANGLE AT DIFFERENT LOCATIONS	245
FIGURE 6.52 A COMPARISON BETWEEN THE LOCAL PEAK TEMPERATURES FOR DIFFERENT ROTATIONAL SPEEDS WITH AND WITHOUT PIN TAPER ANGLE AT DIFFERENT LOCATIONS .	246
FIGURE 6.53 FLOW VELOCITY FIELD FOR DIFFERENT ROTATIONAL SPEED AT UNDERNEATH THE SHOULDER IN EXISTENCE OF THE TAPER ANGLE	246
FIGURE 6.54 A COMPARISON BETWEEN THE MAXIMUM SHEAR STRESS VALUES WHEN USING DIFFERENT ROTATIONAL SPEEDS AND PIN TAPER ANGLES	247
FIGURE 6.55 TEMPERATURE DISTRIBUTION FOR THE VERTICAL PLANE AT DIFFERENT TIME STEPS CALCULATED FOR AXIAL LOADS 9.7MPa AND 12.7 MPa IN THE EXISTENCE OF TAPER ANGLE	248
FIGURE 6.56 COMPARISON BETWEEN THE TEMPERATURE DISTRIBUTION WHEN WELDING WITH AND WITHOUT PIN TAPER ANGLE FOR AXIAL LOADS OF 9.7MPa AND 12.7MPa	249
FIGURE 6.57 STATIC TEMPERATURE CONTOURS FOR DIFFERENT AXIAL LOAD A=9.7MPa, B=11.2MPa, C=12.7MPa, D=14.2MPa IN THE EXISTENCE OF PIN TAPER ANGLE	250
FIGURE 6.58 GLOBAL PEAK TEMPERATURE FOR DIFFERENT AXIAL LOADS WITH AND WITHOUT TAPER ANGLE.....	250
FIGURE 6.59 LOCAL PEAK TEMPERATURE FOR DIFFERENT AXIAL LOADS WITH AND WITHOUT TAPER ANGLE AT DIFFERENT LOCATIONS	251
FIGURE 6.60 A COMPARISON BETWEEN THE LOCAL PEAK TEMPERATURES FOR DIFFERENT AXIAL LOADS WITH AND WITHOUT TAPER ANGLE AT DIFFERENT LOCATIONS	251
FIGURE 6.61 A COMPARISON BETWEEN THE MAXIMUM SHEAR STRESS VALUES WHEN USING DIFFERENT AXIAL LOADS AND PIN TAPER ANGLES	251
FIGURE 6.62 PREDICTION MODEL OF T_{MAX} IN EXISTENCE OF PIN TAPER ANGLE.....	253

List of Tables

TABLE 3-1 DYNAMIC MESH SETTINGS.....	93
TABLE 3-2 WORKPIECE COMPOSITION. [27].....	96
TABLE 3-3 THERMOPHYSICAL PROPERTIES OF THE WORKPIECE. [27].....	96
TABLE 3-4 MATERIAL CONSTANT AND OTHER VALUES FOR AA6061. [27].....	96
TABLE 3-5 MESH INDEPENDENCE RESULTS	98
TABLE 3-6 TIME STEP INDEPENDENCE RESULTS	100
TABLE 4-1 HEAT GENERATION FORMULAS OF TOOLS WITH DIFFERENT PIN PROFILES	112
TABLE 4-2 PROCESS PARAMETERS AND THEIR RANGES.....	116
TABLE 5-1 HEAT GENERATION FORMULAS OF TOOLS WITH DIFFERENT ECCENTRIC PIN PROFILES	157
TABLE 5-2 THE PROPOSED NUMERICAL EXPERIMENTS AND RANGES OF PARAMETERS	160
TABLE 6-1 HEAT GENERATION FORMULAS OF TOOLS WITH DIFFERENT TAPERED ECCENTRIC PIN PROFILES (NO. OF FACES FROM 7 TO 12).....	205
TABLE 6-2 HEAT GENERATION FORMULAS OF TOOLS WITH DIFFERENT TAPERED ECCENTRIC PIN PROFILES (NO. OF FACES FROM 13 AND UPWARD).....	206
TABLE 6-3 DETAILS OF THE DESIGNED NUMERICAL EXPERIMENTS(FROM EX1 TO EX.13).....	209
TABLE 6-4 DETAILS OF THE DESIGNED NUMERICAL EXPERIMENTS(FROM EX14 TO EX.25).....	210

NOMENCLATURE

V	Tool Translational speed (m/sec)
F	Downward Force (N)
P	Contact (Axial) Pressure (Pa)
Q	Heat generated amount (W)
k	Thermal Conductivity (W/(m.K))
T	Temperature (K)
T_a	The ambient Temperature (K)
h	Convective Heat Transfer Coefficient (W/m ² .K)
Z	The Zener-Hollomon Parameter
\dot{A}	Material Constant (1/sec)
n	Material Constant
\dot{Q}	Activation Energy (KJ/mol)
R	Universal Gas Constant (J/mol.K)
cp	Specific Heat (J/kg. K)
HL	Enthalpy (J)
hl	Sensible Enthalpy (J)
T_{ref}	Reference Temperature (K)
LT	Latent Heat (J)
x_1	TMAZ Design Variable (m)
x_2	TMAZ Design Variable (m)
R_s	Shoulder Radius (m)
R_p	Pin Radius (m)

R_{pt}	Pin Top Base Radius (m)
R_{pb}	Pin Bottom Base Radius (m)
H	Pin Height (m)
N	Number of Pin Side Faces
C	Courant number
Δt	Time Step (sec)
Δx	The spacing of the grid in the numerical model
a	The pin side length
s	Apothem
e	Eccentricity Distance

GREEK SYMBOLS

ω	Tool Rotational Speed (r.p.m)
β	Liquid Fraction
$\tau_{contact}$	Contact Shear Stress (Pa)
$\tau_{friction}$	Frictional Shear Stress (Pa)
μ	Friction Coefficient
ε	The Stefan-Boltzmann Constant ($W/m^2 \cdot K^4$)
σ_E	The effective stress (Pa)
α	Material Constant (MPa^{-1})
$\dot{\varepsilon}$	Strain Rate
η	The fluid Viscosity (Pa.sec)
ρ	Material Density (kg/m^3)
π	Pi
γ	Taper Angle

SUBSCRIPTS

<i>a</i>	Ambient
<i>E</i>	Effective
<i>x</i>	The property in the direction of <i>x</i>
<i>y</i>	The property in the direction of <i>y</i>
<i>z</i>	The property in the direction of <i>z</i>
<i>total</i>	The total heat generated from the tool (W)

ACRONYM

FSW	Friction Stir Welding
SSW	Solid-State Welding
TMAZ	Thermo-mechanical Affected Zone
FVM	Finite Volume Method
HAZ	Heat Affected Zone
UDF	User Defined Function
SIMPLE	Semi-Implicit Method for Pressure Linked Equations
PRESTO	Pressure Staggering Option

CHAPTER 1: INTRODUCTION

In manufacturing and production processes, welding and joining of materials are highly demanded. Welding is a process in which the heat or heat and pressure are used to join two or more pieces of similar or dissimilar materials. In the conventional welding processes, the material is heated to melt along the joint line and then cooled to solidify where the welded joint is formed. In view of the welding heat input, material conditions and dimensions, those welding processes could fail to produce a sound welded joint. Therefore, alternative processes have been developed. Friction Stir Welding (FSW) is a relatively new process which is increasingly utilised particularly for those alloys that are difficult to be welded by the conventional welding processes. However, much remains to be carried out for improving of FSW in terms of applicability and quality. Accordingly, a better understanding of the several physical phenomena during the process is essential. Hence, this chapter presents a detailed introduction to friction stir welding regarding the basic principles and the process applications as well as its advantages and disadvantages. Then, the most important variables of the process and their effects will be provided. This is followed by a discussion of the approaches that can be used to study FSW technique. Finally, the motivation for conducting the current work is given which defines the main research aims.

1.1 Solid-State Welding

When joining metals, the procedures can be differentiated into solid state bonding, fusion welding, brazing, soldering and adhesive bonding. When the melting of the sides of the work piece occurs during fusion welding processes, the pieces of metal are joined after the molten puddle solidifies. This is the stage where a filler metal might be introduced. In brazing and soldering, the filler metal is drawn in between the parts to be joined after it melts, which has a melting temperature less than the base metals. Glue is the filler material in adhesion and bonding. Concerning solid state methods, the joint can be formed by deformation or atomic diffusion where the melting will not occur in any way [1, 2].

In SSW (Solid-State Welding), the coalescence occurs between the faying surfaces at temperature below the melting temperature of the base metals where the joining area devoid of any filler metal. SSW is more relevant when it is necessary to join different metals, particularly for those applications that demand dissimilar material properties. In these processes, the key factors are the pressure and deformation which play a significant role in the provision bonding. In some SSW techniques such as the rotary friction welding, the tops and bottoms of the abutting surfaces are locally distorted because of the high pressure where the diffusion bonding is formed. In some others like Friction Stir Welding (FSW), the deformation bonding is produced where the applied pressures are greater than material yield strength which lead to a huge deformation [1, 2].

1.2 Friction Welding

Friction welding is solid-state welding which has various types such as rotary friction welding, linear friction welding, orbital friction welding and friction stir welding. In the rotary friction welding, diverse types of relative motion can be used to produce the friction needed to accomplish the weld. Hence, several mechanisms have been employed like the inertia-drive welding and the direct- drive welding. This is where one component is kept stationary as the other is rotated or the two components are rotated in opposite directions. Figure 1.1, shows a sample welded by the rotary friction welding.

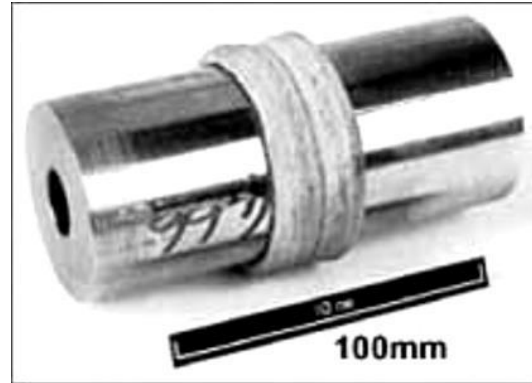


Figure 1.1 Rotary Friction Welding[3]

Figure 1.2, shows the direct- drive welding process which has three significant phases where the first phase is a friction phase whereby the heat is produced. In the second one, the rotation is terminated, and it is known as a stopping (Breaking) phase. Then, the forging phase in which the pieces are joined using the pressure. The axial pressure and the rotational speed are the major process variables as a function of time[3].

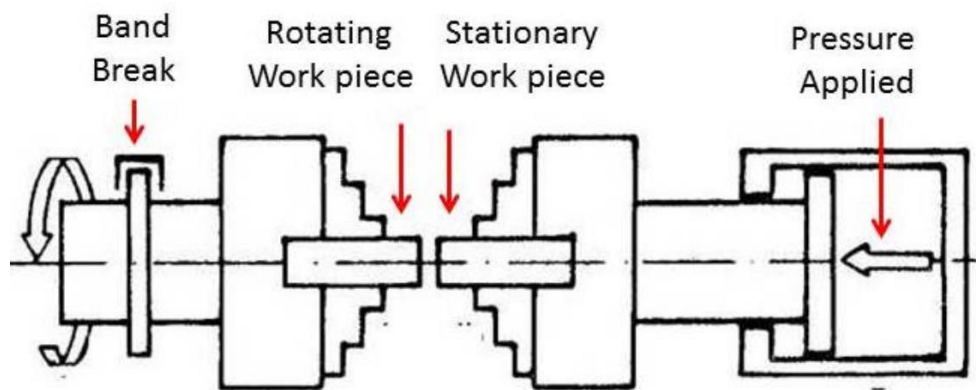


Figure 1.2 Direct – Drive rotary friction welding[4]

As shown in figure 1.3, the same machine is utilised for the inertia-drive welding where the only difference is that the flywheel in inertia-drive welding machine is tied to the spindle that holds the rotating piece. Therefore, the energy input is regulated by the flywheel which means the momentum of inertia is a very important variable. This difference results in making a continuous decline in friction speed in the friction phase, whereby the axial pressure and the friction speed are also significant variables[3].

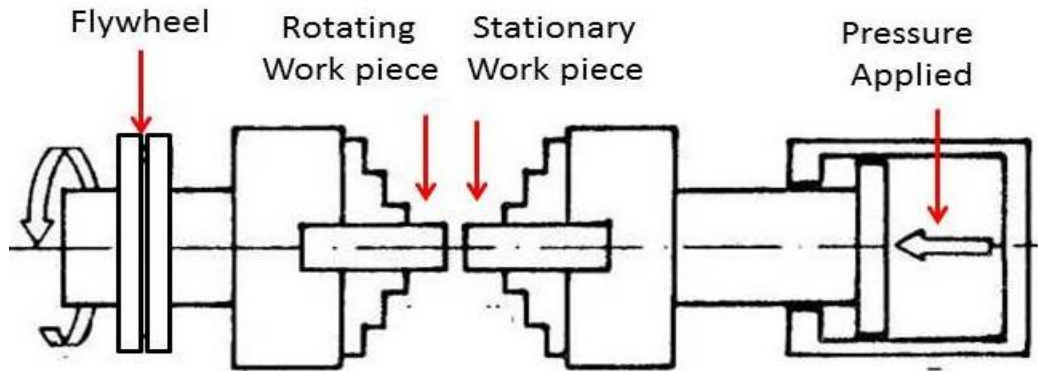


Figure 1.3 Inertia – Drive rotary friction welding[4]

Apart from the above techniques, the linear and orbital friction welding have been developed for special part geometries. In linear friction welding, the oscillating motion is relative between the parts to be welded while the parts rotate in the same direction in the orbital friction welding but with their axes offset by certain distance [3]. Figure 1.4, depicts the different motions in the linear and orbital friction welding.

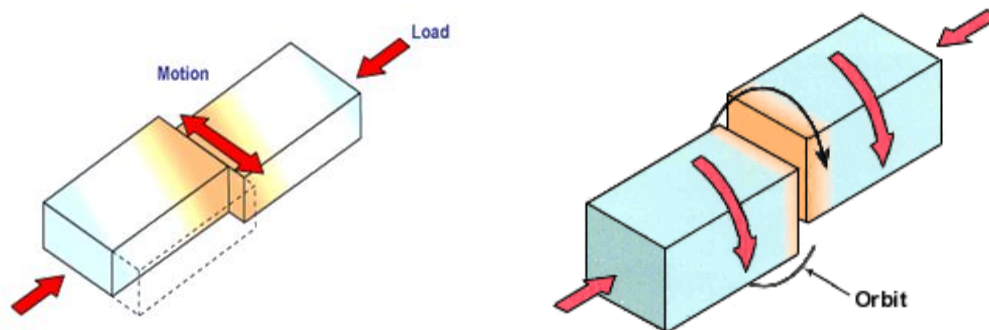


Figure 1.4 Linear and orbital friction welding[5]

1.3 Friction stir welding

Friction Stir Welding (FSW) was patented in 1991 by The Welding Institute, Cambridge, UK. It is a novel solid-state welding process where the first welded material was Aluminium. In FSW process a non-consumable rotary tool consisting a shoulder and a pin is brought in between the adjacent plates needed to be welded. This stage is called plunging, where the tool penetrates gradually in the workpiece due to the axial load applied by machine. Then, dwelling stage in which the tool keeps rotating in the same position where the material is preheated. After that the tool is forced to move along the joint line in the welding stage. Figure 1.5, demonstrates the key features

of FSW in a butt joint where the main regions of the welded zone are included. When the tool rotates anticlockwise or clockwise and moves with a certain speed, the advancing side can be described as the region where the rotational movement is in the similar direction of the translational movement. The retreating side will be on the faced region where the rotational movement is in the converse direction of the translational movement. There are three major functions for the tool which are the heat generation and the material stirring to form the joint as well as suppressing of the hot material by the tool shoulder so that it is not flushed away [1].

Apart from the friction between the work piece and the tool, the severe plastic deformation also creates heat. That can be understood as the material surround the pin is softened by the localized heating and then affected by the tool rotation and translation. A solid state joint will be created according to the proper control of the tool action and the influence on the work piece [1]. Figure 1.5, shows the tool main parts and the different important areas in the work piece and the welded joint.

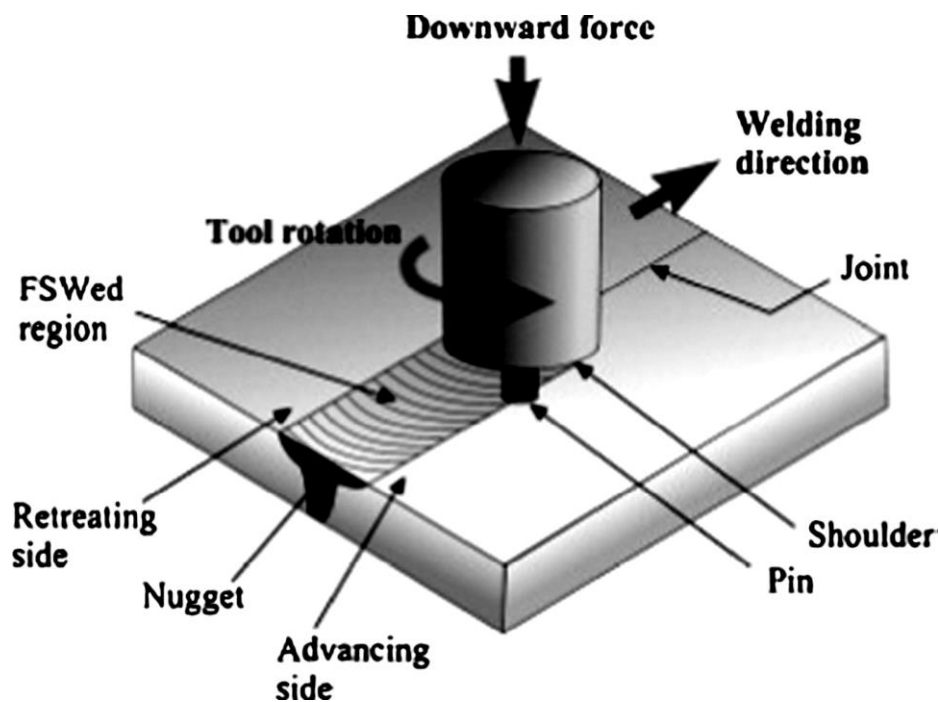


Figure 1.5 Friction stir welding in a butt joint[6]

1.3.1 Definitions

Tool shoulder: this is the part of the tool that contacts the work piece at the surface. The tool shoulder might have scrolls negatively or positively to boost the inward flow of material. The positive one is a superficial growth but the negative one is a depression in its surface. The outer surface of the shoulder is commonly designed to be in a cylindrical shape while the bottom surface can be flat, concave or convex[1].

Tool pin (probe): this is the part of the tool that is inserted into the work piece. The most common pin profiles are the conical and cylindrical profiles. The pin can also be designed to be threaded or with a step spiral design [1].

Leading edge: this is the section where the shoulder joins the cold work piece material and it is represented at the front side of the tool [1].

Trailing edge: it is the rear side of tool which affects the micro-structural evolution particularly after the material deforming by the pin. The reason is that the trailing part keeps pumping the heat to the work piece even after the pin has passed the region[1].

Tool rotational and translational rates: these are defined as the speeds at which the tool rotates and travel along the joint line respectively [1].

Tilt angle: as shown in figure 1.6 ,it is the angle of inclination of the spindle shaft on the plane normal to the workpiece [1].

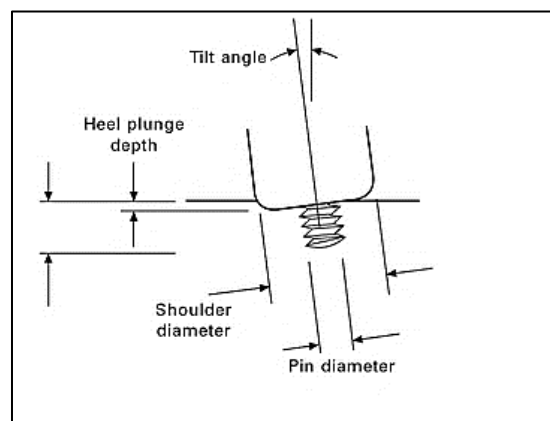


Figure 1.6 Tilt angle [7]

Plunge depth and plunge rate: Plunge depth can be defined as the maximum penetration of the tool shoulder into the workpiece while the plunge rate is the rate at which the tool is introduced into the workpiece [1].

Plunge force: It is the vertical force applied on the tool which is necessary to keep the tool position at / below the workpiece surface [1].

Parent metal: these are material parts that are far away from the weld and have not been thermally affected (microstructure or mechanical properties) or distorted [1].

Heat affected zone (HAZ): it is the section that takes place near the weld centre and it has undergone modification in terms of the mechanical properties or the microstructure due to the effect of the thermal cycle [1].

Thermo-mechanically affected zone (TMAZ): this is a section where some of the thermal influences and the plastic distortion occur because of the friction stir welding tool and the heat generated [1].

Weld nugget: this is the region that is totally re-crystallized [1].

In figure 1.7, the above discussed zones and their locations are clearly depicted related to each other.

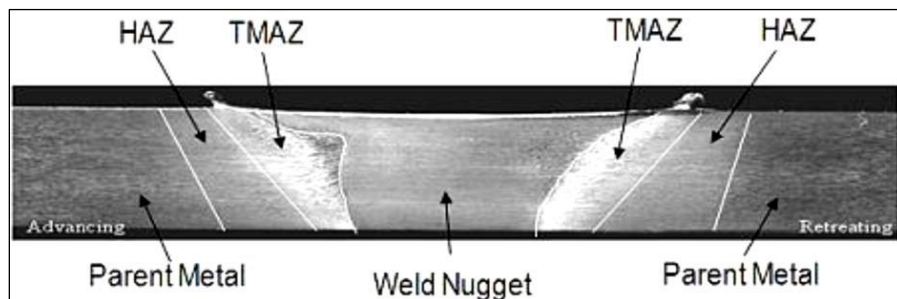


Figure 1.7 Friction stir welding zone [8]

1.3.2 Advantages and limitations

No melting occurs in friction stir welding as the maximum temperatures in friction stir welding are lower than those in the conventional welding [6]. FSW is considered a green technology due to its energy efficiency and environmental friendliness. This is because there are no dangerous emissions as the consumable materials like shielding gases and fluxes are not used. The

solidification cracking and incompatibility of composition are also not expected since the filler metals are not used. Furthermore, this manufacturing process can be used in joining of different materials. It's clear that FSW has obtained a significant value because of its capability of welding those materials that are not possible to be welded by fusion, like; high strength aluminium alloys, including 2XXX series (Copper principle alloying element) and 7XXX series (Zinc-magnesium) [1]. Below are more benefits of FSW that are listed by the welding institute (TWI) [5].

- Low distortion and shrinkage, even in the long welds.
- Outstanding mechanical properties in fatigue, tensile and bend test.
- Devoid of spatter.
- Does not have porosity.
- Capable of working in all positions. Has neither pickling, grinding nor brushing in a mass production.
- Diverse kinds of joints can be welded and extensive variety of thickness.

Despite of all mentioned advantages, FSW requires large forces to press and move the tool. Consequently, to accomplish the welding process accurately the workpiece needs to be strongly clamped as well as the rigidity of the equipment must be high. Compared to the manual welding processes, FSW has lack in flexibility which leads to difficulty when the welds are not linear and when the workpiece thickness is varied. The exit hole that takes place at the end of the weld, the quick tool worn out and the relative slow traverse rate are considered limitations as well [9].

1.3.3 Applications of friction stir welding

Although, friction stir welding is relatively new process compared to the conventional welding processes it has experienced a rapid utilisation in a wide variety of applications. As it was mentioned before that aluminium was the first welded material by FSW and day by day it appeared to be appropriate to most of aluminium alloys particularly high strength aluminium. Besides, FSW can be used to join materials such as copper, lead, magnesium, zinc, titanium and steel [10].

To some extent, riveting was replaced by FSW in the aerospace industry where the costs of manufacturing has decreased. Thus, structures and components like fuselages, wings, empennages and fuel tanks have been effectively welded [10]. In the automotive industry, reducing the body weight and the energy consumption are common demands. That has made the manufacturers

thinking seriously in using of the lightweight alloys such as aluminium with the aid of friction stir welding. Hence, FSW was integrated into manufacturing of different components such door and floor panels, drive shafts, and space frames. Encouragingly, the results in some cases revealed that the new body of vehicle is stiffer than the precursor and lighter by 110kg. For its efficiency in welding of large components with less residual stresses and distortions, FSW has been employed in naval applications. Different materials and components have been successfully welded particularly those aluminium shipboard panels that are assembled by single sided FSWs of long extruded profiles [11].



Figure 1.8 Different applications of Friction Stir Welding [5, 12]

1.3.4 Process parameters

FSW is regulated by certain variables just like any other welding process. These variables are the tool rotational speed ω , the welding traverse speed V , the downward force F , the tool design and the tilt angle θ . Stirring of the material around the tool results from the rotation of the tool but this stirred material is moved from the front to the back of the pin by the translation of the tool. It is

worth to mention that the weld quality is also affected by the axial pressure, that can be understood as the overheating and the thinning of the joint might be consequences of applying very high pressures while the low pressures lead to inadequate heating and cavities. The main role of the tilt angle is to produce a sound weld with smooth tool shoulder [13].

One of the most important variables which directly influence the power needed for the process, heat generation, and the homogeneity of the welded joint and plastic flow is the tool design. When it comes to welding of thin plates, the shoulder surface has the major part in generation of heat by friction whereas in thicker plates; the pin role becomes more efficient at the same time. Any change in the tool form could influence the whole welding process or at least affect the major role of the tool. For instance, the pressure under the shoulder is boosted through the tool with a conical shoulder while the shoulder concavity works to contain the displaced material due to the plunging action [13]. Figure 1.9, shows the interaction between the workpiece material and the welding tool which consists a conical shoulder and a threaded pin.

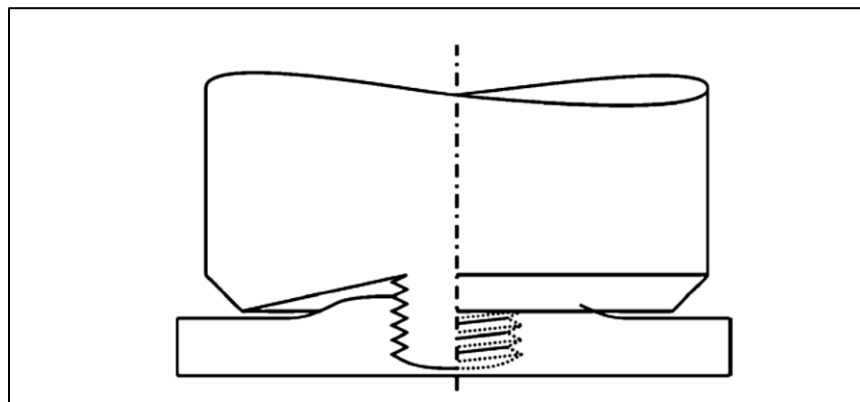


Figure 1.9 FSW with a tool consists a conical shoulder and a threaded probe [13]

Many studies have been carried out in order to investigate the effects of tool geometry in friction stir welding. In those works, different developments were suggested and examined where the shoulder and the pin shapes have been considered as the main criteria in the development. Regarding the shoulder, the side and the bottom surfaces are mainly used to modify the shoulder shape. In view of that, the straight cylindrical shape is typically used for the side surface while the conical one is sometimes used. For the shoulder bottom surface, three different types have been commonly employed which are flat, concave, and convex. Despite the fact that the flat is the simplest design and the smooth convex is successfully used in certain conditions, the concave

profile has become the most popular because of the advantages. i.e. preventing the material escaping away from the shoulder sides, enhancement of material stirring and nugget integrity by introducing higher forging pressures. From another point of view, it was approved that the end features of the shoulder increase the frictional activity and deformation which in role improve the heat generation, material movement, and weld quality. Smooth or featureless, scrolls, ridges, knurling, grooves and concentric circles were some of the suggested profile which can be applied for the above mentioned types of the shoulder bottom surface [14, 15].

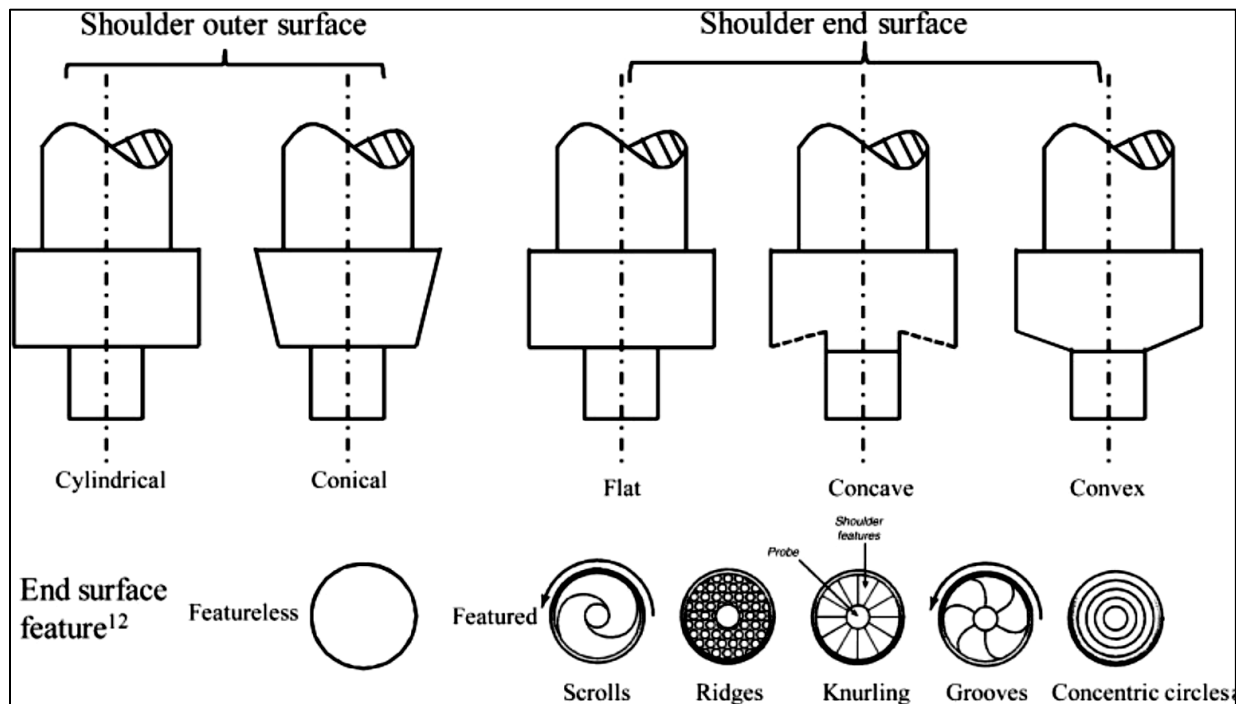


Figure 1.10 Shoulder shapes and features[14]

The pin shape is no less important than the shoulder where it can affect deformational and frictional heating as well as playing a major role in obtaining desirable weld. The pin bottom surface might be flat or rounded; the rounded surface helps to increase the life of the tool through the eliminating of local stresses while the forge force is reduced. However, the flat bottom is mostly used which can be attributed to the high forge force and the simplicity of manufacturing. Concerning the pin side surface, cylindrical and tapered shapes are used but the cylindrical is usually used particularly for low thick materials. Improving of the process performance may be through the pin side surface where it could also have features including threads, flats or flutes. Over the last period, numerous pin profiles have been suggested and examined based on the pin shape, dimension, and position;

however, there is still an opportunity for designing new effective tools which would develop FSW [14, 16].

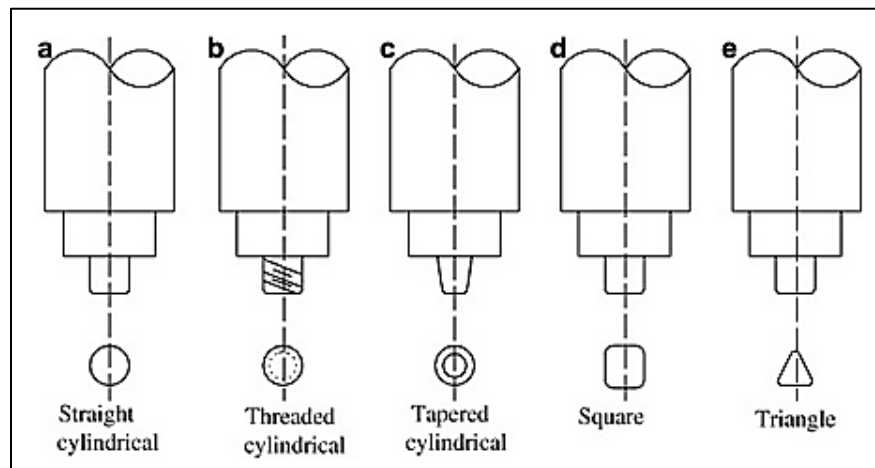


Figure 1.11 Some of tool pin profiles[17]

In terms of welded joint quality, all above mentioned variables contribute to determine the characteristic of the joint. Interestingly, studying the effects of the process parameters gives a wide understanding to how FSW affects the joint properties. Throughout the process, joint properties are highly influenced by heat generation and dissipation that is why it is significant investigating the role of those parameters in controlling the process thermal features and related results. Furthermore, a great attention should be given to the influence of the process parameters on the flow of the material. Significantly, formation of defects is mainly a consequence of the material movement [7].

1.4 Heat generation in friction stir welding

In the process of FSW, losses caused by micro-structural effects are simply the difference between the power input and the generated heat which is introduced into the weld using the tool. It is important to know that the translational speed is much lower than the peripheral speed of the probe and shoulder. Additionally, the high shear stresses at the tool/work piece interface drive viscous dissipation in the work piece material to be used. As a result, the behaviour of the contact interface is needed to be represented in the heat generation modeling with the presence of viscous dissipation. Actually, the contact condition at the interface can be different; where the material can slip or sticks to the tool. Sticking implies that the material moves at the velocity of the tool whereas slipping means the tool velocity may be higher than the material velocity. When it comes to contact

condition between the material and the tool surface, an analytical model of heat generation in FSW was developed by Schmidt et al [18]. The section below expounds on this model.

1.4.1 Contact condition

When illustrating the shear forces between the contacted surfaces, the Coulomb law of friction is applied because it computes the contact shear stress:

$$\tau_{contact} = \tau_{friction} = P \cdot \mu \quad (1.1)$$

where μ is the friction coefficient and P is the contact pressure. Coulomb's law computes the mutual motion if two infinitesimal segments are considered to investigate the contact condition. On the other hand, the internal stress is not considered and the Coulomb's law normal understanding is built on rigid contact couples. In order to have better demonstration for the contact condition in FSW process, Schmidt et al described three diverse states of contact.

- **Sticking condition:** If the yield shear stress of the underlying matrix is less than the friction shear stress, the surface of matrix will stick to the moving tool surface segment. An equilibrium state will occur due to the acceleration of the matrix segment which means the material is moving at the tool velocity. The achieving of equilibrium means fulfilling of the sticking condition [1].
- **Sliding condition:** This is the situation where the internal matrix yield shear stress is greater than the contact shear stress. [1].
- **Partial sliding/sticking:** The partial sliding/sticking condition is the equilibrium that is launched when the dynamic contact shear stress is equivalent to the internal yield shear stress as a result of a quasi-stationary plastic deformation rate [1].

1.4.2 Heat generation from friction

One of the two main sources of heat generation is friction between the tool and work piece surface. When the frictional heat generation phenomenon is taken into consideration and in relation to the French Scientists G. Amonton and C.D. Coulomb, there are three empirical laws that preside over the friction between any two solids:

- Frictional force as a function of normal load. The static and dynamic coefficients of friction do not rely on the load.
- The coefficients of friction do not rely on the macroscopic area of contact between the bodies.

- The dynamic coefficient of friction does not rely on the relative velocity between the two bodies. Being a second source of heat production in FSW the localized plastic deformation process taking place in the bulk of the work piece can contribute to an important extent to the heat added to the weld. The plastic deformation energy that resulted from the conversion of the weld power input can be divided into a portion stored in the microstructure and another converted to heat. Even though there are no experimental measurements been reported for these individual portions, the numerical simulations revealed that the heat acquired from bulk plastic deformation fluctuates from 2 and 20% [2].

Analytically, the total heat production Q_{total} as a result of friction can be differentiated into three main parts. To begin with; the heat generated under the tool shoulder Q_1 , secondly; the heat generated at the tool probe side Q_2 , and lastly the heat produced at the tool probe tip Q_3 [2].

$$Q_{total} = Q_1 + Q_2 + Q_3 \quad (1.2)$$

1.4.3 Heat dissipation

As it has been illustrated, the heat produced in FSW is a result of the effect of friction and plastic deformation of the material to be welded. In fact, the useful amount of the generated heat is utilized in welding and resulting in HAZ and TMAZ depending on the thermal conductivity of the base material. However, the other parts of heat generated can be majorly represented in the losses to the tool and backing plate conductively as well as a marginal loss to the atmosphere convectively and radiatively.

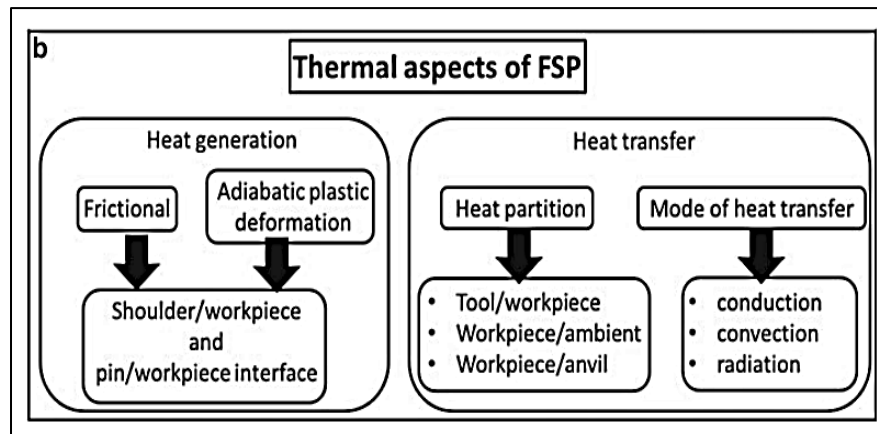


Figure 1.12 Thermal aspects of FSW [6]

The heat lost to the tool is a relatively small portion which can be computed by measuring the temperature at two points along the tool axis and applying a simple heat flow model. Additionally, heat loss from the workpiece top surface can be estimated by taking into account the convection and radiation heat transfer involved in equation (1.3). However, the radiative heat losses are regarded as negligible because of its amount which is quite small [7, 13, 19].

$$k \frac{\partial T}{\partial z} = \varepsilon(T^4 - T_a^4) + h(T - T_a) \quad (1.3)$$

where, k is the thermal conductivity, ε is the Stefan-Boltzmann Constant, h is the convective heat transfer coefficient and T_a is the ambient temperature. Regarding the heat loss from the workpiece bottom surface, it signifies the most of FSW process heat losses that dissipates through the backing plate because of the clamping action between the work piece and the backing plate. The contact conditions also greatly affect the transferred heat amount, and this is the reason why they have to be dealt with carefully particularly in the modeling process. Diverse possibilities have been recommended for instance no backing plate where the lower surface of the work piece is assumed adiabatic or perfect contact between backing plate and the work piece. Moreover, the perfect contact under the tool region is also advisable and lastly, introducing the value of the convection coefficient between them as well [13].

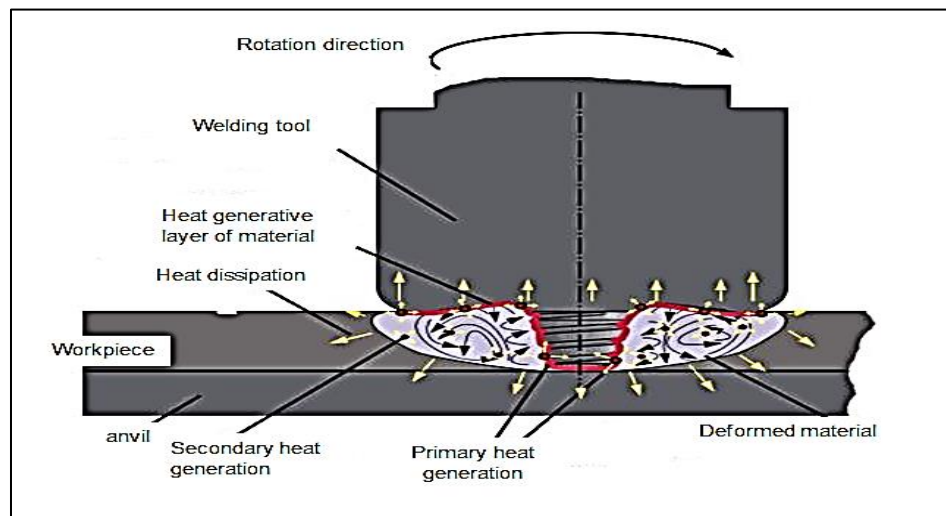


Figure 1.13 Mechanisms of heat generation and dissipation in FSW [6]

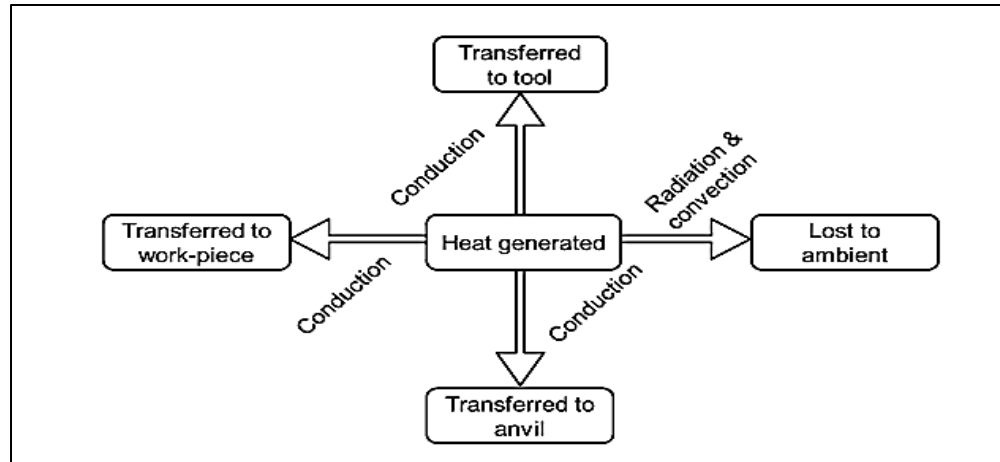


Figure 1.14 Heat transfer processes occurring during FSW [6]

Negative effects from the thermal cycle of welding might take place in the heat affected zone and the zone of plastic deformation. The aspects of welding thermal cycles can be the heat flux generated, rate of heating, peak temperature, temperature distributions, cooling endpoints, cooling rates of heated zones. By knowing the above aspects in detail, a lot can be done to explain how welding affects properties and microstructure of the given material [20].

The microstructures of the welds as well as the resultant mechanical properties of the weld, grain size and grain boundary characteristics are directly influenced by the temperature distribution around and within the stirred zone. Therefore, the information about temperature distribution is of great significance in estimating numerous thermal aspects that results in controlling the process and acquiring sound weld by avoiding the imperfection sources. For instance, the final grain size that determines the strength, toughness, fatigue resistance and corrosion of the weld joint is a result of grain growth rate which in turn is highly affected by the maximum temperature. However, when it comes to virtual measurements of temperature distribution in the stirring zone there are complications because of the severe plastic deformation occurring when the tool is moving [2, 21].

1.5 Metal flow in friction stir welding

Despite the complication of material flow in FSW, it is of great importance to understand the nature of flow that aid in optimal tool design and to accomplish a sound weld. Material flow relies mainly on process parameters (tool rotation rate and direction, that is anticlockwise or clockwise, travel speed, plunge depth, spindle angle), the tool geometry (pin and shoulder design, relative dimension of pin and shoulder), the characteristics of the material to be welded, and work piece

temperature [13]. The non-Newtonian fluid flow approach has been used successfully to clarify the deformation behaviour in FSW. That can be accredited to the constitutive behaviour of metals where the strain does not rely on the flow stress. This type of flow is treated on the hypothesis that it is the same as incompressible and governed by energy equation, continuity equation and momentum equation [1, 2] .

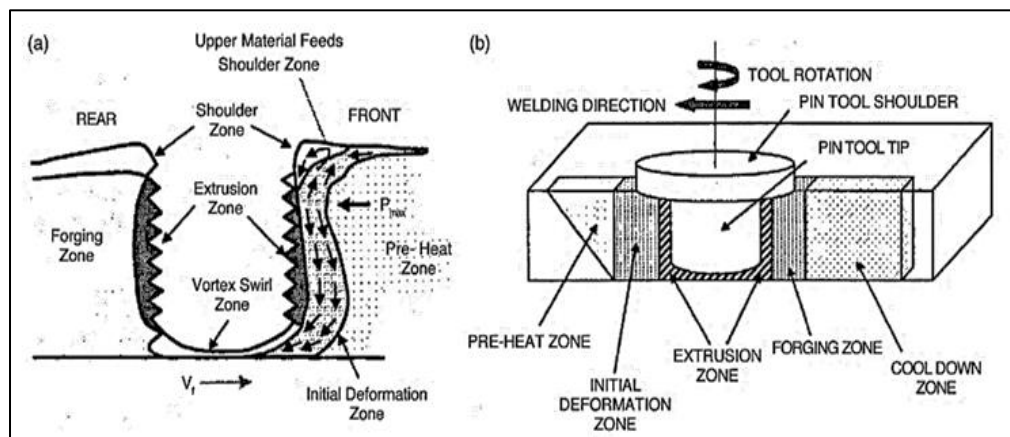


Figure 1.15 Metal flow patterns and metallurgical processing zones developed in FSW [6]

Many experiments have been performed to clarify the deformation and to understand the flow behaviour by using marker materials implanted into the work piece. The majority of these experiments have however depicted two types of deformations. The first one occurs at interface between the work piece and the tool shoulder, whereas the second is at the interface between work piece and the tool pin [1].

As presented in the figure Fig. 1.16 (a, b) the marker material indicates how the material deforms in the retreating and advancing Zone sides at the shoulder and work piece interface. The marker is transferred from advancing side to the retreating side by the tool and vice versa, even so; the dissimilarity is that the direction of advancing side material movement is vertically downwards into the work piece while the movement of retreating side material is vertically up pushed to the work piece surface. Some of the material may also be pushed out as a flash depending on the welding conditions [6].

In the figure 1.16, c and d show the movement of marker material caused by the deformation at the tool pin and the work piece interface. At the advancing side the marker material is moved close to its initial position. The marker material at the retreating is pushed which is the same as the case

of work piece interface and the tool shoulder. Concerning the deformation at the tool pin bottom and for some extent, it is same as deformation at the shoulder where the dissimilarity is accredited to the anvil constraint [6].

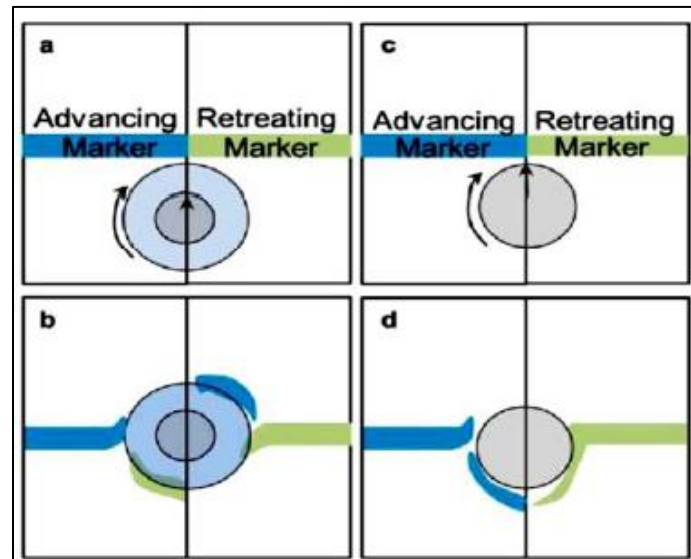


Figure 1.16(a, b, c, d) The material transport in the shoulder/workpiece interface region and in the tool pin/workpiece interface region interface [1]

The kinematic explanation of the metal motion was applied in introducing a physical model for the metal flow. The figure below demonstrates how three incompressible flow fields are merged to form two different currents. The model has a ring vortex field which is laid over on a rotation field where the two fields are translated along the weld panel [1].

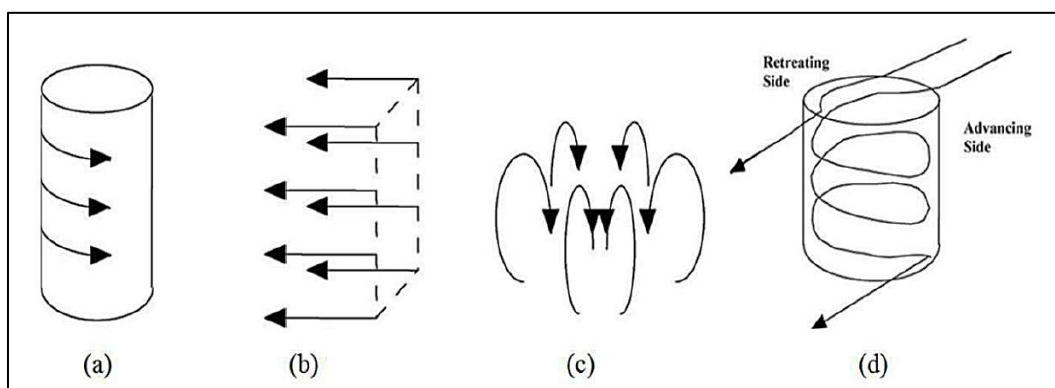


Figure 1.17 Incompressible flow fields in FSW [1]

It is not the nature of deformation alone that affects the flow, but it is also strongly linked to the thermal cycle of FSW. The thermal history that relies on the value of heat generated by the friction between the tool shoulder/pin and the work piece, together with the heat generated by the plastic working of the material determine the nature of metal flow.

1.6 Modelling of friction stir welding

Because FSW is a relatively modern process and still being improved, several features of the process have not yet been fully understood despite the fact that lots of experimental investigations have been carried out. The experimental investigations were often time consuming and costly particularly in the works that have focused on adjusting input FSW parameters. For the same purpose also, alternative investigations are used such as the computational tools which are very important for comprehension of the effects of input parameters [6].

Analytical and numerical methods have a vital function in the sense of keeping the goals of the model in view and taking on a suitable level of complication. Numerical FSW Modeling is possible basing on analyses and methods applied in the other processes like friction welding, machining, extrusion, rolling, and forging. Remarkably, assessment of the temperature field in FSW is commonly one of the main issues that help to understand and expect the changes in structure and properties of material being welded. Along the last few years, Computational fluid Dynamic (CFD) has been one of the very efficient and convenient methods for process numerical modeling which can simulate temperature distribution and material flow [6].

1.7 Motivation

It is well established in friction stir welding, parameters such as rotational speed, translational speed, and the tool geometry control the character of the weld. These parameters determine the amount of energy input to the weld and the rate of heat generation at the tool/material interface. Hence, peak joint temperature and temperature profile in the region near the joint can have a significant impact on the plastic deformation zone and heat affected zones, as well as the joint properties. The tool geometry is determined by geometrical aspects related to dimensions and shapes of both the pin and the shoulder. Although, various studies have been carried out considering different tool pin profiles to improve the mechanical strength of welded joint, but the influences of the pin shape and position on the thermal aspects have been rarely reported [16, 22].

In view of understanding the physical phenomena associated with FSW, particularly those represented in the thermomechanical interrelations, the experimental work has often showed that it is both costly and time consuming, which leads to the need of using alternative (cheaper and faster) approaches. Hence, the motivation behind carrying out this research is to conduct detailed parametric studies on various aspects of FSW thermal cycle using tools with different pin profiles and positions.

Proper pin design can lead to effective FSW process which also means broadening the process's applicability. It is essentially being known that the temperature field in FSW would be affected by the pin profile throughout the frictional activities or material transporting process. Regardless of the features on the pin side face, circular sided pin is used to some extent. However, polygonal pin can enhance the mechanical strength of the joint which might be attributed to the change in the thermal performance that can impact the grain size and the final weld microstructure. Analysing the thermal field, when using tools with polygonal pins, is crucial, giving useful information about the heat input and the thermal losses throughout the process. In view of that, material's maximum temperature that can be reached is directly related to the thermal activities, and hence, maximum temperature becomes one of the primary thermal field diagnostics parameters. Moreover, analysing the thermal field considering the polygonal pin geometric aspects, together with other process parameters, leads to a better understanding of the interdependent relationships, and give rise to the formulation of prediction models for the material's maximum temperature.

The position of the tool pin can possibly change where the pin's eccentricity might result from offsetting of the pin position, relative to the shoulder position. This eccentricity, along with high rotational speed, is likely to impact the temperature distribution, as well as the maximum temperature that can be reasoned by the change in the heat generation rate and the enhancement of the material transfer. Hence, it has become very important to analyse the thermal field using eccentric pins as their thermal behaviour differs significantly from concentric pins; the frictional area and the heat transfer effectiveness are different when using the eccentric pin.

The inclination of the pin side face could also determine the material thickness that can be welded. For instance, the tapered tool pins are preferred when welding thick sheets, especially when processing temperatures are low, at which the material flow is insufficient on the advancing side.

Therefore, it is almost impossible to neglect the pin side's inclination that can alter the temperature distribution in the vicinity of the material. Furthermore, due to severely limited thermal analyses studies conducted on alloy plates of higher thickness (around 10 to 12 mm), the author is particularly interested in understanding the thermal behaviour in such cases.

1.8 Research aims

Based on the aforementioned motivations, the specific aims formulated for this research study are divided into the following:

1. Thermal characterisation of friction stir welding using tools with polygonal pins.
2. Thermal characterisation of friction stir welding using tools with eccentric pins.
3. Thermal characterisation of friction stir welding using tools with tapered pins.

To find existing knowledge gaps in these aspects, the next chapter presents a detailed review of relevant and contemporary published literature.

1.9 Structure of the thesis

According to the discussed topics in the previous sections as well as the logical connection involved in achieving the research aims, this thesis is divided into seven main chapters which are briefly described in this section.

Chapter 1 is an introduction to the Friction Stir Welding as its one of the modern and promising joining processes. This introduction is represented in an overview which contains theoretical basis, important definitions, process parameters, and main physical phenomena in FSW. Furthermore, different modelling approaches of FSW are addressed. Then, the motivation for conducting the current research work is given which defines the main areas to be critically reviewed in the next chapter.

Chapter 2 consists the available research in the field of FSW which are critically reviewed. It provides a review of the published literature that is related to the CFD modeling of friction stir welding. A detailed review is also included for the published works regarding the use of tools with polygonal pins, eccentric polygonal pins and tapered eccentric polygonal pins in FSW. Moreover, the scope of research has been provided according to the areas in which the current work is going to be performed.

Chapter 3 highlights the detailed steps in building of CFD model for FSW as well as the advanced modelling technique that are adopted in order to make the model more realistic. Several spaces in this chapter were specified to presenting and discussing how the geometry of computation domain was created and the implemented meshing technique. In order to solve the main equations that mimic the physical behaviour in the computation domain, the solver settings and the appropriate boundary conditions have been included.

Chapter 4 mainly presents the thermal characterisation of the FSW when using tools with polygonal pins whereas the analytical derivations of the heat generation equations have been explained in detail. Subsequently, under different geometrical and operational variables, the temperature field within a thick workpiece has been transiently analysed in the presence of polygonal pin. Based on the thermal analyse conducted, semi-empirical prediction model for the peak temperature was developed.

Chapter 5 sheds light on the thermal characterisation of the FSW when the concept of pin eccentricity is implemented where the analytical derivations of the heat generation equations have been clarified in detail using tools with different eccentric polygonal pins. In terms of the thermal changes accompanying to the variation in the geometrical and operational parameters, a transient analyse has been carried out for the temperature field within a thick workpiece in the presence of eccentric polygonal pin. Consequently, semi-empirical prediction model for the peak temperature was developed

Chapter 6 consists of a study on the thermal characterisation of the FSW whereas the concept of the pin tapering has been considered. As the heat input is affected, the heat generation equations have been established in the presence of taper angle which represents the value and severity of the pin tapering. Within the same range of parameters in Chapter 5, the temperature field within a thick workpiece was numerically and transiently simulated to capture the effect of those proposed parameters. However, the effect of the pin tapering on the thermal field is the highlight of the chapter. Consequently, semi-empirical prediction model for the peak temperature was developed.

Chapter 7 presents the conclusions of the finding that obtained from the previous chapters. It provides a revision and monitoring of the achievements compared to the aims and objectives as well as a summary of the contribution to the existence knowledge regarding CFD modeling of

FSW and the thermal mapping within the workpiece. Lastly, the author proposed recommendations for the possible future work.

CHAPTER 2: LITERATURE REVIEW

Based on the information and facts presented and discussed in Chapter one which are associated to the FSW variables and their effect on the thermal behaviour, this chapter provides literature review that emphasises on the gaps in the contemporary knowledge. It starts by reviewing the CFD models of FSW and then presents the published works and studies regarding the employment of tools with polygonal pins, tools with eccentric polygonal pins and tools with tapered eccentric polygonal pins. Accordingly, the scope of research as well as its specific objectives are defined.

2.1 CFD Modelling of Friction Stir Welding

One of the earliest attempts of FSW modelling has been presented by P. Ulysse [23]. In this work, the aim has been to validate the model results with available experimental data and investigating the effect of the tool speeds on the welding temperatures by conducting parametric studies. From three dimensional analyses, it has been found that a reasonable agreement between the computed and the measured temperatures; additionally, the increase in the translational speed causes a decreasing in the maximum temperature while the opposite effect resulted from the increase in the rotational speed. The model has given a good understanding for the effect of tool speeds but the analysis was a steady state and limited to only one simple smooth tool.

In the published work by Colegrove and Shercliff [24], the application of the computational fluid dynamics (CFD) code was described to modelling the 3-dimensional metal flow in friction stir welding (FSW). The primary goal was to gain a better understanding of the material flow around a complex FSW tool and demonstrate the effects of tool rake angle and the rotation speed. To do this, a flow model was developed that included coupled thermal and flow analysis, heat generation, heat loss to the backing plate and the tool, convective heat loss from the top surface of the plate. Figure 2.1, depicts the main regions in the computation domain of the model. As it is able to handle the thermomechanical changes that occur near the tool surface, CFD package (FLUENT) has been selected for the modelling work. To solve the model, the problem was considered a steady state and the tool motion was simulated by considering a fluid flow in a partial strip from the welded plate.

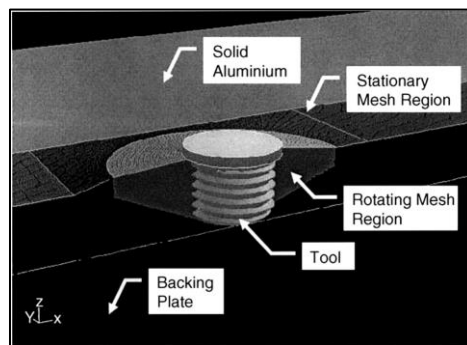


Figure 2.1 Description of the different regions used for the models [24]

This work has demonstrated how the CFD package, FLUENT can be used to analyse the thermal activities and material flow in FSW. Additionally, as can be seen in figure 2.2, the rotational speed has shown a greater effect than the welding speed on the peak temperature. In contrary, it was noted that the instantaneous changes in the flow components are much more difficult to calculate and require a full transient analysis. Furthermore, the size of the deformation zone and the peak temperature values were larger than that observed experimentally.

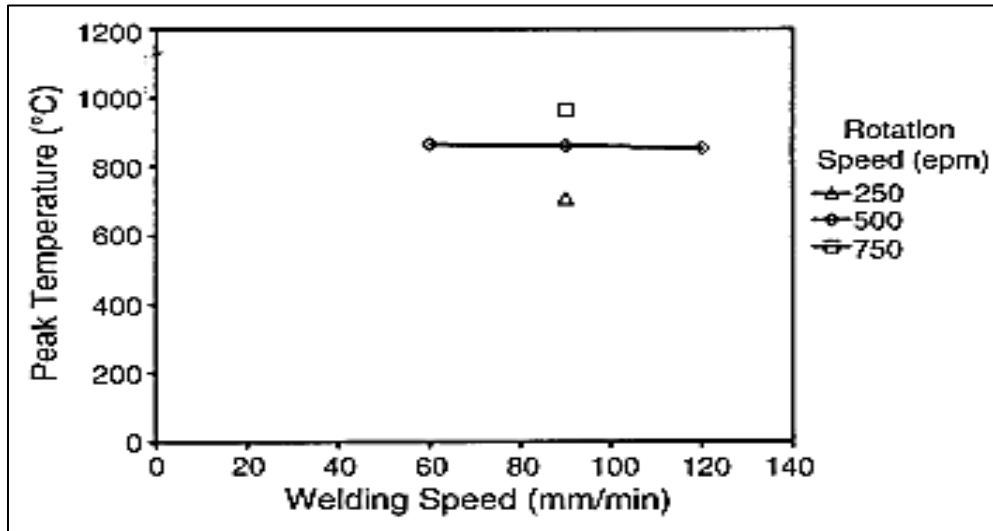


Figure 2.2 Peak temperature against translational and rotational speeds [24]

In order to achieve a correct calculation of viscosity, Crawford et. al [25] conducted a study to evaluate two different flow models which are viscoplastic and Couette. For simulating the process, a three-dimensional CFD model through the package FLUENT was used as shown in figure 2.3. Couette model suggests that the viscosity of material can be correlated as the viscosity of a fluid, intermediate between two concentric cylinders, which have two different diameters and rotating speeds. On the other hand, the Visco-Plastic fluid flow model in which the flow stress is dependent on the strain rate and the value of temperature as the TMAZ is presumed to be a rigid visco-plastic material. By using The Zener-Hollomon parameter, the effective flow stress can be expressed as follows [24, 26-30]:

$$\sigma_E = \frac{1}{\alpha} \ln \left[\left(\frac{Z}{\dot{A}} \right)^{\frac{1}{n}} + \left(\left(1 + \frac{Z}{\dot{A}} \right)^{\frac{2}{n}} \right)^{\frac{1}{2}} \right] \quad (2.1)$$

And

$$Z = \dot{\epsilon} \exp\left(\frac{Q}{RT}\right) \quad (2.2)$$

where, Z is the Zener-Hollomon parameter, T is the temperature, Q is the active energy, R is the universal gas constant, α , n , and A are the material constants. In view of that, different values of viscosity are considered according to the approximation of the viscosity of the plasticised metal proposed by Sheppard and Wright [24, 28] in which the ratio of the effective stress and the strain rate is used as

$$\eta = \frac{\sigma_E}{3\dot{\epsilon}} \quad (2.3)$$

where η is the material viscosity, σ_E is the effective stress and $\dot{\epsilon}$ is the strain rate. The author concluded that more accurate prediction of temperature profile was obtained from the viscoplastic flow. However, the problem was solved as steady state and the CFD model was built for incomplete penetration FSW process. Furthermore, the heat transfer for the support table was not included and the welded plate was completely assumed as a fluid flow domain.

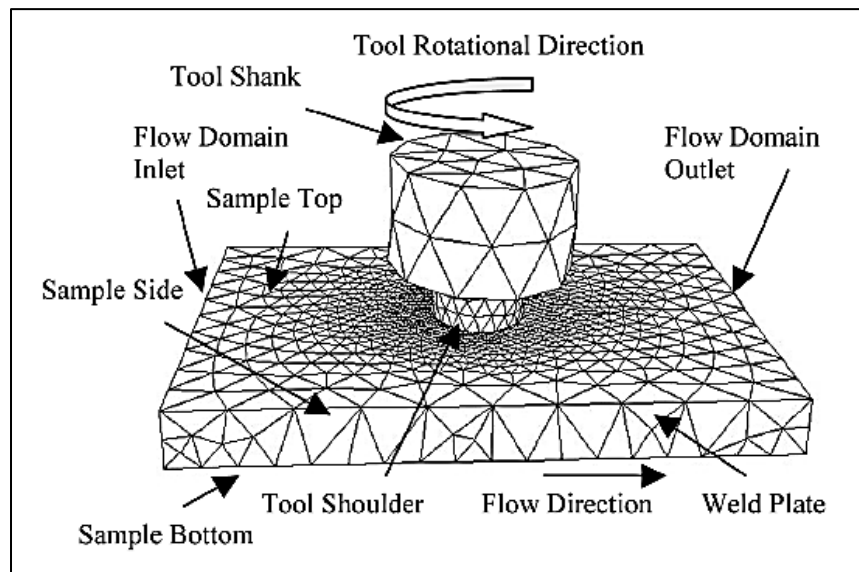


Figure 2.3 The welding model [25]

R. Nandan et. al [30] simulated friction stir welding process of 304 stainless steel where the temperature and flow fields were examined. Authors used three dimensional CFD model in which the heat generation amount was calculated using analytical formula and provided at the

tool/workpiece interface as a heat flux. Based on the obtained results, it was observed that the estimated peak temperature from the calculated thermal cycle has recorded higher values than those recorded for FSW of aluminium. Additionally, a significant plastic flow taking place close to the tool which means the heat is mainly transferred convectively. Accordingly, the unrealistic presumed region of fluid in the model might be properly re estimated. Moreover, this study lacks in-depth analysis of the thermal field as the model has solved the problem as steady state.

Atharifar et al.[31] used computational fluid dynamics (CFD) to study the material flow in the FSW process. Authors assumed tools with a right-handed threaded pin and the time – temperature dependent properties have been considered where FLUENT was employed to solve the coupled thermal and fluid flow equations spatially. Figure Figure 2.4, shows the solution domain and the boundaries of the model used. The model was validated by the measured temperature for the same and the results of this model have shown good agreement with the experimental data and the accuracy was improved compared to the previous models. However, to decrease the computation cost and avoiding the meshing difficulties a cylindrical computation domain has been assumed with a diameter equals to twice of the tool shoulder diameter which is an approximation.

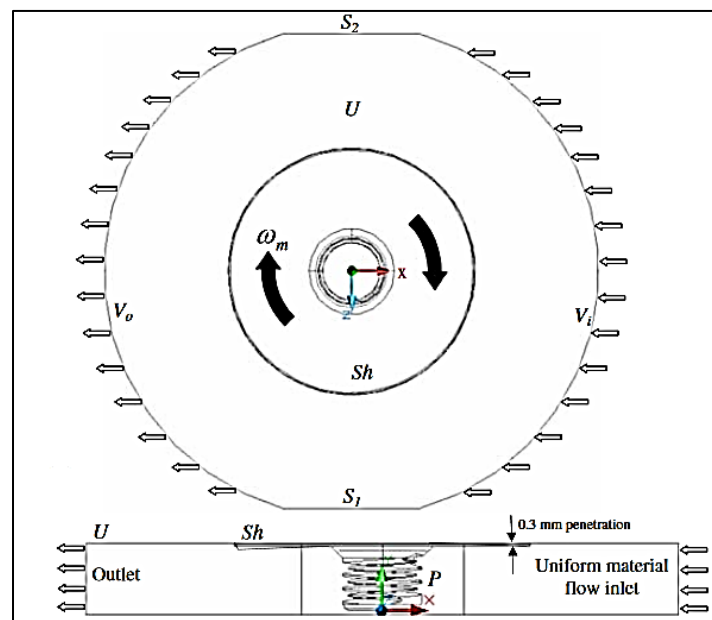


Figure 2.4 Solution domain and the boundaries[31]

Aljoaba et al. [32] have developed a three dimensional CFD model to simulate FSW using the STAR CCM+ commercial software. To investigate the effects of tool rotational speed on

temperature, strain rate, flow stress and material velocity fields in and around the processed nugget, user defined subroutines were developed and implemented to calculate the dynamic viscosity of the material which is mainly a function of local values of temperature. It was assumed that the heat generated at the interface between the tool and workpiece as a heat flux which is a frictional heat and the heat loss from the top and bottom of the workpiece was considered. As a steady state problem, continuity, momentum and energy equations were solved in a computation domain that was assumed to be liquid within the actual dimension of the workpiece as shown in figure 2.5. In general, this CFD model represents a useful tool where good estimation for the material behaviour was provided. It was particularly found that the average grain size increases when the rotational speed increases which can be reasoned to the increase in the temperature. Nevertheless, temperature of workpiece sides were kept fixed at the room temperature and the effects of other welding parameters have not been included in the analysis.

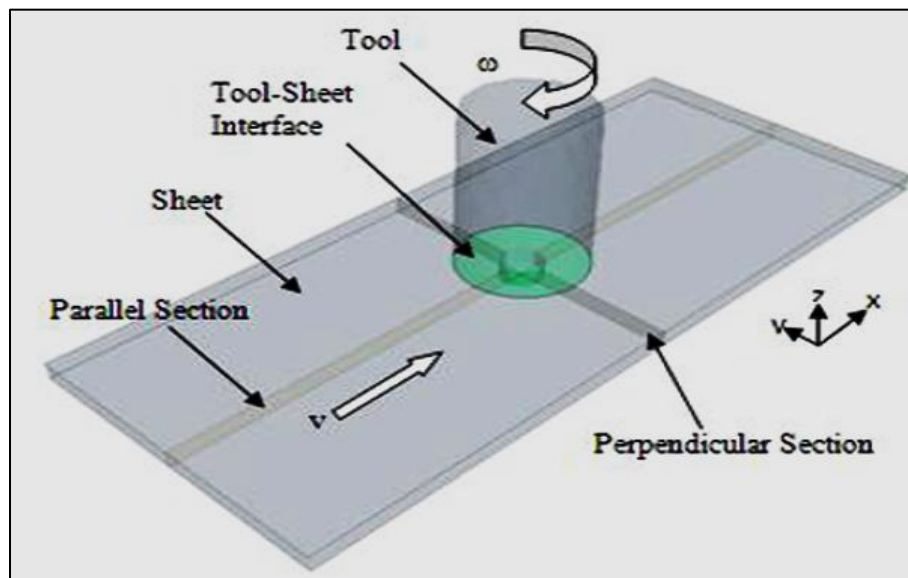


Figure 2.5 Model's geometry [32]

To understand how the velocity distribution is seriously affected by the tool geometry, San-Bao Lin et al. [33] have developed a three-dimensional FSW model based on fluid mechanics using the commercial CFD software, FLUENT. At the vicinity of the tool, the value of viscosity is still very high because of the high rates of strain (10^4 Pa and greater) which means a very low Reynolds number (approx. 10^{-5}). That is why the laminar flow conditions have been considered for the material movement near the welding tool. With three types of pin geometry and a flow domain of

200mm × 100mm × 8mm as depicted in figure 2.6, authors have assumed that the material transport in the welding process is steady state, laminar, viscous and non-Newtonian liquid flow. Thermally, the tool surface was presumed adiabatic while there was a convective heat transfer from all workpiece sides. Although, the simulation result agreed well with the “marker insert technique” experiments, the whole computation domain is represented as a fluid and the tool motion was defined by creating a flow past the rotating tool which is not true in reality.

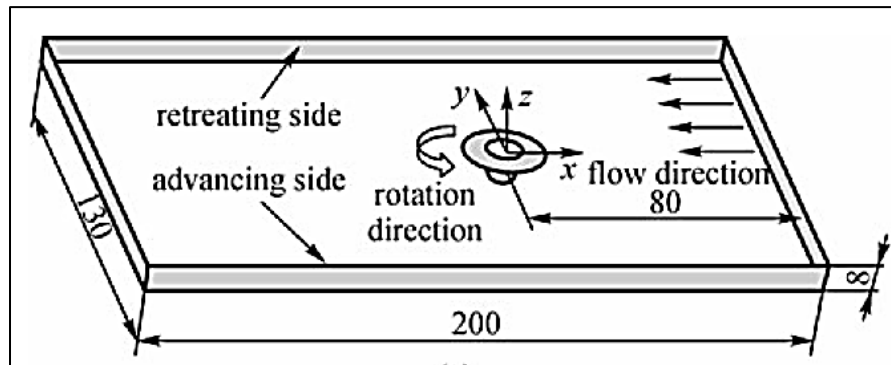


Figure 2.6 Schematic drawing of the three-dimensional flow domain [33]

A three-dimensional transient CFD model of FSW of Mg alloy was proposed by Zhenzhen Yu et al. [34]. The model was used to investigate the material flow and monitor the thermal history in FSW process of a plate with dimensions of 320mm × 180mm × 6.5mm. To capture the material flow induced by the movement of the threaded tool pin, a dynamic mesh method, combining both Lagrangian and Eulerian formulations were used. Figure 2.7, shows the main solid and fluid regions of the computation domain. Experimentally, temperature profiles were recorded to validate the predicted transient temperature. Moreover, two kinds of pin (threaded and smooth) were used to study the influence of the thread on the simulated results and material flow. In this transient model, the governing equations were treated using the finite volume method and solved through the computational fluid dynamics solver, ANSYS/ FLUENT. To estimate the process heat input, the heat generated at the contact surface between the tool and the workpiece has been calculated using an equation developed by Schmidt and Hattel [13], and then applied as a heat flux. Additionally, the process efficiency concept was considered to estimate the portion of the heat generated that is lost to the tool through conduction. Eventhough, good agreement was shown by the results with the experimental measurements, defining the tool motion through the flow velocity is still an approximation. Furthermore, the fluid region has been also assumed along to the welding

path. On the other hand, to decrease the computation time required for the simulation the authors have reduced the original dimensions of the plate that was used in the experimental work.

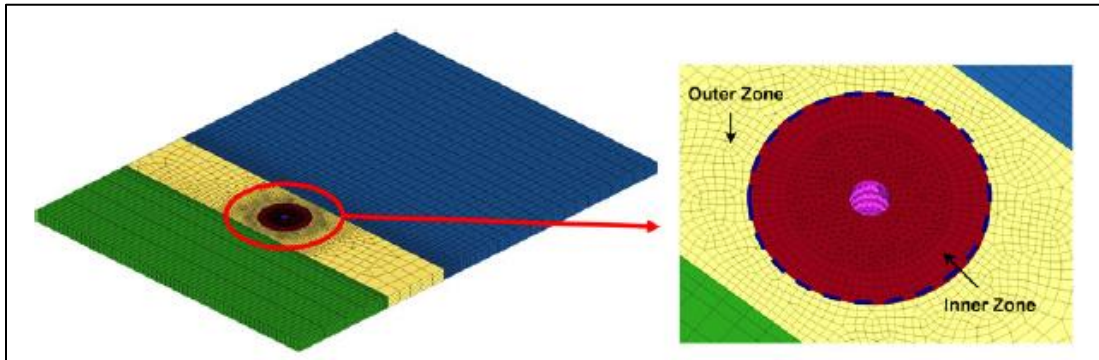


Figure 2.7 Overview of the solid and fluid regions in the model [34]

In the work carried out by H. Mohanty et al.[35] CFD model using FLUENT software was developed to the material steady flow and heat transfer of series 1100 aluminium alloy with respect to different tool geometries where straight and tapered cylindrical tool pin were considered. As shown in figure 2.8, the computation domain was a fluid region which has dimensions of $60\text{mm} \times 60\text{mm} \times 6\text{mm}$ and the material flow presumed to be laminar. For defining the process total heat input from different tool surface, Schimdt and Hattel's [13, 36] analytical heat generation model has been employed where the amount of calculated heat was applied as a heat flux at the contact interface. In order to reduce the simulation time, the dimensions of the computational region were smaller than those used for the plates in the experimental work. Heat convection between workpiece and the surrounding was assumed and the conduction heat transfer to the tool as well. However, heat loss to the tables under the workpiece was ignored.

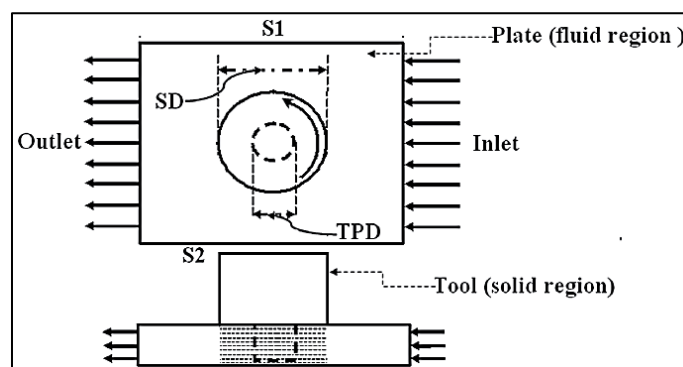


Figure 2.8 Schematic drawing of the computational model [35]

In terms of quantitatively describing the three dimensional material flow, FSW process with a conical pin was simulated by W.U. Chuan-song et al. [29]. The computed results were compared with FSW experiments on 6mm thickness of 2024 Al alloy that were conducted using marker inserted method and evaluated in metallographic ways. Figure 2.9, shows the shape of computation domain and the tool position related to model boundaries. The model assumes that the material sticks to the tool surface, so the material velocity is the same as the tool surface while the other flow domain surfaces like the top, the bottom, and the sides are modelled as moving walls. The calculated overall mode of material flow was consistent with the visualized results. Moreover, the rotational speeds have shown a significant impact on the flow field velocity components. Though, only one process parameter has been considered in this study, authors have concluded that further investigations are still needed by considering more process variables to give a comprehensive understanding of the interactions and the thermo-mechanical changes.

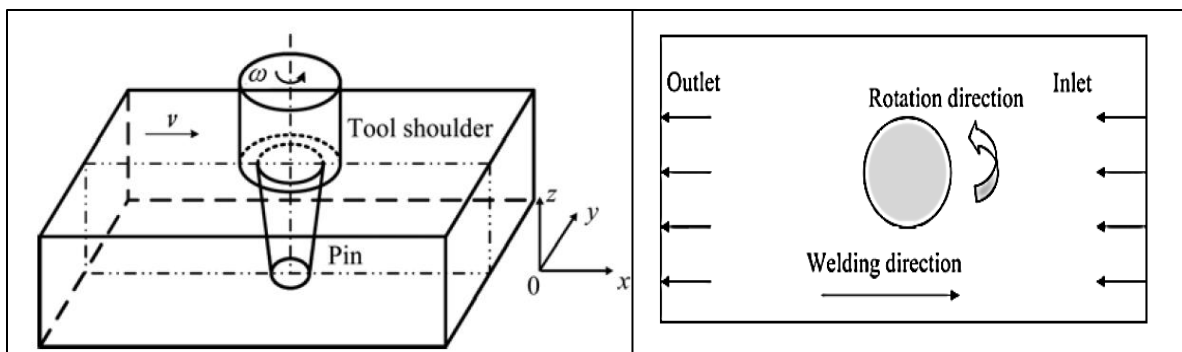


Figure 2.9 Schematic sketch of FSW system and boundary conditions [29]

G.Chen et al.[37] have quantitatively studied both the total heat generation and the spatial distribution of the heat flux. For doing that, a thermomechanical coupled model based on computational fluid dynamics using ANSYS Fluent was developed. Moreover, simulations using different tool rotational speeds were carried out to examine the effect of the change in the speed on both the total heat generation and the spatial distribution of heat flux. In the study, the geometric model was obtained by subtracting the tool from the workpiece, whereas the tilt angle and the concave shoulder were ignored. Workpiece with dimensions of 60mm × 40mm × 3.1mm from Aluminium alloy 6061 was selected to be used. The relationship between the total heat generation and the rotating rate was found to be proportional of 0.75ω and a radial distribution function was defined to describe the heat flux. Furthermore, the maximum temperature has been registered just under the shoulder and the model could show the slight difference between the temperature on the

advancing side and the retreating side. However, the study has been carried out under steady state conditions and it can be expanded by undertaking other thermal and flow related parameters and geometrical parameters as well.

J. Shude et al. [38] have published a study includes an investigation of the effect of flute geometry on material flow velocity by using ANSYS FLUENT. A tool with half-screw pin and a tool with a tapered-flute pin were suggested in order to improve material flow behaviour during FSW and avoid the root flaws of welds which are the most common defects. Three kinds of rotational tools were discussed; two of them are designed to improve material flow velocity between the tip of the tool and the bottom of workpiece. Ti6Al4V titanium alloy has been chosen as studied subject, where it was supposed to be fused liquid. Moreover, the material properties were kept unchanged. To solve the model, the RNG k- ϵ turbulent model and non-slip boundary conditions were used. In the results, it was seen that the tool with half-screw pin and the tool with tapered-flute pin increased material flow velocity near the bottom of the workpiece. However, the results still need to be validated.

H.Cho et al. [39] utilised an Eulerian finite volume approach with steady state conditions to simulate FSW processes in which ferritic stainless steel 409 has been considered to weld. Figure 2.10, depicts the model dimensions and the tool location related to the model boundaries and the material flow direction. The acquired data from the simulation has been compared with the measured temperature and obtained microstructure. The tool used had a flat surface and no tilt angle, also the viscosity was considered in the model as a function of local strain rate, temperature and characteristics of material. Likewise, the texture around the FSW tool was predicted from the computed velocity gradients along the streamlines of the flow field. Researchers considered the partial sticking contact condition and dependent temperature properties. Thus, all formulations were incorporated into FLUENT using a user defined function (UDF). Moreover, the heat generated at the interface between the vertical and horizontal surfaces of the tool and the workpiece was given as well as the initial conditions. The model has revealed that the streamlines around the tool are mostly circular and the temperature is highly dependent on the friction. Although, the model demonstrates a reasonable accuracy, the thermal history has been calculated from steady state temperature where the total welding distance was converted to the time spent when using the same welding speed.

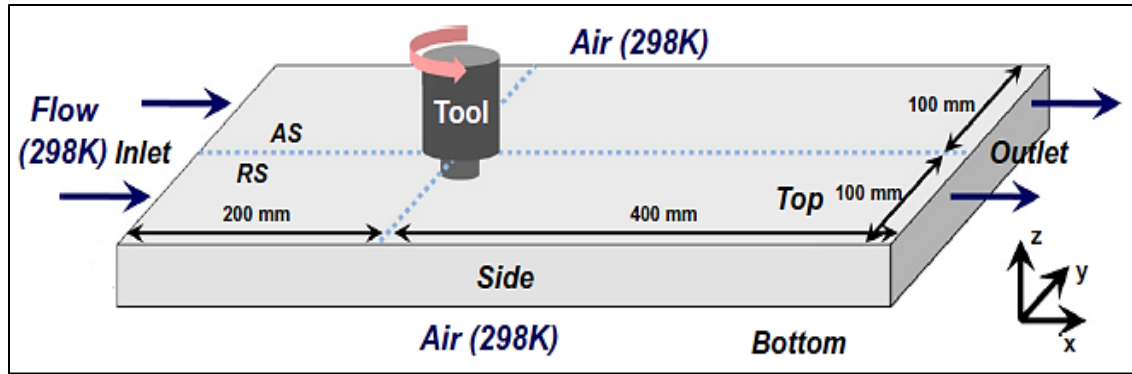


Figure 2.10 A schematic view of the model [39]

Using CFD, a model was created by G.Q. Chen et al. [40] based on the interactive force between the tool and the material. In this work, the temperature distribution was calculated and experimentally verified while the velocity on the tool material boundary and the shape of the stir zone are investigated based on the simulation results. The model assumes that the quasi-steady state was reached during the process and the boundary between the workpiece on the advancing and retreating sides was not considered because of the rigid clamping of the workpiece. The tetragonal grids were used to mesh the calculation domain and the heat dissipation to the air and the fixtures were assumed. Interestingly, because of the lower temperature reached by the material near the pin compared to that acquired by the material close the shoulder, it was found that the shear stress on the pin/material interface is relatively higher than that on the shoulder/material interface. However, the welding speed has been identified through the material flow while the tool kept rotating at the same location. Thermally, the heat losses to the tool were ignored and the welding thermal cycle was drawn based on the spatial temperature distribution and the travel speed.

S.Kang et al. [26] modelled FSW by imposing a rotational affected zone along with using Eulerian approach. Two models were proposed to define the rotational zone (Thermomechanical Affected Zone) TMAZ; the first one in which only the tool/workpiece contact area is forced to rotate; while the second defines a constant volume for a rotational region around the tool. The calculated temperature distribution from both models was compared and validated with experimental data. Thereafter, for the second model that has shown better agreement with the experimental results, a parametric study was carried out for finding out the best shape of the TMAZ where some dimensional variables have been changed. The first variable is the radial difference between the

shoulder radius and the upper radius of the proposed rotating zone while the second variable is the radial difference between the pin radius and the lower radius of the proposed rotating zone. This study revealed that the optimum size of the rotating zone is achieved when the upper radius is 1mm larger than the shoulder radius and the lower radius is 2-3mm larger than the pin radius. However, the model assumed the problem as a steady state and the whole workpiece volume is a fluid as well as defining the transitional motion of the tool by material flow.

A computational fluid dynamic model for FSW was presented by Z. Zhang et al. [41]. As shown in figure 2.11, the model dimensions were 200mm×120mm×7mm where the forces acting on the welding tool have been calculated according to the obtained pressure. Based on the frictional forces, the process heat generation was calculated and simplified as a heat flux on the contacting area between the tool and the workpiece. For modelling, the velocity of material at the contact surface was given and a user defined function has been used to define the material properties and heat generation. After experimental validation of the force distribution, two analytical methods were proposed for the calculations of the fatigue stress on the welding tool. However, the velocity inlets were used to define the tool transverse speed and fluid based computation domain was considered as well as steady state conditions. Moreover, no thermal analysis has been carried out.

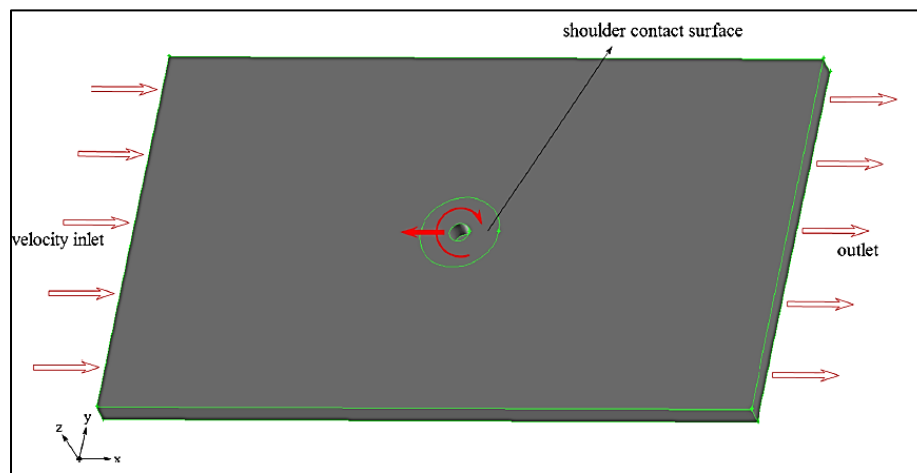


Figure 2.11 Schematic of FSW plate [41]

Further exploring the FSW technique, a thermal analysis along with the material flow has been carried out by A.K. Kadian et al. [27] for aluminium alloy AA6061 welded by FSW. In this work, a comparative study has presented the significance of conducting the analysis with and without the use of temperature dependent properties on the finite volume models where laminar and turbulent

models were used. The results of the laminar model have been more satisfactory than those from the turbulent model with less time consumption. Although, the thermal history of the welding process was transiently monitored, parametric study or in-depth thermal analysis has not been carried out.

2.1.1 Summary of Literature regarding CFD Modelling of friction stir welding

Based on the above presented literature review, it can be generally concluded that CFD modelling of FSW can play a significant role in visualising the fundamental aspects of the process, as well as avoiding the cost of experiments that are often performed to analyse the influence of different welding parameters. Notably, it seems that the CFD analysis of friction stir welding is still facing challenges as the process involves complex phenomena represented in the interrelated mechanisms and thermal processes. Instead of the steady state analysis, transient models can provide more details on the thermal and deformation histories. In terms of enhancing the accuracy of CFD models and making it more realistic, defining the fluid region is a key issue as it is related to the physical changes during the process such as the thermal activities [26]. However, the literature indicated that fluid region is still common assumption when using CFD tool in the modeling of FSW. On the other hand, it can be also summarised from the published literature that the fluid velocity inlets are mostly used to define the tool transverse speed which is an approximation.

2.2 Friction stir welding using tools with polygonal pins

H. Fujii et al. [42] published a research study in which 5mm thick sheets of Aluminium were friction stir welded to investigate the effect of the tool shape on the mechanical properties and the microstructure. Additionally, two welding tools with threaded and non-threaded cylindrical pins were used as well as one more with triangular pin profile. This study has revealed that for aluminium alloys that have a relatively high resistance of deformation, the triangular prism pin has given the best results particularly at high rotational speeds. However, a limited pin shapes have been included in the study and no detailed information regarding the thermal behaviour within the workpiece has been presented.

K. Elangovan et al. [19] carried out an investigation to comprehend the effects of the rotational speed and the pin profile on friction stir welded zone formation. To this end, authors employed three different rotational speeds 1500rpm, 1600rpm, 1700rpm and five different pin profiles

including the triangle and square shapes in joining of two Aluminium plates AA2219 with dimensions of 300mm ×150mm ×6mm each. The results in this investigation have shown that the optimum mechanical properties and free defect welds have been produced by using the tool with a square pin. Irrespective of the achievements, more comprehensive analysis could be conducted using a wide range of process geometrical and operational parameters particularly on the thermal impacts that have a significant role in the zone formation.

K. Elangovan et al. [43] conducted experiments to study the effects of the axial force and the pin profile on friction stir processed zone formation. Experiments were being carried out to weld AA6061 aluminium plates with a thickness of 6mm and the axial force range has been changed during the experimentation from 6kN to 8kN. Five welding tools have been used in this analysis which have different pin profiles including the triangle and square shapes. Some discussion has been included based on the microscopic examination and the tensile test where it was found that among the pins used, square pin profile has given a sound weld with the best quality and no defects. However, the range of investigation was limited and could be expanded by including more geometrical and operational parameters as well as their influences on the thermal aspects during welding.

K. Elangovan et al. [17] extended their own works [19, 43] by studying the effects of tool pin profile and tool shoulder diameter, where the diameters considered were 15mm, 18mm and 21mm. It was found that the optimum mechanical properties and metallurgical structure have been attained when using the square pin profiled with 18mm shoulder diameter. Again, the study would have included more geometrical and operational parameters. Moreover, the influences of geometrical and operational parameters on the thermal aspects during welding can be studied.

S.J. Vijay et al. [44] carried out an experimental study on the effects of tool pin profiles on microstructure and tensile strength while friction stir welding of 6mm thickness of ceramic matrix composites (Al–TiB₂ MMCs). In view of the number of pin side faces, polygonal pins with 4, 6 and 8 faces were employed as shown in figure 2.12. The shoulder diameter to pin diameter ratio (D/d) of 2.8, 3 and 3.2 have been considered. The obtained results have shown that the tensile strength and the microstructure of the welded joint are affected by the change in the pin profiles.

Furthermore, it was found that the tool with square pin has provided highest tensile strength amongst the others. However, the analysis did not include any information regarding the thermal changes accompanying the use of varied pin profiles which might play an important role in estimation of the final microstructure and mechanical properties of the welded joint.



Figure 2.12 FSW tools with different pin profiles and shoulder/pin diameter ratios [44]

P Biswas et al. [45] published a research study in which 6mm of a commercial grade aluminium was friction stir welded in order to experimentally detect the effects of the pin profile, the rotational and translational speed on the mechanical properties and microstructural features of the welded joints. The range of investigations was $\omega = 1000$ to 1400rpm and $V = 80$ to 160 mm/min in addition to five various pin profiles including the hexagonal profile. However, the analysis of the thermal field within the workpiece has not been included in the study and a very limited number of polygonal pins were considered.

S. Gopalakrishnan et al. [46] developed a mathematical model to predict the ultimate tensile strength for welds of Aluminium matrix titanium carbide reinforced composite (Al-TiC_p). different welding variables were considered like axial force, welding speed, rotational speed, the percentage of TiC and the pin profile. In doing so, a study has been carried out using the aforementioned parameters and friction stir welds were made for plates of square butt joint, having a size 100mm × 50mm × 6mm. Five welding tools have been used in this analysis which having different pin profiles including the straight square and hexagonal shapes. Generally, in terms of the ultimate tensile strength the welded specimens showed a high efficiency compared to the base material. Moreover, the model revealed that the tool pin profile and the welding speed recorded the highest effects on the tensile strength. However, the range of straight polygonal pin profiles

would have been expanded and no information has been presented regarding the process thermal activities and their role in forming of the welded joints.

R. Palanivel et al. [47] applied FSW to join 6mm thickness of dissimilar aluminium alloys (AA6351-T6 and AA5083-H111), where the main goal of the study was to investigate the influence of the tool rotational speed and the pin profile on the microstructure and the tensile strength of the welded joints. For this reason, they used three different rotational speed and five different pin profiles including straight square, straight hexagon and straight octagon. The findings revealed that the highest tensile strength was achieved when using rotational speed of 950 r.p.m and a pin with squared profile. However, the study does not present any insight into the temperature distribution and thermal profile within the workpiece.

D. Vijayan et al. [48] examined how the tool pin profiles in FSW of dissimilar aluminium alloys (AA 2024 and AA 6061) affect the tensile properties of welds along with other process parameters such as rotational speed, welding speed, and axial load. By considering the three proposed different pin profiles, the discussion on the results depicted that the square pin profile produced the highest ultimate tensile strength. However, the study is severely limited to the use of only one polygonal pin and no information regarding any thermal analysis for the process is provided.

M. Mehta et al. [22] carried out an investigation on the adhesion of plasticised material on pin surface. Because of the very high values of stresses that are achieved when using the polygonal pins, authors presumed various polygonal pins (triangle, square, pentagon, hexagon, and cylindrical) and welding parameters in the study to analyse the extent of undesirable adhesion which would lead to lose the pin functionality. Depending on the ratio of welding speed to tool rotational speed, the results showed that the pin geometry has caused the most impact at high ratio where the pins that have less than six sides recorded the optimum reaction to the adhesion. However, the study is severely limited to the adhesion phenomenon and no information regarding the thermal process aspects has been presented.

It is worth mentioning that based on the tool design, the heat generation and the maximum temperature during FSW are influenced by the shape of the pin and its surface nature due to the forces of friction [1]. In other words, pin shape can affect the strength and the grain size of the weld which means the effectiveness of FSW joint. In the view of modeling, different

methodologies were assumed to estimate the heat generation. Accordingly, V.S.Gadakh et al. [49] proposed analytical models to estimate the frictional heat generation for tools with different pin shapes including triangular, square, pentagon and hexagon. In term of temperature, the data from the literature was used to validate the proposed model. However, this study could be expanded by covering more polygonal pins. The authors concluded that precise results can be achieved only when considering the original values of parameters which were experimentally used. Moreover, the expression used to validate the model should have been for the same working material.

N. Gharaibeh et al. [50] carried out a parametric study to experimentally investigate the effects of the welding variables on the microstructure and mechanical properties of 6mm thick of Aluminium alloy (6061). The range of investigations was $\omega = 560$ to 1300rpm, $V = 0.5$ to 2.5mm/sec as well as three varied pin profiles (triangular, square, hexagon). It was found that better microstructure was given by the hexagonal pin while the square pin produced the highest ultimate tensile strength. However, no information regarding the thermal activities during welding has been reported.

2.2.1 Summary of Literature regarding Friction Stir Welding using tool with polygonal pins

Based on the above presented literature review for the friction stir welding using tool with polygonal pins, it can be summarised that the FSW tool pin designing is still a field of research as more possibilities of polygonal pin profiles can be considered. Moreover, the published literature is severely limited in terms of the thermal field analysis within the workpiece particularly the thicker ones and in the view of modeling, it is decisively needed to estimate the heat generation amount. From another point of view, there is a lack in the relationships for the process thermal aspects that include both the geometrical and operational parameters.

2.3 Friction stir welding using tool with Eccentric polygonal pins

V. Firouzdar et al. [51] conducted an experimental study to investigate the consequence of the changes in material position related to the welding tool on the heat input and joint strength in Al-to-Mg Friction Stir Welding. Plates with 1.6mm thickness have been welded by a tool having 10mm shoulder diameter and 4mm cylindrical pin diameter. Pin lengths of 1.3mm and 1.5mm have been used to join butt and lap joints respectively. The authors have used two ways to implement the concept of material position which are tool offset and swapping the position of

material alloys between the advancing and the retreating sides. Temperature progress has been monitored at particular points located on the advancing and retreating sides. Additionally, the tensile test has been carried out to estimate the material strength for all welded specimens. For both type of joints, results demonstrated that the material position related to the welding tool has a significant effect considering the welded material temperature and strength. However, no detailed information regarding the changing in the thermal field has been reported and the study is limited as only the conventional cylindrical tool has been used.

F. Gratecap et al. [52] have experimentally conducted an investigation to understand the influence of the tool eccentricity on the material flow pattern. Although, the shoulder and the pin have been concentric, they eccentrically moved as the origin of the eccentricity resulted from the way in which the tool is attached with its holder. In this work, the material of the workpiece used is Aluminium 2017-T4 with thickness of 4mm. Moreover, four different tools have been employed which are cylindrical without pin, cylindrical with conical pin, and two cylindrical tools with three and four milled faces at the bottom. The results revealed that the successful welding can be achieved even in existence of the eccentricity. Furthermore, two different paths of material flow have been observed which are represented in movement of the material that is underneath the shoulder and the other is produced by the pin. However, only one very small value of eccentricity has been considered in this study and the changes in thermal field within the specimen have not been analysed.

Z. Liang et al. [53] have carried out an experimental study to improve the mechanical properties of the Al/Mg dissimilar FSW joints based on the investigation and understanding of the effects of tool rotational speed and tool offset on the macro-microstructure of the joint as well as the tensile fracture mode. To make the joints, 3mm thick Aluminium and Magnesium plates have been used along with a tool with shoulder diameter of 12mm, pin diameter of 4mm and pin length of 2.5mm. The tool rotational speed has been varied from 600r.p.m to 1000r.p.m and the tool offset had different values which are 0 offset, 1mm offset to Mg, no offset, and 1 mm to Al. As a result, it is possible to have a joint with much improved ductility and keeping the strength high. However, more tool designs and welding parameters can be considered to improve the properties. Additionally, investigating the thermal history for the welding processes can be beneficial in prediction of the final microstructure of the joint.

C. Tingey et al. [54] have experimentally verified to what extent the yield strength of friction stir welded DH36 steel can be affected when the tool deviates from the weld centreline. To achieve the goal of this study, several joints with 6mm thickness have been welded where some of them deviated to the advancing side while the others deviated to the retreating side. A tool with 5.7mm height was employed where the pin and shoulder were spirally and conically shaped. The authors reported that during friction stir welding with tool centreline deviation, the process can give an accepted yield strength when the welding speed and the rotational speed are 250mm/min and 450rpm respectively. However, this study cannot be considered for diagnosing the effects of the tool or the pin eccentricity on the flow and thermal fields in friction stir welding.

M. Yuqing et al. [55] have used Aluminium alloy 7075 with 10 mm thick and some tools with eccentric pins to investigate the influence of tool pin eccentricity on weld microstructure and mechanical properties. Amongst the others, the specimen that has been welded by a pin with 0.2 mm eccentricity recorded the highest tensile strength as well as elongation. However, this study can be broadened as the thermal features of the welding cycle have not been studied.

N Guo et al. [56] carried out a study to investigate the role of tool eccentricity in the formation of periodic banded structures. In doing so, lead plates with 7mm thickness have been used to produce FS welded joints where the eccentricities of 60 μ m and 400 μ m have been considered for both the shoulder and the pin. In addition, the microstructures of the produced welds have been observed and the characteristics of the tool motion were mathematically calculated in order to explain the mechanism in which the banded structures form. The study revealed that the existence of eccentricity enhances the variation in the tool motion from advancing side to the retreating side which in role leads to changes in the surface periodic banded structures. However, the study is limited by the fact that the tool pin eccentricity has not been singularly considered. On the other hand, no detailed information regarding the welding thermal field has been presented.

A.R.S. Essa et al. [57] have developed an analytical model of heat generation for a tool with eccentric cylindrical pin in FSW. The eccentricities of 0, 0.2, 0.8 were employed and the proposed model matched with the model presented by previous authors[13]. As can be seen in figure 2.13, the results which have been experimentally obtained show that higher temperature is reached when using cylindrical pin without eccentricity than eccentric cylindrical pin. Moreover, according to

the results from the numerical simulation, the peak temperature decreases due to increase in the pin eccentricity. However, the study can be expanded to cover other pin shapes.

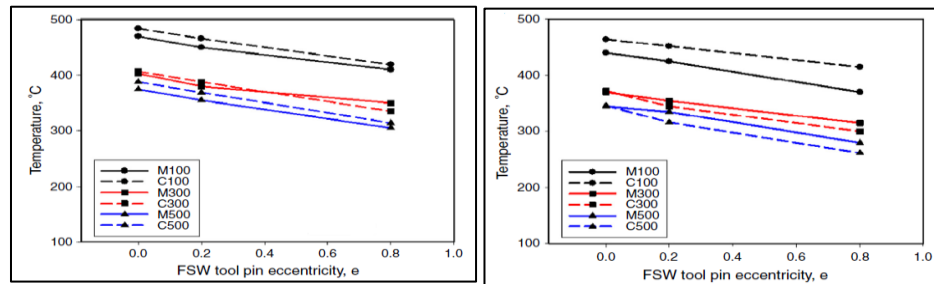


Figure 2.13 The effect of the tool pin eccentricity on the peak temperature for (a) AA1050-H12, (b) AA5754-H24 at different welding speeds [57]

M. Azizieh et al. [58] have experimentally considered the tool position, the tool rotational speed and the tool travel speed to investigate the mechanical properties and the microstructure in FSW of AA1100 and AZ31. For welding, plates of 3mm thickness have been prepared and a tool with 18mm shoulder diameter, 5mm pin diameter and 2.7mm pin length has been used as well. As shown in figure 2.14, five tool positions have been used which have 0 offset, 1.5mm offset to AA1100, 2.5mm offset to AA1100, 1.5mm offset to AZ31 and 2.5mm offset to AZ31. The values of rotational speed have been used are 420, 480, 570, 660, 750, 800 and 1000 r.p.m while the values of travel speed are 15, 20, and 30 mm/min. The authors concluded that the sound weld can be achieved by offsetting the tool toward AZ31 while the very high and low rotational speeds lead to defect formation as the liquation will be excessive and the material flow is low, respectively. Although, the peak temperature has been monitored to explain the relationship between the rotational speed, hardness and higher intermetallics formation, no detailed information regarding the changes in the thermal field has been reported. Furthermore, the study can be expanded to cover other geometric parameters such as pin eccentricity.

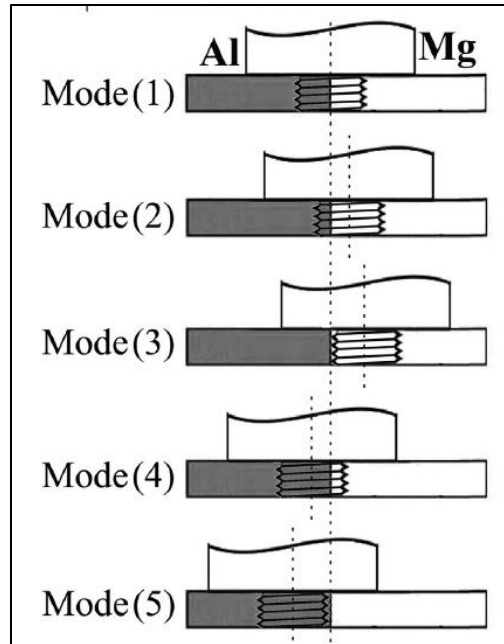


Figure 2.14 Modes of tool offset [58]

L.H. Shah et al. [59] have used plates with 9.5mm thickness of aluminium A6061 to experimentally investigate and understand how the material flow would be affected due to the tool eccentricity. In this study, a tool with threaded conical pin has been used to make the joints and two values of tool eccentricity (0 and 0.2mm) were considered along with a rotational speed of 1200r.p.m and travel speed of 63mm/min. As a result, the material flow has enhanced due to the eccentricity particularly in the nugget zone as well as the soft areas in the same region. However, no detailed information regarding the changing in the thermal field has been reported. Furthermore, the study can be expanded to cover other geometric parameters such as pin eccentricity.

2.3.1 Summary of Literature regarding Friction Stir Welding using tool with Eccentric polygonal pins

Based on the presented literature review regarding using of eccentric pins, some gaps in the knowledge were clearly highlighted. In most of the studies that have considered the concept of eccentricity, the tool pin and shoulder still have the same axis of rotation and both having an offset with respect to the weld centreline. Hence, the effect of the pin eccentricity has not been solely verified particularly for those tools with polygonal pins. The previous studies had a very limited concern on the thermal field analysis as they have been mostly focused on the analysis of the material flow and its effect on the microstructure as well as the mechanical properties. Also, the

above-mentioned works have shown lack in developing the relationships for the process thermal aspects that include both the geometrical and operational parameters.

2.4 Friction stir welding using tool with Tapered Eccentric polygonal pins

In their research work, N. S. Sundaram et al. [60] have carried out a set of experiments in which 5mm thickness of dissimilar aluminium alloys AA2024 and AA5083 have been FS welded. These experiments have been aimed to investigate the effects of the process's parameters such as tool pin profile, tool rotational speed, welding speed, and tool axial force on the mechanical properties of the welded joints. Consequently, prediction models have been developed to calculate the ultimate tensile strength and tensile elongation. As shown in figure 2.15, four tools among the five tools that have been used in the study had tapered pins, namely grooved tapered Cylinder, Tapered Square, Tapered Hexagon, and Paddle Shape. According to the results, it was found that the joints welded by the tapered hexagon tool recorded the highest tensile elongation while the lowest has been for those joints that were welded by the straight cylindrical tool. However, this study can be extended to give information about the thermal field and covering more pin profiles.

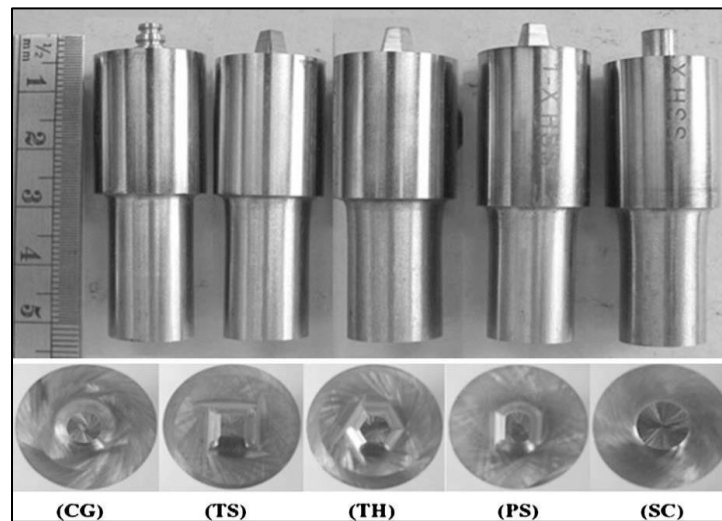


Figure 2.15 Different profiles of tapered tool pins [60]

S.J. Vijay et al. [44] have conducted an experimental work in which eighteen different tools were employed. Nine of them had tapered polygonal pins and were divided in three groups. The first group includes three tapered squared pins with three different values of shoulder and pin diameter ratio (D/d) (2.8, 3, 3.2) while the other two groups included hexagon and octagon pins with the same values of (D/d). Samples with 6mm thickness from metal matrix composites (MMCs) which

is ceramic matrix composites (Al–TiB₂ MMCs) have been welded in this study for investigating and understanding to what extent the pin shape can impact the joint efficiency in terms of the microstructure and the tensile strength. The study has revealed that the stirred region becomes smaller when using tapered pins compared with that resulted from the straight ones, while the grains become coarser. Although, a relatively high number of tools with several pin profiles have been used, other profiles can be studied. On the other hand, the study has been devoid of any information regarding the changes in the thermal field that might happen when using different pin profiles.

O. Lorrain et al. [61] have experimentally analysed the material flow in friction stir welding of 4mm thickness of Aluminium 7020-T6. The joints have been produced using several values of operational parameters and two tools having different pins which are a straight cylindrical pin and tapered cylindrical pin with three flats. It was found that even if the plunge force and the rotational speed increase, the region affected by the shoulder rotation becomes less thick when using tapered pin rather than the straight pin. The study is limited in terms of the geometrical parameters that have been considered. Moreover, no information regarding the thermal field has been reported.

C. N. Suresha et al. [62] have performed an experimental study of FS welding of Aluminium alloy AA7075-T6 with 5mm thickness to estimate the most influencing parameter on the tensile strength as well as the optimum parameters in welding of such alloys. Two different tools with straight and conical pins have been used in this study along with several values of tool rotational speed, weld traversing speed, and plunge depth. It was observed that the rotational speed has exhibited the highest influence on the strength amongst other parameters and the tool with conical pin shape produced more efficient joint than produced by the one having a straight shape. However, more geometrical parameters related to the pin can be covered and no information has been presented regarding the effect of the considered parameters on the thermal field within the workpiece.

San-Bao Lin et al. [33] have numerically studied the effect of the tool pin geometry on the material velocity field during friction stir welding. To conduct the simulation, straight pin tool, tapered pin tool and threaded tapered pin tool have been assumed by the authors as well as a flow domain of (200mm × 100mm × 8mm). It was concluded that the pin has a significant effect on the velocity field which can be considered as a criterion to optimise the tool design. However, the study has

been devoid of any information regarding the changing in the thermal field that might happen when using different pin profiles.

P. Biswas et al. [45] published a research study in which 6mm thick commercial grade Aluminium was friction stir welded in order to experimentally detect the effects of the pin profile and the rotational speed on the mechanical properties and microstructural features of the welded joints. The range of investigations was $\omega = 1000$ to 1400rpm and $V = 80$ to 160 mm/min in addition to five tools with different pin profiles where three of them are tapered as depicted in figure 2.16. The obtained results have shown that the tools with tapered pins produced joints with the highest mechanical properties. However, more geometrical parameters related to the pin can be covered and no information has been presented regarding the effect of the considered parameters on the thermal field within the workpiece.

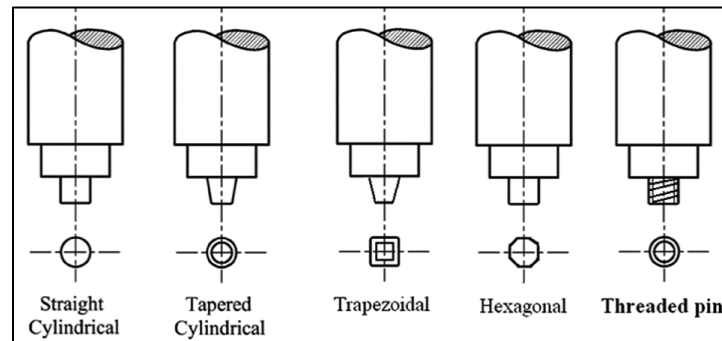


Figure 2.16 Different tool pins geometries [45]

S. Gopalakrishnan et al. [46] developed a mathematical model to predict the ultimate tensile strength for welds of Aluminium matrix titanium carbide reinforced composite (Al-TiCp) as a function of welding variables like axial force, welding speed, rotational speed, the percentage of TiC, and the pin profile. In doing so, a study has been carried out using the aforementioned parameters to prepare friction stir welds for plates of square butt joint and size of 100mm \times 50mm \times 6mm. Five welding tools have been used in this analysis which have different polygonal pins including tapered square, tapered hexagonal and tapered octagonal shapes. It has been found that the tool with tapered square pin offered the maximum tensile strength. However, no information regarding the process thermal activities and their role in forming of the welded joints have been provided.

In the work carried out by H. Mohanty et al. [35] CFD model using FLUENT software has been developed to analyse the material flow and heat transfer in the weldment. A workpiece of series 1100 aluminium alloy with dimensions of $60\text{mm} \times 60\text{mm} \times 6\text{mm}$ has been used as well as different tool pin geometries. i.e. straight cylindrical pin with a diameter of 5mm and tapered cylindrical tool pin with diameters of 6 and 5mm have been considered. For both cases, the temperature distribution has been estimated as shown in figure 2.17, where the higher peak temperature was recorded in the case of tapered pin because its surface area is greater than that for the straight one. However, the study has been carried out under steady state conditions. Better understanding could have been achieved if it was a transient model. Additionally, other prospects can be offered if more tapering levels and other geometrical parameters such as the eccentricity have been covered.

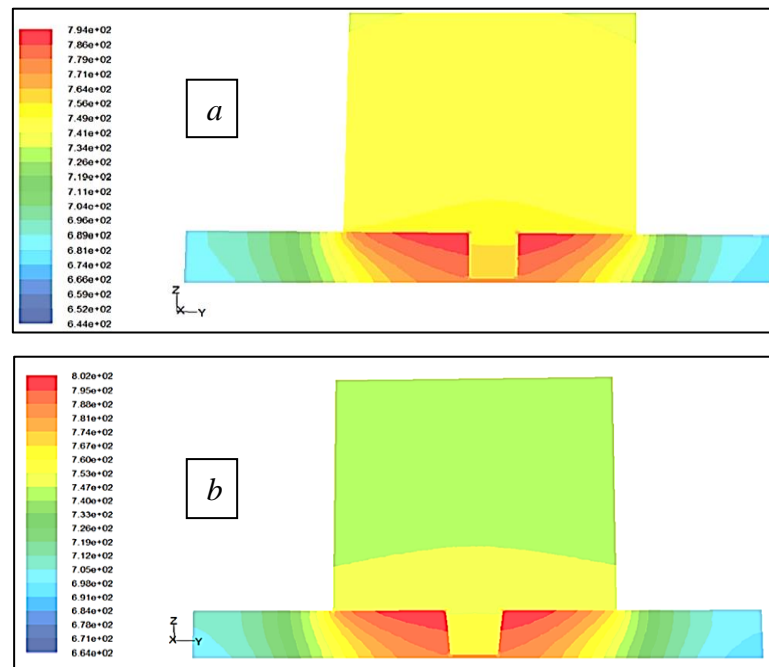


Figure 2.17 Temperature contours: a) straight pin, b) tapered pin [35]

S.D. Ji et al. [63] have numerically studied the influence of both the shoulder and pin geometries on the flow behaviour of welded material which would help to avoid the welding defects. In this work, the ANSYS FLUENT software based on the finite volume method has been used to establish a CFD model. This model included a computation domain of $150\text{mm} \times 50\text{mm} \times 6\text{mm}$ and a tool with shoulder diameter of 14mm and conical pin with taper angle of 20° whereas the pin base diameter and the pin bottom diameter were 5.3mm and 3mm, respectively. The results have shown

that the velocity of the material flow increases when the cone angle decreases. However, more tapered pins with different faces can be studied. Furthermore, the study has been devoid of any information regarding the changes in the thermal field that might happen when using different pin profiles.

V. S. Gadakh et al. [64] have published a research work in which an analytical model has been developed to estimate the heat generation amount in friction stir welding when using a tool with tapered cylindrical pin. Subsequently, for different material the effect of the change in the taper angle on the maximum temperature has been investigated and discussed. It was found that less temperature would be obtained if the surface area of the tapered pin was smaller than that for a straight one and in the view of this, the maximum temperature decreases when the taper angle increases. However, more tapered pins with different faces can be studied and for more understanding, other thermal features would have been beneficial to present.

K. Ramanjaneyulu et al. [65] have conducted an experimental study to verify the physical effect of pin profile in friction stir welding. As shown in figure 2.18, different tapered polygonal pins with 14° taper angle have been employed to fabricate joints of AA2014-T6 Aluminium alloy with 5mm thickness. The thermal cycle at a point close to the pin was monitored and the mechanical properties of the joints such as tensile strength and hardness have been examined as well as the metallurgical characterization. It was found that the temperature has witnessed a rapid increase in the case of hexagonal pin compared to the other types and it has also been concluded that the weld quality might be highly affected for thicker workpieces. However, more tapered polygonal pins can be studied and for more understanding, other thermal features would have been likely to present.

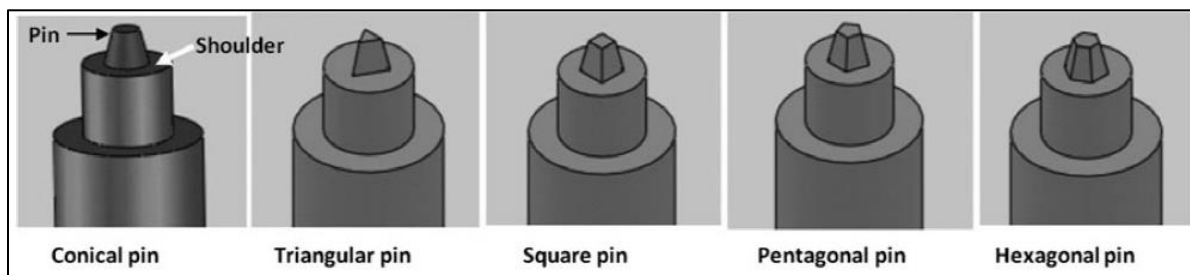


Figure 2.18 Various tapered polygonal pins [65]

M. Mehta et al. [16] conducted a numerical study which aims to analyse the heat transfer in friction stir welding of Aluminium alloy (AA2014- T6) with 5mm thickness and investigating the impact of the polygonal pins on the thermal aspects. For this purpose, finite element software ABAQUS was employed to build three-dimensional model along with four different tapered polygonal pins (tapered triangular, tapered square, tapered pentagon, and tapered hexagon) with the same taper angle. After providing the analytical estimation of frictional heat generation, the calculated heat amount is then applied as a surface heat flux at the tool-workpiece interface. The model has been validated where the numerical calculated thermal cycle agreed with the experimental data for the same. The findings have also revealed that the peak temperature increases as the number of faces increase. Moreover, as depicted in figure 2.19 the maximum shear stress has also been calculated to show the variations in its values according to the change in the pin sides number and corresponding temperature. However, the study was conducted in steady state conditions and limited to the pin geometry as well as the number of polygon sides. Furthermore, the effect of taper angle has not been included.

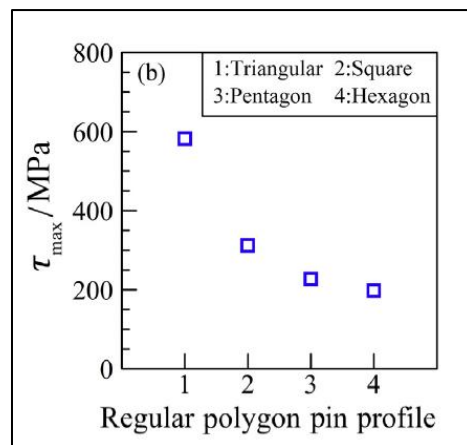


Figure 2.19 Estimated values of maximum shear stress [16]

N. H. Othman et al. [66] have studied the effect of the change in the pin taper tool ratio (maximum pin diameter / minimum pin diameter) on the welded joint microstructure along with different values of rotational and translational speeds. Six pin taper tool ratio which ranged from 6:6 to 6:1 have been considered in this study where 6mm thick Magnesium AZ31 alloy has been used to produce the welded joints and then the microstructure was examined. It has been observed that the joints that were welded by small pin diameters of 1mm and 2mm have presented the best weld appearance. Moreover, 6:1 taper pin ratio has offered highest tensile strength and low heat input.

However, more tapered pins with different side shapes can be studied with other geometrical parameters. Moreover, no information has been presented regarding the effect of the considered parameters on the thermal field within the workpiece.

M. Al-moussawi et al. [67] have built a three dimensional-CFD model to studying the temperature and velocity fields as well as the shear stress under steady state conditions. To do this, eight welded joints have been fabricated and modelled using $500 \times 400 \times 6$ mm of DH36 steel plates where the temperature has been recorded at three different points. The authors have considered several values of rotational and transverse speeds. Besides, to avoid the difficulty in modeling of the threads on the tool pin, a tool with smooth tapered pin was used. The results have shown that the peak temperature was recorded at just the shoulder underneath where the shoulder has experienced low shear stress at high rotational speeds. In contrary, the shear stress registered elevated values at high translational speeds. However, more tapered pins with different side shapes can be studied.

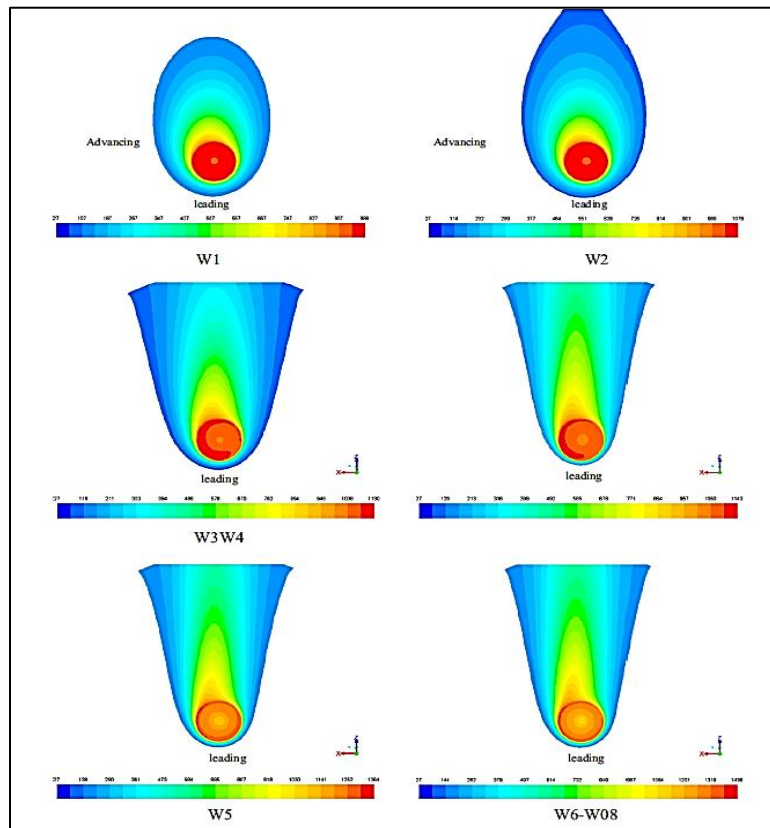


Figure 2.20 Steady state- temperature contours for six different conditions [67]

2.4.1 Summary of literature regarding Friction Stir Welding using tool with Tapered Eccentric polygonal pins

The majority of the published works presented in the literature review above have focused on how the welding microstructure and mechanical properties are affected by different welding parameters while few of them included information about the welding thermal cycle and its changes over time. Eventhough, it was observed that several tapered polygonal pins have been included, more profiles still need to be studied particularly those having eccentric pins. It can also be summarised from the aforementioned literature review that there has been a lack in the relationships between the geometrical and operational parameters with the thermal aspects of FSW.

2.5 Scope of Research

In terms of microstructure and mechanical properties of the FS welded joint, it was obviously noticed from the reviewed literature in this chapter that the pin shape and position have an importance. That can be attributed to their role in the thermal changes and the severity of material deformation. Furthermore, due to the difficulty that is often faced to monitor the thermal features in the experimental studies as the tool rotates and propagates, a detailed information regarding the temperature distribution and thermal history within the workpiece has not been easily achieved especially with a wide range of geometrical parameters. Although, this is possible by modeling the process using the computational tools, models need to be developed to achieve higher degree of reality by mimicking real world conditions. Additionally, it is possible to conduct thermal investigations with a wide range of variables to test more pin profiles and positions.

According to the studies in the previous sections, the main areas of research for FSW using different pin profiles and positions have been identified. The first is the thermal field diagnostics of FSW using tools with different polygonal pins. Estimating the heat generation amount is important to quantify the thermal features of FSW accurately. A customised approach is needed to determine the value of heat generation for all proposed tools with polygonal pins. Moreover, as the CFD tools are suggested to be used for further analysis of the thermal field, CFD model needs to be generated with more realistic features compared to the current CFD models that are used for FSW. Then, by using the CFD model, detailed numerical investigations needs to be carried out in

order to analyse the effect of geometric and operational parameters on the thermal field within the workpiece.

The second main area of research identified is the thermal field diagnostics of FSW using tools with different eccentric polygonal pins. Similar to the previous point, a special approach is needed to estimate the heat generation value when using tools with eccentric polygonal pins. Subsequently, as the welding thermal cycle changes according to varied pin positions related to the rotating axis, the thermal field within the workpiece needs to be analysed. Furthermore, detailed numerical investigations need to be carried out for analysing the effects of geometric and operational parameters on the thermal field within the workpiece.

The third main research area identified for further research is the thermal analysis of FSW using tools with different tapered eccentric polygonal pins. Due to the change in the pin surface area, the heat generation is expected to be different; hence, special attention is required to estimate the heat generation while using tools with tapered eccentric polygonal pins. Consequently, as the welding thermal cycle varies according to the tapering severity, the thermal field within the workpiece needs to be analysed. Furthermore, detailed numerical investigations need to be carried out for analysing the effect of geometric and operational parameters on the thermal field within the workpiece.

2.6 Specific Research objectives

This work presents an attempt for better understanding of the variations in the thermal characteristics within the workpieces welded using FSW. A careful estimation of the heat generated during FSW is required. Listed below are the research objectives that have been identified to achieve the main aims of this study:

1. To develop a more realistic CFD model to simulate FSW process.
2. To develop analytical equations for determination of the heat generated during FSW process while using tools with polygonal pin profiles.
3. To establish the effects of geometrical and operational parameters of FSW with polygonal pins on the temperature distribution and peak temperature within the workpiece.
4. Development of a semi-empirical relationship for the peak temperature within the workpiece while using polygonal pin profiles.

5. To develop analytical correlations for determining the heat generation while using tools with eccentric polygonal pin profiles.
6. To determine the effects of geometrical and operational parameters of FSW using eccentric polygonal pins on the temperature distribution and peak temperature within the workpiece.
7. Development of a semi-empirical correlation for the peak temperature within the workpiece while using tools with eccentric polygonal pin profiles.
8. To develop analytical equations for determining the heat generation while using tools with tapered eccentric polygonal pin profiles.
9. To analyse the effects of geometrical and operational parameters of FSW with tapered eccentric polygonal pins on the temperature distribution and peak temperature within the workpiece.
10. Development of a semi-empirical relationship for the peak temperature within the workpiece while using tool with tapered eccentric polygonal pin profiles.

In view of the above-mentioned objectives, and to make them satisfactorily achievable, advanced Computational Fluid Dynamics based techniques are used in this work to simulate the thermal field within the FS welded specimens. The following chapter presents the numerical methodology and the steps that were considered to develop a more realistic numerical model.

CHAPTER 3: CFD MODELLING OF FRICTION STIR WELDING

In order to achieve the research objectives that have been previously identified, the thermal cycle in FSW has been numerically simulated using advanced Computational Fluid Dynamic (CFD) techniques. By avoiding the unnecessary assumptions, the gap between the reality and the CFD models that are currently in existence can be narrowed. Therefore, this chapter presents a detailed methodology using the amount of heat generated during FSW along-with advanced CFD techniques to develop a more realistic and applicable model. ANSYS Fluent 17.0 has been used in the development of the numerical model, which is three dimensional, transient and is based on limited fluid region. A more realistic approach has been used for the translational motion of the tool. A detailed description of the geometric modelling and meshing of the computation domain has been presented, along with the suitable solver settings and the boundary conditions. Validating the proposed numerical model has been carried out by verifying the numerical results against published experimental measurements of the same.

3.1 The governing equations

CFD uses numerical methods to analyse the systems involving the fluid flow and the heat transfer and that basically depends on the governing equations of the fluid flow in their continuum forms. Therefore, the material flow in FSW is governed by mass and momentum conservation equations [2, 27], while to describe the heat transfer process, energy conservation equation is used. In these equations the mathematical statements of the conservation laws of physics are represented. The continuity equation is given by

$$\frac{du}{dx} + \frac{dv}{dy} + \frac{dw}{dz} = 0 \quad (3.1)$$

where u , v , and w are the velocities in x , y , and z directions, respectively. While, Navier-Stokes equation governs the momentum conservation in x , y , and z directions:

$$\frac{\partial u}{\partial t} + u \frac{\partial u}{\partial x} + v \frac{\partial u}{\partial y} + w \frac{\partial u}{\partial z} = F_x - \frac{1}{\rho} \frac{\partial p}{\partial x} + \eta \left(\frac{\partial^2 u}{\partial x^2} + \frac{\partial^2 u}{\partial y^2} + \frac{\partial^2 u}{\partial z^2} \right) \quad (3.2)$$

$$\frac{\partial v}{\partial t} + u \frac{\partial v}{\partial x} + v \frac{\partial v}{\partial y} + w \frac{\partial v}{\partial z} = F_y - \frac{1}{\rho} \frac{\partial p}{\partial y} + \eta \left(\frac{\partial^2 v}{\partial x^2} + \frac{\partial^2 v}{\partial y^2} + \frac{\partial^2 v}{\partial z^2} \right) \quad (3.3)$$

$$\frac{\partial w}{\partial t} + u \frac{\partial w}{\partial x} + v \frac{\partial w}{\partial y} + w \frac{\partial w}{\partial z} = F_w - \frac{1}{\rho} \frac{\partial p}{\partial z} + \eta \left(\frac{\partial^2 w}{\partial x^2} + \frac{\partial^2 w}{\partial y^2} + \frac{\partial^2 w}{\partial z^2} \right) \quad (3.4)$$

where F_x , F_y , and F_z are the forces in x , y , and z directions, respectively; p is the static pressure of the flow field; η is the fluid viscosity and ρ is the material density. Also, the energy conservation equation is written as:

$$\rho c p \left(\frac{\partial T}{\partial t} + u \frac{\partial T}{\partial x} + v \frac{\partial T}{\partial y} + w \frac{\partial T}{\partial z} \right) = k \left(\frac{\partial^2 T}{\partial x^2} + \frac{\partial^2 T}{\partial y^2} + \frac{\partial^2 T}{\partial z^2} \right) \quad (3.5)$$

where T is the temperature, cp is the specific heat, and k is the thermal conductivity. By using the finite volume method, the governing equations for 3-D transient heat transfer and material flow are discretized and solved using ANSYS/FLUENT 17.0 [68]. For those who are interested in the numerical solutions of such engineering problems, different related titles are recommended here [69-74] which present wide areas to discuss the treatment of incompressible, compressible and viscous flows as well as heat transfer problems.

3.2 Pre-Processing

Since the beginning of FSW modelling, CFD technique has shown high capability to simulate the material flow and heat transfer during this welding process. Developing CFD model is basically accomplished in three main stages, Pre-Processing, Solver Execution and Post-Processing. As a first stage in CFD simulation process, Pre-Processing includes describing the computation domain (the main regions and the geometry) and dividing the domain into smaller sub-domain which is known as the mesh. This section provides details of the geometric modelling and the meshing of the computation domain.

3.2.1 Model Regions and Geometry

Using the Design Modeller facility in Ansys 17.0, the geometric details of the model have been created. As it can be seen in figure 3.1, the current numerical model has two main regions; the first one represents the thermomechanical affected zone (TMAZ) around the tool. This zone is treated as a fluid region which has a conical shape where, its dimensions are estimated based on design variables " x_1 " and " x_2 " as displayed in figure 3.2. According to Kang et al. [26], the dimensions of this rotational zone " x_1 " and " x_2 " are 1mm and 2.5mm, respectively. The second region represents the other part of the workpiece which is treated as a solid region.

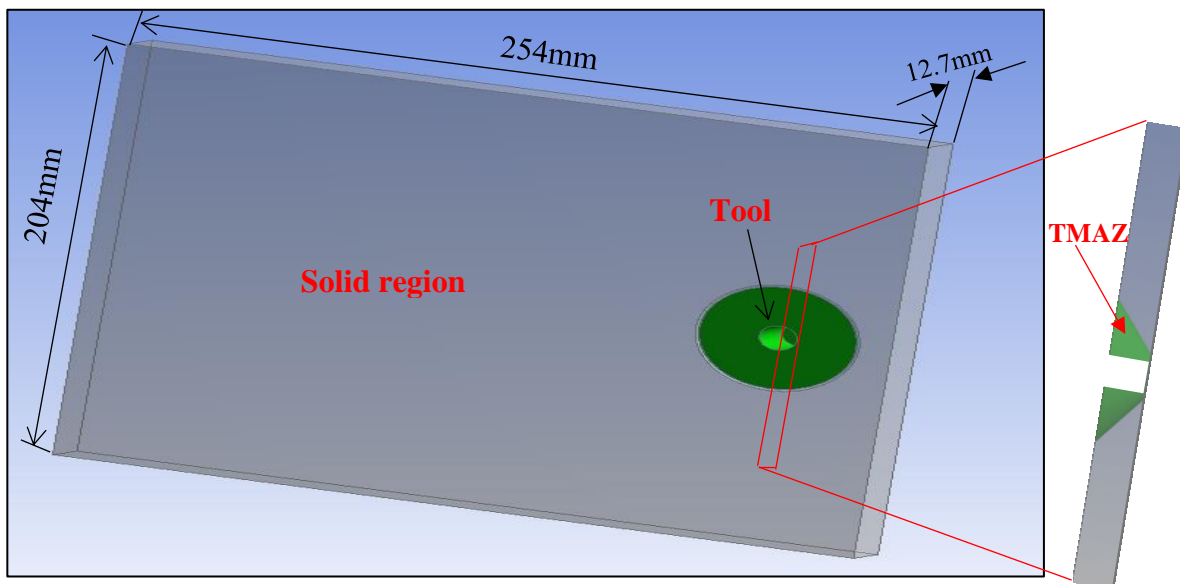


Figure 3.1 The main regions in the computation domain

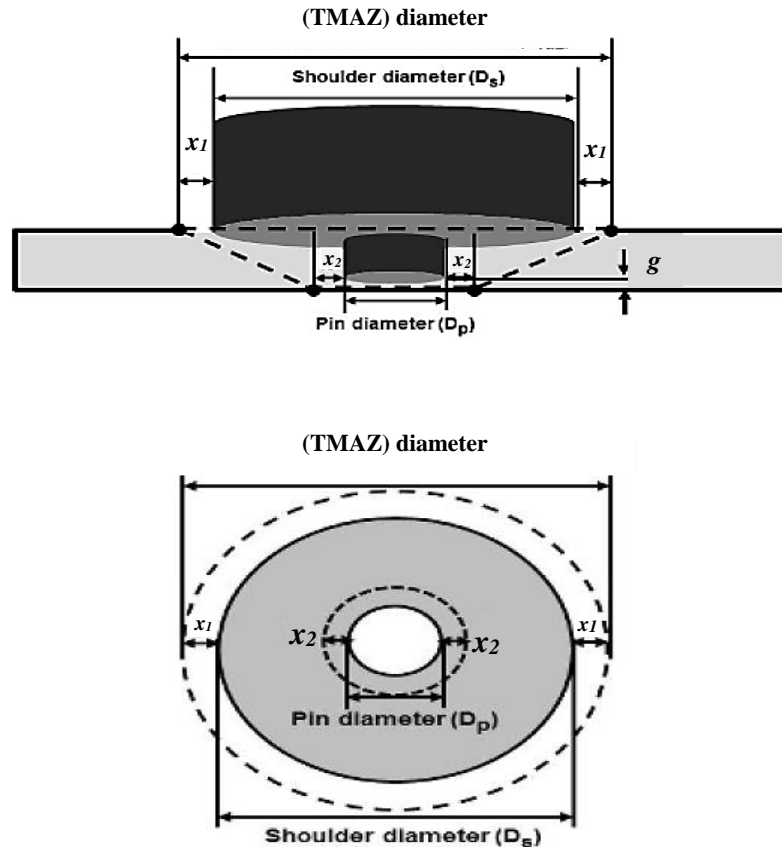


Figure 3.2 TMAZ details

Based on practical dimensions from the literature [28], the numerical model of the computational domain consists of volumes of two plates of aluminium alloy AA6061, in contact with each other. The tool, consisting of the shoulder and the pin is being inserted into the workpiece at the interface of the two plates. The tool pin has a cylindrical profile with a radius of 6mm and a length of 12.0mm, where the shoulder has a constant radius of 25mm. The tool was simulated as a wall after cutting its material volume from the workpiece. The dimensions of each plate to be welded are 254mm x 102mm x 12.7mm.

3.2.2 Meshing of the Computational Domain

The mesh quality and providing the minimum number of elements have been carefully considered during the meshing of the computational domain. Moreover, looking at the objectives of the current study which aim to achieve a more realistic model, the tool motion has also considered in

estimation of the meshing techniques. Accordingly, the rotation of the tool has been specified using sliding mesh technique in the TMAZ [75], as it does not make any approximation on the profile of the moving tool[68]. Generally, as the distance from the tool increases, a gradient change in the temperature takes place. However, compared to the locations that are far away from the tool; the temperature spatial gradient in the vicinity around the tool is severe [34]. Therefore, and purposefully (TMAZ) has been finely meshed to capture this level of gradient. As per the geometries of the tool and the workpiece, tetrahedral elements are easier to create with accepted level of skewness rather than other types of elements [76]. Thus, these kinds of elements have been chosen for meshing the whole regions of the computation domain where the number of elements reached around 700,000 elements. As the value of skewness is a criterion to measure the mesh quality, the created mesh has recorded a skewness of 0.62. That means the mesh quality is good as the high values of skewness is not recommended and should be less than 0.95 according to ANSYS. Figure 3.3, shows meshing of the computation domain in which two cross sections were taken to display the varied zones and how gradually meshed. It is worth mentioning that the mesh shown in the figure is an initial mesh which will be used in the dwelling stage of the welding process where the tool has only rotational motion.

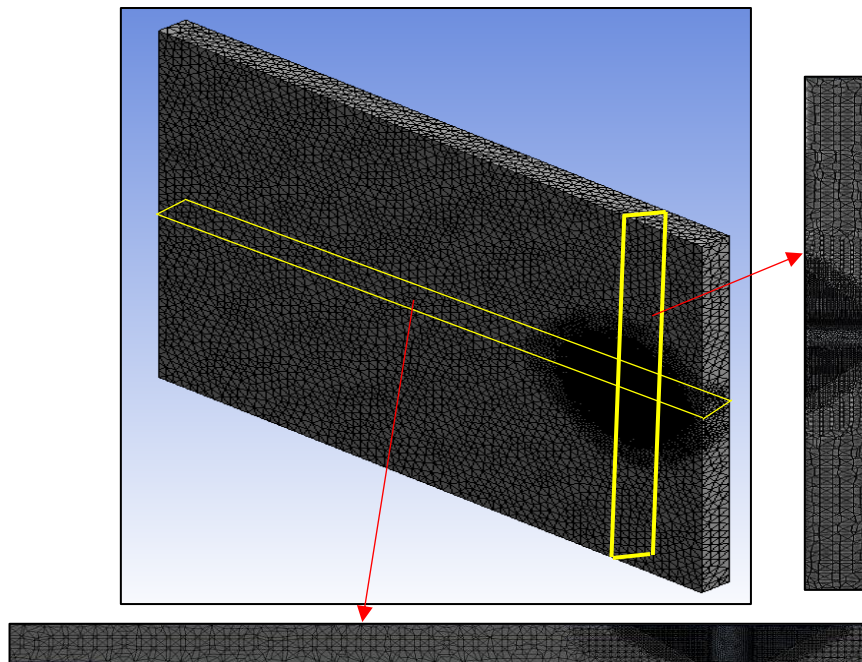


Figure 3.3 Meshing of the computation domain

As previously explained, the tool has two types of motion in the welding stage of FSW where it rotates and translates along the joint line. Furthermore, it is noteworthy that in the common CFD models of FSW, defining the translational tool motion in terms of inlet flow velocity is still an approximation. Hence, in the current study a new methodology was proposed to avoid this approximation and getting the realistic movement of the tool. In this methodology, the translational motion of the tool has been specified using dynamic mesh technique, and considering the path followed by the tool as a solid region, rather than fluid. Accordingly, a continuous change of the mesh is taking place with the time while the tool traveling [75].

3.2.3 Dynamic Mesh

Dynamic mesh differs from the time-constant mesh in that the cells might disappear, merge or at least change their shape during the time dependent simulation. According to the translational movement of TMAZ which represents the tool motion, the cell boundaries will move with this prescribed motion. Consequently, the boundary elements adjacent to TMAZ will deform to keep the mesh consistency and the nodes corresponding to the deformed mesh will be updated. In the current study, User Defined Function (UDF) subroutine was prepared to apply both of travel and rotational motion [Appendix A-2]. In order to avoid the mesh to be invalidated, three different methods are provided by Fluent to update the dynamic mesh which are smoothing, layering and remeshing. Layering cannot be used for the tetrahedral mesh while both smoothing and remeshing are recommended. Therefore, they have been selected to update the mesh in the deforming zone which is the area between the conical outer boundary of TMAZ and the outer boundaries of the workpiece.

Regarding smoothing, the spring-based scheme was used with Spring Constant Factor of 0.5. This means that the edges between the nodes are treated by the spring-based scheme a network of connected springs with Spring Constant Factor of 0.5. In other words, expanding and compression of the edges can take place due to the deformation of the mesh nodes at the dynamic boundaries according to the specified motion. As the edges expand and compress, imaginary spring force is generated on the nodes. This fictitious force and the updated displacement of the nodes are proportional to each other. Figure 3.4, shows the smoothing process after twenty time steps from the beginning of translational motion. In fact, the spring-based smoothing scheme is only helpful

when the displacements of the boundaries are small where it cannot accommodate the large displacements. Thus, remeshing method has been used along with smoothing to treat all the boundaries movement whether is small or big which means the complete updating of deforming mesh.

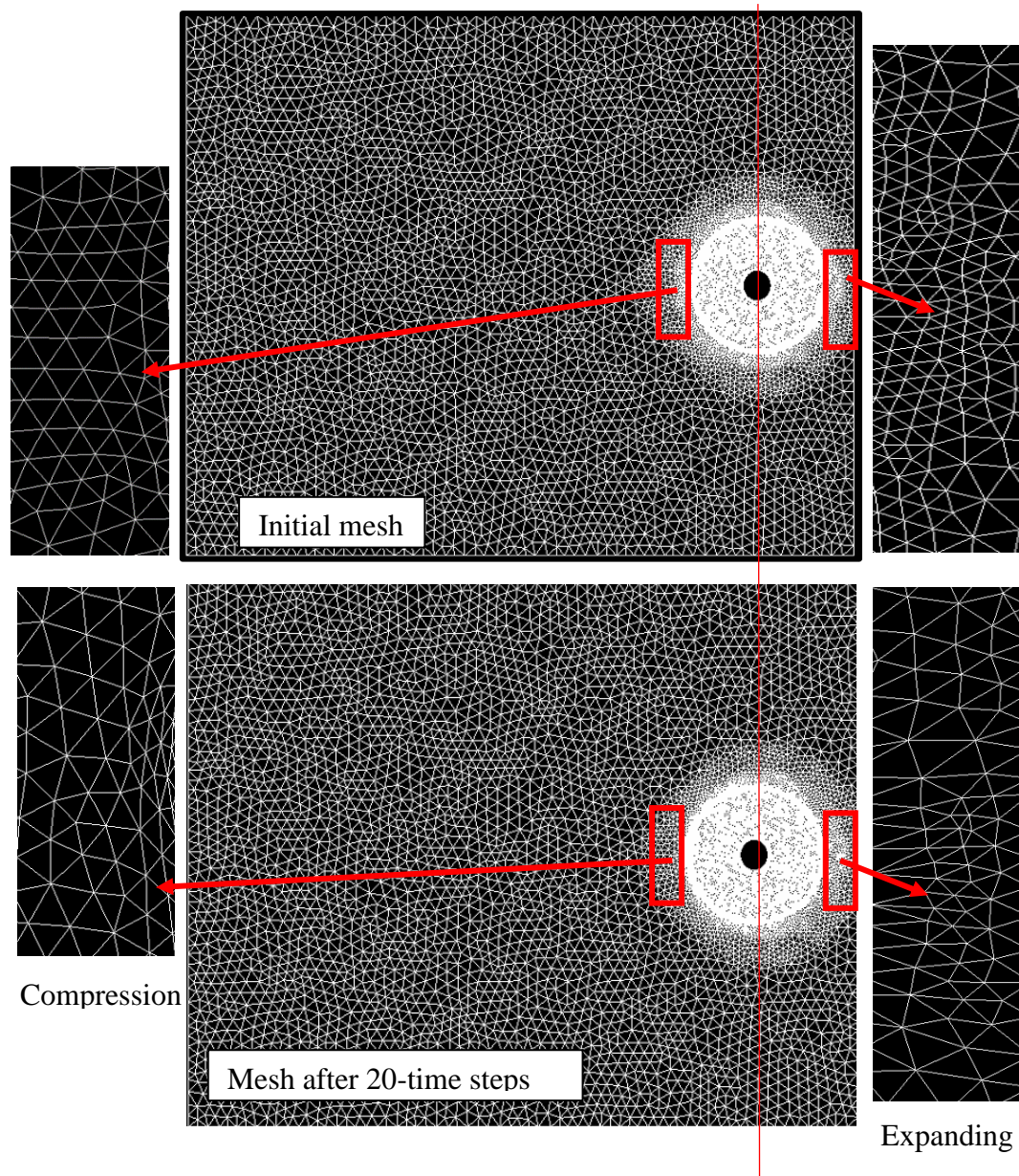


Figure 3.4 Smoothing process

In the process of remeshing, all the cells in the deforming zone are examined according to the mesh criteria that had been set by the user. Consequently, the ones that fail to meet these criteria are marked and then new meshes are locally patched in the area around those cells. After that, the entire zone will be remeshed just in case of failing the local remeshing in creation of a better mesh as depicted in figure 3.5. In table 3-1, the parameters of remeshing process used for the dynamic mesh are listed where the size criteria and the skewness of the mesh are shown.

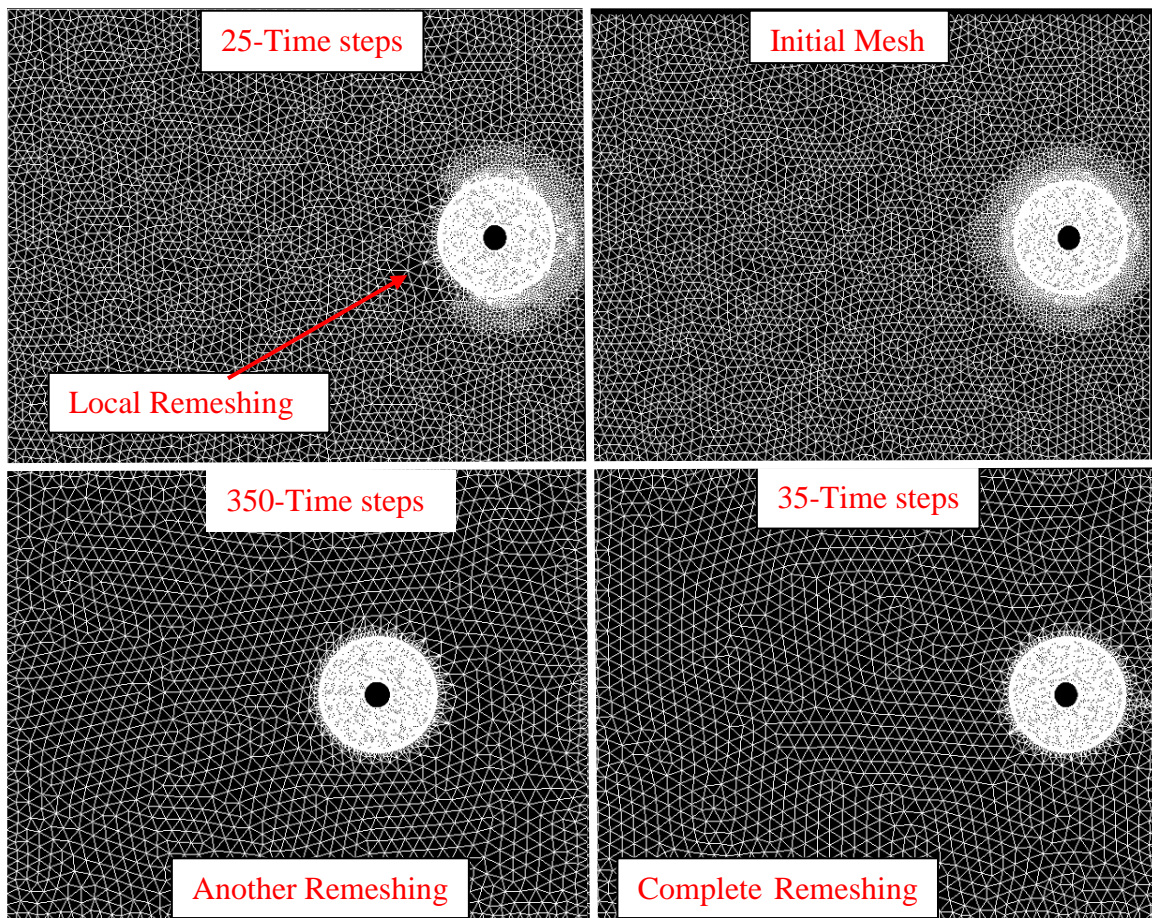


Figure 3.5 Remeshing process

Table 3-1 Dynamic Mesh Settings

Remeshing Parameters	
Minimum Length Scale	0.000149 mm
Maximum Length Scale	0.005753 mm
Maximum cell skewness	0.8
Maximum face skewness	0.7

3.3 Solver Execution

The Solver Execution in CFD consists of the setting of the physical model, the material properties and the boundary conditions. To solve the governing equations spatially and transiently in the computation domain, the solver called Fluent was used in the present study which is already included in the CFD package Ansys 17.0. the main steps of solving and running the simulation will be provided in the following sections.

3.3.1 Selection of the Physical Models

For simplifying of the current model building, some assumptions have been considered such as no-slipping condition at the contact surface between the tool and the workpiece as it has been experimentally proved to be closer to the real situation [67] . In addition to that no tilt angle was given to the welding tool, while only conduction and convection heat transfer are considered [7, 13, 19]. Moreover, the heat generation due to tool travel speed is neglected as it is very small [77]. In the vicinity of the welding tool, and due to the resultant heat generation from the rotational speed of the tool, the liquid material behaves as non-Newtonian, viscoplastic, laminar and incompressible fluid [2, 27]. Therefore, viscous laminar model that is available in Fluent was used in this study with reasonable accuracy. Besides that, as far as the effects of thermal changes during the process are concerned it is worth mentioning that in some real cases of FSW, melting temperature could be reached if the welding parameters have not been carefully controlled which in role causes a high heat input. That is why solidification/melting model was also proposed to be used among the other models that are available in the commercial CFD package.

3.3.2 Solidification / Melting Model

Fluent is equipped with solidification / melting model which has ability to cope with a wide range of solidification and melting problems. For some engineering processes such as casting and melting, solidification/melting model can solve the phase change that is likely to happen whether at constant temperature or over temperature range which means for pure metals or binary alloys respectively [78]. On the other hand, solidification / melting model is only available with the segregated solver while it is not when using the coupled solvers. Furthermore, compressible flows cannot be treated by solidification and melting model [68].

Depending on a certain technique called enthalpy–porosity technique, the Solidification/Melting Models are solved in Fluent. As there is no an explicit tracking of the melt interface, the amount of liquid with respect to the same cell volume in the domain is calculated which is named as the liquid fraction. The calculation of the liquid fraction at each iteration are carried out based on an enthalpy balance. The mushy zone is another significant feature in this model which represents the zone in which the liquid fraction is distinguished between 0 and 1. As a porous medium, the mushy region is modelled whereas the decrease in porosity grades from 1 to 0 as long as the material solidifies. When the full solidification of material takes place, the porosity reaches zero [68].

For the Solidification/Melting Model, the temperature is basically calculated based on a defined relation between enthalpy and temperature whereas the enthalpy is considered as the primary variable [79]. Therefore, the energy equation is expressed as [68, 78]

$$\partial_t(\rho HL) + \nabla(\rho \vec{v} HL) = \nabla(k \nabla T) + O \quad (3.6)$$

where HL is enthalpy, ρ is the density of the material, \vec{v} is the fluid velocity and O is the source term. The enthalpy HL can be calculated as

$$HL = hl + \Delta HL \quad (3.7)$$

where hl is the sensible enthalpy, ΔHL is the content of latent heat that might be changed from 0 (solid) to 1 (liquid). In order to define the sensible enthalpy equation, the following equation is used

$$hl = hl_{ref} + \int_{T_{ref}}^T cp \Delta T \quad (3.8)$$

where hl_{ref} is the reference enthalpy, T_{ref} is the reference temperature, cp is the specific heat.

As previously mentioned, the content of latent heat that might be changed from 0 (solid) to 1 (liquid). Another variable can be defined which is LT , where it is the latent heat of the phase change material. Then, the content of latent heat can be expressed in terms of LT [68, 78].

$$\Delta HL = \beta \cdot LT \quad (3.9)$$

where β is the liquid fraction that can be calculated as following

$$\beta = 0 \text{ if } T < T_{solidus}$$

$$\beta = 1 \text{ if } T > T_{liquidus}$$

$$\beta = \frac{T - T_{SOLIDUS}}{T_{LIQUIDUS} - T_{SOLIDUS}} \quad \text{if } T_{solidus} < T < T_{liquidus} \quad (3.10)$$

3.3.3 Material Properties

Aluminium alloy (AA6061) was used in this study where its chemical composition is summarized in table 3.2 and the temperature dependent thermophysical properties such as the thermal conductivity and specific heat have been considered. Table 3.3, provides the equations of these thermophysical properties of the workpiece. Basically, the fluid medium in (TMAZ) was defined as liquid aluminium with a density of 2700 kg/m^3 . Remarkably, the volume of fluid zone in the computation domain is small which is one of the current model's advantages as it minimises the inaccurate values of temperature distribution [26, 34]. Moreover, as the constant viscosity would affect the results, different values of viscosity are considered according to the approximation of the viscosity of the plasticised metal proposed by Sheppard and Wright [24, 28] in which the ratio of the effective stress and the strain rate is used as

$$\eta = \frac{\sigma_E}{3\dot{\epsilon}} \quad (2.3)$$

where η is the material viscosity, σ_E is the effective stress and $\dot{\epsilon}$ is the strain rate. The Zener-Hollomon parameter [24, 26-28] is used to obtain the value of σ_E as follows

$$\sigma_E = \frac{1}{\alpha} \ln \left[\left(\frac{Z}{\dot{A}} \right)^{\frac{1}{n}} + \left(\left(1 + \frac{Z}{\dot{A}} \right)^{\frac{2}{n}} \right)^{\frac{1}{2}} \right] \quad (2.1)$$

And

$$Z = \dot{\epsilon} \exp \left(\frac{\dot{Q}}{RT} \right) \quad (2.2)$$

where, Z is the Zener-Hollomon parameter, T is the temperature, \dot{Q} is the active energy, R is the universal gas constant, α , n , and \dot{A} are the material constants which their values are listed in table 3.4 for AA6061. Based on this approximation, a User Defined Function (UDF) subroutine was used to estimate the values of viscosity [Appendix A-1].

Table 3-2 Workpiece composition. [27]

Element	Al	Cu	Si	Mg	Cr	Mn,Ti, Zn, others
Wt. (%)	95.8 – 98.6	0.15 – 0.4	0.4 – 0.8	0.8 – 1.2	0.04 – 0.35	<1

Table 3-3 Thermophysical properties of the workpiece. [27]

Specific heat (J.kg ⁻¹ . K ⁻¹)	794.58 + 0.5051T – 0.00004 T ²
Thermal conductivity (W.m ⁻¹ . K ⁻¹)	96.442+0.2466 T- 0.00009 T ²

Table 3-4 Material constant and other values for AA6061. [27]

Constant	\dot{Q} [KJ/mol]	R [J/mol· K]	α [MPa ⁻¹]	n	\dot{A} [s ⁻¹]
Value	191	8.314	1/60.7	5.33	1.63 x 10 ¹³

3.3.4 Boundary Conditions

The workpiece walls and the translating tool wall are the boundary types that have been specified. With a view to simulate the two real motions of the tool, it has been specified with rotational and travel speeds of 637rpm 1.59mm/s, respectively. Those speeds represent practical values which were taken from the literature [28] where User Defined Function (UDF) subroutine was prepared

to apply both of travel and rotational speed of the tool [Appendix A-2]. Thermally, to define the process of heat generation, a heat flux was applied to the tool surface after it had been calculated by the analytical heat generation equation given as [49]

$$Q = \frac{2}{3} \pi \mu \omega P (R_{Shoulder}^3 + 3 R_{prob}^2 H_{prob}) \quad (3.11)$$

where, μ is the friction coefficient taken as 0.4 [64], ω is the rotational speed of the tool, P is the plunging pressure which was kept at 12.7Mpa. As the heat generation is given by the above equation, 85% of process efficiency was adopted [34] and then divided by the total surface area of the tool to give the heat flux. During the heat transfer analysis, the convection heat transfer coefficient from the top and side surfaces of the workpiece are $25\text{W/m}^2\text{ }^\circ\text{C}$, and whereas the bottom surface is supported by a backing plate, the coefficient value is considered as $200\text{W/m}^2\text{ }^\circ\text{C}$ [26, 80].

3.3.5 Solver Setting and Convergence Criteria

In order to get an accurate prediction of the heat flow and the temperature distribution in the computation domain, application-based solver settings are mainly required. Pressure-based segregated solver along with SIMPLE algorithm has been used in the current study as the Pressure-based segregated solver can be used for a wide range of flow systems as well as the less memory needed for storage rather than that required for coupled solvers. Furthermore, SIMPLE algorithm is robust which means it is memory efficient. By using the SIMPLE algorithm, the velocity field can be obtained through solving the momentum equation while for obtaining the new pressure distribution, the pressure equation is formulated and solved. Then, velocity magnitudes will be corrected [74, 81]. In terms of computing pressure gradient, the interpolation is required for calculating cell-face pressures. In doing so, Green – Gauss Node – based gradient evaluation approach has been used as it is strongly recommendable for tetrahedral mesh and more accurate than other approaches. Moreover, to complete the interpolation process, PRESTO scheme was selected for its efficiency when treating the highly swirling flows, the steep pressure gradient and the strongly curved domains. On the other hand, second order upwind scheme has been chosen for the momentum and the energy. The reason is that, the second order upwind scheme can guarantee more accurate results and it is essential with tetrahedral mesh, also when the flow and the grid are not aligned [74, 81].

The converged solution means a stable state in the solution. In other words, no variations in the flow parameters when the iterative process of the solver is considered. By looking at solving the heat flow problem with a reasonable accuracy, getting to a converged solution is mainly required [82]. In the current study, the convergence criteria that have been considered are the default criteria in ANSYS 17.0 which are 0.001 for the continuity and momentum while 0.000001 for the energy. Accordingly, when the change in the continuity, velocities and energy becomes below the corresponding criterion that means the solution is converged.

3.4 Mesh Independence Test

In order to conduct the independence test for the primary mesh, three different meshes were used as shown in table 3.4. As the maximum temperature has been recorded at a point with a transverse distance of 8mm from the weld centre and a depth of 2mm from the top surface of the workpiece, the test results showed that the calculated value of maximum temperature approaches to the experimental value as long as the mesh is refined. Additionally, the difference is less than 1% between the meshes with 350000 and 700000 elements while the difference was around 0.65% between the meshes with 700000 elements and 1.4 million elements. Accordingly, in terms of reducing the computation cost along with an acceptable accurate predicting; the mesh with 700000 elements has been nominated for further analysis.

Table 3-5 Mesh Independence Results

Mesh	Measured Max. Temperature(K)	Max. Temperature(K)	Difference (%)
350000	835(562 °C)	808.86 (535.86 °C)	
700000	835(562 °C)	814.09 (541.09 °C)	0.97
1400000	835(562 °C)	817.62(544.62 °C)	0.65

3.5 Time Step Independence Test

In a view of the solution stability and accuracy, time step independence test has a significant role. As earlier mentioned, that both sliding and deforming mesh are employed in the current model, hence there is a need to determine the optimum time step for both techniques. It is worth noting that dynamic mesh is predominantly much critical and dominant than sliding as it is sensitive to fail at any time step even it was advanced in the computation time. That is why, guarantee a successful dynamic mesh over the total computation time has the highest priority. For instance,

several considerations should be taken in account to avoid negative cell volume problem. Consequently, it is obvious that conducting the test is complicated whereas different procedures would be undertaken to harmonise the time step.

To start with, Courant number concept is used to ensure that the solution will become stable. In essence, Courant number should be less than 1 which can be defined as [83]:

$$C = \frac{V \Delta t}{\Delta x} < 1 \quad (3.12)$$

where V is the speed, Δt is the time step of the numerical model, and Δx is the spacing of the grid in the numerical model. The time step that was chosen for achieving the criteria is 0.1 second and the minimum spacing of the grid in the numerical model is 0.16250mm. By considering the translational speed, the resultant Courant number is 0.9784 which meets the condition as it is less than 1. Now, the question is for what extent the negative cell volume can be avoided within this time step size. In order to avoid the mesh to be invalidated, the volume mesh is updated using the spring-based smoothing with Spring Constant Factor of 0.5 as this mesh motion method is normally employed for those zones are meshed with a triangular or tetrahedral mesh. Another method was used which is local cell remeshing for its ability to affect tetrahedral cell types where the maximum cell skewness was 0.8 [68, 84].

After circumventing the problem that might happen within the dynamic mesh and by considering that 0.1second is the maximum reference step size that must not be exceeded, the concern is now about how to evade the effect of the change in the time step on the results particularly for the primary mesh. When talking about the primary mesh that means the period from the welding process in which the tool is only rotating and not translating. In other words, the moments in which the mesh is working without deforming and the sliding mesh is playing the key role. Hence, to investigate that effect and carrying out the time step independence test; three-time steps of 0.1sec, 0.066666sec, and 0.0333333sec were suggested under the above estimated maximum reference step size. These three proposed time steps represent the length of time during which the tool will rotate 1.061rev (382.2degree), 0.7076rev (254.8degree), 0.3538rev (127.4degree) respectively.

Table 3.5, displays the three-different values of proposed time steps along with the values of the maximum temperature that were recorded for those time steps at a point with a transverse distance of 8mm from the weld centre and a depth of 2mm from the top surface of the workpiece. In terms

of the time step effect, it can be clearly seen that by increasing the time step from 0.033 to 0.1sec the difference percentage is just 0.71% which indicates that numerical results are insignificantly influenced.

Table 3-6 Time step independence results

Time step (sec)	Max. Temperature K(C°)	Difference (%)
0.033	818K(545C°)	
0.066	816.2K(543.2C°)	0.33%
0.1	814.09K(541.09C)	0.71%

From the above and in view of the computation cost specifically when dealing with a thermal cycle duration of 100sec parallel with using of dynamic mesh, the time step of 0.1sec was nominated for future analysis.

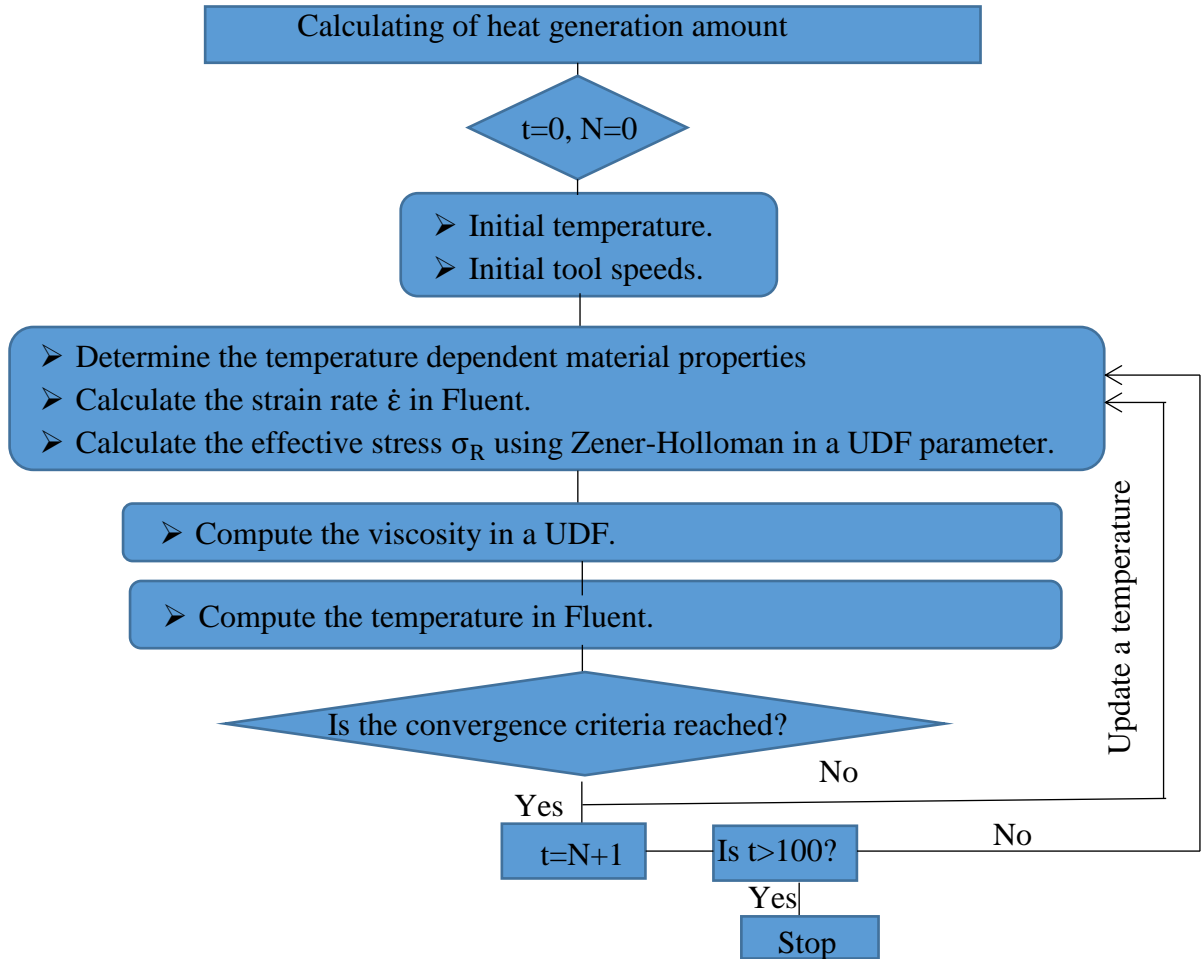
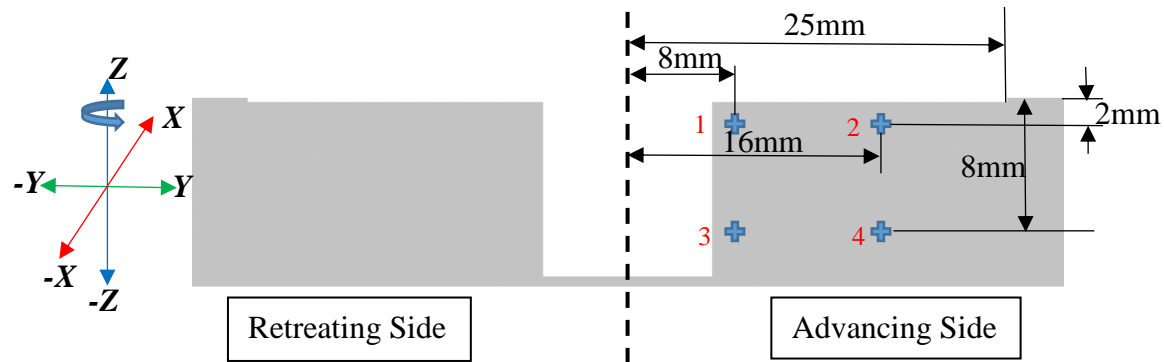


Figure 3.6 Calculation flow chart

3.6 Benchmark Tests

The numerical results' benchmarking is required to validate the current proposed model. Therefore, the CFD predicted time-dependent temperature was recorded for 100 seconds of operation at 4 points located in the advancing side, two of them (point 1 and 2) having a transverse distance of 8mm and 16mm from the weld centre at a depth of 2mm from the top surface of the workpiece. The other two points (3 and 4) having the same transverse distances but at a depth of 8mm from the top surface of the workpiece. The predicted temperatures at the four points verified against published experimental data for aluminium alloy (AA6061) by R. Nandan et al. [28].



X: Translational movement direction.

Z: Axis of the rotational movement.

Figure 3.7 Locations of monitoring points related to the tool and workpiece dimensions

Figures 3.8a, 3.9a, 3.10a, and 3.11a illustrate the calculated temperature profiles from the current developed CFD model and the traditional CFD model (baseline) [24, 29, 32, 33, 35, 39, 41] at the four monitoring locations against the measured ones. Generally, the trend of the temperature at each point represents a thermal cycle of 100sec, in which the points are heated up until the peak temperature is achieved and then start to cool down. In the figures, it can be seen that the current CFD model has room of improvement where the accuracy has increased. Furthermore, the current CFD results and the experimental results are in better agreement where the averages of error percentages for points 1, 2, 3 and 4 are 4.23%, 5.89%, 5.02% and 4.35% respectively. Besides, figures 3.8b, 3.9b, 3.10b, and 3.11b show the difference between the temperature values calculated from CFD and those obtained from the experimental results. Within error band ranged from 0 to maximum $\pm 10\%$, it can be seen that most of the data lies in this range. Thus, it can be concluded that the current numerical model represents the physical model of FSW [82].

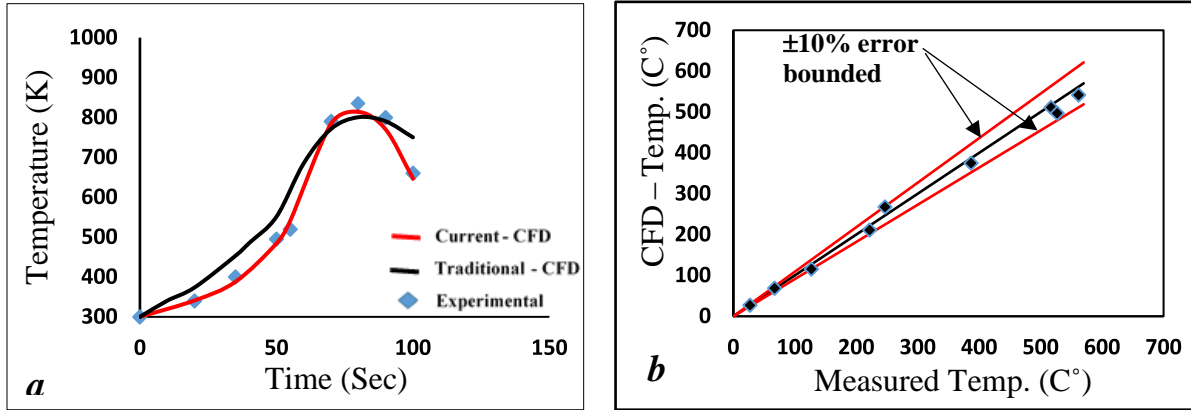


Figure 3.8(a) calculated and measured temperatures at point1 (b) the difference between calculated and measured temperatures at point1.

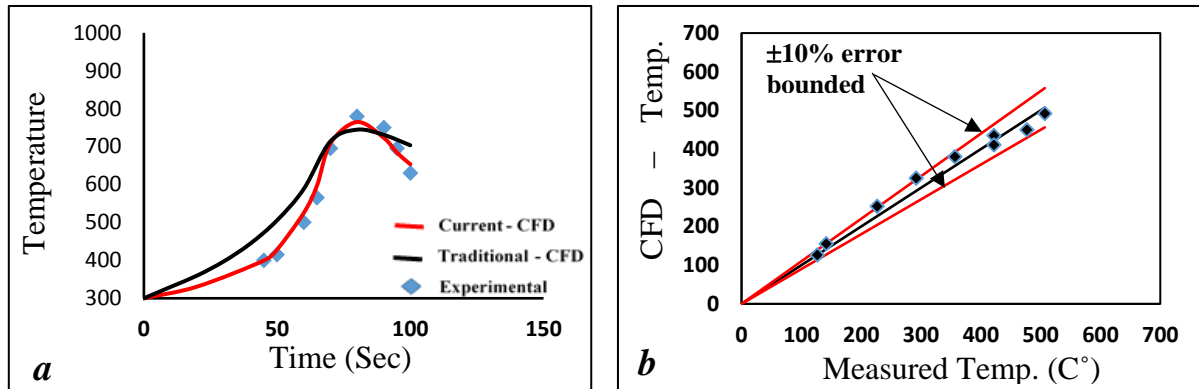


Figure 3.9(a) Calculated and measured temperatures at point 2 (b) the difference between calculated and measured temperatures at point 2.

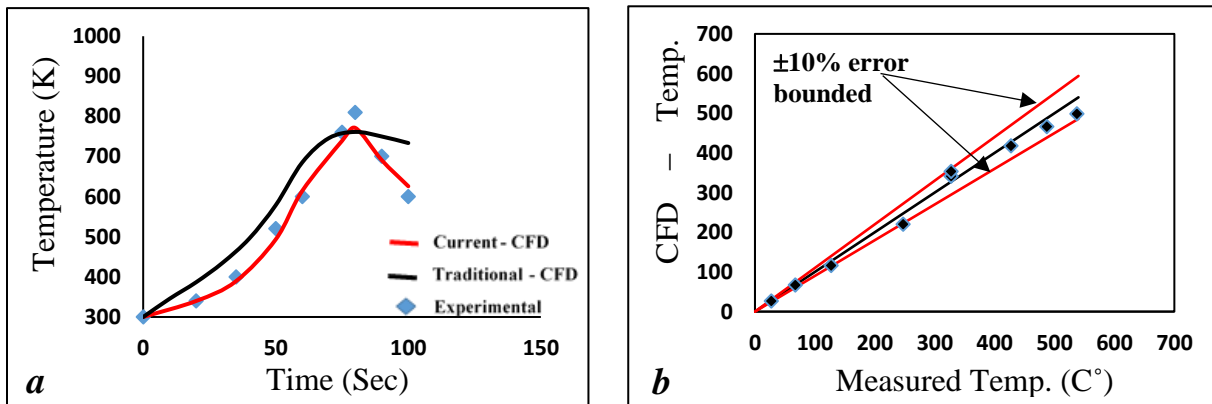


Figure 3.10(a) Calculated and measured temperatures at point 3 (b) the difference between calculated and measured temperatures at point 3.

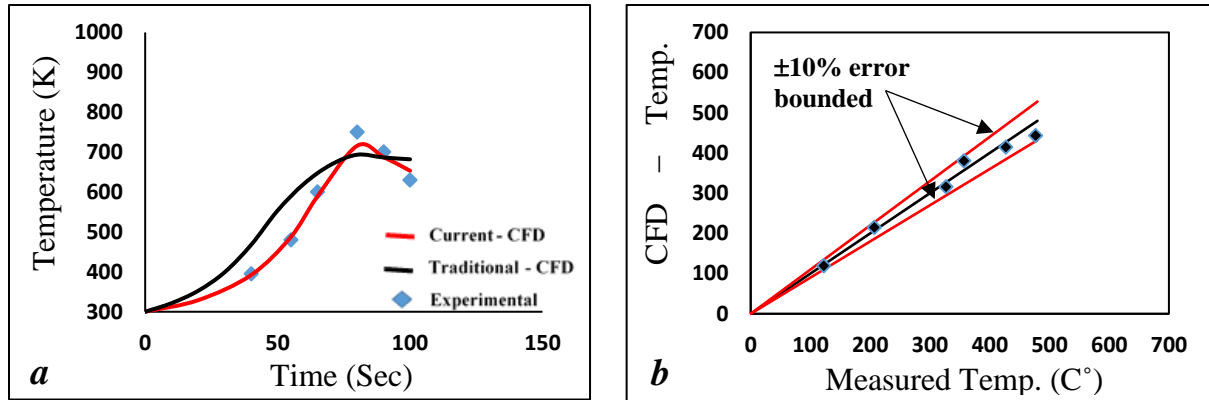


Figure 3.11(a) Calculated and measured temperatures at point 4 (b) the difference between calculated and measured temperatures at point 4.

CHAPTER 4: THERMAL CHARACTERISATION OF FRICTION STIR WELDING USING TOOL WITH POLYGONAL PINS

In order to have a better understanding of the nature of thermal changes accompanying FSW, this chapter presents how the proposed CFD methodology can be used to describe the thermal field associated to the FSW when using tool with polygonal pins. The effect of different geometrical and operational parameters on the temperature distribution and peak temperature within a thick FS welded workpiece has been investigated. Moreover, based on the investigation conducted, a semi-empirical prediction model for the peak temperature has been developed.

4.1 Analytical Modeling of Heat Generation from a Tool with Concentric Pin

Based on the objectives formulated in chapter 2, several FSW tools having different polygonal pin profiles have been investigated. In this section, a tool with Heptagonal pin profile has been chosen to demonstrate the detailed steps of developing the analytical models of the heat generated by these tools during the FSW process. The analytical models of the considered cases have been established based on the analytical models developed by Schmidt et al [13] and Gadakh et al [49]. In figure 4.1(a, b, c), the schematic of tools with different polygonal pins and the main regions of heat generation are shown, where Q_1 is the heat generated at the tool shoulder base, Q_2 is the heat generated at the sides of the tool pin and Q_3 represents the heat generated at the pin tip. Summation of these gives the overall heat amount Q_{total} produced due to the friction between the tool surfaces and the workpiece.

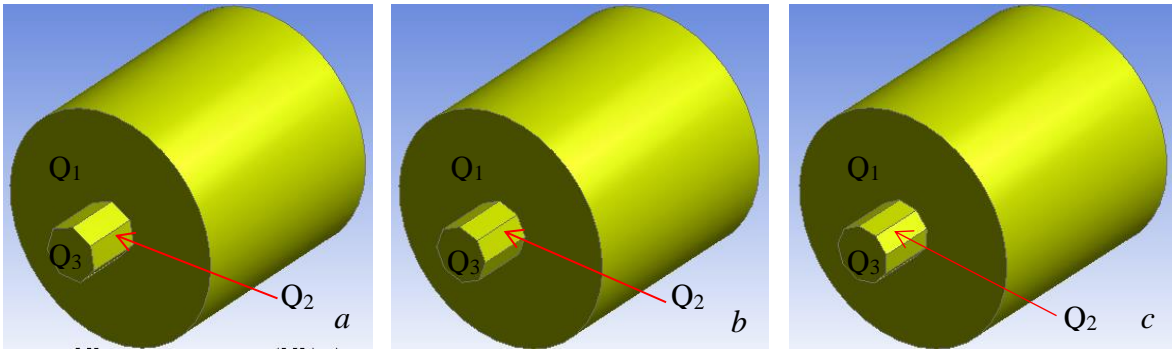


Figure 4.1 Tools with different pin profiles (a) Heptagon, (b) Octagon, (c) Nonagon.

4.2 Heat Generation from a tool with Concentric Heptagonal Pin

Uniform contact shear stress $\tau_{contact}$ is generally considered in FSW, while at the contact interface, sliding condition of the shearing is also regarded. Hence, the frictional shear stress $\tau_{friction}$ is estimated for this condition as $\tau_{contact} = \tau_{friction} = P \cdot \mu$, where P is the applied force per unit area of the shoulder base. Heat generated only due to friction is considered which means that the heat amount from deformation is neglected. The general equation for heat generation is [49]

$$dQ = \omega \cdot dM = \omega \cdot r \cdot dF = \omega \cdot r \cdot \tau_{contact} \cdot dA \quad (4.1)$$

where ω is the angular velocity, dM is the infinitesimal segment torque, r is the distance from the considered area to the centre of rotation, dF is the infinitesimal segment force that produces the torque, and dA is the infinitesimal segment area exposed to a uniform contact shear stress $\tau_{contact}$.

4.2.1 Heat Generation from Shoulder Base

To calculate the net frictional heat generation from shoulder base, the heat generated at the pin tip should be subtracted from the heat generated at the shoulder base. Figure 4.2 shows the effective shoulder base area at which the heat is generated. Thus, the considered area segment $dA = r \cdot d\theta \cdot dr$ generates heat

$$dQ = \omega \cdot r \cdot \tau_{\text{contact}} \cdot r \cdot d\theta \cdot dr \quad (4.2)$$

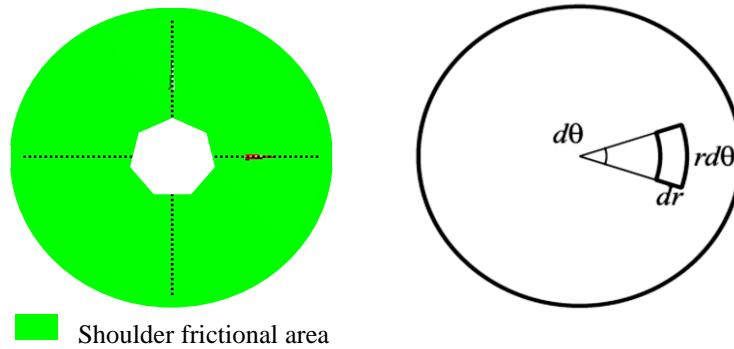


Figure 4.2 Shoulder effective area and the infinitesimal segment area for the tool with heptagonal pin profile

By integrating eq. 4.2 over the area from 0 to R_s , the net heat generation at the shoulder base Q_1 can be expressed as:

$$Q_1 = \int_0^{2\pi} \int_0^{R_s} \omega \cdot r^2 \cdot \tau_{\text{contact}} \cdot d\theta \cdot dr - Q_3 \quad (4.3)$$

where R_s is the shoulder radius. Thus:

$$Q_1 = \frac{2}{3} \pi \cdot \omega \cdot \tau_{\text{contact}} \cdot R_s^3 - Q_3 \quad (4.4)$$

4.2.2 Heat Generation from Pin Side Surfaces

To calculate the heat generation from the pin side surfaces, the main dimensions of the pin side need to be defined first. For a heptagonal pin, it can be seen in figure 4.3(a, b, c) that the pin is described by the following dimensions:

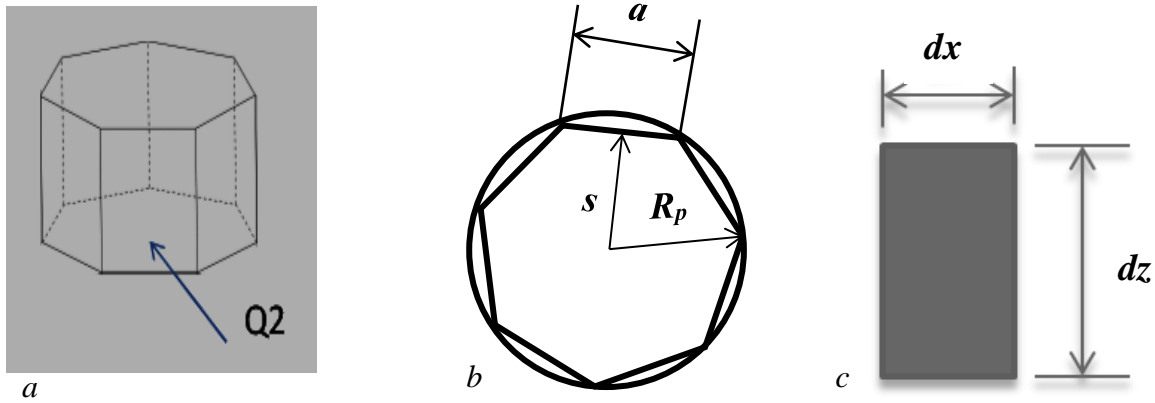
a is the side length.

s is the apothem that indicates the distance from the centre to the midpoint of a side.

R_p is the radius of the polygon's circumcircle.

H is the pin height.

Also, the infinitesimal segment area on each side of Heptagon is shown in figure 4.3 where $dA = dx \cdot dz$.



4.3 Main trigonometric dimensions of Heptagon and the infinitesimal segment area of each side

Therefore, over the pin side surface area, the heat generation equation can be written according to the following;

$$dQ = \omega \cdot s \cdot \tau_{contact} \cdot dx \cdot dz \quad (4.5)$$

By integrating eq. (4.5) over the side pin surface area from 0 to H , it gives the heat generation at one segment of pin side surface. In order to estimate the overall heat generation from the pin side, the equation should be multiplied by 7 for Heptagonal pin.

$$dQ = Q_2 = 7 \int_0^a \int_0^H \omega \cdot \tau_{contact} \cdot s \cdot dx \cdot dz \quad (4.6)$$

$$Q_2 = 7 (\omega \cdot \tau_{contact} \cdot s \cdot a \cdot H) \quad (4.7)$$

As in a regular polygon, the distance from the centre to any vertex indicates the radius of the polygon R_p , the relationship between this radius and the side length is

$$R_p = \frac{a}{2 \sin\left(\frac{180}{n}\right)} \quad (4.8)$$

where, n is the number of pin sides.

The relationship between the radius and the apothem is [85]

$$Rp = \frac{s}{\cos\left(\frac{180}{n}\right)} \quad (4.9)$$

By equating the equations 4.8 and 4.9, the apothem can be expressed as a function of the side length:

$$\begin{aligned} \frac{s}{\cos\left(\frac{180}{n}\right)} &= \frac{a}{2\sin\left(\frac{180}{n}\right)} \\ s &= \left(\frac{a}{2} \cot \frac{180}{n}\right) \end{aligned} \quad (4.10)$$

when $n=7$, s is equal to $1.0382 a$.

Substituting s in eq. (4.7), the final equation of heat generation at the pin side surfaces can be expressed as:

$$Q_2 = 7.2678 (\omega \cdot \tau_{contact} \cdot a^2 \cdot H) \quad (4.11)$$

4.2.3 Heat Generation from the Pin Tip

A flat pin tip surface has been considered in this study, which has been also divided into fourteen sections as shown in figure 4.4. Using polar coordinates, the heat generation equation for each section is expressed as:

$$dQ = \omega \cdot r \cdot \tau_{contact} \cdot r \cdot d\theta \cdot dr \quad (4.2)$$

By integration eq. (4.2) over the pin tip surface area from 0 to R_p , and using the multiplying factor 14 which denotes the fourteen sections that form the heptagonal tip surface, the heat generation from the pin tip Q_3 can be computed as:

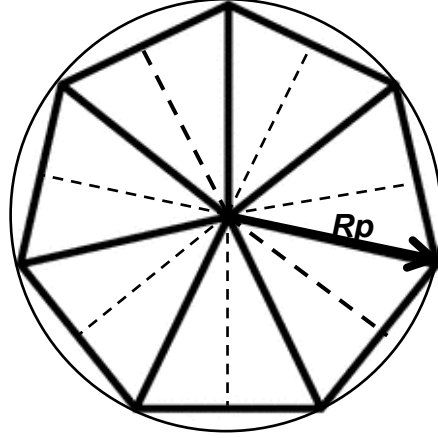
$$Q_3 = 14 \int_0^{\theta=\frac{\pi}{7}} \int_0^{Rp} \omega \cdot r^2 \cdot \tau_{contact} \cdot d\theta \cdot dr \quad (4.12)$$

In Eqn. 4.8, R_p is equal to $1.1523a$ when $n=7$. Therefore

$$Q_3 = 14 \int_0^{\theta=\frac{\pi}{7}} \int_0^{Rp=1.1523a} \omega \cdot r^2 \cdot \tau_{contact} \cdot d\theta \cdot dr \quad (4.13)$$

$$Q_3 = 14 \left[\frac{\pi}{7} \cdot \omega \cdot \tau_{contact} \cdot \left(\frac{(1.1523a)^3}{3} \right) \right] \quad (4.14)$$

$$Q_3 = \left[\frac{2 \times 1.53 \pi \cdot \omega \cdot \tau_{contact} \cdot a^3}{3} \right] \quad (4.15)$$



4.4 Schematic of the heptagonal pin tip

4.2.4 Total Heat Generation from the Tool with Concentric Heptagonal Pin

Using eqs. (4.4), (4.11) and (4.15), the total heat generation from the tool with heptagonal pin can be computed as:

$$Q_{total} = \frac{2}{3} \pi \cdot \omega \cdot \tau_{contact} \cdot R_s^3 - \left[\frac{2 \times 1.53 \pi \cdot \omega \cdot \tau_{contact} \cdot a^3}{3} \right] + 7.2678 (\omega \cdot \tau_{contact} \cdot a^2 \cdot H) + \left[\frac{2 \times 1.53 \pi \cdot \omega \cdot \tau_{contact} \cdot a^3}{3} \right] \quad (4.16)$$

$$Q_{total} = \frac{2}{3} \pi \cdot \omega \cdot \tau_{contact} \cdot R_s^3 + 7.2678 (\omega \cdot \tau_{contact} \cdot a^2 \cdot H) \quad (4.17)$$

Rearranging eq. (4.17)

$$Q_{total} = \frac{2}{3} \pi \cdot \omega \cdot \tau_{contact} (R_s^3 + 7.2678 \times \frac{3}{2\pi} a^2 \cdot H) \quad (4.18)$$

$$Q_{total} = \frac{2}{3} \pi \cdot \omega \cdot \tau_{contact} (R_s^3 + 3.47189 a^2 \cdot H) \quad (4.19)$$

Or

$$Q_{total} = \frac{2}{3} \pi \cdot \omega \cdot \tau_{contact} (R_s^3 + 3.47189 \left(\frac{R_p}{1.1523} \right)^2 \cdot H) \quad (4.20)$$

$$Q_{total} = \frac{2}{3}\pi \cdot \omega \cdot \tau_{contact} (R_s^3 + 2.61477 Rp^2 \cdot H) \quad (4.21)$$

Similarly, for the other tools with polygonal pin profiles that have a higher number of side faces, the heat generation expressions have been developed using the same analytical approach. Based on the number of pin faces, the heat generation expressions are listed in table (4-1).

Table 4-1 heat generation formulas of tools with different pin profiles

Pin Profile	No. of Faces	Equation
Heptagonal	7	$Q_{total} = \frac{2}{3} \pi \cdot \omega \cdot \tau_{contact} (R_s^3 + 2.61477 Rp^2 \cdot H)$
Octagonal	8	$Q_{total} = \frac{2}{3} \pi \cdot \omega \cdot \tau_{contact} (R_s^3 + 2.7018 Rp^2 \cdot H)$
Nonagonal	9	$Q_{total} = \frac{2}{3} \pi \cdot \omega \cdot \tau_{contact} (R_s^3 + 2.7632 Rp^2 \cdot H)$
Decagon	10	$Q_{total} = \frac{2}{3} \pi \cdot \omega \cdot \tau_{contact} (R_s^3 + 2.80756 Rp^2 \cdot H)$
Undecagon	11	$Q_{total} = \frac{2}{3} \pi \cdot \omega \cdot \tau_{contact} (R_s^3 + 2.8402 Rp^2 \cdot H)$
Dodecagon	12	$Q_{total} = \frac{2}{3} \pi \cdot \omega \cdot \tau_{contact} (R_s^3 + 2.8658 Rp^2 \cdot H)$
13-gon	13	$Q_{total} = \frac{2}{3} \pi \cdot \omega \cdot \tau_{contact} (R_s^3 + 2.8856 Rp^2 \cdot H)$
14-gon	14	$Q_{total} = \frac{2}{3} \pi \cdot \omega \cdot \tau_{contact} (R_s^3 + 2.90122 Rp^2 \cdot H)$
15-gon	15	$Q_{total} = \frac{2}{3} \pi \cdot \omega \cdot \tau_{contact} (R_s^3 + 2.9141 Rp^2 \cdot H)$
25-gon	25	$Q_{total} = \frac{2}{3} \pi \cdot \omega \cdot \tau_{contact} (R_s^3 + 2.9684 Rp^2 \cdot H)$
30-gon	30	$Q_{total} = \frac{2}{3} \pi \cdot \omega \cdot \tau_{contact} (R_s^3 + 2.979 Rp^2 \cdot H)$
40-gon	40	$Q_{total} = \frac{2}{3} \pi \cdot \omega \cdot \tau_{contact} (R_s^3 + 2.988 Rp^2 \cdot H)$

By comparing the developed expressions in the table with each other, it can be seen that all the terms in the equations are the same except those related to the pin radius. Accordingly, a general equation can be expressed as:

$$Q_{total} = \frac{2}{3}\pi \cdot \omega \cdot \tau_{contact} (R_s^3 + C_n \cdot R p^2 \cdot H) \quad (4.22)$$

where C_n has different values according to the number of polygon faces.

All above derived heat generation equations have been used for the same aluminium FSW welding process and conditions in chapter 3. After calculating the heat amount from the analytical equations for all proposed cases, they were plotted in figure 4.5 and compared with the calculated heat generated for the tool with cylindrical pin profile. It can be seen that the total heat produced by the tool increases as the numbers of polygon faces increase. Total heat generated from a tool having 7 side faces has been calculated to be 11878W, which increases to reach 11987W as the number of faces increases to 25. As the number of faces further increase, the increase in the total heat generation from the tool is very small. The reason for this is that the number of faces has increased so much where the pin shape approaches the cylindrical shape, which depicts maximum heat generation. Approaching 12010W as the number of faces increase, 12010W being the heat amount of the cylindrical pin. At this point, the frictional forces are maximum due to more exposed area of the pin.

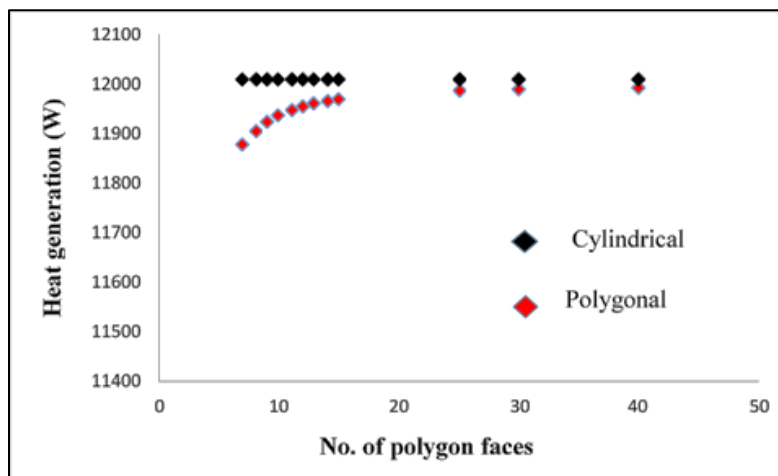


Figure 4.5 Heat generation variations w.r.t the number of sides of a concentric polygon tool

4.3 Thermal Analysis of FSW when using Concentric Polygonal Pins

Through the numerical analysis that will be carried out on the FSW process, heat transfer phenomenon and temperature distribution have been analysed. Similar to the other welding techniques, peak joint temperature and temperature profile in the region near the joint can have a significant impact on the plastic deformation zone, heat affected zones, and joint properties. In essence, they influence the final microstructure and residual stress state developed in the joint which affects the global features of the welded joint [86]. Therefore, the current CFD model with the aid of the analytical heat generation correlations have been used to estimate the effects of the different geometrical and operational parameters on the thermal field of FSW process.

In order to examine how number of pin faces might affect the maximum temperature, Heptagonal, Octagonal, and Nonagonal pin profiles have been used along with the welding parameters described in chapter 3. The maximum temperature has been locally monitored where it was recorded for a thermal cycle of 100 seconds at the four points that were defined in chapter 3 as shown in figure 3.7. As plotted in figure 4.124.6, the maximum temperature has scored the same value for each single point against different number of faces. For example, the maximum local temperature at point 1 were recorded to be 807.9K, 808.1K and 808.27K for the cases of Heptagonal, Octagonal, and Nonagonal pin profiles, respectively. Referring to the heat generation amounts in figure 4.5, it seems that the increase in the heat amount along with the increase in the number of faces is not that much high to cause an increase in the local temperature, particularly when considering the high thermal conductivity of aluminium as well as the plate thickness which enhances the heat transfer process. From another point of view, the distances between the four locations cause the difference in the temperature values where the highest temperature is expected to be close to the shoulder surface. As the temperature trend was the same for the three proposed tools and to reduce the number of numerical experiments, octagonal pin was nominated for further investigations.

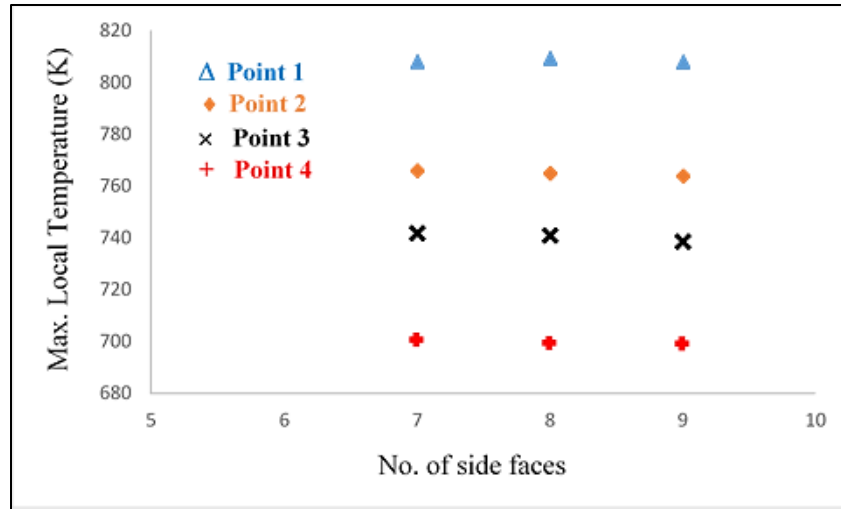


Figure 4.6 Local Maximum Temperature at four different points

As the next section aims at understanding the effects of a wide range of geometrical and operational parameters on the thermal characterisations of FSW, several process variables have been taken into consideration. The range of the chosen variables has been specified based on the practical values of these parameters and the model capability. As presented in table 4-2, a set of numerical experiments have been proposed to investigate the effects of the selected parameters which are shoulder size, pin size, pin height, material thickness, tool rotational speed and axial load. In this set of numerical experiments, the effect of each variable has been addressed by four different values as shown in the table by the yellow shaded cells.

Table 4-2 Process parameters and their ranges

No.	Shoulder Radius(mm)	Pin Radius(mm)	Pin Height(mm)	Material Thickness (mm)	Rotational Speed(rpm)	Axial load (MPa)
EX.1	13	6	12	12.7	637	12.7
EX.2	17	6	12	12.7	637	12.7
EX.3	21	6	12	12.7	637	12.7
EX.4	25	6	12	12.7	637	12.7
EX.5	25	3	12	12.7	637	12.7
EX.6	25	9	12	12.7	637	12.7
EX.7	25	12	12	12.7	637	12.7
EX.8	25	6	11	12.7	637	12.7
EX.9	25	6	10	12.7	637	12.7
EX.10	25	6	9	12.7	637	12.7
EX.11	25	6	12	14.7	637	12.7
EX.12	25	6	12	16.7	637	12.7
EX.13	24	6	12	18.7	637	12.7
EX.14	24	6	12	12.7	237	12.7
EX.15	24	6	12	12.7	437	12.7
EX.16	24	6	12	12.7	837	12.7
EX.17	24	6	12	12.7	637	9.7
EX.18	24	6	12	12.7	637	11.2
EX.19	24	6	12	12.7	637	14.2

4.3.1 Effects of Geometrical Parameters on the Thermal field of FSW

As mentioned in chapters 1 and 2, heat generation and heat transfer during FSW are significantly affected by the tool geometry and dimensions of the workpiece. In other words, factors such as

shoulder diameters, pin size as well as the workpiece thickness are important when the thermomechanical activities are interested. By considering the difficulties in tool manufacturing, using the experimental work to study the effects of the geometrical parameters is time consuming and costly. Conversely, the current CFD model has advantages for carrying out qualitative and quantitative analysis of the effects of various geometry related parameters of FSW at different conditions.

4.3.1.1 Effects of Shoulder Diameter on the Thermal field of FSW

To visualise how the change in the shoulder diameter may influence the thermal field, four different diameters have been used which are 26mm, 34mm, 42mm and 50mm. Moreover, the temperature distribution throughout the workpiece was monitored which helps to detect the global maximum temperature. Different time instances from the welding cycle (100sec) were selected to show the time dependent change that would occur to the temperature profile during the welding process when using shoulder diameters of 26mm and 50mm. Figure 4.7 illustrates the temperature contours on a vertical plane at the weld centre line whereas dwelling and welding stages are represented. Overall, when tracking the temperature distribution along the pin length, it's clear that the lower temperature zone is at the pin bottom end (tip) and tends to increase towards the shoulder base. Two reasons are likely to be behind this trend; the rate of heat generation at the pin tip is lower than that around the pin side surface as the frictional area is relatively smaller. Secondly, the existence of the highest heat generation zone near to the upper end of the pin where the shoulder-workpiece interface. From the figure, it can also be seen in the temperature scales that the maximum temperature in case of 50mm shoulder diameter is much higher than that for 26mm. This means that the increase in the shoulder size leads to an increase in the temperature which is referred to the increase in the frictional area. In terms of the process time, the temperature distribution at early stage from the welding process indicates that the material has witnessed very high heating rates. At times 1sec, 3sec and 5sec which are part of dwelling time the maximum temperature has been recorded to be 578.6K, 750.9K and 815.3K respectively for a shoulder radius of 25mm. After 40 seconds, at a moment in which the tool has already changed its position; the temperature has increased to 836.1K.

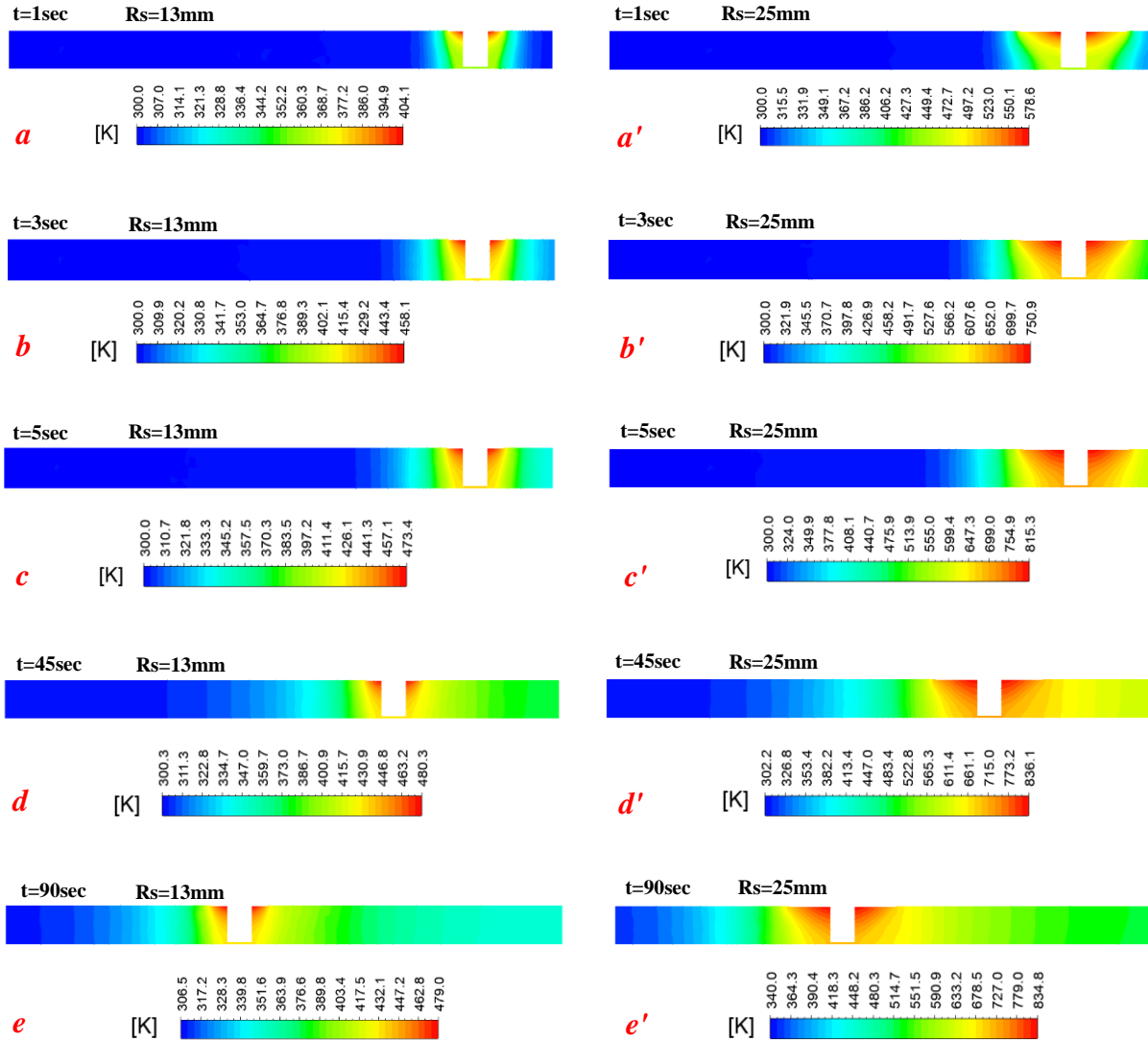


Figure 4.7 Temperature distribution vertical plane at different time steps calculated for shoulder diameters of 26mm and 50mm

To explain the variation in the temperature distribution due to the change in the shoulder size, instantaneous snapshots were taken at the plane where maximum temperature is expected to be recorded. This plane includes the contact region between the shoulder and the workpiece where the global peak temperature is likely to be achieved [87]. As the greatest component of heating is due to the friction between the shoulder and the workpiece, it can be generally seen in figure 4.8 (a,b,c,d) that the hottest area is in the vicinity of the tool. Although, the high temperature contours around the tool are almost symmetrically distributed, the temperature gradient is steeper in front of the tool than behind. That can be attributed to the decrease in material diffusivity due to the heat

accumulation at the rear of tool and for this reason the heat dissipation becomes slower. Conversely, at the leading zone where some parts of the workpiece are still at room temperature, the temperature profile demonstrates that the heat is rapidly dissipated. At the temperature scale in d when the shoulder radius is 25mm, the minimum temperature is 320K which is higher than the room temperature. That means the workpiece is completely affected by the highest supplied heat by this size of shoulder compared to the other sizes. In view of this, it can be also observed in the figure that the growth in the different regions of contours from *a* to *d* is dramatically.

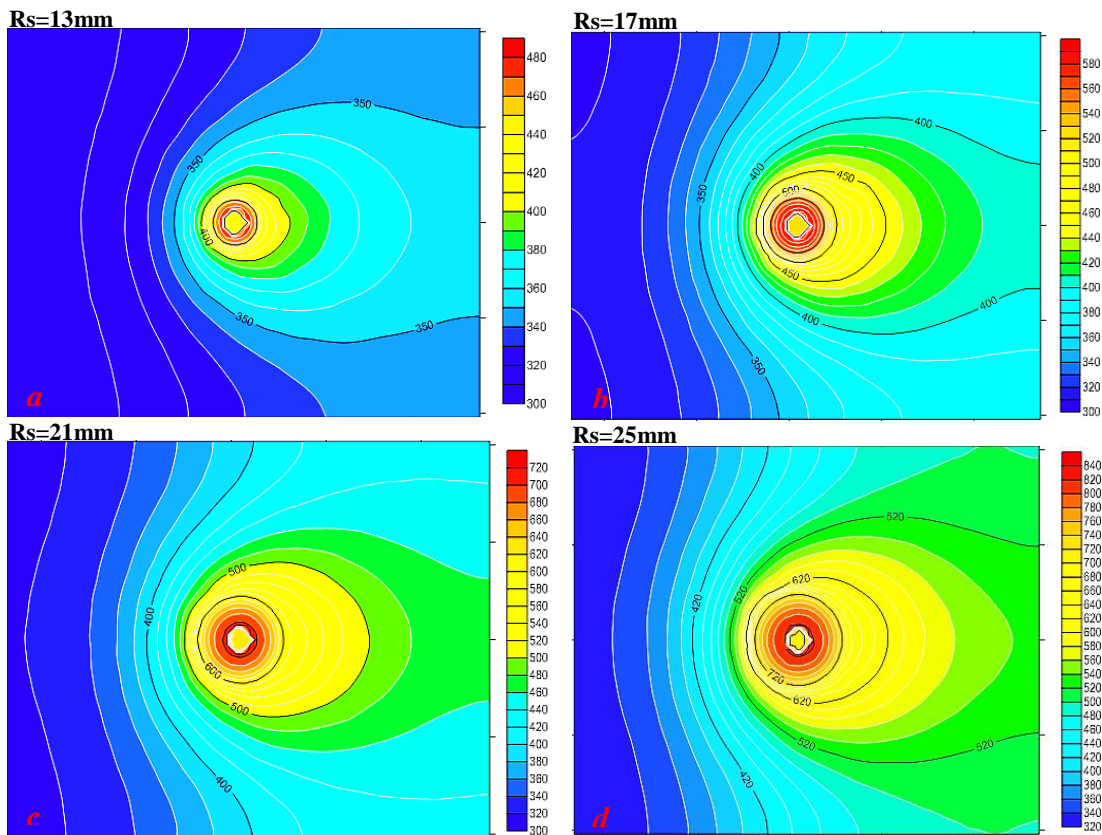


Figure 4.8 Static temperature contours for different shoulder diameters *a*=26mm, *b*=34mm, *c*=42mm, *d*=50mm.

Figure 4.9, depicts the values of the global peak temperatures against the shoulder sizes. It can be seen that the global peak temperature also increases when the shoulder diameter increase. For instance, the global peak temperature has scored 481K, 597K, 720K and 848K for diameters of 26mm, 34mm, 42mm and 50mm, respectively.

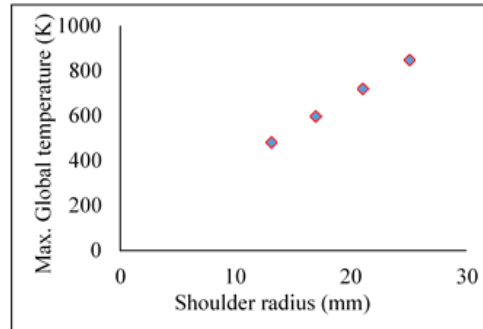


Figure 4.9 Max. Global peak temperature for different shoulder radiuses (13mm, 17mm, 21mm, 25mm)

Figure 4.10 (*a,b*) depicts snapshots for the velocity vectors of the material flow during FSW when using shoulder diameters of 26mm and 50mm where the planes in *a* and *b* have been taken at the same position just underneath the shoulder. Because of the effect of the change in the shoulder size (contact area), it can be clearly seen that the flow field in *b* is wider than that in *a*. Moreover, the maximum flow velocity increased from 0.976m/s to 1.763m/s when the shoulder size changed from 26mm to 50mm. Accordingly, the volume of the stirring zone becomes greater and deformations of the material are severer. In the reality, as the frictional heat generation is enhanced due to the increase in the shoulder diameter, the increase in the localised plastic deformation can contribute to an extent to the heat added to the weld.

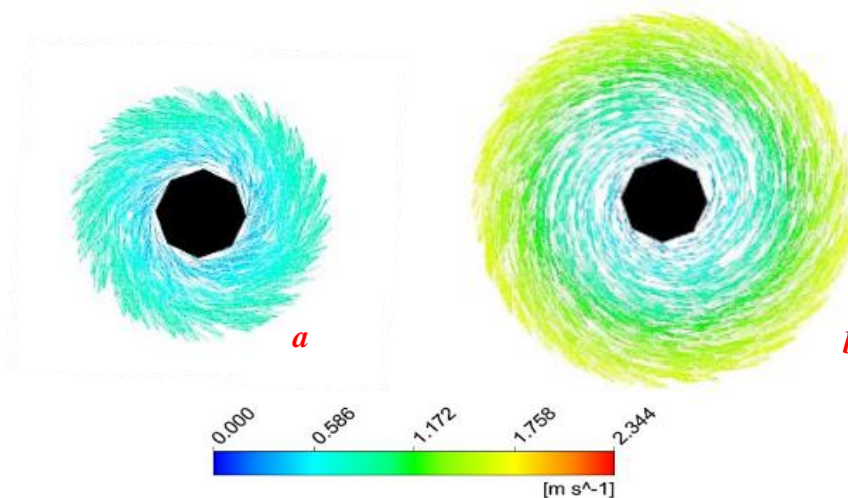


Figure 4.10 Flow velocity field for different shoulder diameters $a=26\text{mm}$, $b=50\text{mm}$

In order to understand the local trend of the maximum temperatures, the welding thermal cycle has been considered. For the numerical experiments conducted with different shoulder diameters, the local peak temperatures have been recorded at four different points (1, 2, 3, and 4) which were specified in chapter 3 and shown in figure 3.53.7. As shown in figure 4.11, it can be seen that the local peak temperature is considerably affected when the shoulder size changes; it increases as the shoulder diameter increases and vice versa. For instance, the local maximum temperatures at point 1 were registered as 809.2K, 690.7K, 571.6K and 461.5K for shoulder radii of 25mm, 21mm, 17mm and 13mm respectively. This is because of the increase in the frictional area (as shoulder diameter increases), which cause an elevation in the amount of heat generation. Besides, when comparing the local peak temperature at points 2 and 3 in figure 4.11, it can be interestingly observed that the value of peak temperature at point 2 is higher than that one at point 3 when the shoulder radii were 25 mm and 21mm while it scored lower values when the shoulder radii were 17mm and 13mm. This trend could be reasoned by locations of the points 2 and 3 relative to the shoulder and pin. In other words, when the shoulder radius is 25mm point 2 will be at just the shoulder underneath where the hottest areas are expected as the shoulder dominates the heat generation. However, when the shoulder radius is 13mm point 2 becomes a bit away from the shoulder which make it in a much cooler region than the region in which point 3 is located.

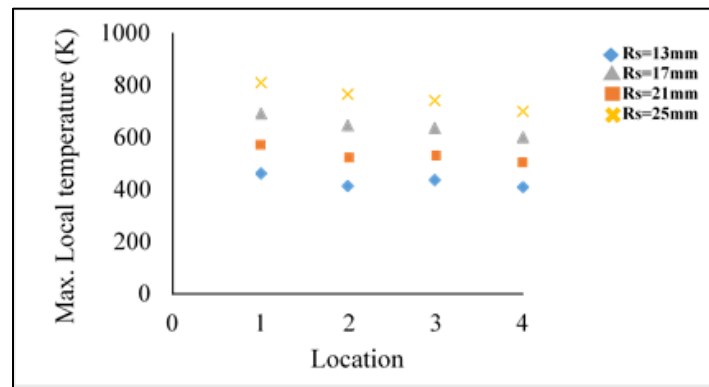


Figure 4.11 Max. Local temperature for different shoulder radiuses at different locations

As the FSW tool rotates and travels through the material of the workpiece, it may be exposed to wearing, deforming and failure. The reason for this is that the tool might experience severe stresses and a reduction in the yield strength of its material at elevated temperature. Therefore, the tool functionality might be affected as the change in the tool shape enhancing of defect generation in

the welded joint [15, 88]. As the stress values are affected by the change in the temperature which is an important factor contributing to the stress distribution [37, 89, 90], figure 4.12 presents the time dependent variation in the maximum shear stress at the tool surface for the proposed shoulder sizes. As the shear stress is directly proportional to the viscosity, it is seen that the values of the maximum wall shear stress are decreasing when the shoulder diameter is increasing. This because of the increase in the frictional area which in role boosting the frictional heating where the viscosity is affected by the increase in the temperature. From another angle of view, the values of maximum shear stress were noticeably higher at the earlier stage of the process than those in latter stages in which the values tend to stabilise according to the material temperature.

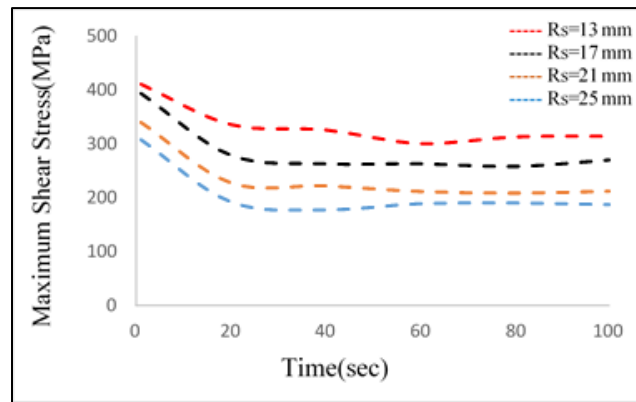


Figure 4.12 Time – dependent variation of the global maximum shear stress for different shoulder diameters

4.3.1.2 Effects of Pin Diameter on the Thermal Field of FSW

Figure 4.21, depicts a comparison between the time dependent temperature distribution when $R_p=3\text{mm}$ and $R_p=6\text{mm}$. It can be noticed for $R_p=3\text{mm}$ that the highest and minimum temperatures that were attained are higher than those recorded for $R_p=6\text{mm}$. Similarly, the heating rate was higher where it has achieved 297.4K/sec at $t=1\text{sec}$ for $R_p=3\text{mm}$ while it was 278.6K/sec for $R_p=6\text{mm}$ at the same time. This would be attributed to the area of shoulder as it becomes smaller when the pin radius grows up where the reduction in the shoulder's area was by 0.01cm^2 .

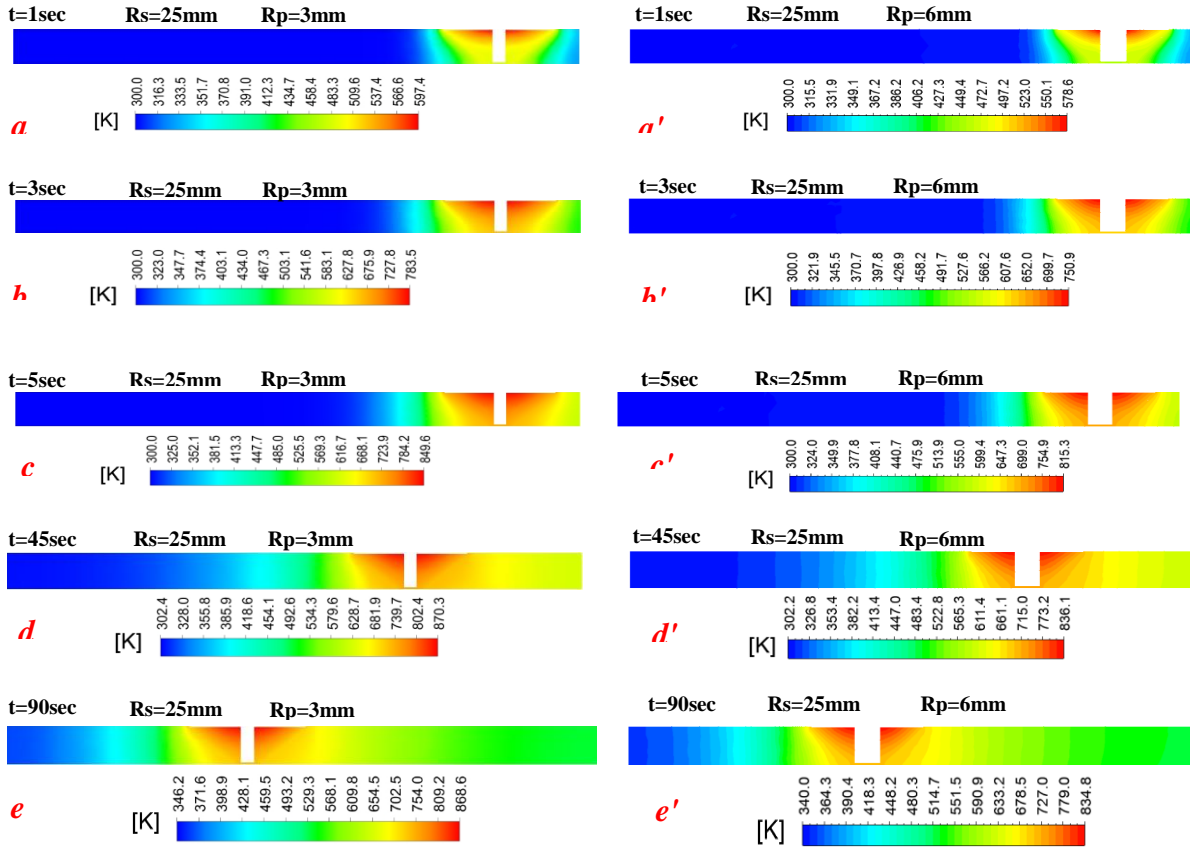


Figure 4.13 Temperature distribution for the weld centre lined vertical plane at different time steps calculated for pin diameters 6mm and 12mm

Figure 4.14(a,b,c,d) depicts the qualitative variation in the temperature distribution for different pin dimensions. Although the increase in the pin size leads to dropping the temperature, it can be observed that the change in the temperature profile is not as significant as when the shoulder size was altered. When the pin radius is 3mm, it is noticeably seen that the material solidus temperature (855K) is exceeded which means that the material parts that have witnessed this temperature become liquid.

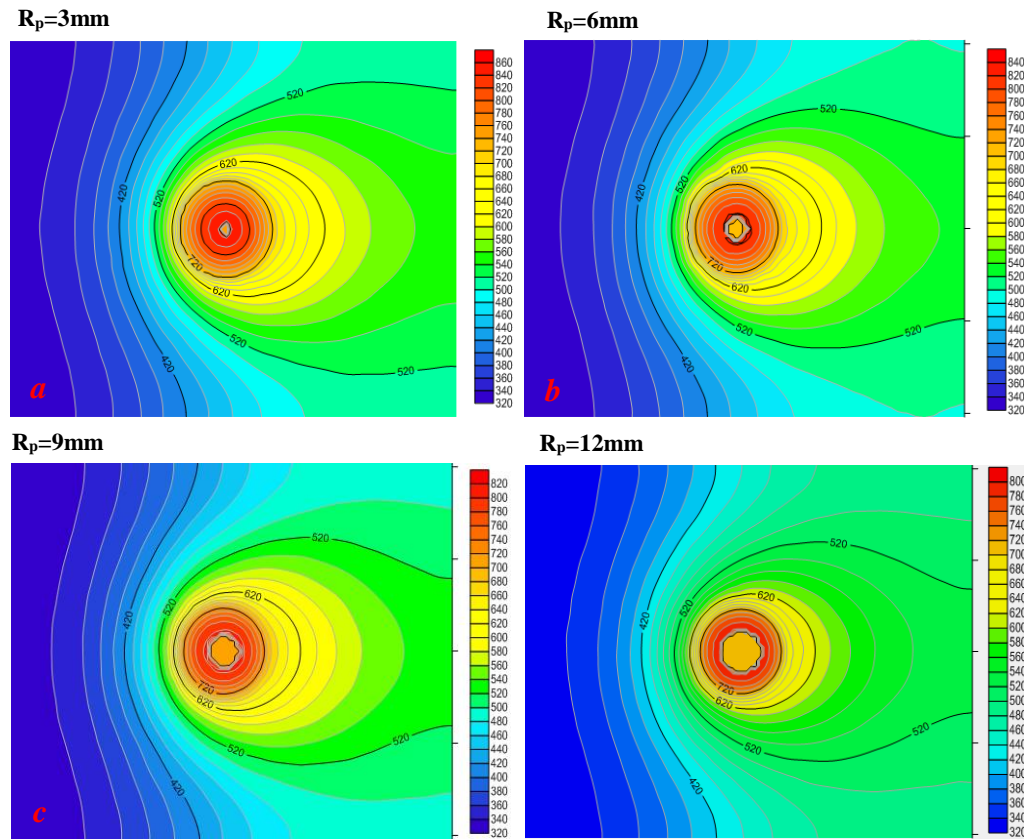


Figure 4.14 Static temperature contours for different pin diameters $a=6\text{mm}$, $b=12\text{mm}$, $c=18\text{mm}$, $d=24\text{mm}$.

As the transient temperature distribution can be monitored over the welding process, the current model has the advantage of estimating the liquid fraction during the process if the temperature is higher than the material solidus temperature. As presented in chapter 3, the amount of liquid with respect to the same cell volume in the calculation domain is named as the liquid fraction (β). Here, it is worth mentioning another significant feature in this model which is the mushy zone. In the mushy zone, the value of the β is distinguished between 0 and 1. In fact, β at certain position and time is equal to zero if the material temperature was lower than the solidus temperature of the material used [68, 78]. For $R_p = 3\text{mm}$ and 6mm , Figure 4.15, shows the liquid fraction contours within the materials being welded together at the same time step in which the temperature distributions were previously presented in figure 4.14(a,b). Although the temperature around the tool has insignificantly exceeded the solidus temperature when $R_p = 3\text{mm}$, the model was able to predict the mushy zone. It can be clearly seen in the magnified section of mushy zone in which the

value of liquid fraction is gradually changing from the minimum of 0% to maximum of 3.3%. These values indicate that a very small amount from the welded material has converted to liquid. On the other hand, the model never predicted any mushy zone when $R_p = 6\text{mm}$ which means that the temperature of the whole workpiece is still under the solidus temperature.

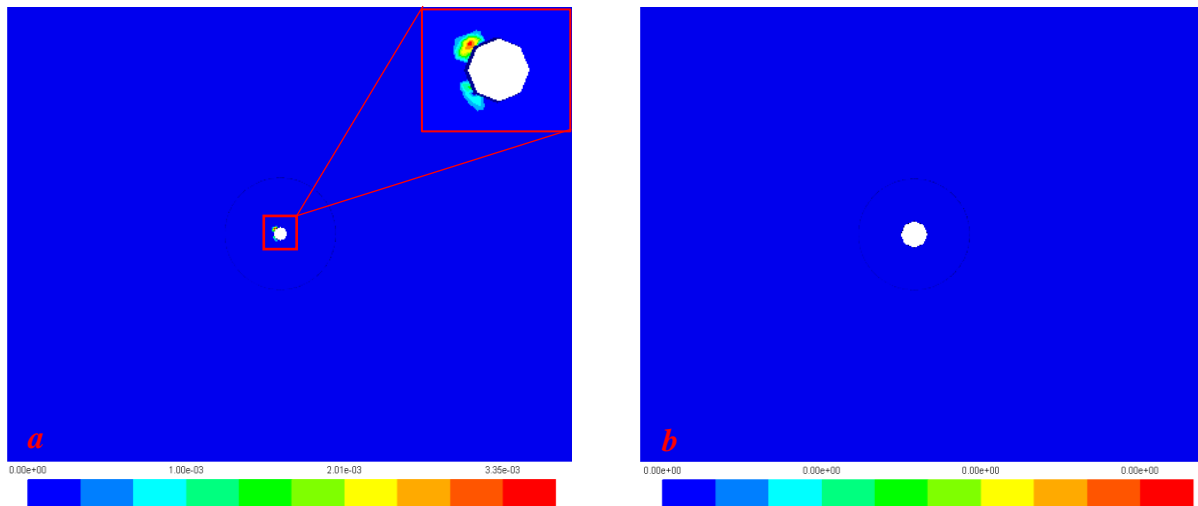


Figure 4.15 Liquid fraction contours for different pin diameters (a) 3mm, (b) 6mm

Figures 4.24 and 4.17 depict that both global and local peak temperatures decrease along with the increase in the pin radius (R_p). For instance, the values of peak temperature as shown in figure 4.284.17 at point 1 recorded 830K, 809.2K and 804.6K when R_p values are 3mm, 6mm and 9mm respectively. As previously stated, all the above differences in the thermal values can be justified by the reduction in the frictional area for the shoulder as the pin diameter increases. However, when R_p is equal to 12mm it is seen that the local and global temperatures have increased to exceed the temperature recorded when R_p is 9mm. This trend can be understood in terms of heat generation in the welding process of thin plates; the shoulder surface is dominant in generating of heat by friction while in thicker plates, the pin role becomes more efficient [6]. Additionally, the increase in the pin size leads to a change in the behaviour of the flow field around the tool which can be recognised in figure 4.18. In the figure, *a* and *b* present the velocity vectors of the material flow at a plane at just underneath the shoulder when $R_p = 3\text{mm}$ and $R_p = 12\text{mm}$ while *c* and *d* show the velocity vectors at a plane at just underneath the pin for the same pin sizes, respectively. Although, the shoulder size was kept the same for both cases, it can be noticed that the vectors represent the minimum velocity (dark blue) in *a* have disappeared in *b* where the minimum velocity recorded

an increase by 0.2m/s. From *c* and *d*, the flow field has witnessed an increase in the volume and both minimum and maximum velocities increased by 0.012m/s and 0.6m/s, respectively. These changes in the stir action redistribute the strain rate and enlarge the deformation region which in role support for extent the heat generated that is mainly acquired from the frictional action. However, as the viscosity increases according to the decrease in the temperature its worth mentioning that the main reason behind the increase in the velocity may be the increase in the linear velocity as the pin radius increases. comparing the trend of global peak temperatures as presented in the figures 4.9 and 4.24, as well as the local peak temperatures as presented in figures 4.11 and 4.28, one can conclude that the change in R_s has greater effect than that of R_p where the maximum temperature is highly affected by the change in R_s rather than R_p .

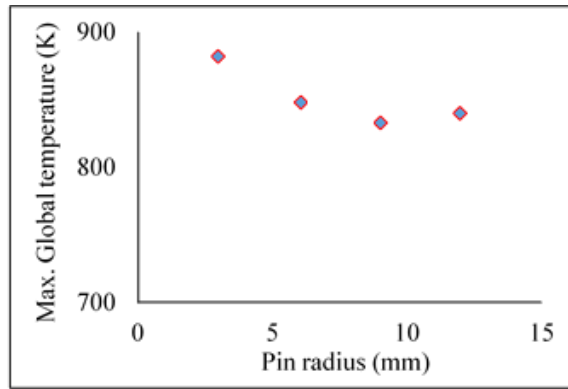


Figure 4.16 Max. Global temperature for different shoulder radiuses

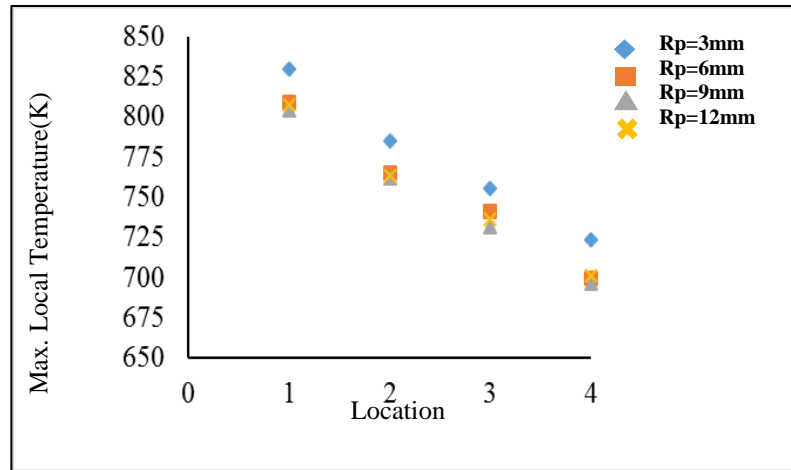


Figure 4.17 Max. Local temperature for different pin radiuses at different locations

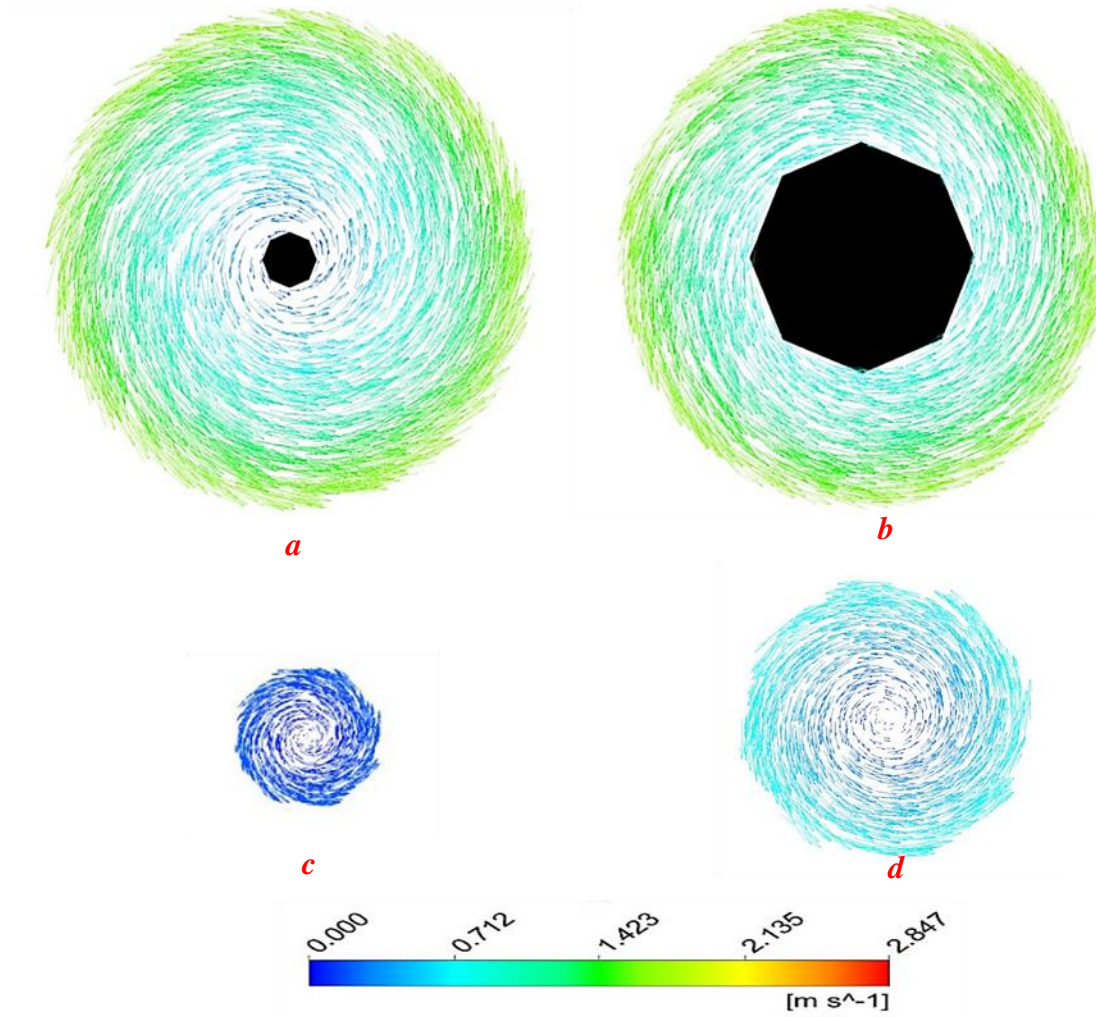


Figure 4.18 Flow velocity field for different pin diameters at underneath the shoulder and the pin

Figure 4.294.19(a,b), depicts a comparison between the trend of time dependent shear stress for varied pin size compared with that for varied shoulder size. In general, the behaviour in both cases is mostly the same where the shear stress values stabilise after experiencing high values at the earlier stages of the process. Nevertheless, in terms of the size range the highest values of shear stress at various pin diameters have not reached those recorded for various shoulder diameters. For instance, it has exceeded 400MPa for $R_s=13\text{mm}$ while 327 MPa was scored for $R_p=12\text{mm}$. In addition, the variation in the shear stress within the range of pin size is not as much as the variation in the shear stress within the range of shoulder size. The reason is that the time dependent

temperature distribution is highly affected by the shoulder diameter than the pin diameter. For example, at the beginning of the thermal cycle the stress ranged from 280MPa, 308MPa, 328MPa and 327MPa for $R_p=3\text{mm}$, 6mm, 9mm and 12mm respectively, while it ranged from 308 MPa, 340 MPa, 394 MPa and 411 MPa for $R_s=25\text{mm}$, 21mm, 17mm and 13mm, respectively.

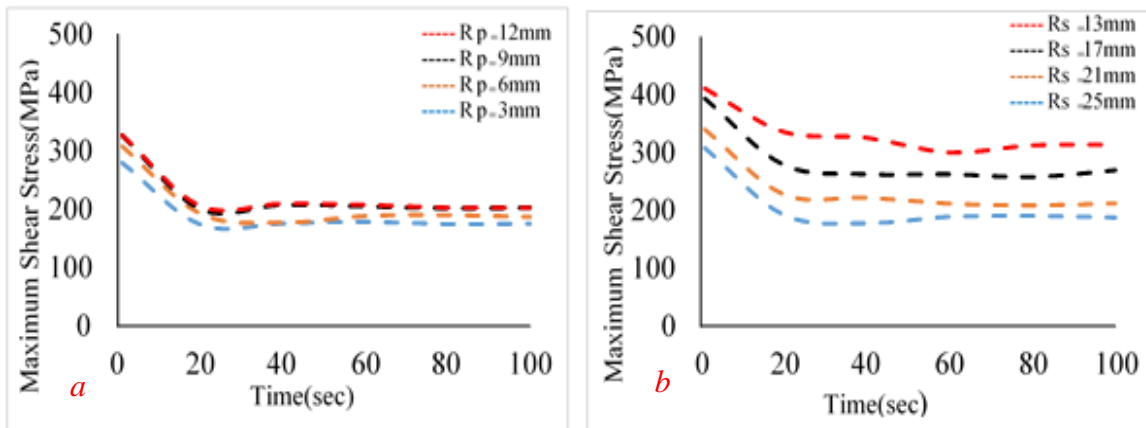


Figure 4.19 A comparison between the shear stress values when using a) different pin sizes and b) different shoulder sizes

4.3.1.3 Effects of Pin Height on the Thermal Field of FSW

Figure 4.30 depicts the evolution in the temperature distribution across the process duration related to the variant pin height and to do so, the welding processes with 9mm and 12mm pin heights were selected. From the figure, it can be seen that the transient evolution in the temperature distribution is not highly impacted when the pin height changes from 9mm to 12mm. This can be recognised when comparing the temperature scale for both cases as the temperature increase does not exceed 10K.

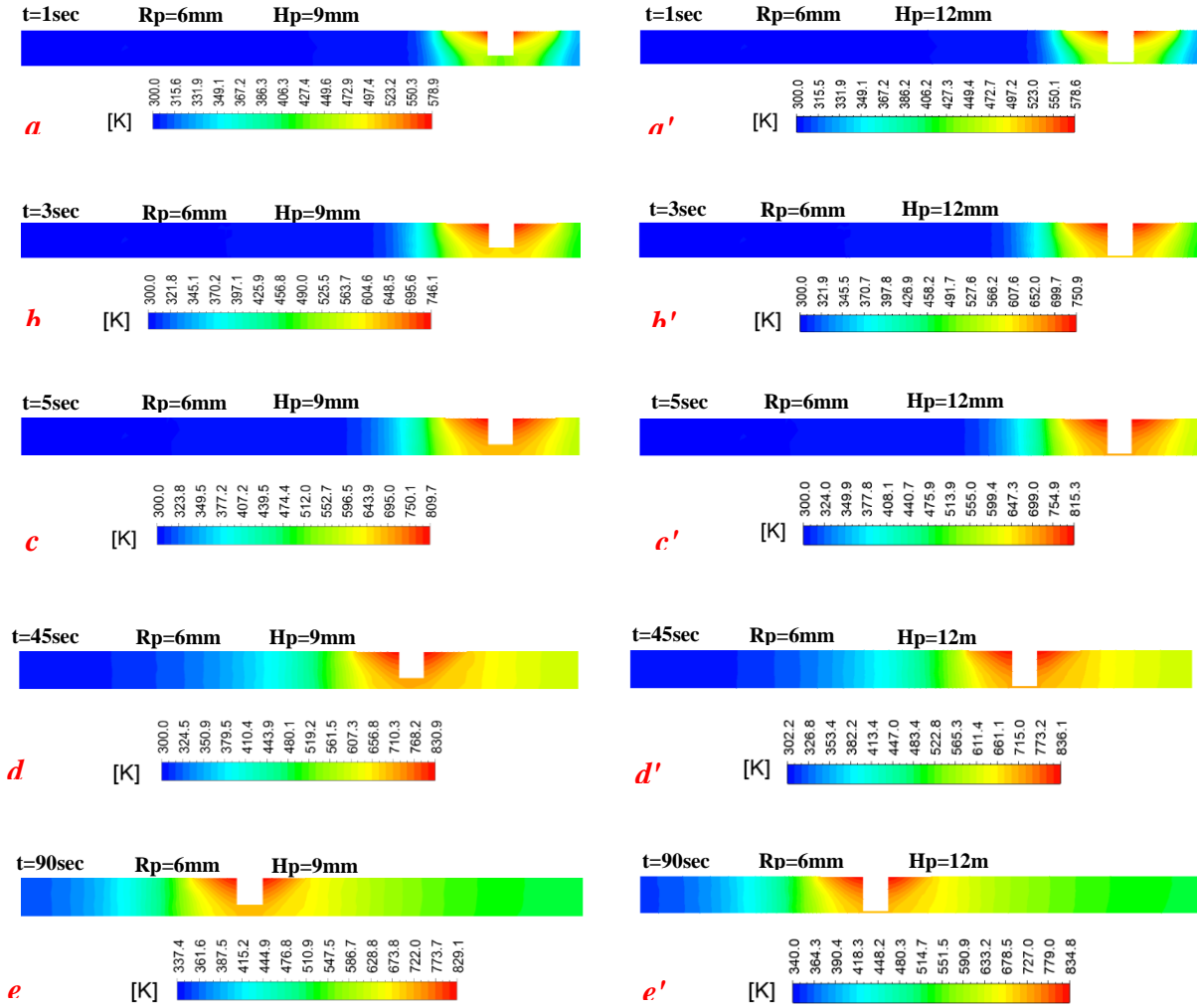


Figure 4.20 Temperature distribution for the vertical plane at different time steps calculated for pin heights 9mm and 12mm

Figure 4.21(a,b,c,d) displays the variation in the temperature distribution due to the change in the pin height. The contours for different cases were taken at the same plane in the study of the shoulder and pin dimension effects. In general, the temperature is normally distributed around the tool and insignificant variation can be observed on the contours according to the change in the pin height. That can be clearly seen when comparing position and form of the lines of 420K, 520K, 620K and 720K in a, b, c and d.

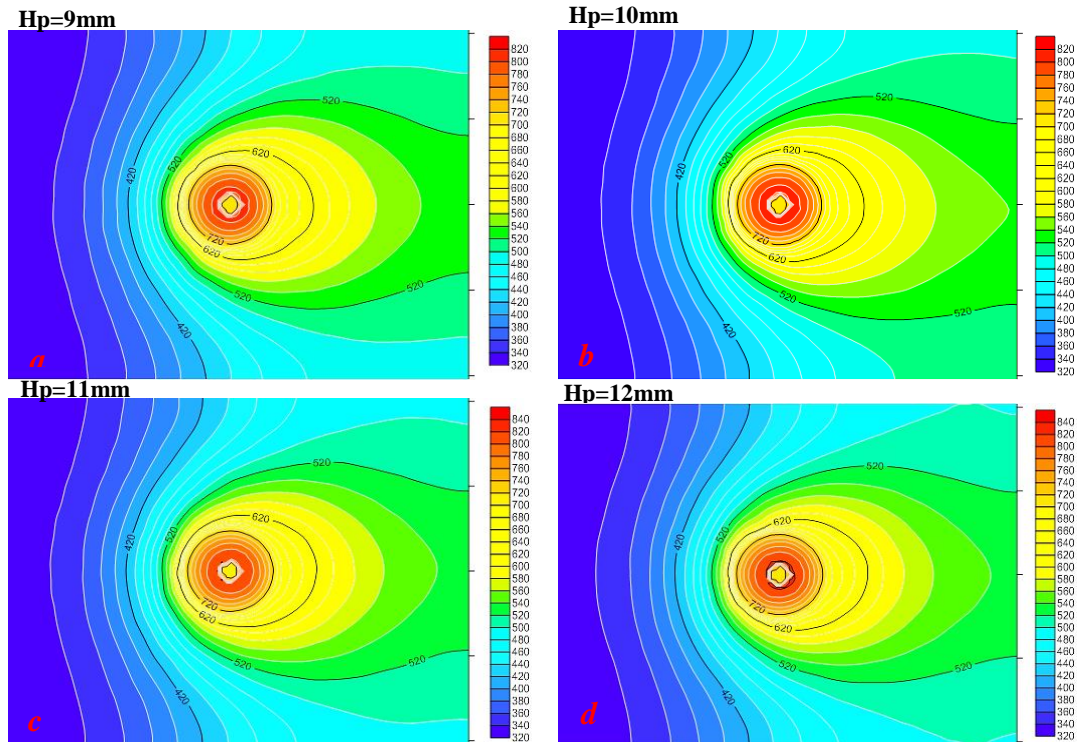


Figure 4.21 Static temperature contours for different pin heights $a=9\text{mm}$, $b=10\text{mm}$, $c=11\text{mm}$, $d=12\text{mm}$

The values of global peak temperature that were registered for different pin heights are depicted in figure 4.22. The results illustrate that the global peak temperature increases when the pin height becomes more which can be mainly ascribed to the increase in the frictional heat as the contact area between the pin side and the workpiece increases. To clarify, the maximum and the minimum global temperatures are 848K and 841K for $H_p = 12\text{mm}$ and $H_p = 9\text{mm}$ respectively. Likewise, the local peak temperature has similar trend as exhibited in figure 4.23. For example, 809K was the highest temperature recorded at the location No.1 when $H_p = 12\text{mm}$ while the lowest peak temperature was 796K for $H_p = 9\text{mm}$ at the same location. However, the impact of the increase in the pin height on the increasing of the temperature is less compared to the other geometrical parameters.

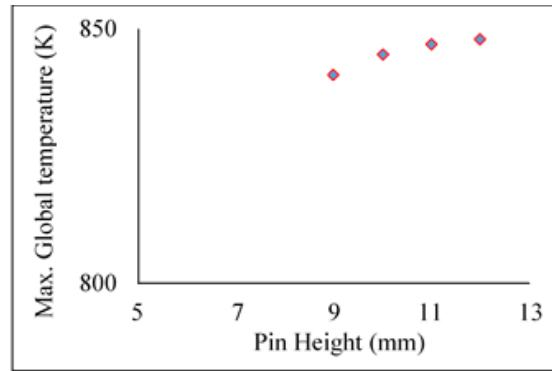


Figure 4.22 Max. Global temperature for different Pin Height

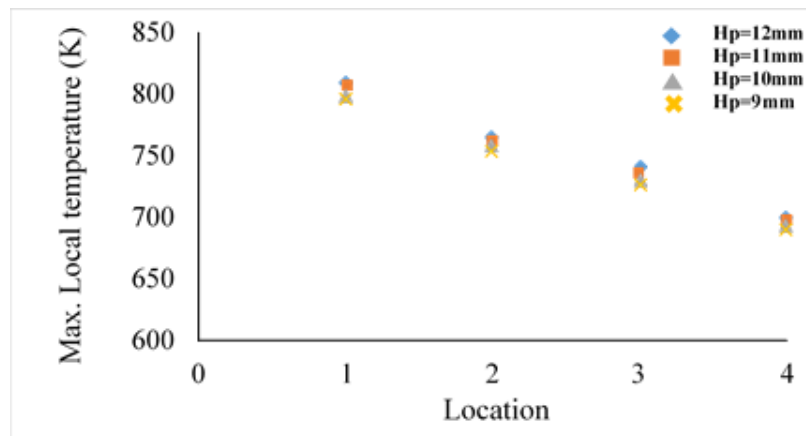


Figure 4.23 Local temperature for different Pin Height at different locations

In figure 4.24 (a,b,c,d) the velocity vectors display that no significant changes can be generally observed on the material flow field neither under the shoulder nor the pin. In other words, within the selected range in the change of pin height the flow velocity has mostly registered the same value with the increase in the pin height excepting that recorded under the pin (c,d) with very small drop. 0.017m/s was the flow minimum velocity under the pin when $H_p = 9\text{mm}$ while 0.0075m/s recorded when $H_p = 12\text{mm}$. This would be attributed to the effect of the bottom surface of the workpiece where the flow in this region may be exposed to higher restriction. Although, the stirred zone has slightly increased according to the increase in the pin height it seems that the drop in the velocity value leads to a decrease in the local plastic deformation which in reality affect its role in the heat generation.

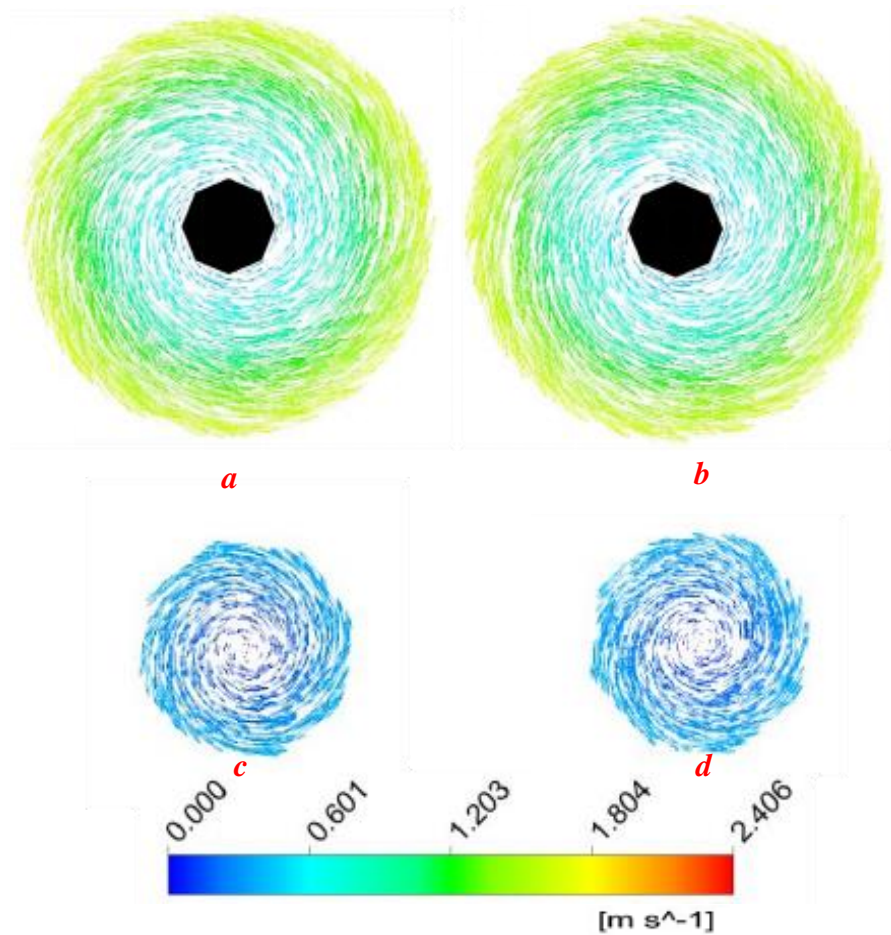


Figure 4.24 Flow velocity field for different pin heights at underneath the shoulder and the pin

In the comparison of the maximum shear stress for different geometrical parameters, it can be implied from figure 4.25 (*a,b,c*) that for the considered range of variation in the pin height the maximum shear stress has not significantly changed which can be clearly seen in figure . That can be related to the unimportant changing in the temperature as the previous thermal analysis revealed which in its role leads to that the material viscosity and softening will not be greatly influenced.

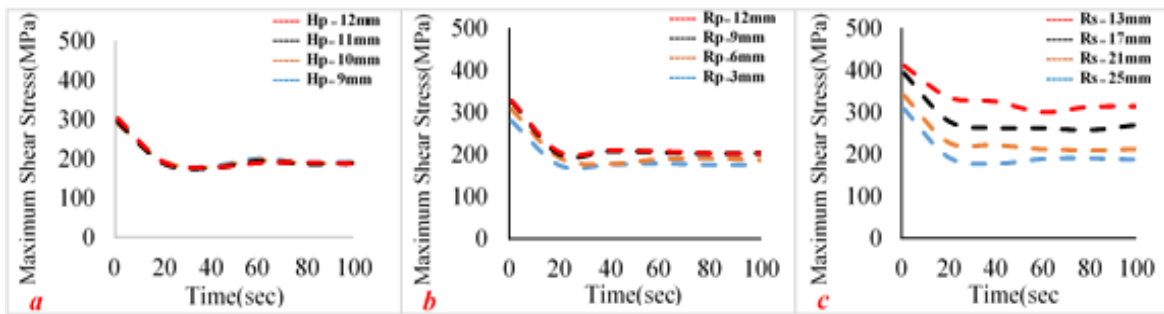


Figure 4.25 A comparison between the time dependent maximum shear stress for different geometrical parameters: (a) variant pin height (b) variant pin diameter (c) variant shoulder diameter

4.3.1.4 Effects of the Workpiece Thickness on the Thermal Field of FSW

Figure 4.36 depicts how the change in the material thickness affects the temperature distribution in the vicinity of the welding tool as different time steps along the welding cycle were chosen when welding plates with thickness of 18.7mm and 12.7mm. The presented contours indicated that the hottest zone around the tool shrinks as the thickness increases and for the two cases under consideration, the difference in the maximum temperature was 28K in the first second of welding time while it has reached around 58K at $t=45$ sec and after. That can be explained on account of the fact that before achieving the quasi-stationary thermal state, the heat conduction develops according to the temperature difference for each lonely case.

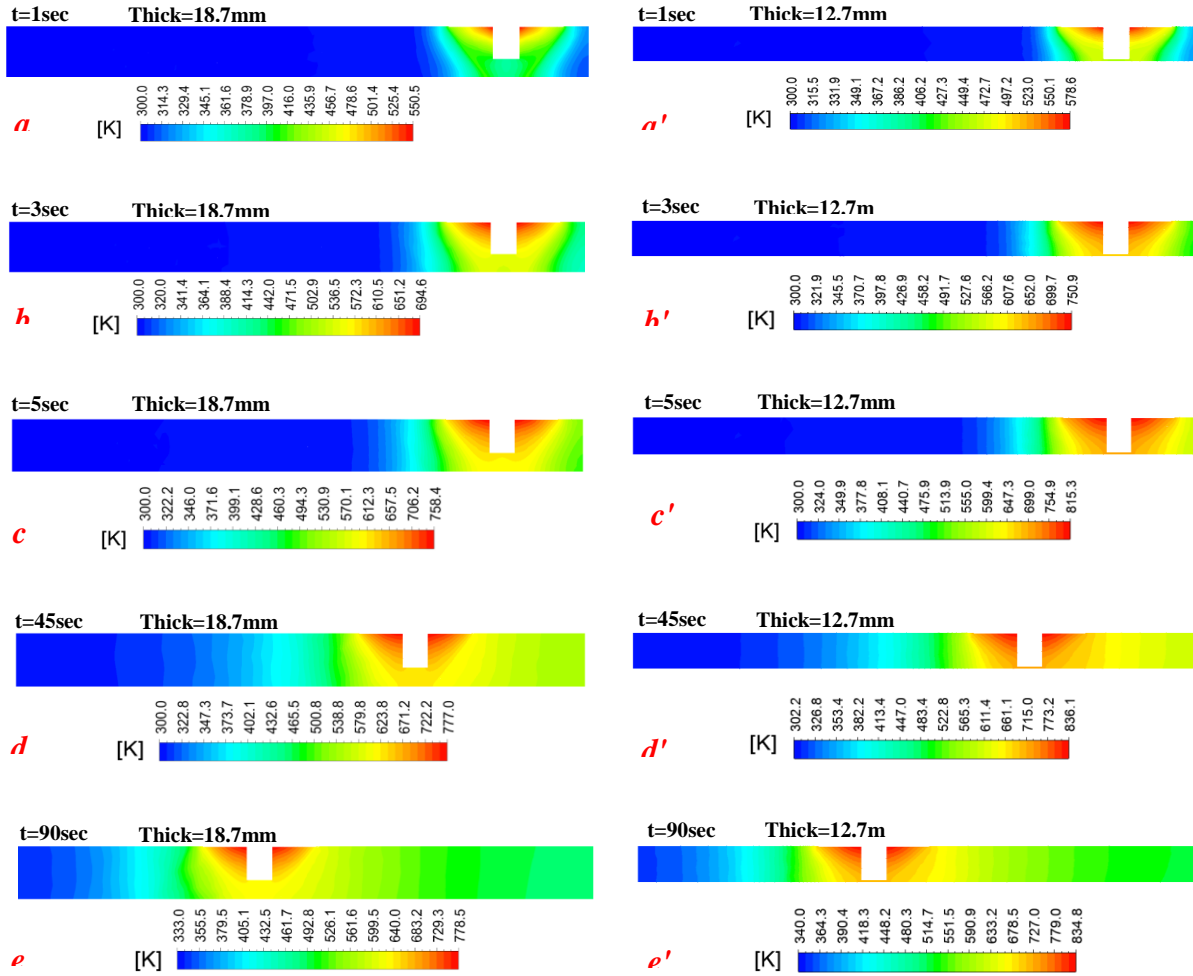


Figure 4.26 Temperature distribution for the vertical plane at different time steps calculated for workpiece thickness 18.7mm and 12.7mm

Figure 4.27(a,b,c,d), depicts the variation in the spatial temperature distribution within the weldment at the same moment for different workpiece thickness. Noticeably, the increase in the plate thickness causes a progressive decrease in the temperature values. Although, the heat input due to the frictional activities are almost the same the temperature gradients are clear as can be seen at the leading, trailing, advancing, and retreating sides. Compared to a, the line of 520K in d has a position closer to the pin and the maximum temperature in the scale is gradually dropping. This happens due to the enhancement of heat dissipation in the thickness direction.

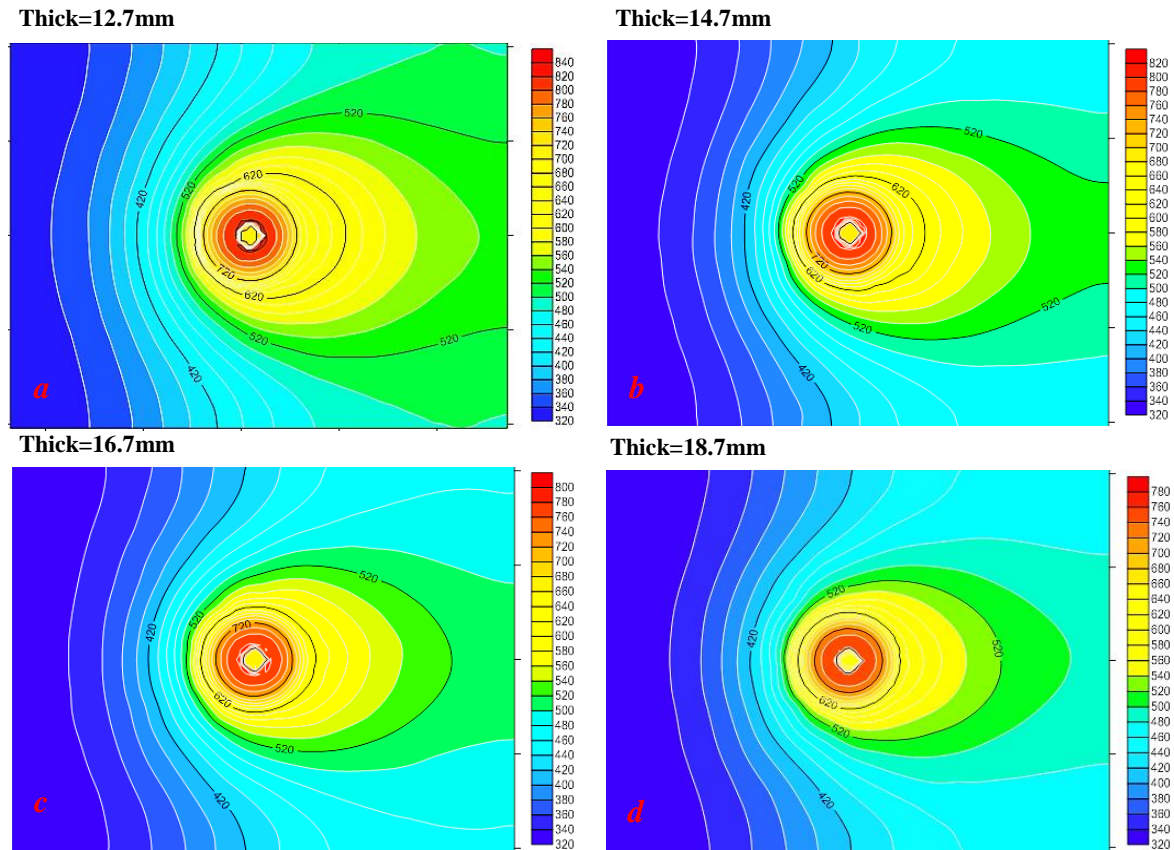


Figure 4.27 Static temperature contours for different workpiece thickness a=12.7mm, b=14.7mm, c=16.7mm, d=18.7mm.

As it can be seen in figures 4.284.28 and 4.294.38, for the same plane and points that were previously defined, the maximum global and local temperatures were calculated along with the variation in the specimen thickness. Thermally, FSW is a heat transfer problem with a moving heat source which is just like the conventional welding processes. The geometry of the weld could affect the thermal features such as heating rate and cooling rate for a given welding parameters (heat input). The increase in the plate thickness leads to an increase in the rate of heat dissipation from the weld zone to the base metal which would give a reason for the decrease in the local and global peak temperature [3]. From another point of view, volume of the stirring zone dose not theoretically change as the tool dimensions still the same which means the contribution of the material deformation in the heat generation is insignificant according to the increase in the plate

thickness. However, as shown in figure 4.30 the maximum flow velocity has witnessed a decrease by 0.1m/s and 0.6m/s at underneath the shoulder and the pin, respectively. This would be reasoned by the decrease in the material softness as the temperature decreases with the increase in the workpiece thickness.

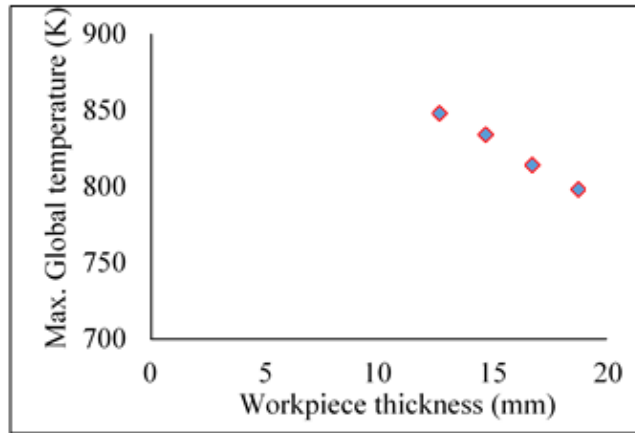


Figure 4.28 Max. Global temperature for different workpiece thickness

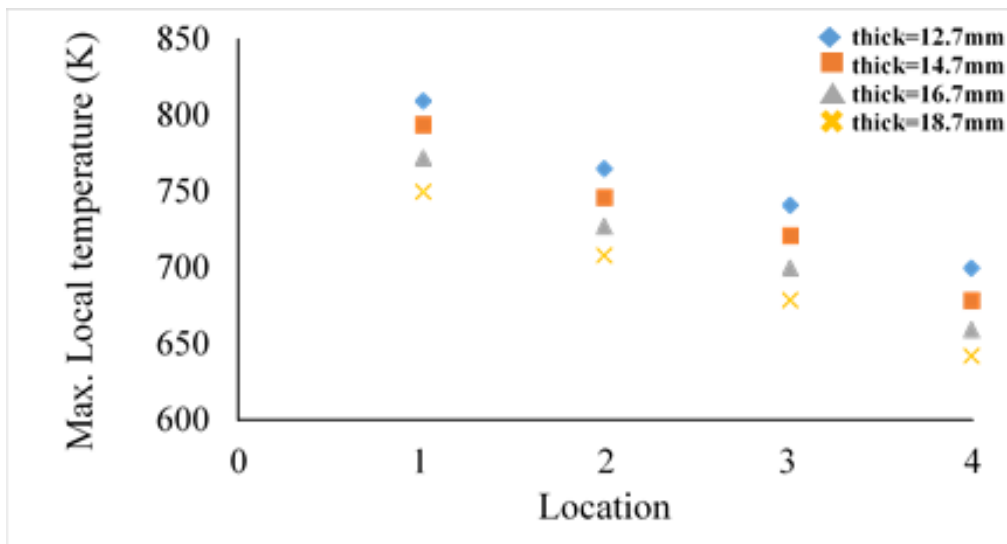


Figure 4.29 Local peak temperature for different workpiece thickness at different locations

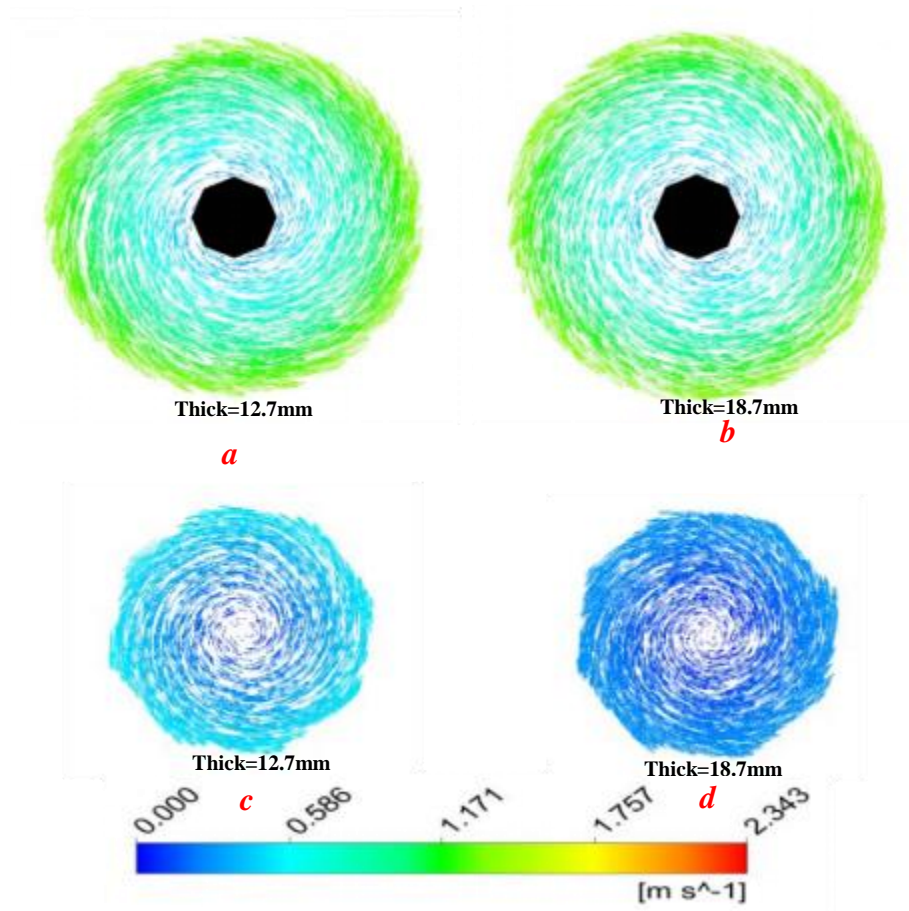


Figure 4.30 Flow velocity field for different workpiece thickness at underneath the shoulder and the pin

Figure 4.31(a,b,c,d), shows the estimated variation in the maximum shear stress experienced by the tool with different material thicknesses in comparison with its trend when the other geometrical parameters are changed. For variant thickness the maximum shear has generally shown a trend resembling those recorded when the tool dimensions are varied. Noticeably, the highest stress value was scored for the plate thickness of 18.7mm whereas the lowest peak temperature was registered among the other thicknesses. The reason is that the material viscosity and stiffness are less thermally influenced which leads to enhance the forces components around the tool. Apart from the impact of the change in the forces acting on the tool due to the change in the tool geometry, the presented results revealed that the shear stress is relatively affected according to the

thermal changes. Additionally, the change in shoulder diameter has the greatest effect on the maximum shear stress.

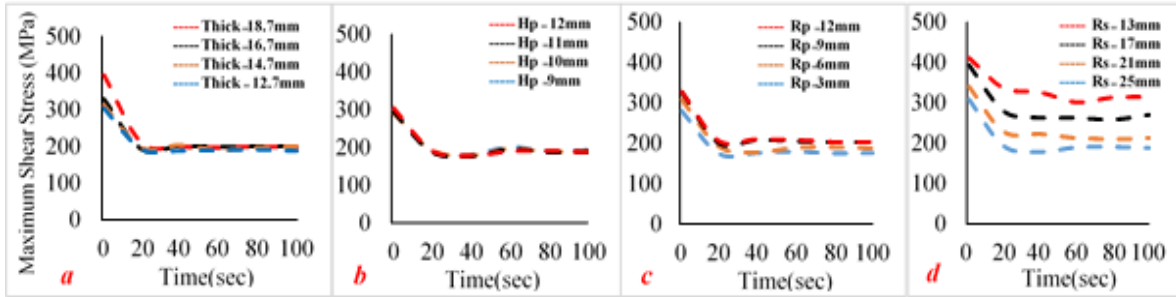


Figure 4.31 A comparison between the time dependent maximum shear stress for variant workpiece thickness against tool geometrical parameters: (a) variant workpiece thickness (b) variant pin height (c) variant pin diameter (d) variant shoulder diameter

4.3.2 Effects of Rotational Speed on the Thermal Field of FSW

Figure 4.32 depicts how the temperature distribution changes according to the variation in the welding rotational speed. That can be obvious in *a* and *b* when tracking the line of 400K while the line of 520K in *c* and *d* gives a clear indication as well. It can be seen from the figure that the hot areas grow up as the rotational speed increases. From another point of view, it seems that the material has witnessed a severe thermal cycle particularly when using the rotational speed of 837r.p.m as shown in figure 4.33 (*a',b',c',d',e'*) whereas the severity manifests in the intensive rise of the workpiece temperature. Accordingly, the temperature in some parts of the workpiece has exceeded the material solidus temperature. For this reason, it was possible to monitor the development in the time dependent liquid fraction over the thermal cycle. Thus, Figure 4.33(*a,b,c,d,e*) presents several contours that exhibit how the liquid fraction in the material being welded would be affected due to the change in the material temperature.

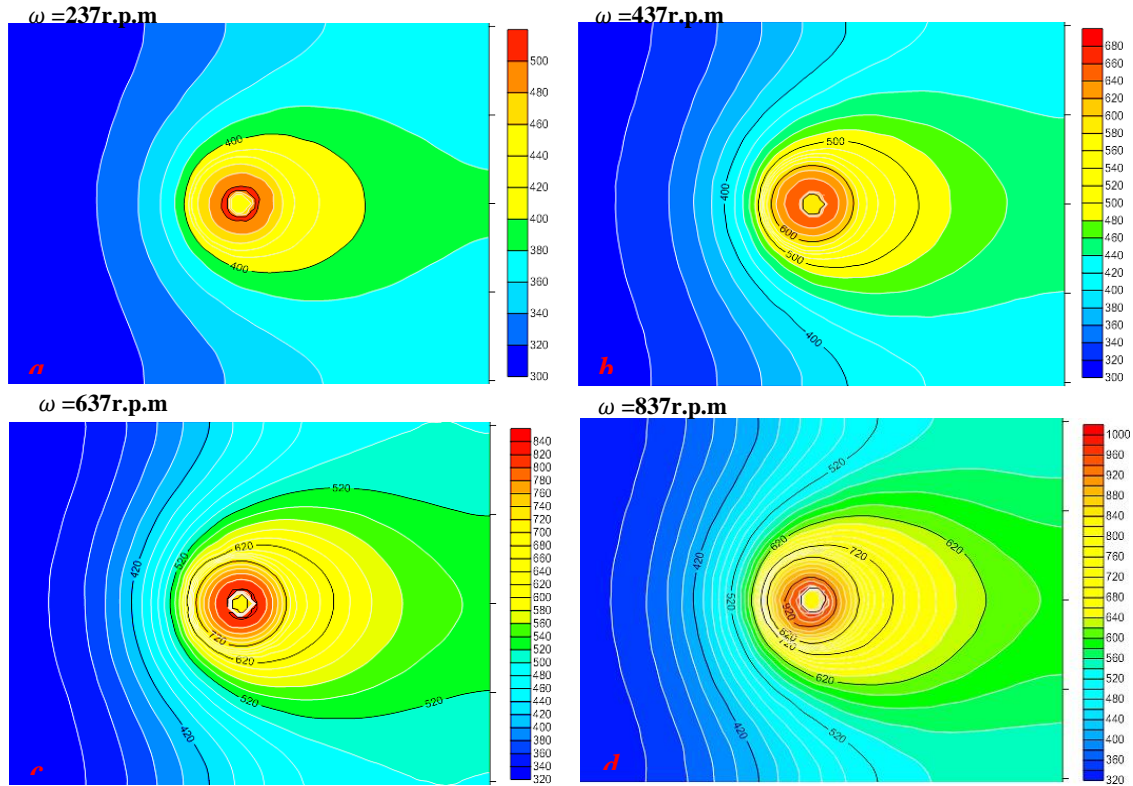


Figure 4.32 static temperature contours for different rotational speed a=237r.p.m, b=437r.p.m, c=637r.p.m, d=837r.p.m.

Because of the elevated heating rate, it can be seen from the figure that the material melting point was reached in the earlier stage of the thermal cycle as the peak temperature that was registered at the moment of 3sec is around 852K. However, until three seconds no liquid has formed as presented in *a* and *b*. After 5sec, the maximum temperature was 929K which means that the melting temperature was already scored in some parts from the workpiece and accordingly the material converts to liquid state in those parts. In *c, d* and *e*, no magnification was needed as it can be seen that the tool is completely surrounded by the mushy zone in which the value of liquid fraction is ranging from the minimum of 0% at the outer face of the mushy zone to the maximum of 100% at the immediate vicinity of the tool. Additionally, the part of the mushy zone that has a high level of liquid fraction has noticeably expanded with the increase in the temperature. After a while, no more expanding will be there as it can be seen when comparing the scale of liquid fraction in *d* and *e*. The values of liquid fraction indicate that a relatively high amount of the welded material has converted to liquid which might cause defects in the welded joint.

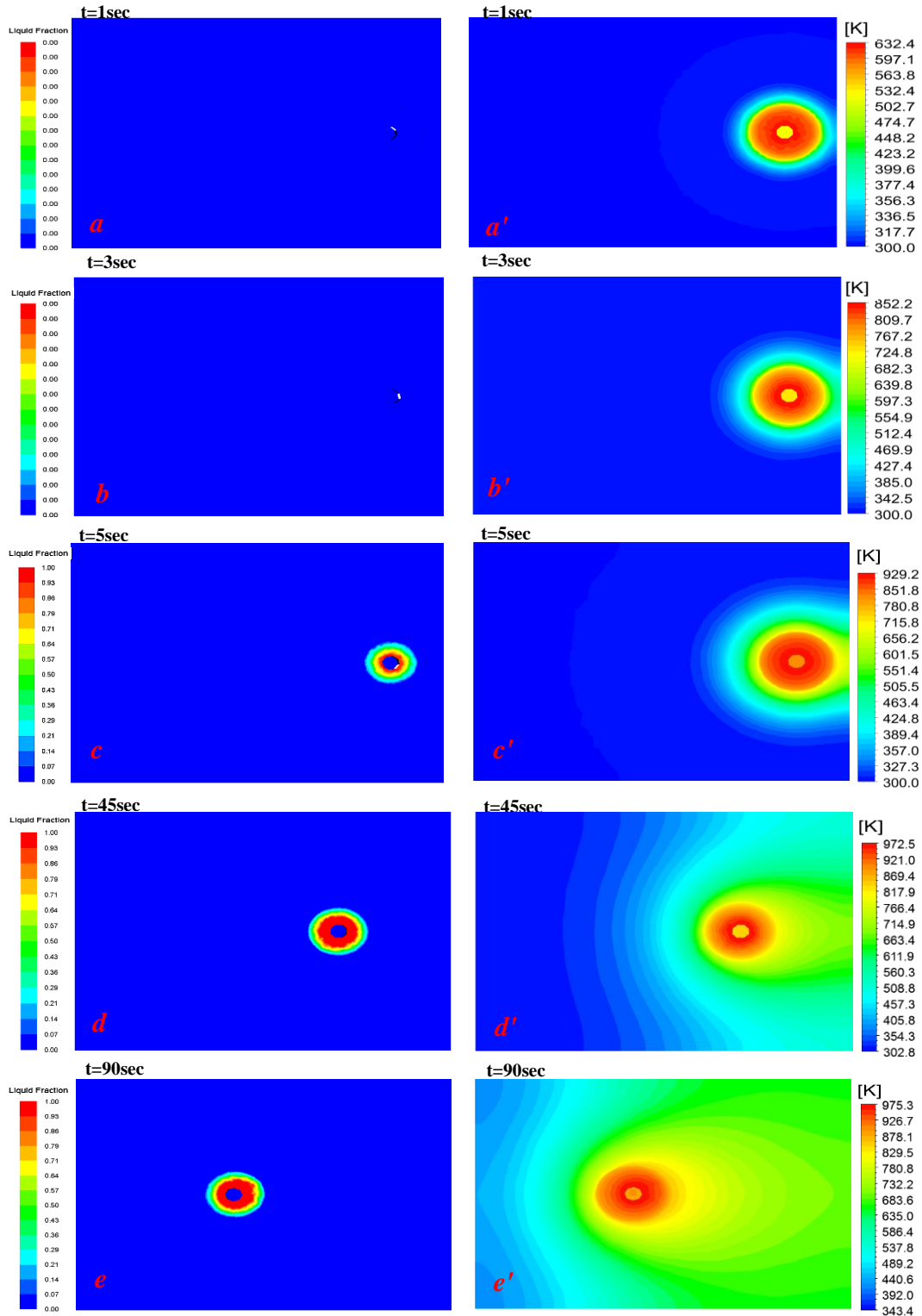


Figure 4.33 Liquid fraction contours corresponding to the temperature rising at different times for $\omega = 837\text{r.p.m}$

Figure 4.34, illustrates that the maximum global temperature is highly sensitive to the rotational speed which recorded 509K at speed of 237rpm while it was 975K for 837rpm. Locally, for different rotational speeds 237,437,637,837r.p.m, it is obvious in figure 4.35 that the increase of rotational speeds of the tool will significantly increase the local peak temperature because the heat input increases. When considering the local peak temperatures for the same rotational speed at the four measuring points (1,2,3,4), it can be remarkably seen that the gradient in the peak temperature is not that much steeper. Although, the distances between four points are kept the same, this trend can be associated to that the shoulder has a large enough size to produce a relatively wide hot zone as well as the high material conductivity which contributes to thermal homogeneity.

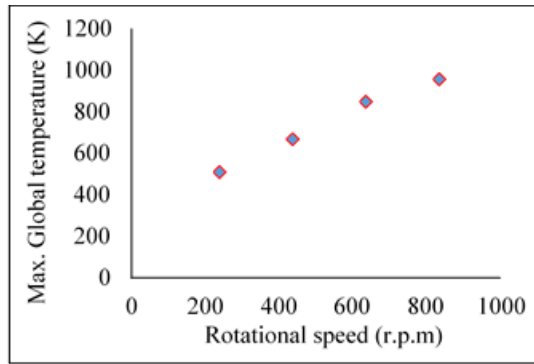


Figure 4.34 Max. Global temperature for different rotational speeds

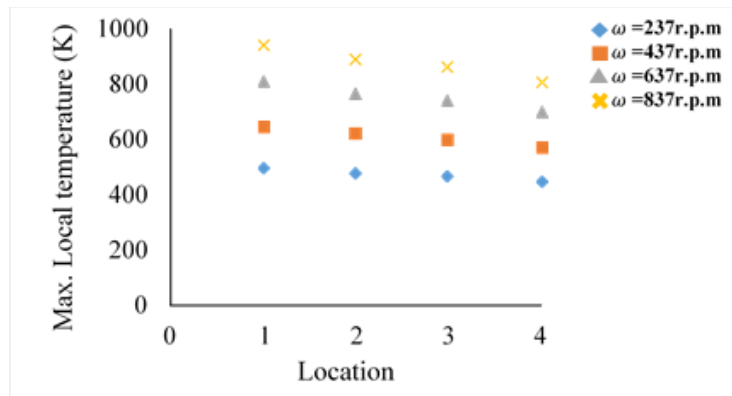


Figure 4.35 Max. Local temperature for different rotational speeds at different locations

In order to explain how the material flow is affected by the change in the tool rotational speed, snapshots for the flow velocity field were taken at the same time in which the temperature distribution was previously depicted. Figure 4.36 shows the velocity fields at underneath the shoulder (a,b) and the pin (c,d) when $\omega = 237\text{r.p.m}$ and $\omega = 837\text{r.p.m}$, respectively. It is clearly

evident that the highest flow rate is directly below the outer edge of the shoulder where the maximum linear velocity can be achieved. From *a* and *b*, the maximum flow velocity has recorded an increase by 1.5m/s against the increase in the rotational speed from 237r.p.m to 837r.p.m while the increase was around 0.4m/s under the pin for the same change in the tool rotational speed as shown in *c* and *d*. In fact, higher rotational speed means higher frictional heat generation and the material becomes soft easily which enhances the flow velocity. Accordingly, heat generation due the material deformation is practically affected particularly at the very high rotational speed.

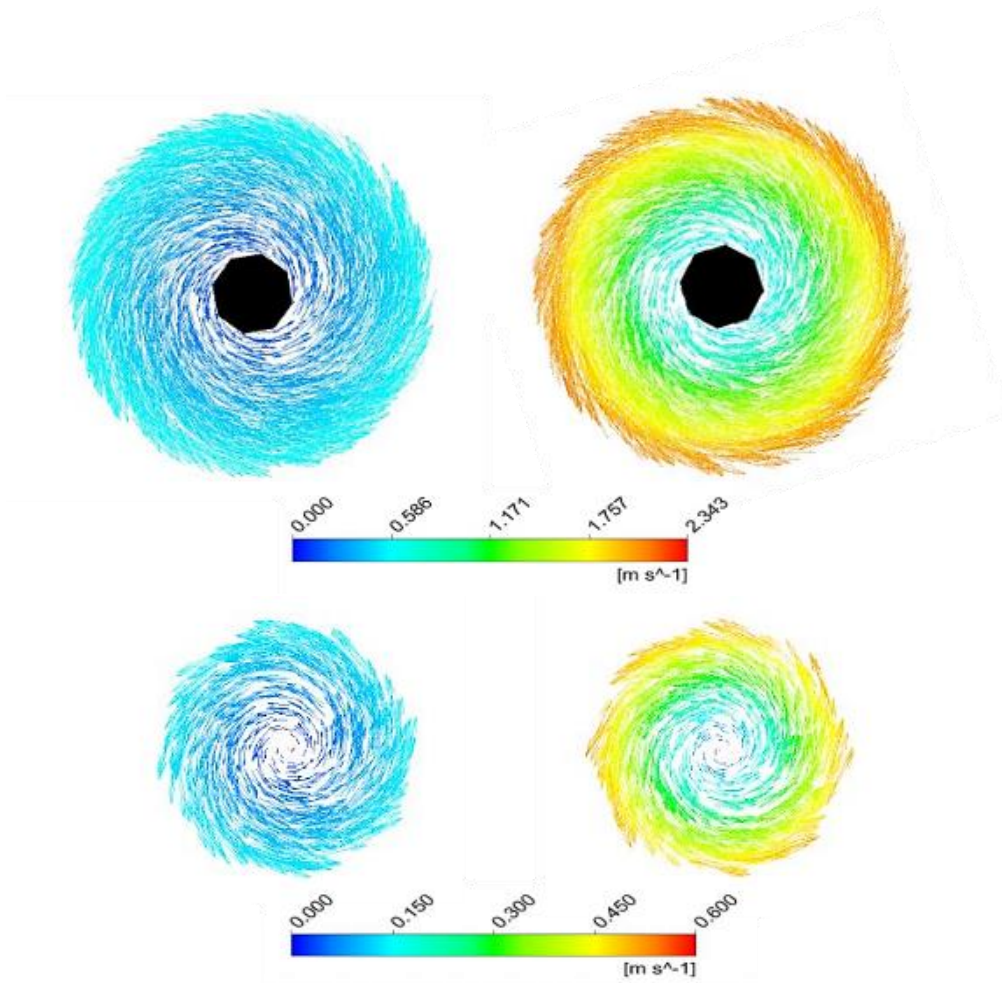


Figure 4.36 Flow velocity field for different rotational speed at underneath the shoulder and the pin

Figure 4.37, shows the variation of the maximum shear stress along the thermal cycle for different welding rotational speeds. Although, the tool geometry and dimensions are the same for all considered cases the shear stress has recorded different values which means the rotational speed has a clear effect on it. For $\omega = 237\text{r.p.m}$, the shear stress reached the highest values among the other cases while the lowest were scored when $\omega = 837\text{r.p.m}$. In case of the lowest speed, the temperature is relatively less compared to the others and the material is not that much soft which in role enhancing the forces around the tool. This finding were reflected in the material behaviour which is expected to show a greater deformation at lower rotational speed [91]. Conversely, in the existence of such high stress the tool pin will probably be broken if its shear strength was exceeded.

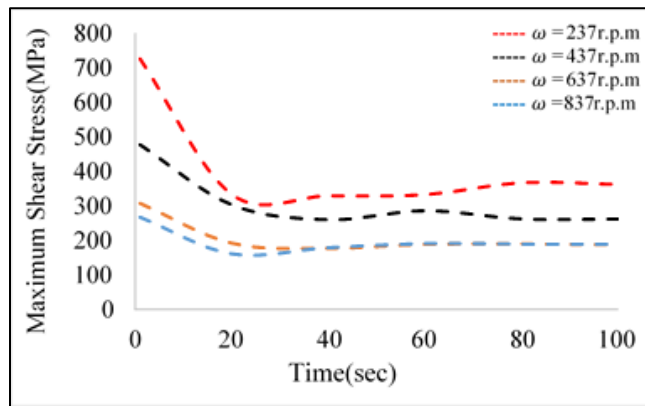


Figure 4.37 Variation of the global maximum shear stress along the process time for different rotational speeds

4.3.3 Effects of Axial Load on the Thermal Field of FSW

In order to investigate the impact of the axial load, four different values of loads have been used as presented in table 4-2, which were ranging from 9.7 MPa to 14.2 MPa. In figure 4.38 (a,b,c,d), it can be seen how the temperature distribution around the tool change with the increase in the axial load where the general trend was similar to that observed when the tool rotational speed is changed. Additionally, the temperature has exceeded the material's solidus temperature for axial load of 14.2 MPa and then the liquid region is expected to appear.

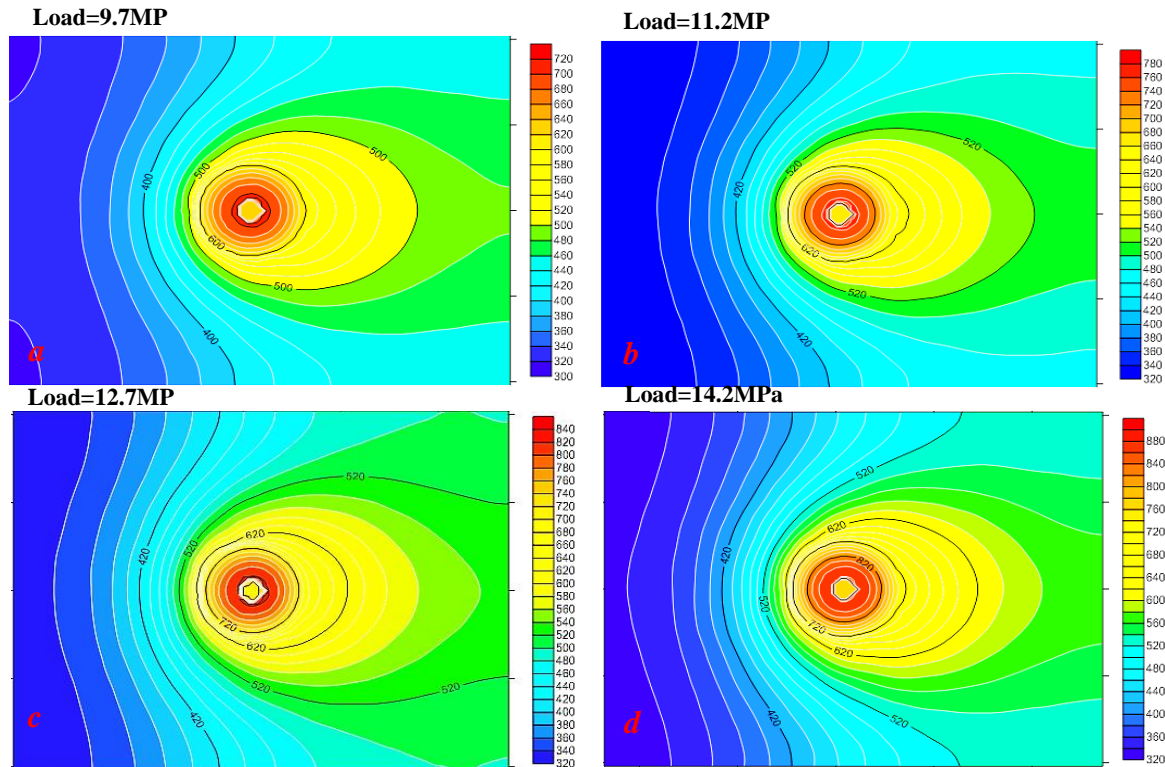


Figure 4.38 Static temperature contours for different axial load a=9.7MPa, b=11.2MPa, c=12.7MPa, d=14.2MPa.

In Figure 4.39, snapshots of liquid fraction at different moments from the thermal cycle were taken to show the transient progression against the change in the temperature when the axial load is 14.2MPa. By keeping in mind that the solidus temperature for the material used is 855K, it can be noticed from the figure that no melting has occurred in the first three seconds even though the average heating rate in this period reached to 96K/sec. However, at $t=5$ sec the model predicted a mushy zone with maximum liquid fraction of 30% as the maximum temperature attained 881K. After a period of the process time, the dimensions of mushy zone expanded whereas the maximum liquid fraction scored 50% at the moment of 45 seconds at which the peak temperature was around 895K. After 90seconds, the mushy zone stabilised, and no change has been recorded on the liquid fraction value compared to its value at the time of 45seconds.

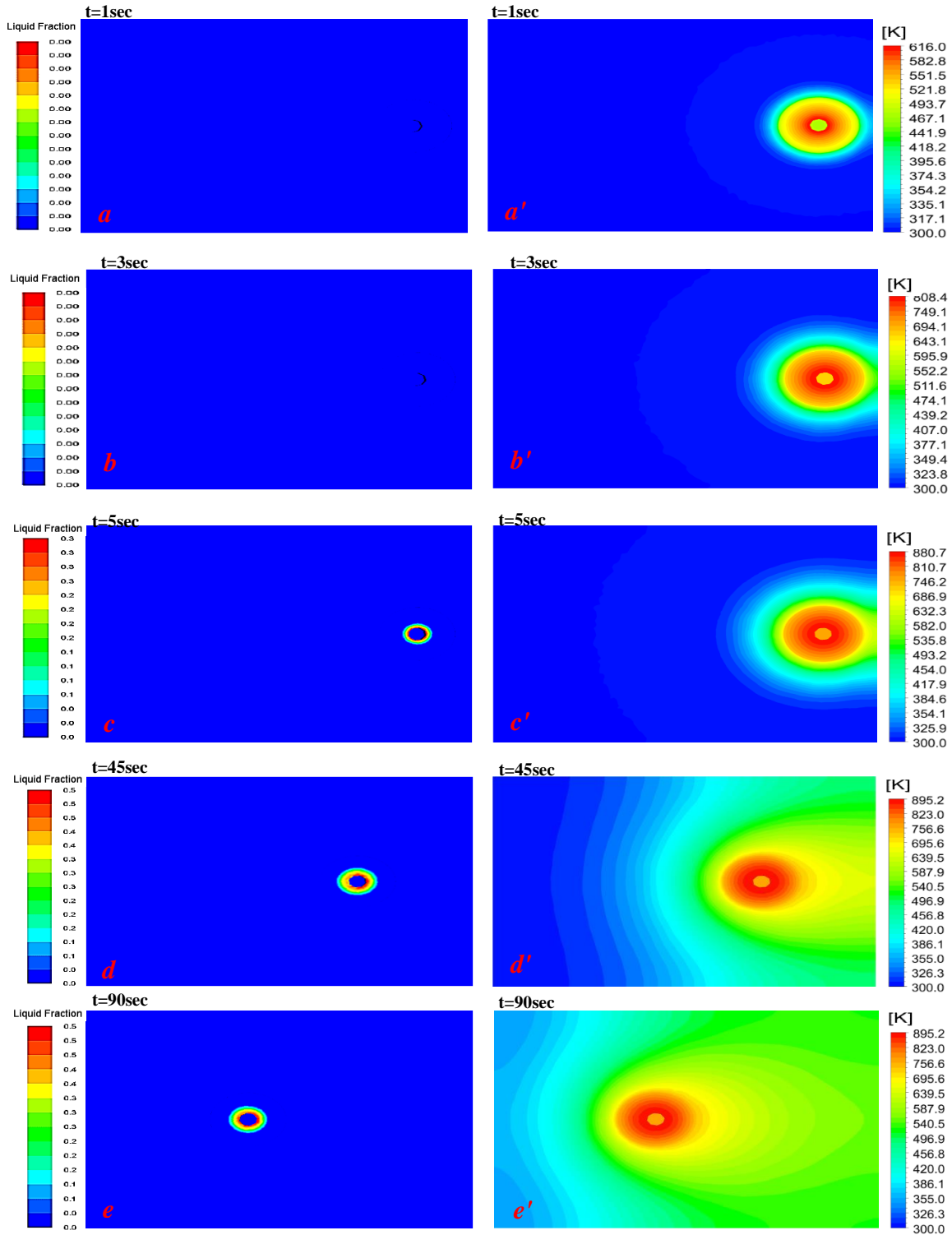


Figure 4.39 Liquid fraction variation corresponding to the temperature rising at different times for axial load = 14.2MPa

It can be seen in figures 4.40 and 4.41 that both global and local peak temperatures increase when the axial load increases. This can be justified by the increase in the frictional forces and the better frictional coupling which lead to boosting the heat generation in the interface between the tool and the workpiece [91]. Furthermore, the strain rate is likely to be increased along with the improvement in the contact between the tool and the workpiece which increases the plastic contribution to the temperature field particularly under the shoulder. However, the model did not capture significant changes in the volume of the stirring zone and the flow velocity under the pin with the considered range of change in axial load as depicted in figure 4.42 . It is worth mentioning that at very high pressure the affected region under the tool can be increased and some defects could adversely appear due to the overheating while undesirable insufficient heating could be a result of a very low pressure [92].

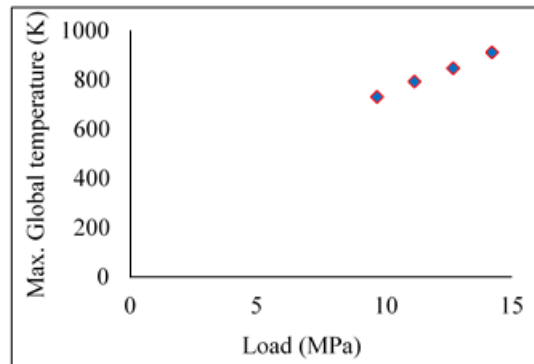


Figure 4.40 Max. Global temperature for different loads

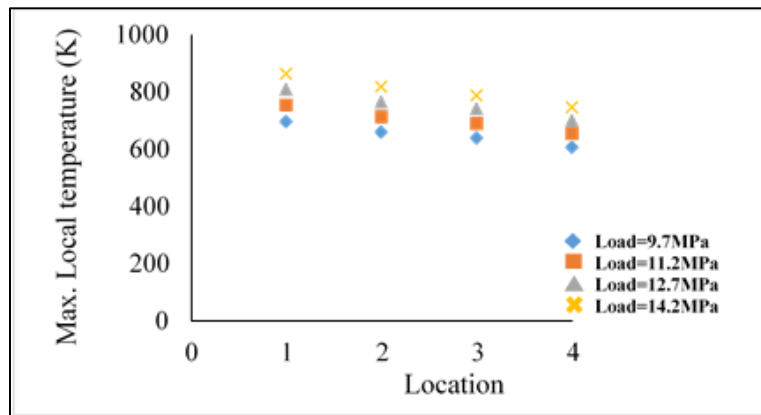


Figure 4.41 Max. Local temperature for different loads at different locations

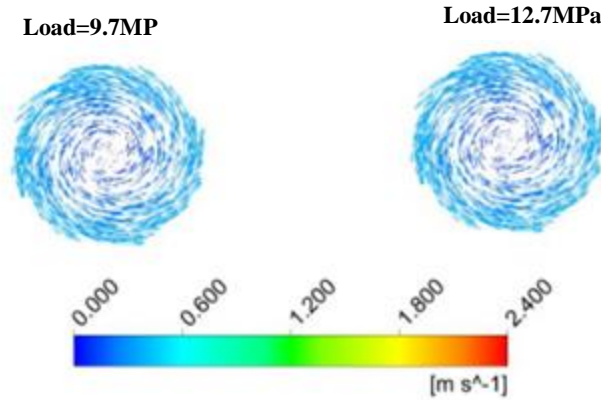


Figure 4.42 Flow velocity field for different axial loads at underneath the shoulder and the pin

As illustrated in figure 4.43 the maximum shear stress changes according to the variation in the axial load. Amongst the other axial load values, 9.7MPa has registered the greatest shear stress (red dashed line) which reached 350MPa at the beginning of the thermal cycle. For all considered axial loads, the highest values of shear stress were recorded at the earlier stage of the thermal cycle,

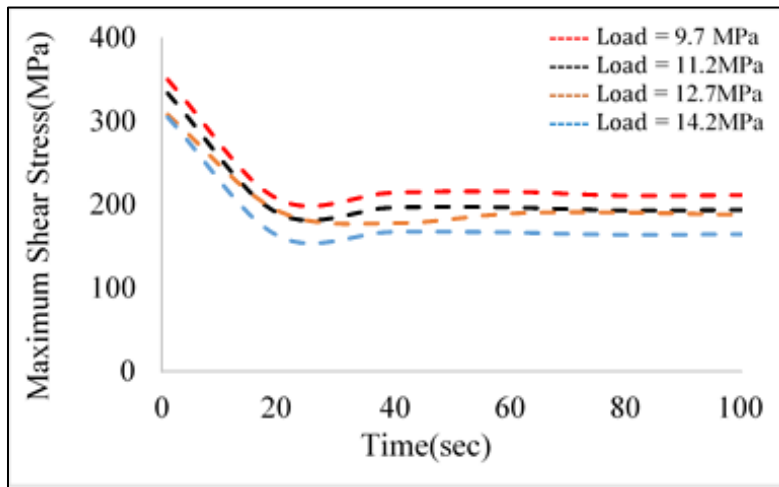


Figure 4.43 Time dependent variation of the maximum shear stress for different axial loads

4.4 Prediction Model of the Peak Temperature

As planned, the last step in this chapter is developing a prediction model for the maximum temperature T_{max} that can be attained during FSW process. According to the literature review and based on the results which were previously presented and discussed in this chapter, both the geometrical and operational parameters that have been considered in the thermal investigation showed an impact on the peak temperature. As a function of these parameters, a novel semi-empirical correlation for predicting the peak temperature can be developed based on the acquired data from CFD experiments and with the aid of an advanced statistical process which is multiple variable regression analysis. Therefore, the dimensionless equation 4.23 has been established to describe the relationship between the temperature ratio $T_{max} / (T_s)$ and the considered variables.

$$\frac{T_{max}}{T_s} = \frac{0.01725 \left(\frac{H}{t}\right)^{0.091} \left(\frac{P}{P_{max}}\right)^{0.5469}}{\left(\frac{V}{\omega R_s}\right)^{0.6022} \left(\frac{N}{R_s * R_p}\right)^{0.1165}} \quad (4.23)$$

where T_s is the solidus temperature of the material to be welded which is equal to 855K in the current study, V is the tool transverse speed, ω is the tool rotational speed, R_s is the shoulder radius, N is the number of pin side faces, H is the pin height, t is the workpiece thickness, P is the axial load, P_{max} is the maximum axial load. Then, eq. 4.23 can be rearranged to find a direct expression to calculate T_{max} as following:

$$T_{max} = \left[\frac{0.01725 \left(\frac{H}{t}\right)^{0.091} \left(\frac{P}{P_{max}}\right)^{0.5469}}{\left(\frac{V}{\omega R_s}\right)^{0.6022} \left(\frac{N}{R_s * R_p}\right)^{0.1165}} \right] \times T_s \quad (4.24)$$

It can be seen from the prediction model that (P/P_{max}) , $(v/\omega R_s)$ have the most significant effect on the peak temperature. Moreover, the peak temperature is proportional to $(H/t, P/P_{max})$ and inversely proportional to $(v/\omega R_s, N.R_p/R_s)$. From eq. (4.24), if the fraction in the brackets has a value greater than 1, this means that some parts of the welded material converted to liquid state. In order to authorise the usefulness of Eqn. 4.24, the average of difference between the values of T_{max} calculated from Eqn. 4.24 and T_{max} values obtained from CFD was estimated to be 5.35%. Furthermore, it is obvious in figure 4.44 that within errors ranged from 0 to maximum $\pm 10\%$, it would be seen that around 90% of the data lies in this range. Thus, it can be concluded that the

prediction model represents the peak temperature with reasonable accuracy. Last but not least, the above expressed equation is valid for the considered ranges of parameters.

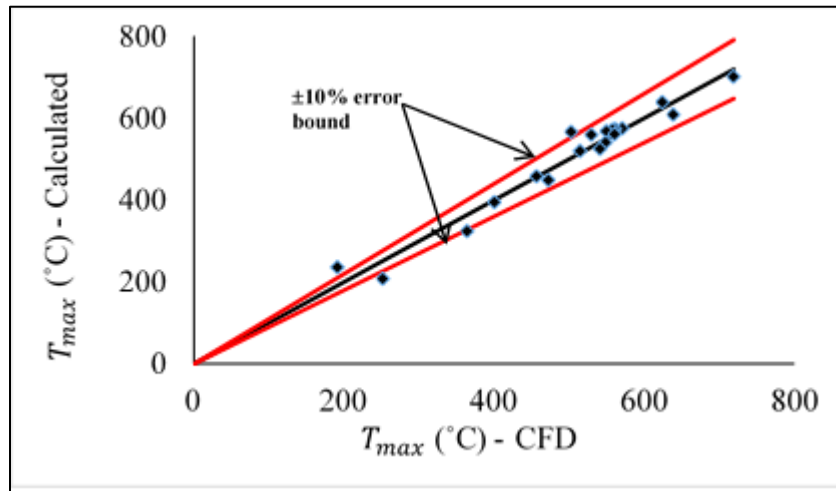


Figure 4.44 prediction model of T_{max}

4.5 Summary of the Thermal Analysis conducted on the FSW using tools with Concentric Polygonal Pins

By using the analytical and CFD approaches, a detailed diagnosis of thermal field behaviour has been provided which revealed the following results:

- Analytically, the increase in the number of polygon faces increases the total amount of heat generated.
- For thick aluminium plates, the increase in the heat amount is not high enough to change the temperature distribution when using polygons with seven faces or more.
- The increase in the tool shoulder size increases the temperature in the workpiece particularly in the tool vicinity.
- For thick workpiece, the increase in the pin diameter leads to a relative decrease in the temperature.
- The temperature is very marginally increased as the pin height increases compared to the other geometrical parameters.
- The increase in the workpiece thickness decreases the temperature in the workpiece.
- The welded material temperature is increased when the tool rotational speed and the axial load increase.

As we wrap up this chapter, it provides the steps for the analytical estimation of the heat generated amount in friction stir welding when using tools with concentric polygonal pin. Additionally, information regarding the thermal field in the thick friction stir welded material has been provided. Moreover, developing a prediction model for the peak temperature which may be helpful in controlling the welding process. For the eccentric polygonal pin that has been reported as a way to get better mechanical properties than that obtained from the one without eccentricity, the next chapter provides the analytical steps to express the heat generation formulas including the geometrical changing in the welding tool. Furthermore, the information obtained from CFD regarding the thermal field in the workpiece when employment of such a tool will be presented.

CHAPTER 5: THERMAL CHARACTERISATION OF FRICTION STIR WELDING USING TOOL WITH ECCENTRIC PINS

This chapter will consider the concept of pin eccentricity and its effects on the thermal field of FSW. In view of this, the chapter begins with a description of the analytical steps to derive equations calculating the heat generated amount due to the friction between the tool and the workpiece when using eccentric polygonal pins. Then, the thermal field analysis within the workpiece has been conducted where the obtained results have been qualitatively and quantitatively analysed. In existence of the eccentricity, the effect of various geometrical and operational parameters on the temperature distribution and the peak temperature was investigated. After that, the predicted results are used to develop a semi-empirical relationship for the peak temperature.

5.1 Analytical Modeling of Heat Generation from a Tool with Eccentric Pin

As it has been presented in the previous chapter, the same analytical approach will be adopted here to derive mathematical relationships calculating the heat generated amount when using such tools. The focal point in this section is how to derive the generated heat equations when the eccentricity is involved. Accordingly, a tool with Eccentric Heptagonal pin profile has been chosen to demonstrate the detailed steps of the analytical modeling for the heat generation during the FSW process which helps to compare their thermal performance with those without eccentricity. The analytical models for all considered cases have been established based on analytical models developed by Schmidt et al [13], Gadakh et al [49], and A.R.S. Essa et al. [57]. In figure 5.1(a, b, c), the schematic of tools with different polygonal pins and the main regions that are related to the heat generation are shown. Q_1 is the generated heat at the tool shoulder base, Q_2 is the heat amount that generated at the sides of the tool pin and Q_3 represents the heat generated at the pin tip. Summation of these gives the overall heat amount Q_{total} produced due to the friction between the tool surfaces and the workpiece. Figure 5.2(a, b, c), shows the offset of the pins related to the original axis which represents the eccentricity.

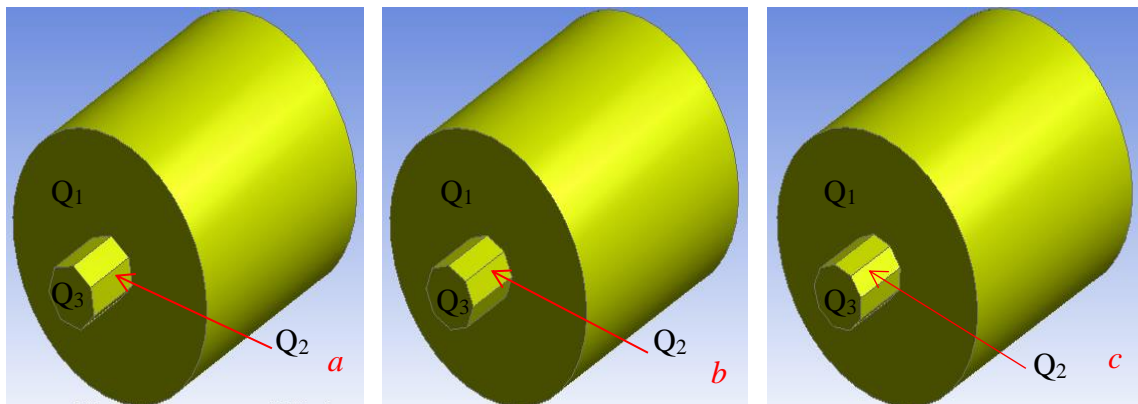


Figure 5.1 Tools with eccentric pins (a) Heptagon, (b) Octagon, (c) Nonagon

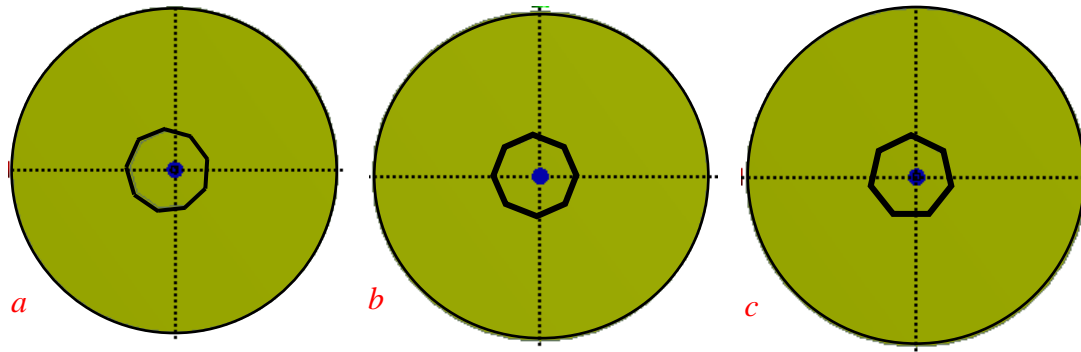


Figure 5.2 The pin eccentricity (a) Eccentric Heptagon, (b) Eccentric Octagon, (c) Eccentric Nonagon

For more explanation, the simplified tool design is sketched in figure 5.3 where e stands to the pin eccentricity.

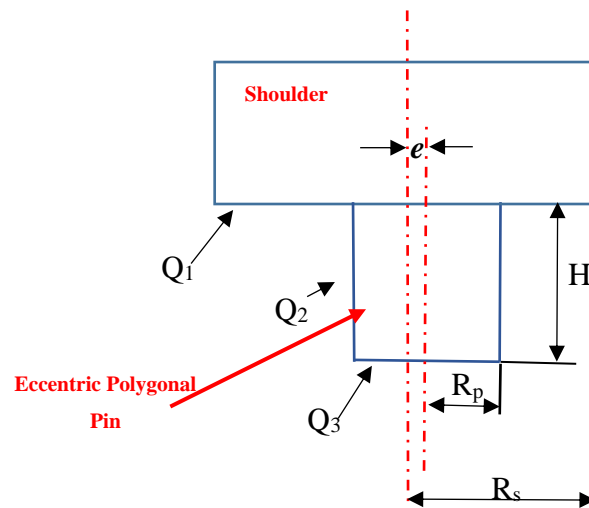


Figure 5.3 schematic drawing of a tool with eccentric polygonal pin

5.2 Heat Generation from a Tool with Eccentric Heptagonal Pin

5.2.1 Heat Generation from Shoulder Base

As the shoulder rotates around the original axis and have the same frictional area presented in section 4.1, the heat generated at the shoulder base can be estimated through Eq. (4.4)

$$Q_1 = \frac{2}{3} \pi \cdot \omega \cdot \tau_{contact} \cdot R_s^3 - Q_3 \quad (4.4)$$

From Eqs. (4.4) and 4.15

$$Q_1 = \frac{2}{3}\pi \cdot \omega \cdot \tau_{contact} \cdot R_s^3 - \left[\frac{2 \times 1.53\pi \cdot \omega \cdot \tau_{contact} \cdot a^3}{3} \right] \quad (5.1)$$

$$Q_1 = \frac{2}{3}\pi \cdot \omega \cdot \tau_{contact} (R_s^3 - 1.53a^3) \quad (5.2)$$

5.2.2 Heat Generation from Pin Side Surfaces

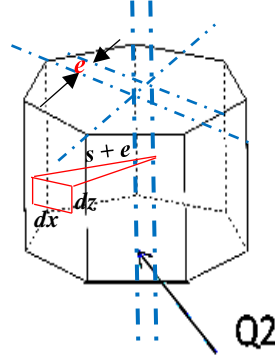


Figure 5.4 Schematic drawing of the frictional zone and the infinitesimal areas related to the Eccentric Heptagonal pin side

In addition to the trigonometric expressions that were defined in section 4.1, the pin consists an eccentricity distance e as shown in figures 5.3 and 5.4. Through the following mathematical derivation of the equation that estimate the heat generated from the pin side surfaces, the term e represents the effect of the eccentricity. Starting with the general equation for heat generation 4.1 which should be multiplied by 7 for Heptagonal pin [49, 57].

$$dQ = \omega \cdot dM = \omega \cdot r \cdot dF = \omega \cdot r \cdot \tau_{contact} \cdot dA \quad (4.1)$$

$$dQ = 7(\omega \cdot (s + e) \cdot \tau_{contact} \cdot dx \cdot dz) \quad (5.3)$$

By integration eq. 5.3, over the frictional area from 0 to H

$$Q_2 = 7 \int_0^a \int_0^H \omega \cdot \tau_{contact} \cdot (s + e) \cdot dx \cdot dz \quad (5.4)$$

$$Q_2 = 7(\omega \cdot (s + e) \cdot \tau_{contact} \cdot a \cdot H) \quad (5.5)$$

From Eqn. 4.10, when $n=7$, s is equal to $1.0382 a$.

$$Q_2 = 7(\omega \cdot \tau_{contact} \cdot (1.0382a + e) \cdot a \cdot H) \quad (5.6)$$

$$Q_2 = 7(\omega \cdot \tau_{contact} \cdot (1.0382a^2 + e \cdot a) \cdot H) \quad (5.7)$$

5.2.3 Heat Generation from the Pin Tip

Figure 5.5, shows the path of the movement of the eccentric heptagonal pin tip where the position and the offset relative to the rotating axis are given. Similar to section 4.1, the contact area is divided into fourteen sections and using the polar coordinate in existence of the eccentricity distance, the heat generation equation for each section is expressed as:

$$dQ = \omega \cdot (r + e) \cdot \tau_{\text{contact}} \cdot (r + e) \cdot d\theta \cdot dr \quad (5.8)$$

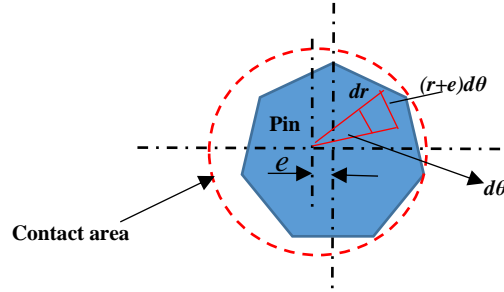


Figure 5.5 Schematic drawing of the frictional zone and the infinitesimal areas related to the Eccentric Heptagonal pin tip

By integration eq. 5.8 over the contact area and using the multiplying factor 14 which denotes the fourteen sections that form the whole frictional area, the heat generation from the pin tip, Q_3 can be computed as:

$$Q_3 = 14 \int_0^{\theta=\frac{\pi}{7}} \int_0^{Rp} \omega \cdot (r + e)^2 \cdot \tau_{\text{contact}} \cdot d\theta \cdot dr \quad (5.9)$$

In eq. 4.8, R_p is equal to $1.1523a$ when $n=7$. Therefore

$$Q_3 = 14 \int_0^{\theta=\frac{\pi}{7}} \int_0^{Rp=1.1523a} \omega \cdot (r + e)^2 \cdot \tau_{\text{contact}} \cdot d\theta \cdot dr \quad (5.10)$$

$$Q_3 = 14 \left[\frac{\pi}{7} \cdot \omega \cdot \tau_{\text{contact}} \cdot \left(\left(\frac{(1.1523a+e)^3}{3} \right) - \frac{e^3}{3} \right) \right] \quad (5.11)$$

$$Q_3 = \frac{2}{3} \pi \cdot \omega \cdot \tau_{\text{contact}} \cdot ((1.1523a + e)^3 - e^3) \quad (5.12)$$

5.2.4 Total Heat Generation from the Tool with Eccentric Heptagonal Pin

Using eqs. (5.2), (5.7) and (5.12), the total heat generation from the tool with eccentric heptagonal pin can be computed as:

$$Q_{total} = \frac{2}{3}\pi \cdot \omega \cdot \tau_{contact} (R_s^3 - 1.53a^3) + 7(\omega \cdot \tau_{contact} \cdot (1.0382a^2 + e \cdot a) \cdot H) + \frac{2}{3}\pi \cdot \omega \cdot \tau_{contact} \cdot ((1.1523a + e)^3 - e^3) \quad (5.13)$$

Rearranging eq. (5.13)

$$Q_{total} = \frac{2}{3}\pi \cdot \omega \cdot \tau_{contact} \left[(R_s^3 - 1.53a^3) + 7 \left(\frac{3}{2\pi} \right) (1.0382a^2 + e \cdot a) \cdot H \right] + (1.1523a + e)^3 - e^3 \quad (5.14)$$

$$Q_{total} = \frac{2}{3}\pi \cdot \omega \cdot \tau_{contact} [(R_s^3 - 1.53a^3) + (3.4717a^2 + 3.3439 \cdot e \cdot a) \cdot H + (1.1523a + e)^3 - e^3] \quad (5.15)$$

From Eqn. 4.8, R_p is equal to $1.1523a$ when $n=7$, hence Eqn. 5.15 can be written as:

$$Q_{total} = \frac{2}{3}\pi \cdot \omega \cdot \tau_{contact} \left[(R_s^3 - R_p^3) + \left(3.4717 \frac{R_p^2}{(1.1523)^2} + 3.3439 \left(e \cdot \frac{R_p}{1.1523} \right) \right) \cdot H + \left(\left(1.1523 \left(\frac{R_p}{1.1523} \right) + e \right)^3 - e^3 \right) \right] \quad (5.16)$$

$$Q_{total} = \frac{2}{3}\pi \cdot \omega \cdot \tau_{contact} \left[(R_s^3 - R_p^3) + (2.6146R_p^2 + 2.9019 e \cdot R_p) \cdot H + \left((R_p + e)^3 - e^3 \right) \right] \quad (5.17)$$

In the case of e equals to zero, the pin is concentric where the heat generation equation (5.17) simplifies to an expression correlates well with the equation (4.21)

In the same way, for the other tools with eccentric polygonal pin profiles that have a higher number of side faces; the heat generation expressions have been developed using the same analytical approach. Based on the number of pin faces, the heat generation expressions are listed in table 5-1.

Table 5-1 heat generation formulas of tools with different eccentric pin profiles

Pin Profile	No. of Faces	Equation
Eccentric Heptagonal	7	$Q_{total} = \frac{2}{3}\pi \cdot \omega \cdot \tau_{contact} \left[\frac{(R_s^3 - R_p^3) + (2.6146R_p^2 + 2.9019 e \cdot R_p) \cdot H}{((R_p + e)^3 - e^3)} + \right]$
Eccentric Octagonal	8	$Q_{total} = \frac{2}{3}\pi \cdot \omega \cdot \tau_{contact} \left[\frac{(R_s^3 - R_p^3) + (2.7018R_p^2 + 2.9246 e \cdot R_p) \cdot H}{((R_p + e)^3 - e^3)} + \right]$
Eccentric Nonagonal	9	$Q_{total} = \frac{2}{3}\pi \cdot \omega \cdot \tau_{contact} \left[\frac{(R_s^3 - R_p^3) + (2.7632R_p^2 + 2.9407 e \cdot R_p) \cdot H}{((R_p + e)^3 - e^3)} + \right]$
Eccentric Decagon	10	$Q_{total} = \frac{2}{3}\pi \cdot \omega \cdot \tau_{contact} \left[\frac{(R_s^3 - R_p^3) + (2.8075R_p^2 + 2.9521 e \cdot R_p) \cdot H}{((R_p + e)^3 - e^3)} + \right]$
Eccentric Undecagon	11	$Q_{total} = \frac{2}{3}\pi \cdot \omega \cdot \tau_{contact} \left[\frac{(R_s^3 - R_p^3) + (2.8402R_p^2 + 2.9604 e \cdot R_p) \cdot H}{((R_p + e)^3 - e^3)} + \right]$
Eccentric Dodecagon	12	$Q_{total} = \frac{2}{3}\pi \cdot \omega \cdot \tau_{contact} \left[\frac{(R_s^3 - R_p^3) + (2.8657R_p^2 + 2.967 e \cdot R_p) \cdot H}{((R_p + e)^3 - e^3)} + \right]$
Eccentric 13-gon	13	$Q_{total} = \frac{2}{3}\pi \cdot \omega \cdot \tau_{contact} \left[\frac{(R_s^3 - R_p^3) + (2.8856R_p^2 + 2.9721 e \cdot R_p) \cdot H}{((R_p + e)^3 - e^3)} + \right]$
Eccentric 14-gon	14	$Q_{total} = \frac{2}{3}\pi \cdot \omega \cdot \tau_{contact} \left[\frac{(R_s^3 - R_p^3) + (2.9012R_p^2 + 2.976 e \cdot R_p) \cdot H}{((R_p + e)^3 - e^3)} + \right]$
Eccentric 15-gon	15	$Q_{total} = \frac{2}{3}\pi \cdot \omega \cdot \tau_{contact} \left[\frac{(R_s^3 - R_p^3) + (2.9141R_p^2 + 2.9794 e \cdot R_p) \cdot H}{((R_p + e)^3 - e^3)} + \right]$
Eccentric 25-gon	25	$Q_{total} = \frac{2}{3}\pi \cdot \omega \cdot \tau_{contact} \left[\frac{(R_s^3 - R_p^3) + (2.9684R_p^2 + 2.9928 e \cdot R_p) \cdot H}{((R_p + e)^3 - e^3)} + \right]$
Eccentric 30-gon	30	$Q_{total} = \frac{2}{3}\pi \cdot \omega \cdot \tau_{contact} \left[\frac{(R_s^3 - R_p^3) + (2.9794R_p^2 + 2.9959 e \cdot R_p) \cdot H}{((R_p + e)^3 - e^3)} + \right]$
Eccentric 40-gon	40	$Q_{total} = \frac{2}{3}\pi \cdot \omega \cdot \tau_{contact} \left[\frac{(R_s^3 - R_p^3) + (2.9884R_p^2 + 2.998 e \cdot R_p) \cdot H}{((R_p + e)^3 - e^3)} + \right]$

By comparing the developed expressions in the table with each other, it can be seen that all the terms in the equations are the same except the numerical coefficients in the terms that related to the heat generation at the pin side surface. Accordingly, a general equation can be expressed as:

$$Q_{total} = \frac{2}{3}\pi \cdot \omega \cdot \tau_{contact} \left[\frac{(R_s^3 - R_p^3) + (c_{n1}R_p^2 + c_{n2} \cdot e \cdot R_p) \cdot H}{((R_p + e)^3 - e^3)} \right] \quad (5.18)$$

where C_{n1} and C_{n2} have different values according to the number of polygon faces.

All above derived heat generation equations have been used for the same aluminium FSW welding process and conditions in chapter 3. After calculating the heat amounts from the analytical equations for different proposed eccentricity distances ranging from 0mm to 0.9mm , they were plotted in figure 5.6 and compared with the calculated heat generated amount from the tool with cylindrical pin profile. It can be seen in the figure that increasing the value of the eccentricity caused an increase of the generated heat as the frictional area increases [51, 57]. For instance, the total heat amount in the case of Decagon pin recorded 11937.4W, 12006.4W, 12078W and 12152W against eccentricities e of 0mm, 0.3mm, 0.6mm, 0.9mm respectively. It is obvious that the thermal performance of the tool is affected according to the variation in the pin eccentricity where the tool with eccentric decagon pin produced a total heat that exceeded the heat amount of the cylindrical pin by 142W when $e=0.9$ mm. On the contrary, it was less than the heat amount of the cylindrical pin by 73W when $e=0$ mm. Accordingly, the heat generation amount increases by 215W when the eccentricity grows from 0mm to 0.9mm.

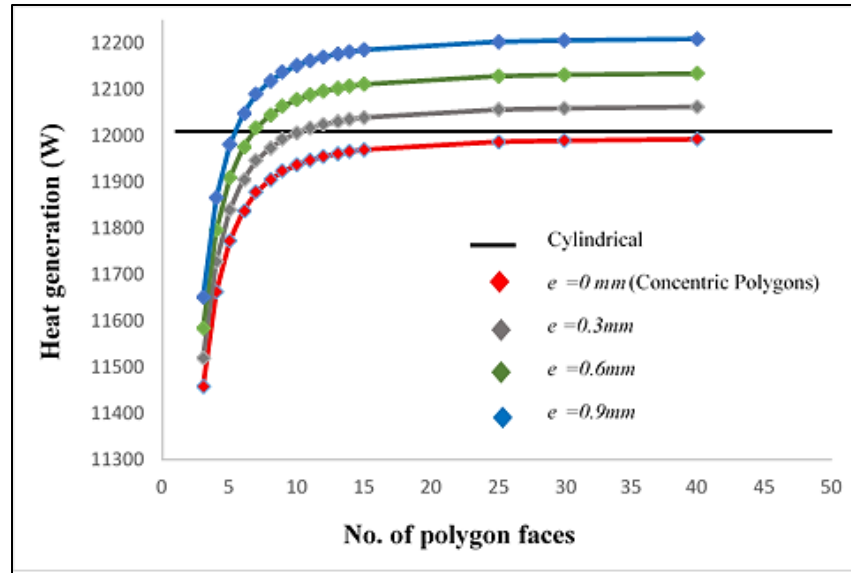


Figure 5.6 Heat generation values with No. of polygon faces for different eccentric distances

5.3 Thermal Field Analysis of FSW when using Eccentric Polygonal Pins

In order to examine how the value of the pin eccentricity might affect the thermal field in FSW especially under several geometrical and operational parameters, the current CFD model will be used along with the new analytical equations that have been developed in the previous sections of this chapter. For the proposed values of pin eccentricity which are 0mm, 0.3mm, 0.6mm and 0.9mm, the tool with octagonal pin profile was chosen to conduct this investigation where meaningful comparisons would be drawn up between the thermal characteristics acquired with the eccentricity and without. As presented in table 5-2, a set of numerical experiments have been proposed to investigate the effects of the selected parameters which are eccentricity, shoulder size, pin size, pin height, material thickness, tool rotational speed and axial load. In this set of numerical experiments, the effect of each variable has been addressed by four different values as shown in the table by the yellow shaded cells.

Table 5-2 The proposed numerical experiments and ranges of parameters

No.	Eccentricity Distance(mm)	Shoulder Radius(mm)	Pin Radius(mm)	Pin Height(mm)	Material Thickness (mm)	Rotational Speed(rpm)	Axial load (MPa)
EX.1	0	25	6	12	12.7	637	12.7
EX.2	0.3	25	6	12	12.7	637	12.7
EX.3	0.6	25	6	12	12.7	637	12.7
EX.4	0.9	25	6	12	12.7	637	12.7
EX.5	0.9	13	6	12	12.7	637	12.7
EX.6	0.9	17	6	12	12.7	637	12.7
EX.7	0.9	21	6	12	12.7	637	12.7
EX.8	0.9	25	3	12	12.7	637	12.7
EX.9	0.9	25	9	12	12.7	637	12.7
EX.10	0.9	25	12	12	12.7	637	12.7
EX.11	0.9	25	6	11	12.7	637	12.7
EX.12	0.9	25	6	10	12.7	637	12.7
EX.13	0.9	25	6	9	12.7	637	12.7
EX.14	0.9	25	6	12	14.7	637	12.7
EX.15	0.9	25	6	12	16.7	637	12.7
EX.16	0.9	24	6	12	18.7	637	12.7
EX.17	0.9	24	6	12	12.7	237	12.7
EX.18	0.9	24	6	12	12.7	437	12.7
EX.19	0.9	24	6	12	12.7	837	12.7
EX.20	0.9	24	6	12	12.7	637	9.7
EX.21	0.9	24	6	12	12.7	637	11.2
EX.22	0.9	24	6	12	12.7	637	14.2

5.3.1 Effects of Geometrical Parameters on the Thermal Field of FSW

5.3.1.1 Effect of Pin Eccentricity on the Thermal Field of FSW

Figure 5.7 indicates the time-dependent temperature distribution from two different thermal cycles corresponding to FS Welded samples using tools with eccentricity of 0mm and 0.9mm. The temperature contours were taken on a vertical plane at the weld centre line whereas dwelling and welding stages are represented. As the pin eccentricity is the only variable changed where the other parameters are kept constant, it can be seen from the figure that the hottest area is more concentrated when $e=0\text{mm}$ than $e=0.9\text{mm}$ particularly at the earlier stage of the process. Also, the scales indicate that the temperature recorded when $e=0.9\text{mm}$ have not interestingly reached those

attained for $e=0\text{mm}$ eventhough the heat input increases by increasing the eccentricity. That could be reasoned by the enhancement in the heat transfer process in the tool vicinity where the cooling rate effect becomes higher [57].

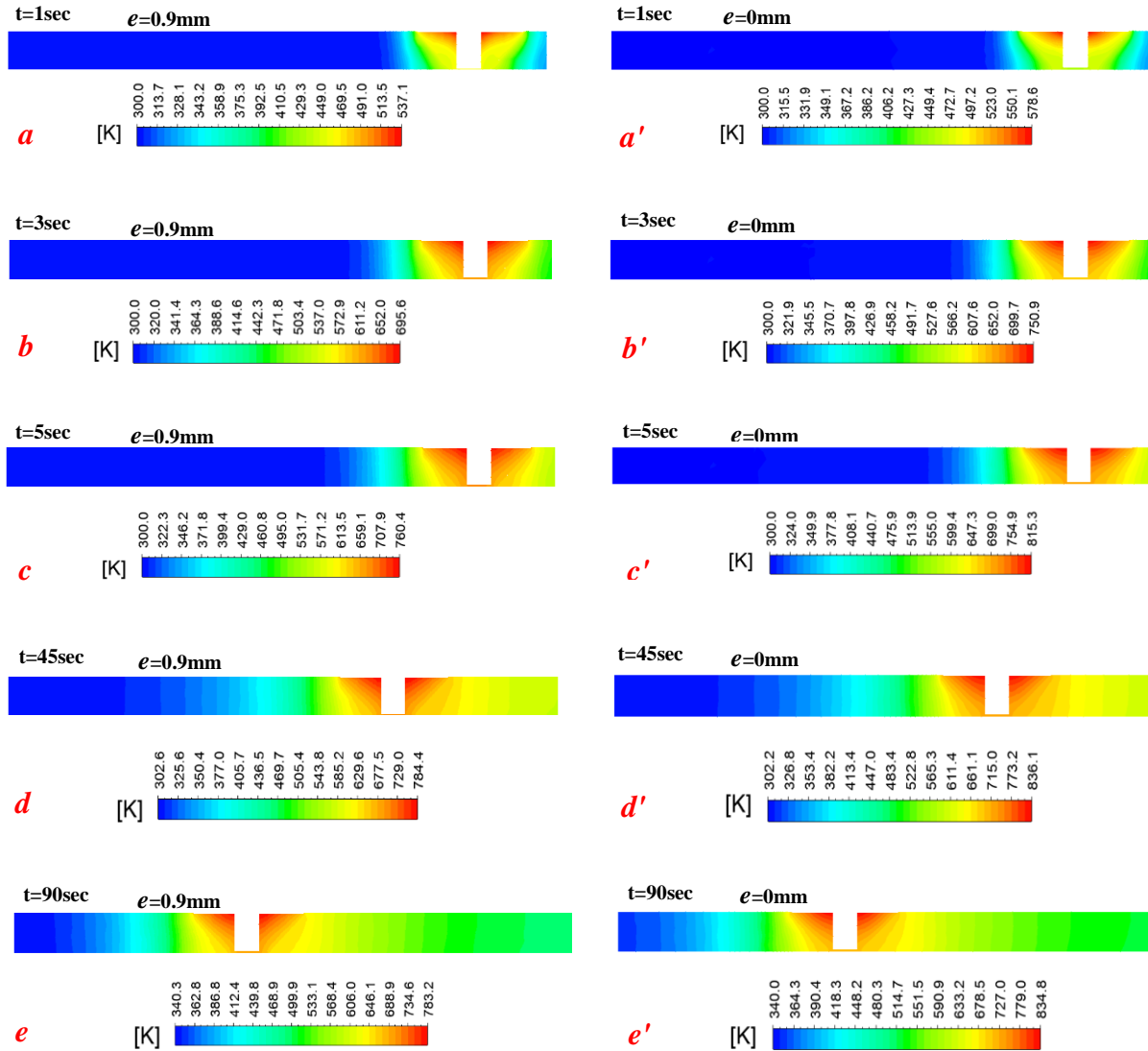


Figure 5.7 temperature distribution for the vertical plane at different time steps calculated for pin eccentricities of 0mm and 0.9mm

As similar as in chapter four and for more explanation of the variation in the temperature distribution due to the change in the pin eccentricity, instantaneous snapshots were taken for the same nominated plane in the previous chapter at which the maximum temperature is expected to take place. Figure 5.12 (*a,b,c,d*) depicts how the temperature is impacted in the range and distribution according to the change in pin offset. It is evident from the figure that the increase in the eccentricity leads to a decrease in the temperature values where the contraction that is happening for the area surrounded by the line of 520K gives a clear indication for this trend.

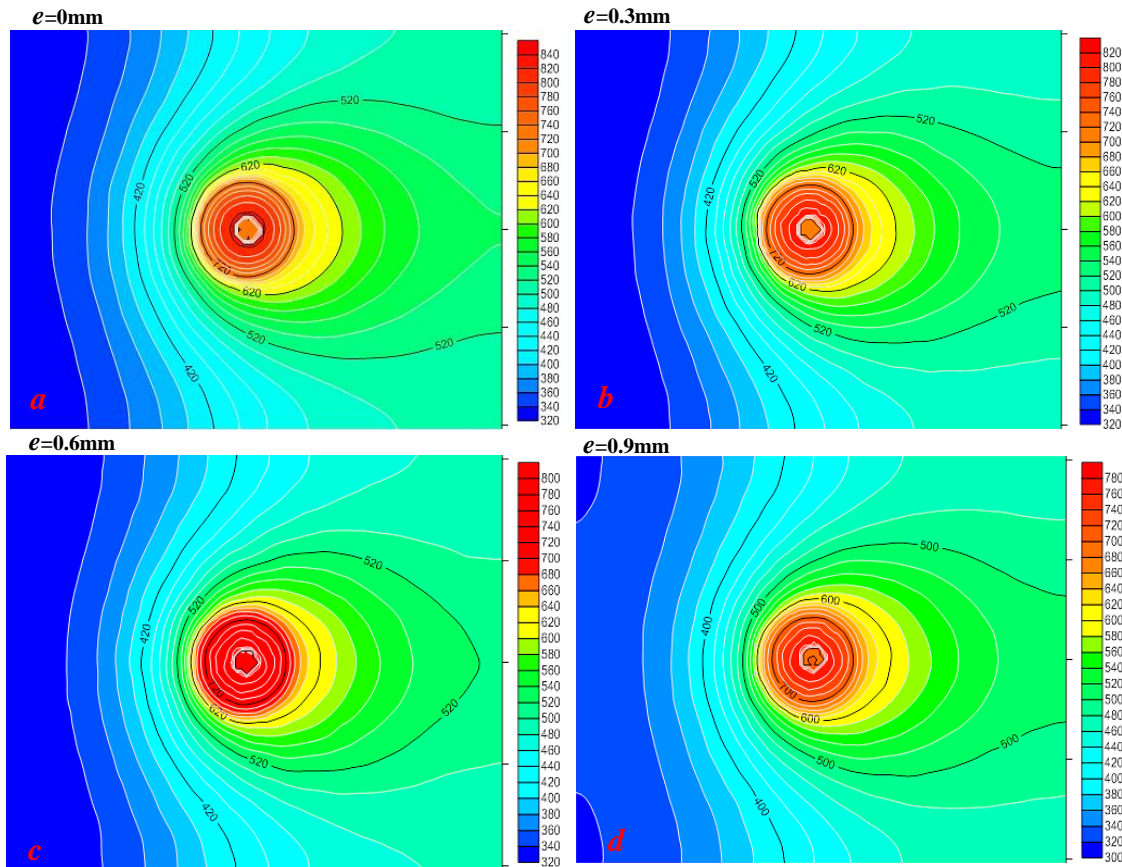


Figure 5.8 static temperature contours for different pin eccentricities $a=0\text{mm}$, $b=0.3\text{mm}$, $c=0.6\text{mm}$, $d=0.9\text{mm}$.

The results presented in figure 5.9 depicts a similar drop in the peak temperature as the value of pin eccentricity grows up which is well agreed with the A.R.S. Essa et al.'s findings [57]. This decrease is mostly shown to be proportional as the difference in temperature between $e=0\text{mm}$ and 0.3mm is 21K while it was 22K between $e=0.6\text{mm}$ and 0.9mm .

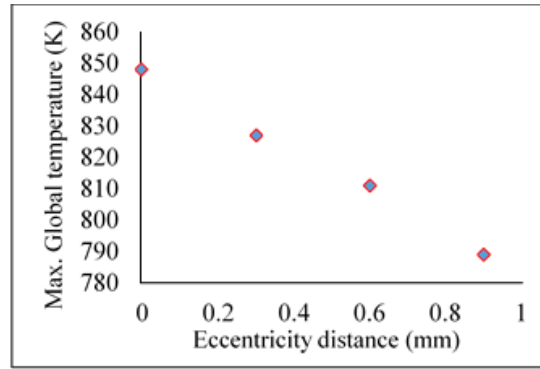


Figure 5.9 Global peak temperature for different pin eccentricities

From figure 5.10, it is again observed that the local peak temperatures were recorded at the same considered points in chapter four has witnessed dropping along with the increase in the pin eccentricity which can be attributed to the cooling rate effect as mentioned before. For further clarification, the path of a hypothetical point “o” can be followed to explain the effect of long path on the heat transfer process [57].

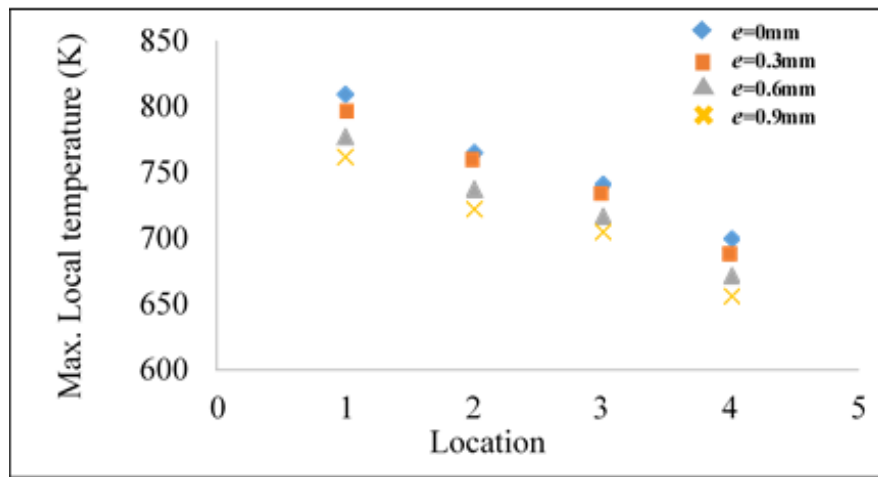


Figure 5.10 Max. Local temperature for different eccentricities at different locations

Now, assuming that the hypothetical point “o” is one of the polygonal vertices which are located on the pin surface. Figure 5.11, shows the paths of the hypothetical point “o” produced by tools with eccentricity of 0 and 0.9mm at the same welding conditions which give the same revolutionary pitch. It was clearly indicated in the figure that the path produced when $e=0.9\text{mm}$ is longer than that when $e=0\text{mm}$ where the cooling rate resulted will be greater as well. That means the role of the eccentricity in the enhancement of heat transfer process is dominant compared to

its role in the enhancement of heat generation. That can be also seen in figure 5.12 where the stirring zone when $e=0.9\text{mm}$ is wider than that when $e=0\text{mm}$. As a result of dropping in temperature, the viscosity has increased by $2.7 \times 10^6 \text{ Kg.m}^{-1}.\text{s}^{-1}$ which led to a decrease by 0.29mm/s in the material velocity under the pin.

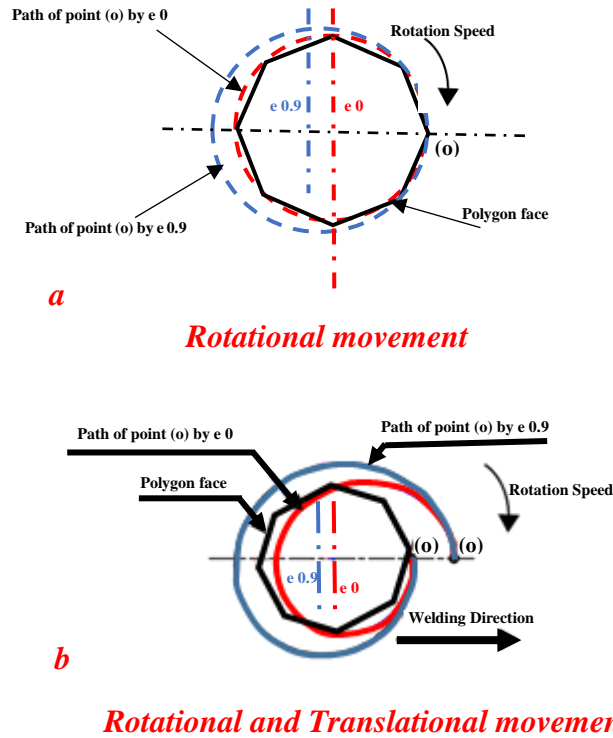


Figure 5.11 Paths of the hypothetical point “o” produced by tools with eccentricity of 0 and 0.9mm

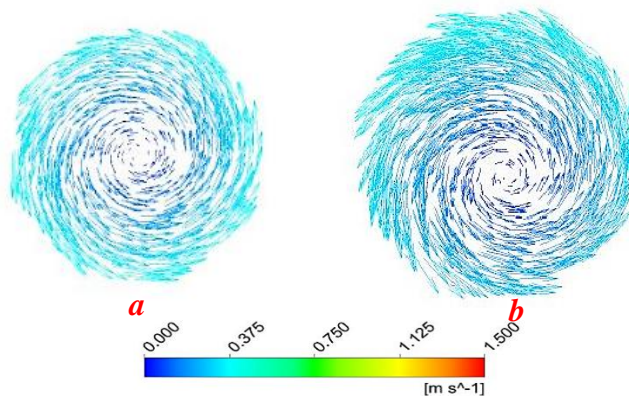


Figure 5.12 Flow velocity field for different eccentricities a=0mm, b=0.9mm

with the corresponding change in the temperature distribution, the shear stress is likely to be changed. Therefore, the results presented in figure 5.13 confirm this trend where the values of the maximum shear stress go up against the growth in the eccentricity. Numerically, the value of maximum shear stress is 308 MPa for $e=0\text{mm}$ while it increases to 363.6 MPa when $e=0.9\text{mm}$. Although, there has been a change in the values of shear stress the highest values still in the earlier stages of the process.

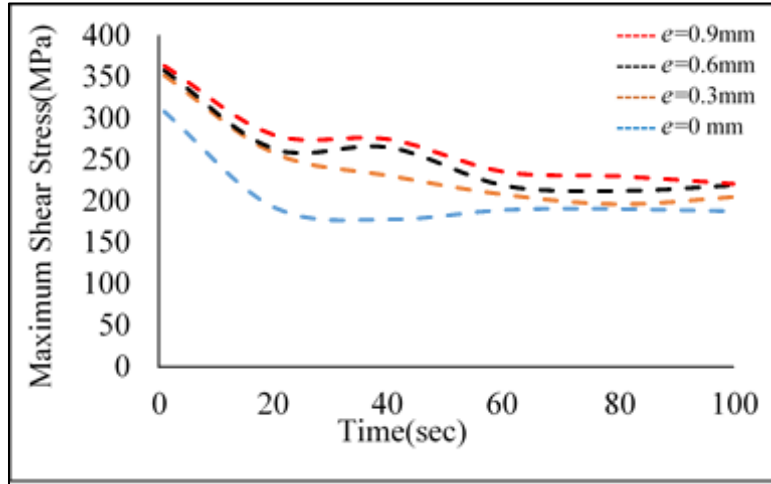


Figure 5.13 Variation of the global maximum shear stress along the process time for different eccentricities

5.3.1.2 Effect of Shoulder Diameter on the Thermal Field of FSW

Figure 5.14 depicts the evolution in the temperature distribution throughout the thermal cycle for two FSW processes with different shoulder diameters under the effect of pin eccentricity. From the figure, the finding that can be seen is generally similar to those displayed in chapter four where the thermal field is significantly affected by the alteration in the shoulder size. To clarify, the increase in the shoulder size leads to elevating in the temperature which was registered 404K at the first second as a maximum temperature in the presented plane when $R_s = 13\text{mm}$ while 537K at the same time when $R_s = 25\text{mm}$. However, in comparison to the results shown in figure 4.7 which were related to the thermal performance of the same tool with concentric pin; one can interestingly notice that the temperatures in the targeted plane have recorded lower values for the tool with eccentric pin than those recorded to the concentric one particularly for the big size of shoulder. This trend can be tangibly recognised in figure 5.18 and especially in *(b, b')* where the

reason for this can be again attributed to that the role of the eccentricity in the enhancement of heat dissipation is dominant eventhough its role in boosting of heat generation. Obvious, the effect of eccentricity in the heat transfer process increases along with the increase in the shoulder size.

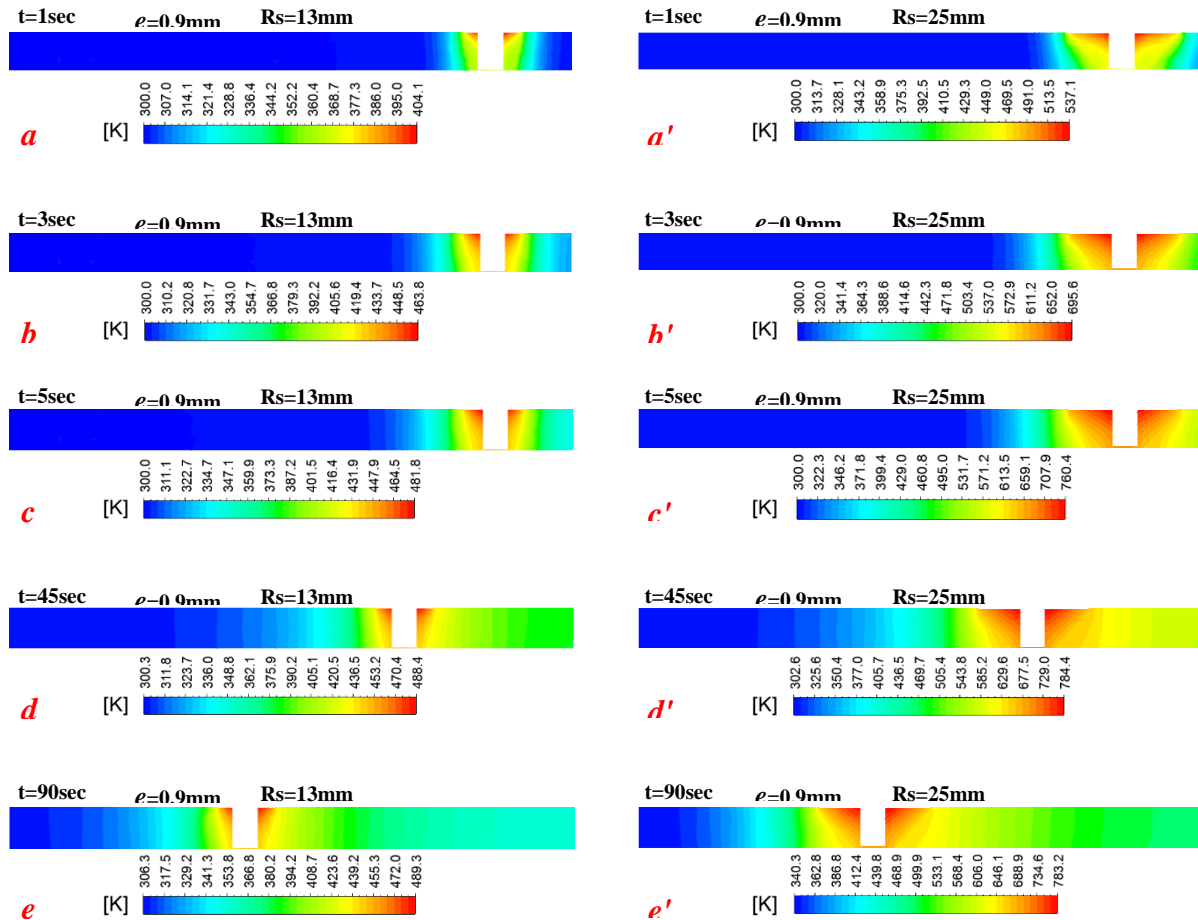


Figure 5.14 temperature distribution for the vertical plane at different time steps calculated for shoulder diameters 26mm and 50mm in the existence of eccentricity

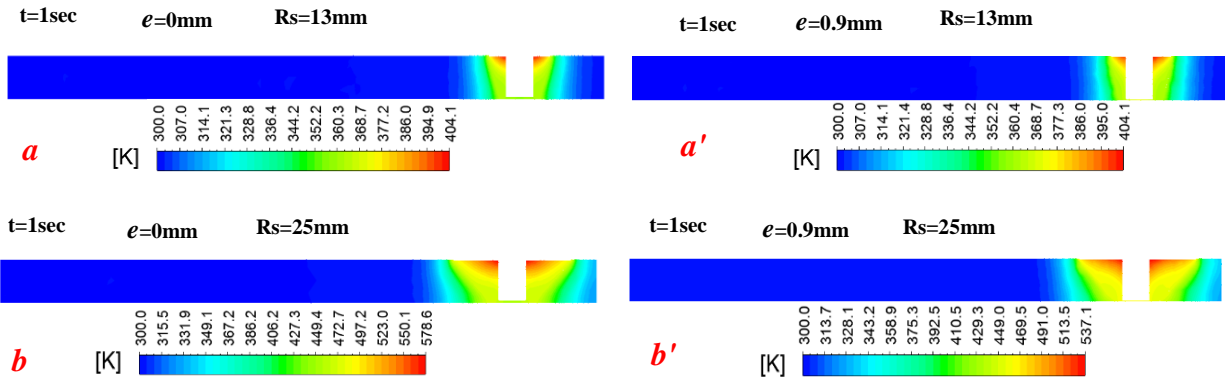


Figure 5.15 Comparison between the temperature distribution when welding with pin eccentricity and with out and for varied shoulder sizes

For the same welding conditions, figure 5.16(a,b,c,d) presents the spatial distribution of temperature at the same moment for different shoulder size. To confirm what was above mentioned, it is worth noticing the behaviour of the line of 400K which expands with the growth in shoulder size. Additionally, by comparing the information in this graph with those depicted in figure 4.8, the instantaneous measured temperature boosts the significant role of the eccentricity in the heat dissipation where the instantaneous temperature profiles in the case of eccentric pin have mostly scored less values against those achieved for the concentric pin. However, it was oddly found that the temperature degrees for $R_s = 13\text{mm}$ with pin eccentricity are slightly higher than those for $R_s = 13\text{mm}$ without pin eccentricity.

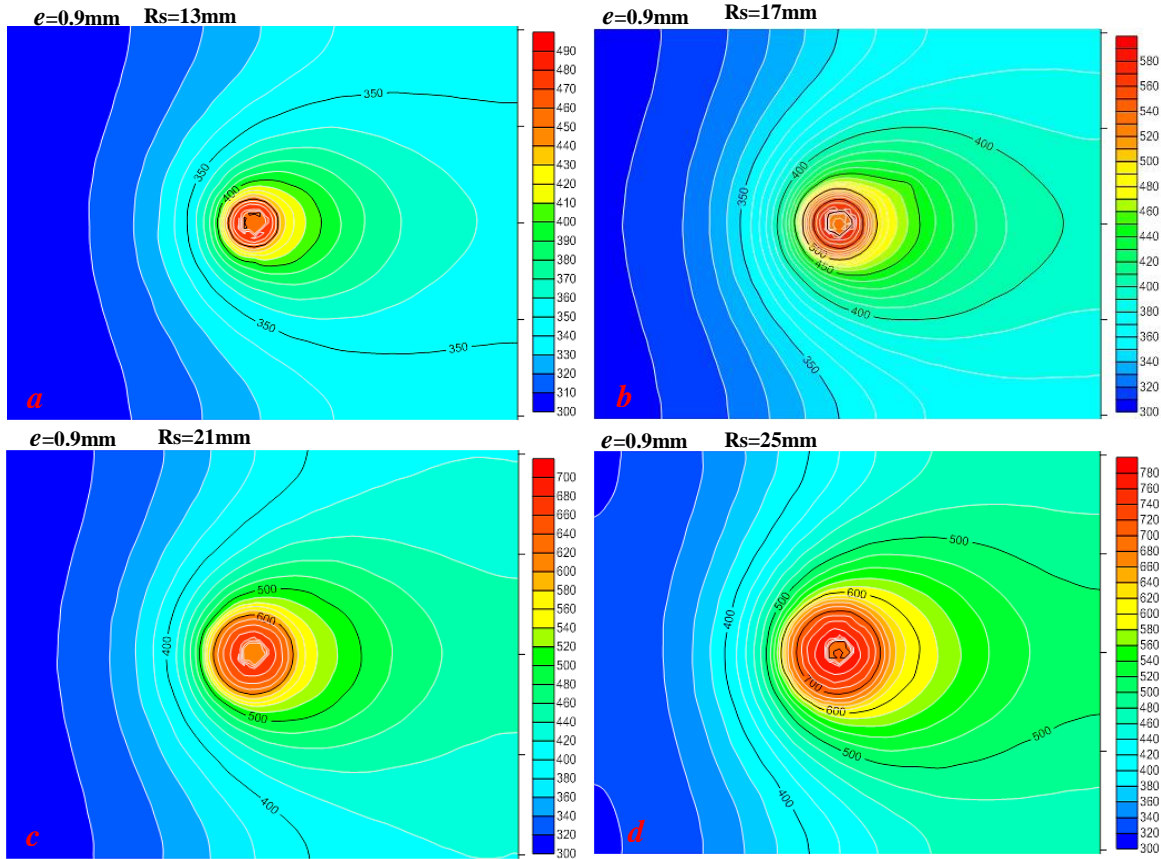


Figure 5.16 static temperature contours for different shoulder diameters $a=26\text{mm}$, $b=34\text{mm}$, $c=42\text{mm}$, $d=50\text{mm}$ under the effect of eccentricity

At the same nominated plane in chapter four, Figure 5.17 displays a comparison between the maximum global temperature that were recorded for different shoulder sizes with pin eccentricity and without. Although, the change in the temperature along with varied shoulder diameters keeps the same trend for both cases a difference can be noticed between the temperature values particularly at the high shoulder sizes. The amount of this difference rises according to the increase of the shoulder size where it was 26K when $R_s = 21\text{mm}$ and 60K for $R_s = 25\text{mm}$. That can be understood in terms of considering the change in the metal viscosity where the viscosity is likely to be decreased corresponding to the temperature raise which improve the heat dissipation particularly with the aid of the eccentricity. Once again for $R_s = 13\text{mm}$ with the eccentricity, the temperature was oddly and slightly above than that for $R_s = 13\text{mm}$ without the eccentricity where the role of the eccentricity in heat generation becomes relatively higher as the material viscosity

still not highly affected by the heat supplied from the shoulder which eliminate the dissipated heat amount. As shown in figure 5.18 and according to the above discussed thermal trend, the model has recorded the same behaviour for the material flow field along with the change in the shoulder size with that depicted in chapter four in the case of concentric pin. In existence of the eccentricity, the maximum velocity increased from 0.93 m/s to 1.73m/s when shoulder size increased from $R_s = 13\text{mm}$ to $R_s = 25\text{mm}$, however; a drop in the velocity values has been detected compared to those recorded when the tool has no eccentricity which approve the role of eccentricity the heat dissipation process.

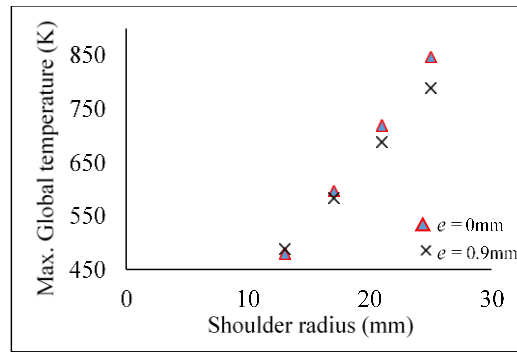


Figure 5.17 Global peak temperature for different shoulder radiuses with eccentricity and without

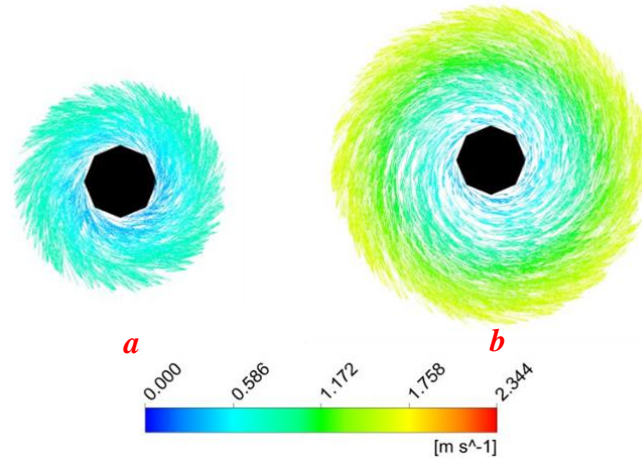


Figure 5.18 Flow velocity field for different shoulder diameters in existence of the eccentricity $a=26\text{mm}$, $b=50\text{mm}$

For further investigating, the local peak temperatures were monitored at the same proposed locations in chapter four. For both cases $e=0$ and $e=0.9$, figure 5.19(a,b) exhibits a comparison between the general behaviour of the local temperature which are agreed where the maximum local temperatures increase according to the increase in the shoulder size. However, another comparison has been critically drawn to visualise the trend of the local peak temperature at each position as the eccentricity and the shoulder size are changed. As shown in figure 5.20 (a,b,c,d), the difference in the local temperature can be seen and its behaviour is as similar as observed for the global peak temperature which was previously mentioned and justified.

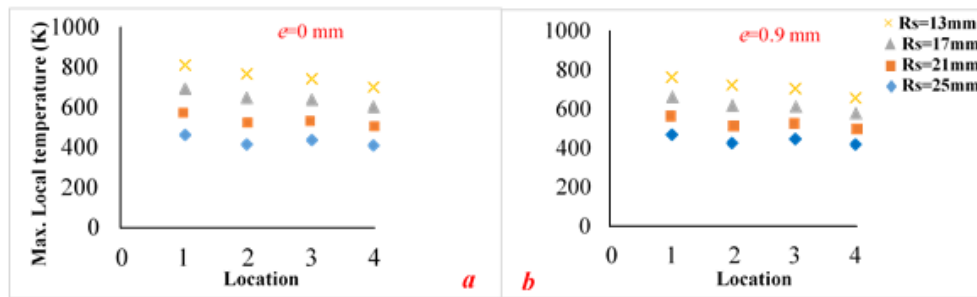


Figure 5.19 Local peak temperature for different shoulder radii with eccentricity and without at different location

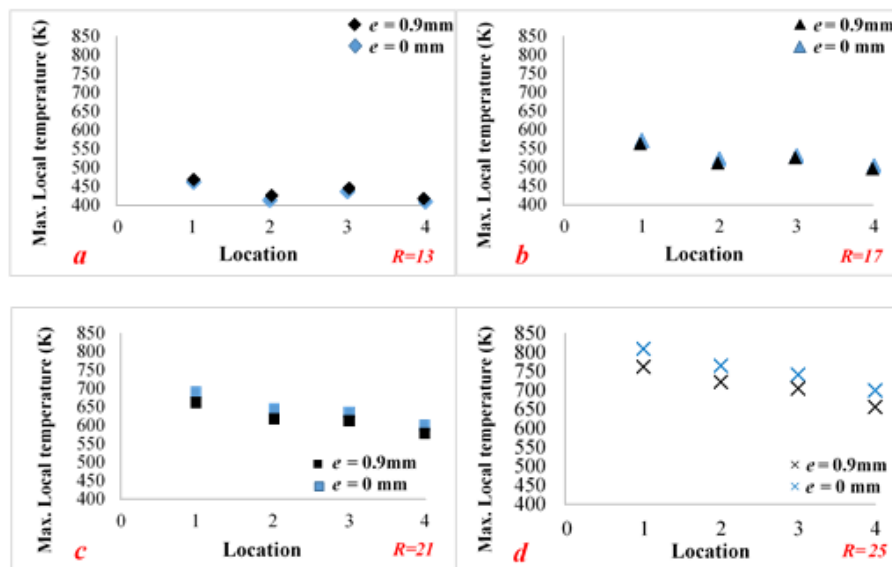


Figure 5.20 A comparison between the local peak temperatures for different shoulder radii with eccentricity and without at different locations

From figure 5.21 (a,b) and in terms of the variation in shoulder size, the values of maximum shear stress at the tool surface for $e=0$ mm and $e=0.9$ mm still behave in the same way. Nevertheless, the findings in the figure indicate that the values of maximum shear stress have witnessed a kind of increase alongside with the increase in the eccentricity for all proposed shoulder sizes. That can be easily estimated for the bigger shoulder sizes as the viscosity is considerably affected according to the temperature changing. For $R_s=13$ mm, it is well obvious that the stress values (Red dashed lines) were marginally affected which can be justified by the small changing in the temperature as shown in figures 5.17, 5.19 and 5.20a.

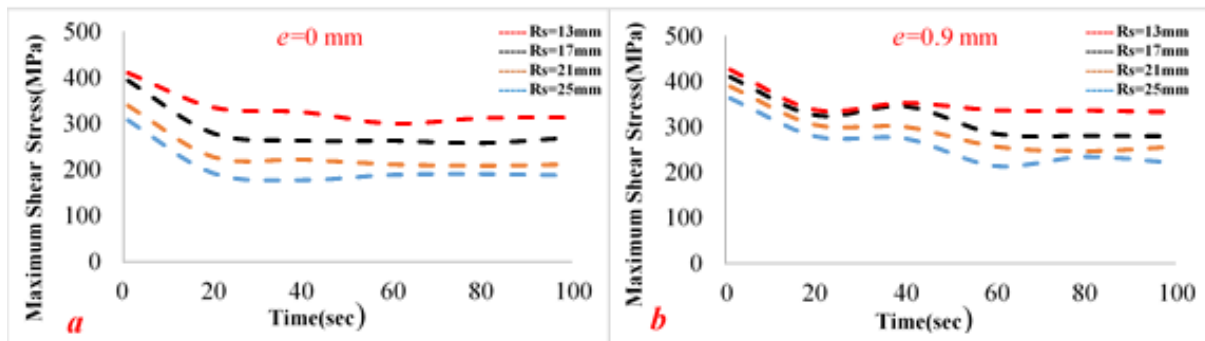


Figure 5.21 a comparison between the shear stress values when using different shoulders and pin eccentricities

5.3.1.3 Effect of pin diameter on the Thermal Field of FSW

For $R_p=3$ mm and $R_p=6$ mm, a comparison between the time dependent temperature profile is depicted in figure 5.22. It can be generally seen that the evolution in the temperature distribution has different rates which can be observed in the hottest areas for both cases. At $t=1$ sec, the temperature values have been higher when $R_p=3$ mm than those for $R_p=6$ mm and the heating rate was greater as well which scored 251.3K/sec and 237.1 K/sec, respectively. Though, figure 5.23 revealed the effect of the eccentricity where the temperature goes down when the values of e moving from 0mm to 0.9mm. for the same pin size considered.

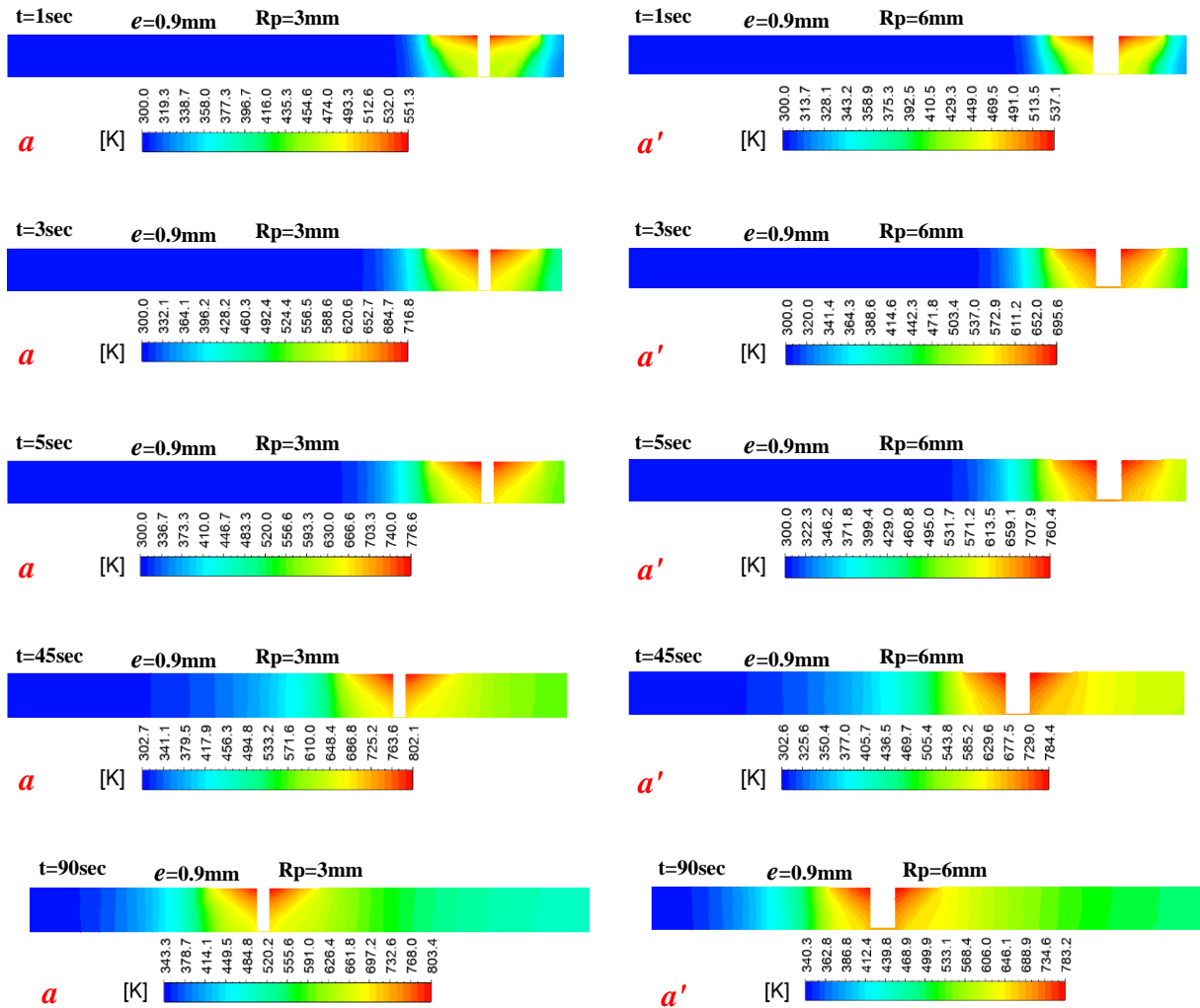


Figure 5.22 temperature distribution for the weld centre lined vertical plane at different time steps calculated for pin diameters 6mm and 12mm in the existence of eccentricity

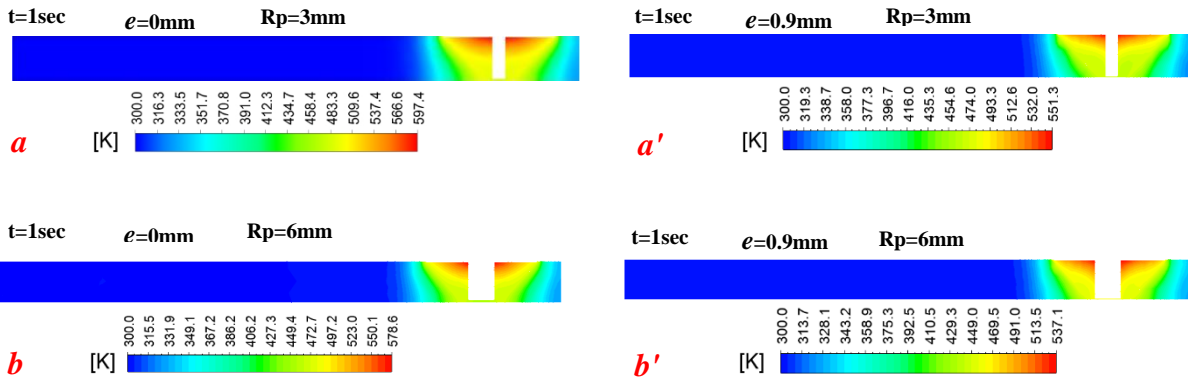


Figure 5.23 Comparison between the temperature distribution when welding with pin eccentricity and without and for varied pin sizes

Figure 5.24(a,b,c,d), depicts the qualitative variation in the temperature distribution for different pin dimensions in existence of the eccentricity. For effective comparison purpose, the temperature scale in the contours has been kept similar in terms of intervals and the coloured areas. In view of that and by tracking the line of 500K, it can be seen that the temperatures descend down when the pin radius increases from 3mm to 6mm and then tend to go up conversely as the pin radius increases from 6mm to 12mm. For more supporting, the results shown in figure 5.25 which corresponding the maximum global temperatures at $e=0.9\text{mm}$ and different pin sizes amply confirm those observations which would be reasoned to the relative and mutual change in the roles of shoulder and pin in the frictional heat generation as clarified in the previous chapter. Additionally, figure 5.25 indicates that the effect of the pin in heat generation has been earlier sensed for $e=0.9\text{mm}$ than for $e=0\text{mm}$ which possibly understood by considering the eccentricity. From another point of view, in comparison to the concentric pin with 3mm, the model couldn't predict any mushy zone for the same eccentric pin as the temperature has not exceeded the solidus temperature of the base metal. That decrease in the temperatures has happened for all values of the pin size as depicted in figure 5.25 because of the heat transfer is enhanced due to the eccentricity. Locally, the comparison that has been held in figure 5.28 indicates a sort of change in the general behaviour of the local peak temperatures at all considered points for the all pin sizes when e increases from 0mm to 0.9mm. This can be more manifest in figure 5.27(a,b,c,d) in which the difference between the local values of temperature can be explained by the balancing between the

change in heat generation rate and heat dissipation rate due to the variation in the pin size and pin eccentricity.

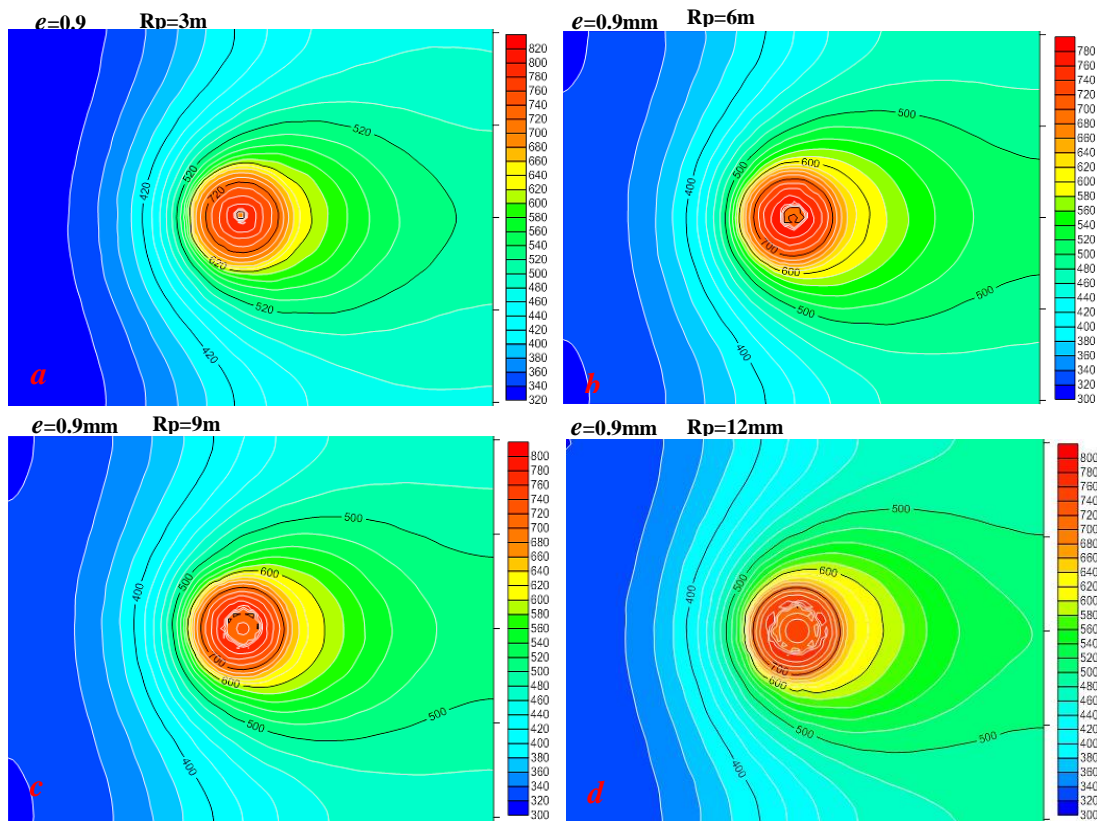


Figure 5.24 static temperature contours for different pin diameters $a=6\text{mm}$, $b=12\text{mm}$, $c=18\text{mm}$, $d=24\text{mm}$ in the existence of eccentricity

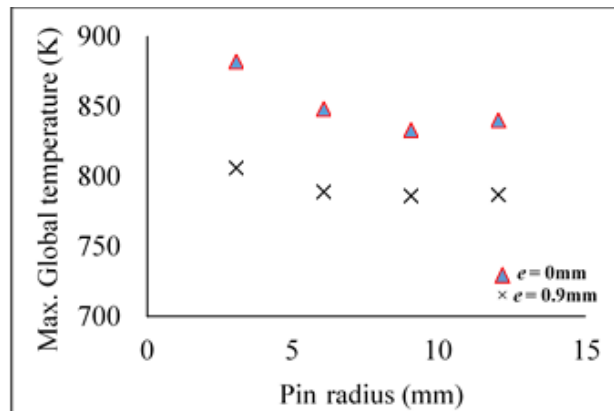


Figure 5.25 Global peak temperature for different pin radiuses with eccentricity and without

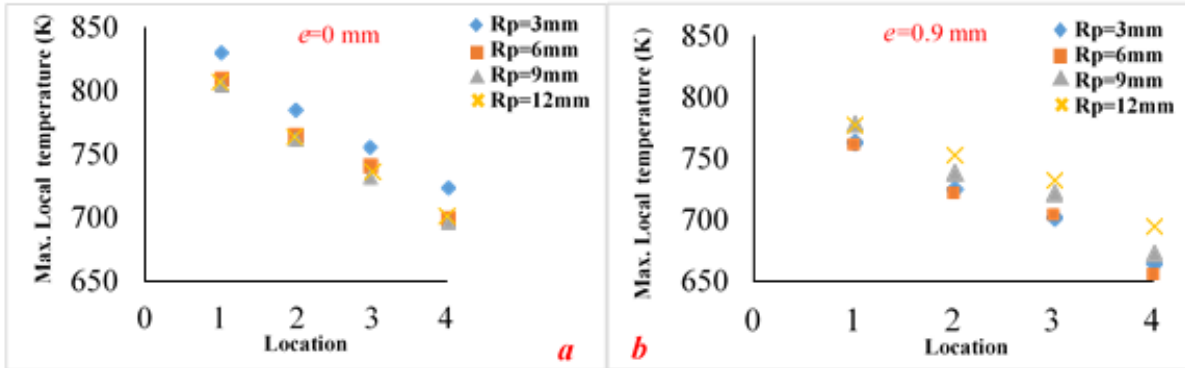


Figure 5.26 Local peak temperature for different pin radii with eccentricity and without at different locations

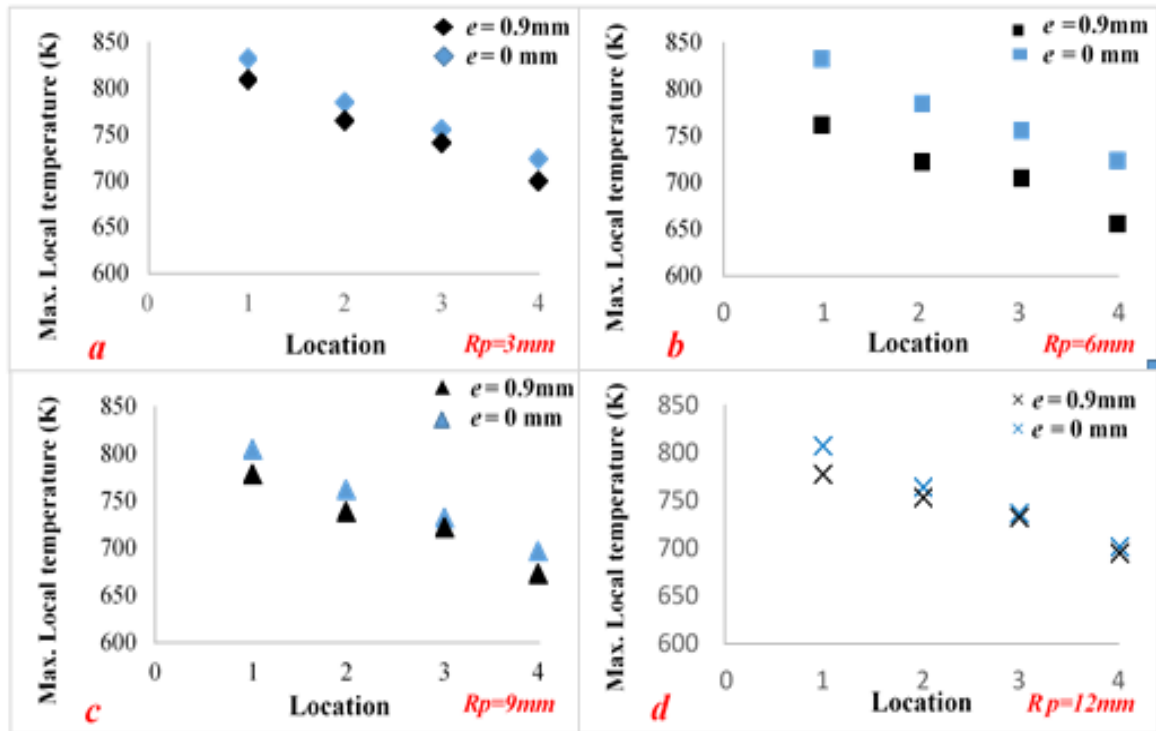


Figure 5.27 A comparison between the local peak temperatures for different pin radii with eccentricity and without at different locations

Regarding the behaviour of the material flow field, which is strongly related to the thermal changes, no significant changes have been generally noticed compared to the concentric pin as the velocity witnessed an increase against the increase in the pin size. As shown in figure 5.28, the field size became bigger when the pin size increased and 0.25m/s was the maximum velocity registered under the pin when $R_p = 3\text{mm}$ while it was 0.83m/s when $R_p = 12\text{mm}$. Again, the increase in the viscosity due to the drop in the temperature did not prevent the velocity from the increase as the linear velocity is increasing corresponding to the increase in the pin size.

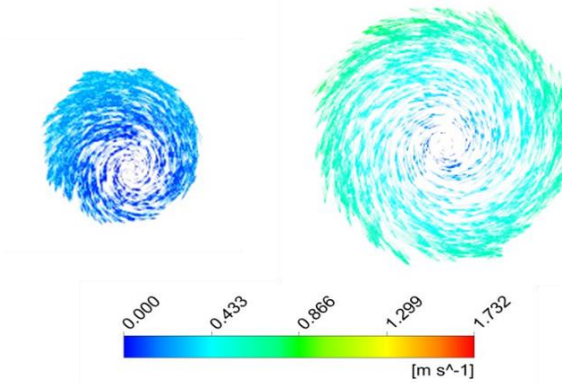


Figure 5.28 Flow velocity field for different pin diameters at underneath the pin in existence of the eccentricity

According to the decrease in the temperature values when using the eccentricity as above presented in figure 5.25, it can be clearly seen in figure 5.29 an increase in the maximum shear stress values for all pin size under consideration. For example, 441.6MPa was recorded for $R_p=12\text{mm}$ and $e=0.9\text{mm}$ at $t=1\text{sec}$ while 327 MPa was the value of the shear stress when $R_p=12\text{mm}$ and $e=0\text{mm}$ at $t=1\text{sec}$.

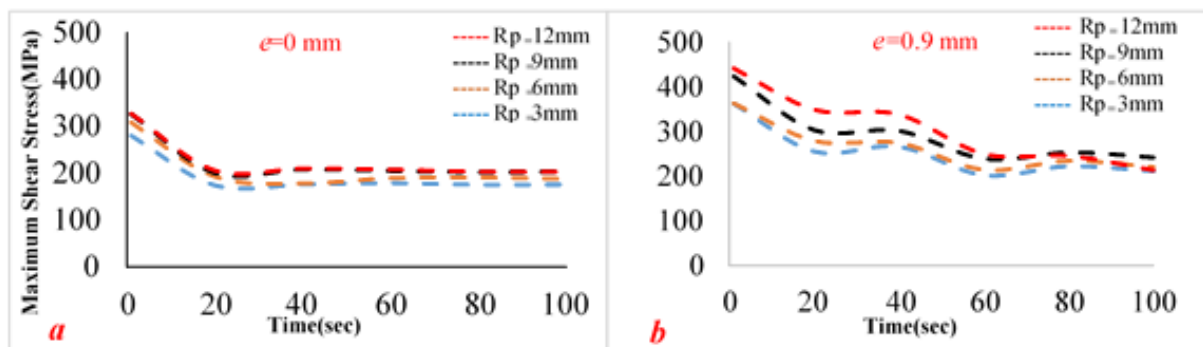


Figure 5.29 a comparison between the shear stress values when using different pin sizes and pin eccentricities

5.3.1.4 The effect of pin Height on the Thermal Field of FSW

The results provided in chapter four which is related to the concentric pin revealed that the transient evolution in the temperature distribution was faintly impacted when the pin height grew from 9mm to 12mm where a slight increase in the temperature has taken place. Although, figure 5.30 presents a similar behaviour for the transient evolution of the temperature distribution when $e=0.9\text{mm}$ the temperature is conversely going down eventhough the additional amount of heat accompanying to growing of the pin height. That can be discussed by considering the pin role in stirring of the welded material which is likely to be increased as the pin height increases and that leads to boost the heat dissipation. Furthermore, figure 5.31 provides a Comparison between the temperature distribution when welding with pin eccentricity and without and for varied pin heights at the same moment.

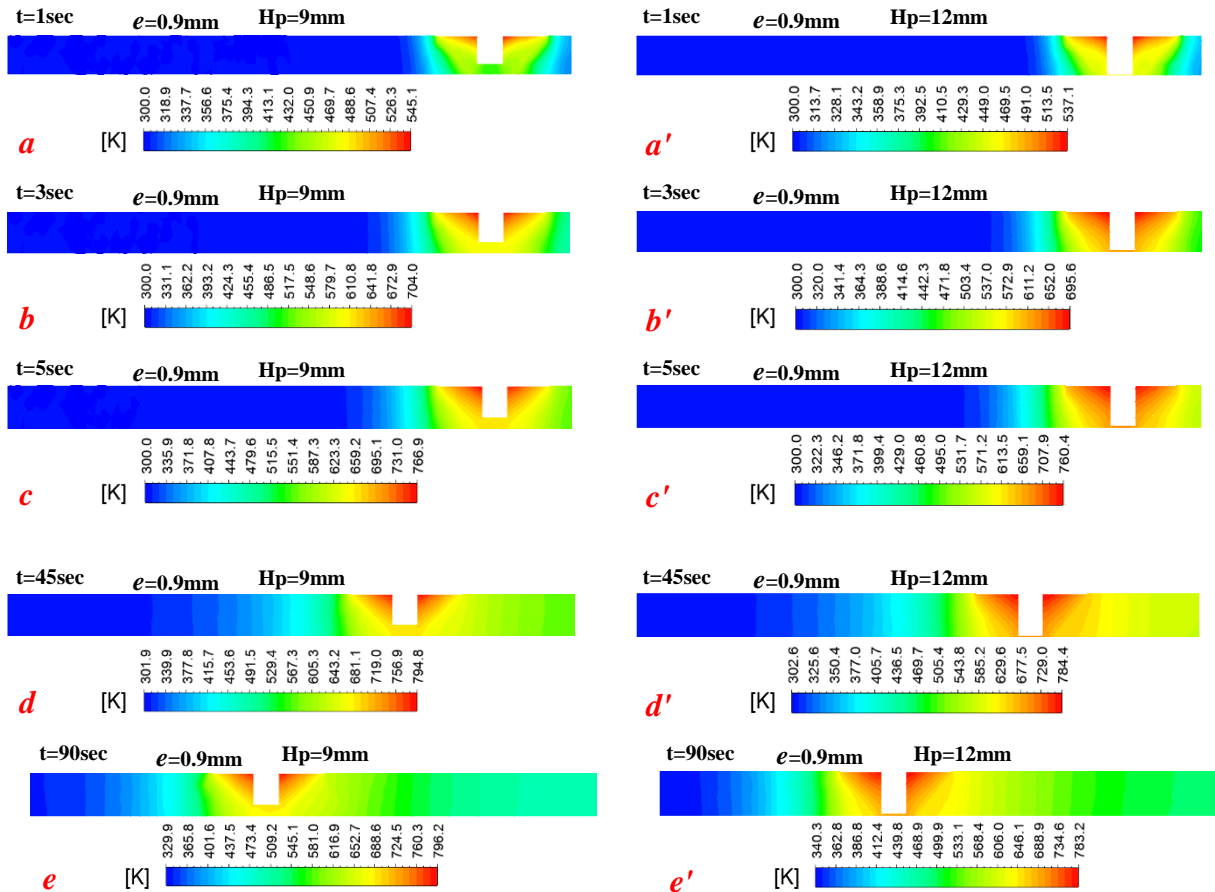


Figure 5.30 Temperature distribution for the weld centre lined vertical plane at different time steps calculated for pin heights of 9mm and 12mm in the existence of eccentricity

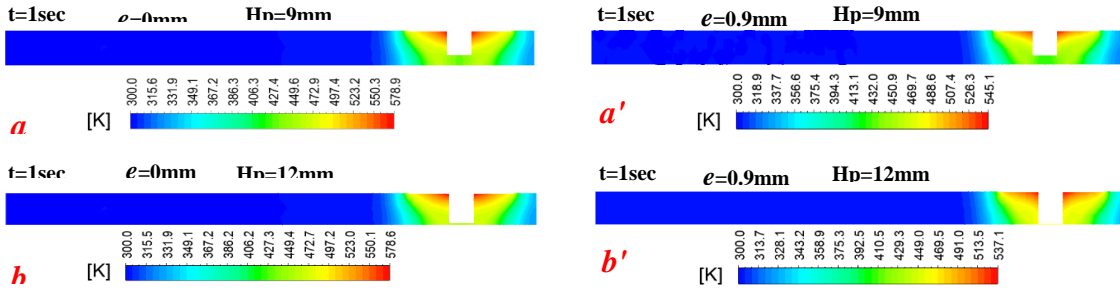


Figure 5.31 Comparison between the temperature distribution when welding with pin eccentricity and without and for varied pin heights

For further investigation and as depicted in figure 5.32(a,b,c,d), the static temperature contours were taken for all cases of pin heights under consideration at the same plane and time. Insignificant variation was observed on the contours along with the change in the pin height. That means the temperature was marginally affected within the range of variation in the pin height even in the existence of the pin eccentricity which is fairly agreed with the above presented results for the selected moments from the welding process. Accordingly, the flow field has witnessed insignificant change as the material viscosity has changed from $3.08 \times 10^6 \text{ Kg.m}^{-1}.\text{s}^{-1}$ to $3.19 \times 10^6 \text{ Kg.m}^{-1}.\text{s}^{-1}$ when the pin height increased from 9mm to 12mm.

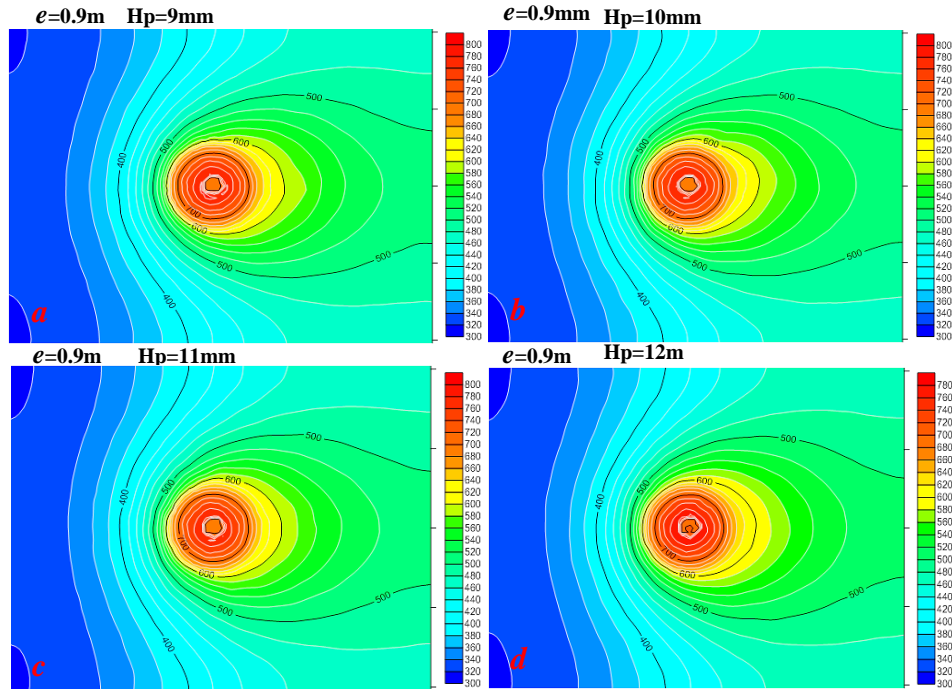


Figure 5.32 Static temperature contours for different pin heights a=9mm, b=10mm, c=11mm, d=12mm in the existence of eccentricity

Figure 5.33 shows how the global peak temperatures when $e=0.9\text{mm}$ for varied pin heights is interestingly behaving in a converse manner to that recorded when $e=0\text{mm}$. Beside the prevailing decrease in the temperatures accompanying to the increase in the eccentricity, it is worthy noticing the gradual growth in the difference between the values of temperature in both cases where it was 44K for $H_p=9\text{mm}$ and 59K was recorded when $H_p=12\text{mm}$. The material viscosity has affected by the eccentricity for the varied pin heights compared to its values that recorded for the concentric pin where it increased by $2.6 \times 10^6 \text{ Kg.m}^{-1}.\text{s}^{-1}$ when the pin height was 12mm .

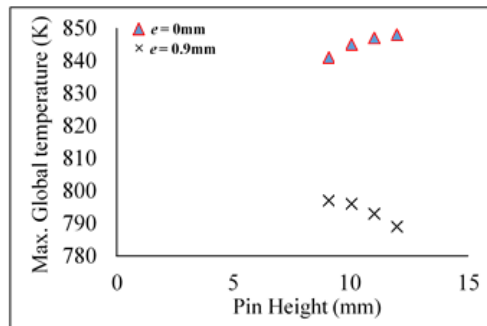


Figure 5.33 Global peak temperature for different pin heights with eccentricity and without

Figure 5.34, depicts the trend of the maximum local temperature registered in the existence of pin eccentricity for different pin heights against those attained when welding without eccentricity for the same pin heights. As well as the global level of temperature, the local maximum temperature is not significantly affected by the change in the pin height. However, the local effect of the eccentricity still obvious as it can be clearly seen in figure 5.35(a,b,c,d). For instance, the temperatures achieved 761.7K when $e=0.9\text{mm}$ and $H_p=12\text{mm}$ at point No.1 while it was 809K for $e=0\text{mm}$ and $H_p=12\text{mm}$ at the same point.

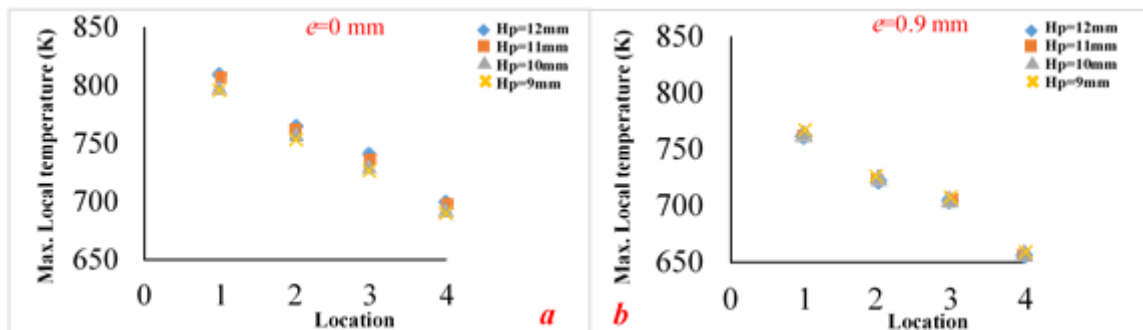


Figure 5.34 Local peak temperature for different pin heights with and without eccentricity at different locations

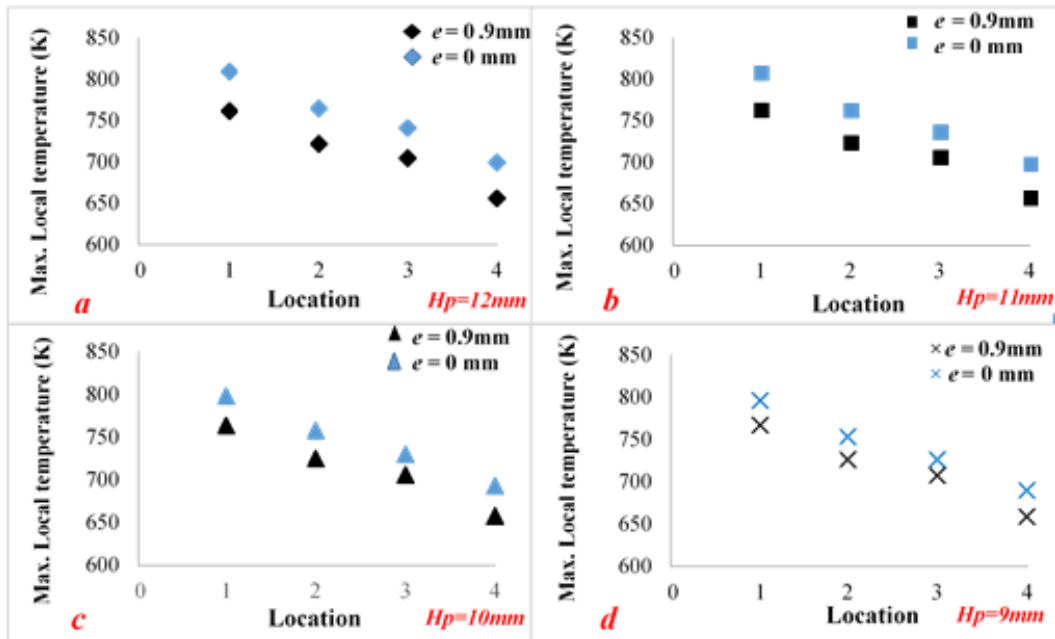


Figure 5.35 A comparison between the local peak temperatures for different pin heights with and without eccentricity at different locations

As shown in figure 5.36 the values of maximum shear stress at the tool surface are expectedly raising up which is mainly due to the effect of eccentricity on the material temperature around the tool. It's also worth seeing that the shear stress trend has mostly unchanged against the change in the pin height which boost the dependency of its values on the material temperature. This means that the unimportant change in the temperature corresponding to the variation in pin height which is previously discussed is not enough to produce a great effect on the stress values.

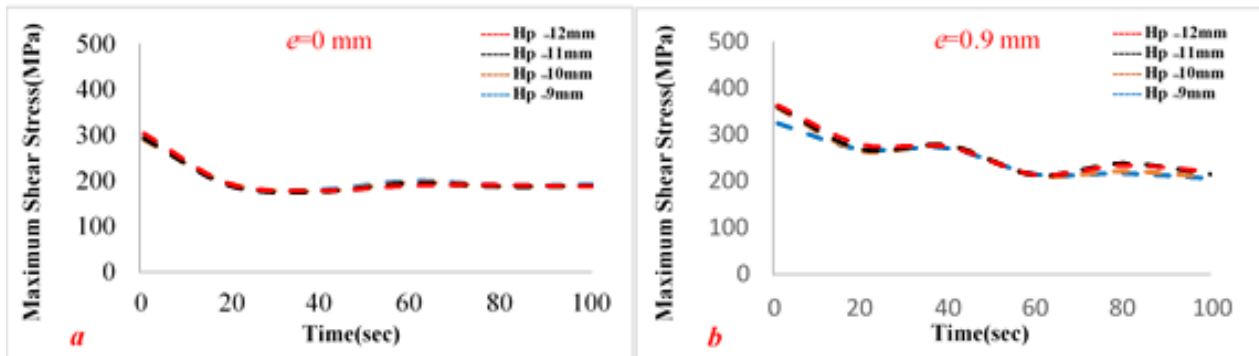


Figure 5.36 A comparison between the shear stress values when using different pin heights and pin eccentricities

5.3.1.5 The effect of the workpiece thickness on the Thermal Field of FSW

On figure 5.37 there appear two set of contours related to the time dependent variation in the temperature distribution through FS welded workpieces with different thickness. It can be visually seen at the onset of the thermal cycle and afterword that the temperature recorded for both cases differ with a rising value which tends to be stabilised after a while. This propensity was similarly noted for welding with the same tool without eccentricity which was presented and discussed in chapter four where the rate of heat dissipation might be increased due to the increase in the plate thickness. Eventhough, the effect of the eccentricity can be vividly specified in figure 5.39 where the level of temperature has gradually dropped down for these tools with eccentricity compared the ones without. For example, 578.6K was the maximum achievable degree when thick=12.7mm and e=0mm while 537.1K when e=0.9mm for the same plate thickness.

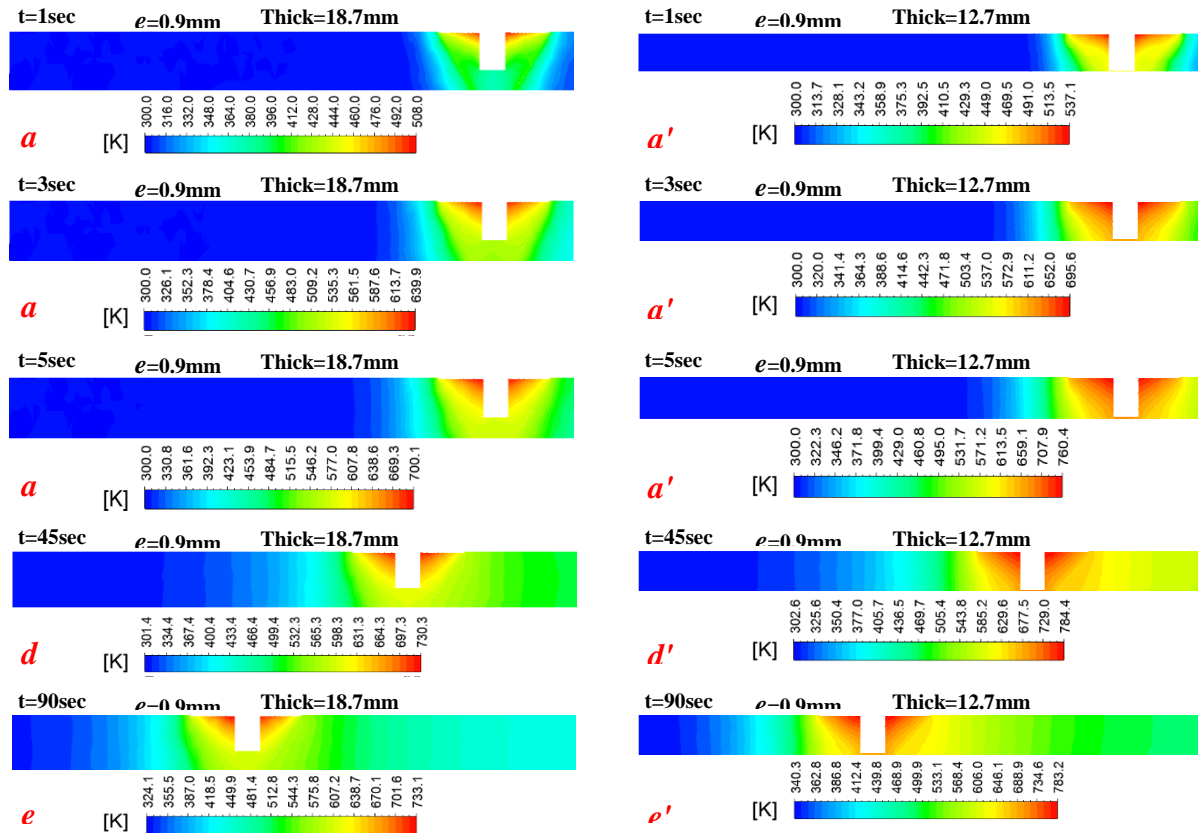


Figure 5.37 temperature distribution for the vertical plane at different time steps calculated for workpiece thickness 18.7mm and 12.7mm in the existence of eccentricity

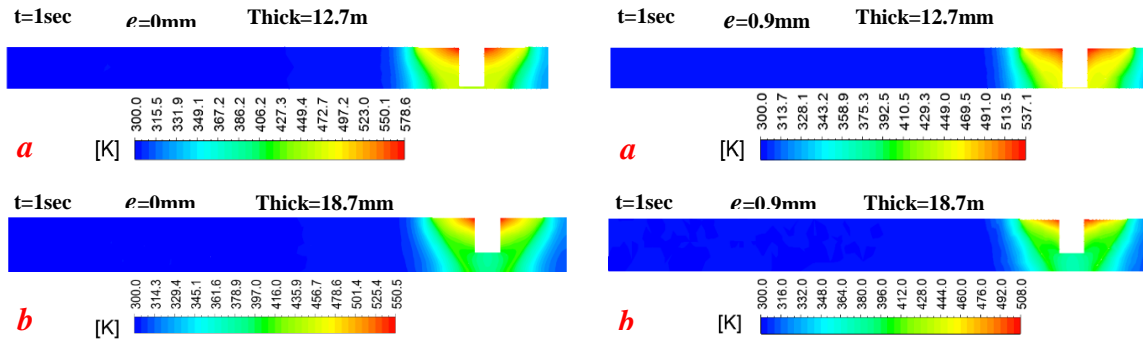


Figure 5.38 Comparison between the temperature distribution when welding with and without pin eccentricity and for varied workpiece thicknesses

Likewise, in existence of the eccentricity the material flow field has shown similar trend versus the variation of the workpiece thickness compared to the concentric pin in chapter four. Additionally, the effect of the pin eccentricity caused a drop in the maximum velocity by 1.1m/s because of the decrease in the material softness eventhough, the increase in the volume of deformation zone due to the eccentricity as depicted in figure 5.39. At the same time, the spatial evolution of temperature within the weldment for all workpiece thicknesses under consideration when $e=0.9\text{mm}$ is given in figure 5.40 (a,b,c,d) where an additional investigation can be achieved. The shrinkage in line 500K can give a clear picture regarding the reduction of temperature corresponding to the increase in the workpiece thickness. Likewise, it can be seen in figures 5.41 and 5.42 that the global and local peak temperatures are witnessing a proportional dropping versus the growing in plate thickness. However, it should be also pointed out from figures 5.41 and 5.43 (a,b,c,d) that these are not the same values as that obtained when there was no eccentricity where the difference remains more or less constant for all thicknesses.

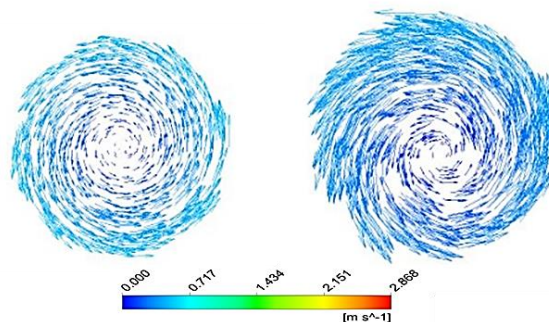


Figure 5.39 Flow velocity field for different workpiece thickness at underneath the pin in existence of eccentricity

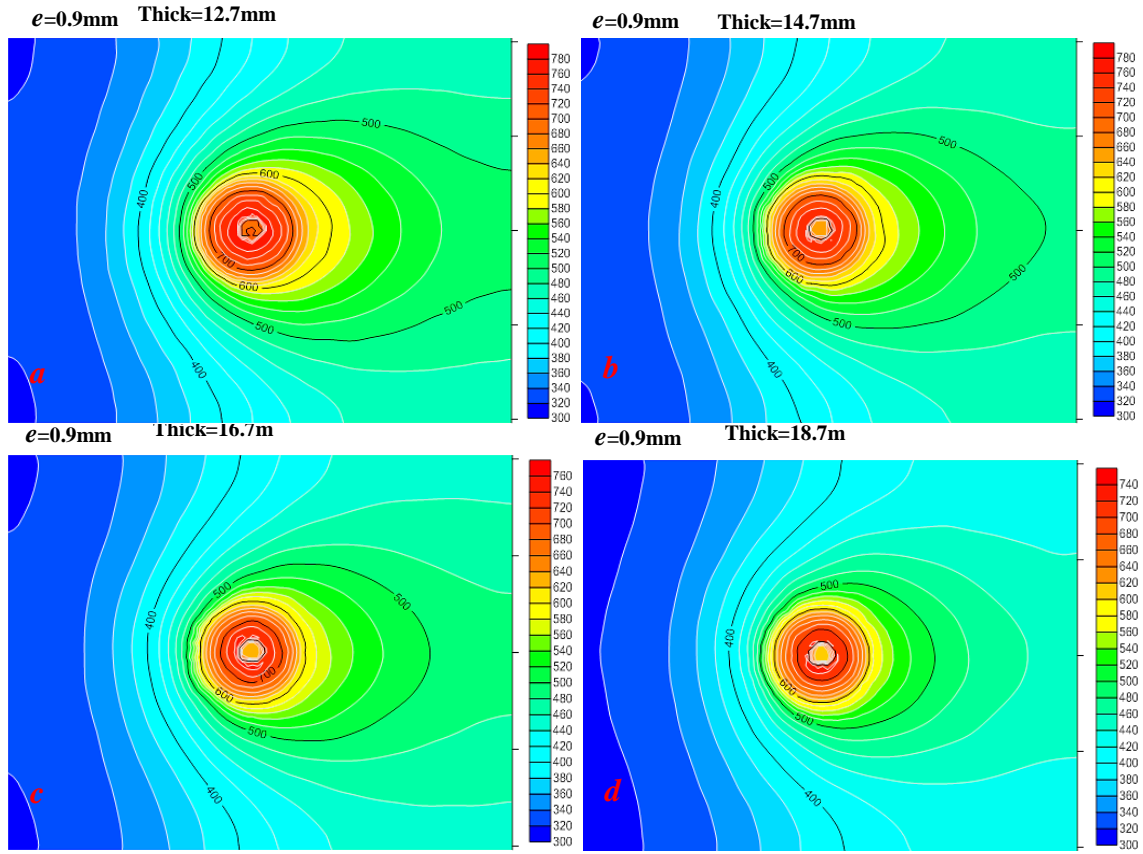


Figure 5.40 Static temperature contours for different workpiece thickness $a=12.7\text{mm}$, $b=14.7\text{mm}$, $c=16.7\text{mm}$, $d=18.7\text{mm}$ in the existence of eccentricity

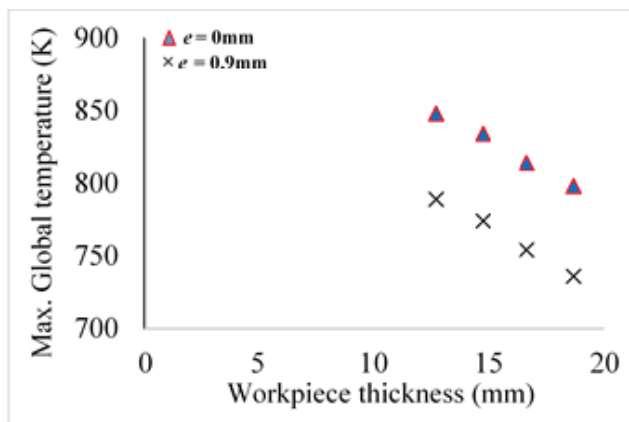


Figure 5.41 Global peak temperature for different workpiece thickness with and without eccentricity

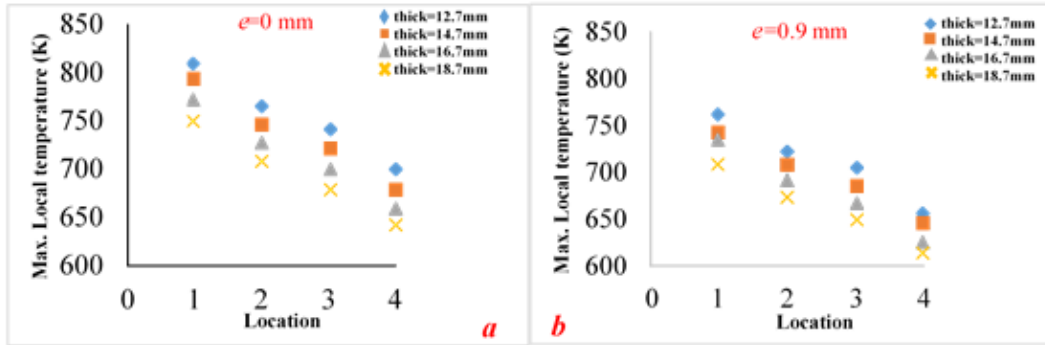


Figure 5.42 Local peak temperature for different workpiece thicknesses with and without eccentricity at different locations

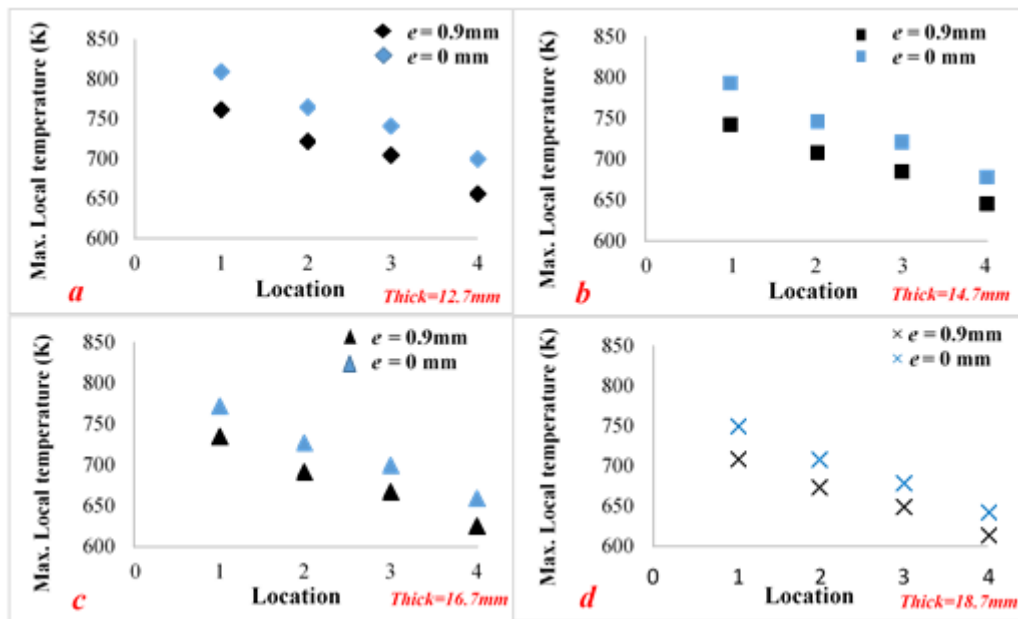


Figure 5.43 A comparison between the local peak temperatures for different workpiece thicknesses with and without eccentricity at different locations

As it can be seen in figure 5.44 that the values of maximum shear stress on the tool surface have increased when the welded material thickness grew up from 12.7mm to 18.7mm. That could be debated in terms of the increase in the temperature differential between the weld zone and the surrounding base material due to the variation in the thickness which in its role enhancing the cooling rate and inducing the stresses [93]. For $e=0.9$ mm, it's worthwhile noting the obvious effect of the eccentricity which remarkably lifting the stress values.

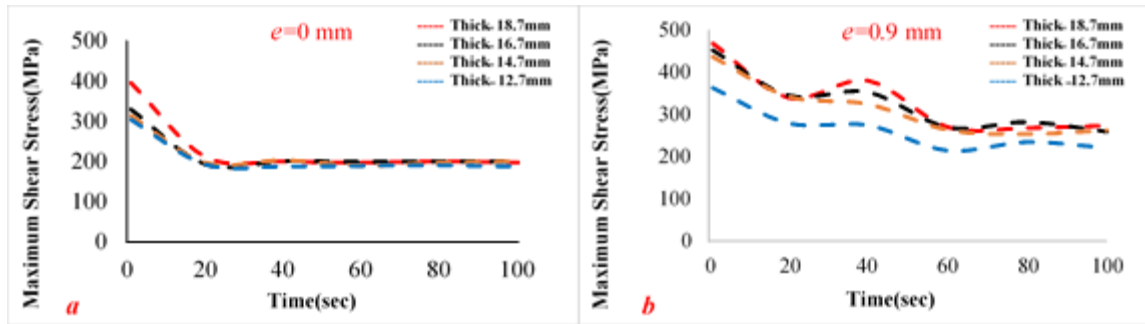


Figure 5.44 a comparison between the maximum shear stress values when using different workpiece thicknesses and pin eccentricities

5.3.2 The effect of rotational speed on the Thermal Field of FSW

The contours in figure 5.45 (a,b,c,d) represent the progress in the thermal field through the weldment due to the variation in the rotational speeds. Expectedly, the change in the field resembles that has happened for the same process when $e=0\text{mm}$ where the increase in the rotational speed is accompanied by an elevating in the temperature. However, the recorded temperature values are not the same values as that obtained when there was no eccentricity. For further investigation, as it can be seen in figure 5.46 a comparison has been transiently drawn to study the thermal field at high rotational speed when $\omega = 837\text{r.p.m}$ for $e=0\text{mm}$ and $e=0.9\text{mm}$. For effective comparison purpose, the temperature scale has been kept similar in terms of intervals, hence the temperature difference between the two thermal cycles has scored around 34K at the onset of the process while it was 52K at advanced stage. Although, the severity of the thermal cycle varies from $e=0\text{mm}$ to $e=0.9\text{mm}$ the temperature level has exceeded the material solidus temperature after $t=3\text{sec}$ in both cases. Therefore, the current used model has monitored the time dependent evolution of the liquid fraction where another meaningful comparison was beneficially drawn to evaluate the influence of the eccentricity on the liquid fraction at the same welding conditions. It can be seen in figure 5.47 that the mushy zone has formed and the liquid achieved 1 at $t=5\text{sec}$ for $e=0\text{mm}$ which is three times of that for $e=0.9\text{mm}$. Additionally, for $e=0.9\text{mm}$ the liquid fraction has not reached 1 even at advanced stage from the thermal cycle ($t=90\text{sec}$).

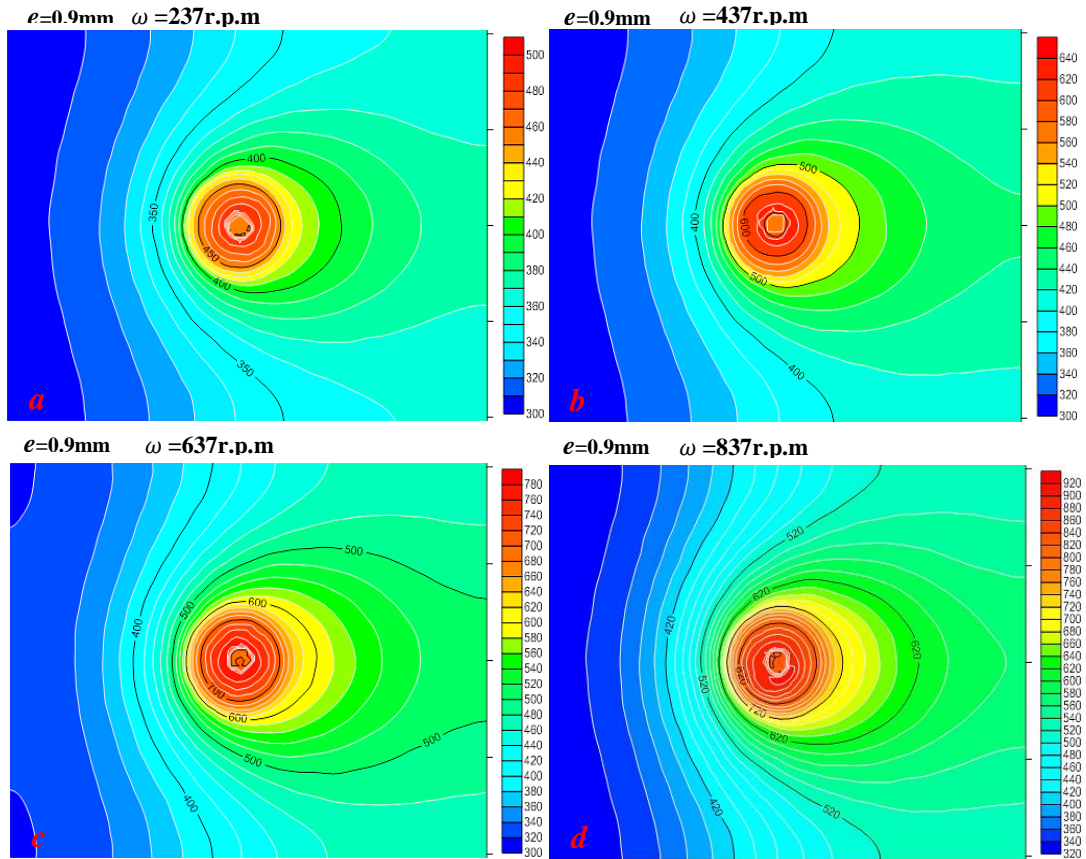


Figure 5.45 static temperature contours for different rotational speed a=237r.p.m, b=437r.p.m, c=637r.p.m, d=837r.p.m in the existence of eccentricity.

In figure 5.48, the change in the maximum temperature along with variation in the rotational speeds keeps the same trend for both cases. However, there is a difference between the temperature values and this amount of difference increases against the rising in the speed values. Hence, it increases from 15K for 237r.p.m to 51K at 837r.p.m. As mentioned before, the role of the eccentricity in heat dissipation becomes relatively higher compared with its role in heat generation as the material viscosity is affected by the additional heat acquired as there is an increase the rotational speed. Although, the behaviour of the flow field is generally as similar as that for the concentric pin against the change in the rotational speed the material maximum velocity decreased particularly at 837r.p.m where the viscosity increased such that under the pin by $0.3 \times 10^3 \text{ Kg.m}^{-1}.\text{s}^{-1}$ due to the eccentricity influence on the heat dissipation. In the same way figures 5.49 and 5.50 reveal that the local peak temperature at several locations is as identical as the global temperature behaves.

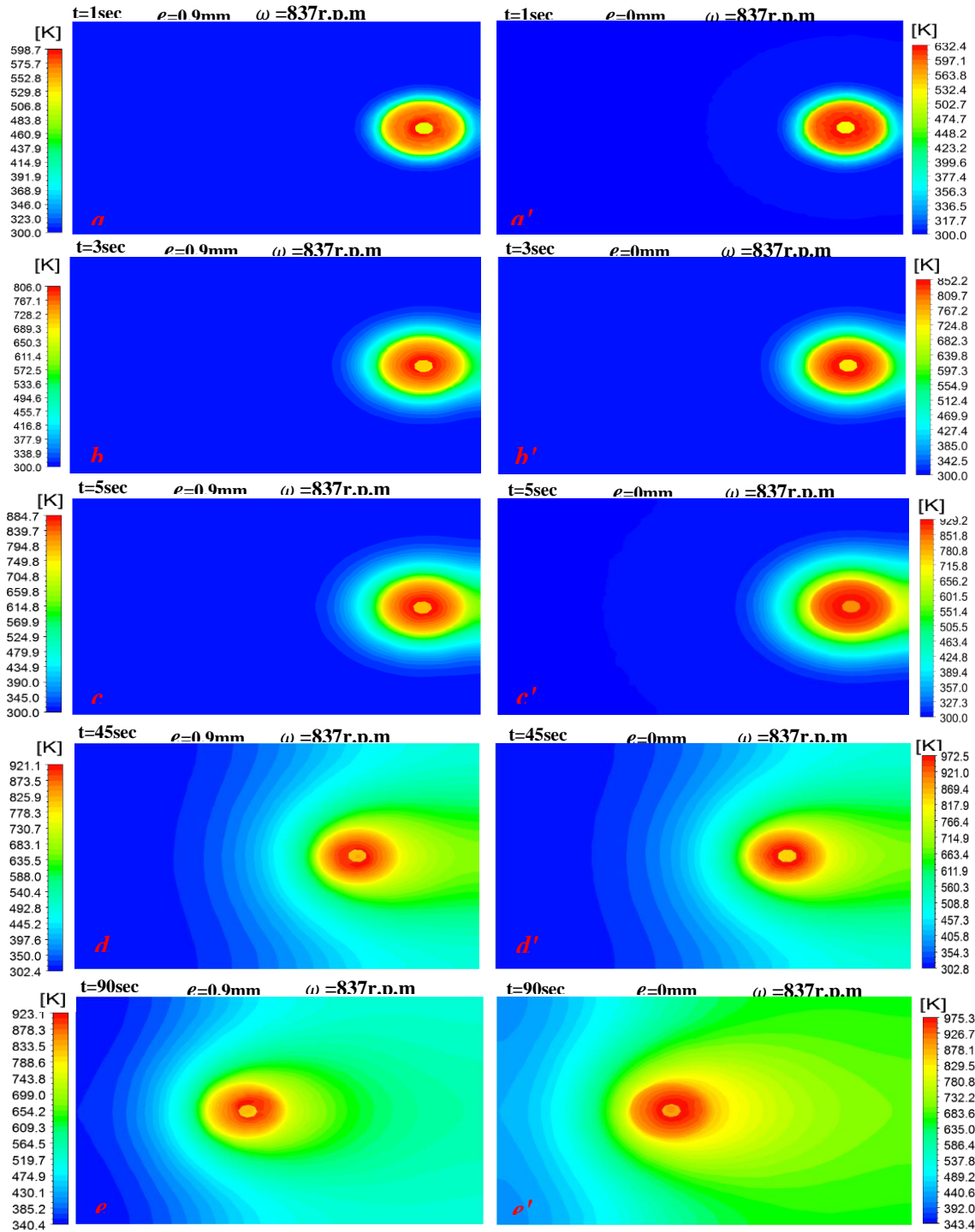


Figure 5.46 Comparison between the temperature distribution when welding with and without pin eccentricity at high rotational speed.

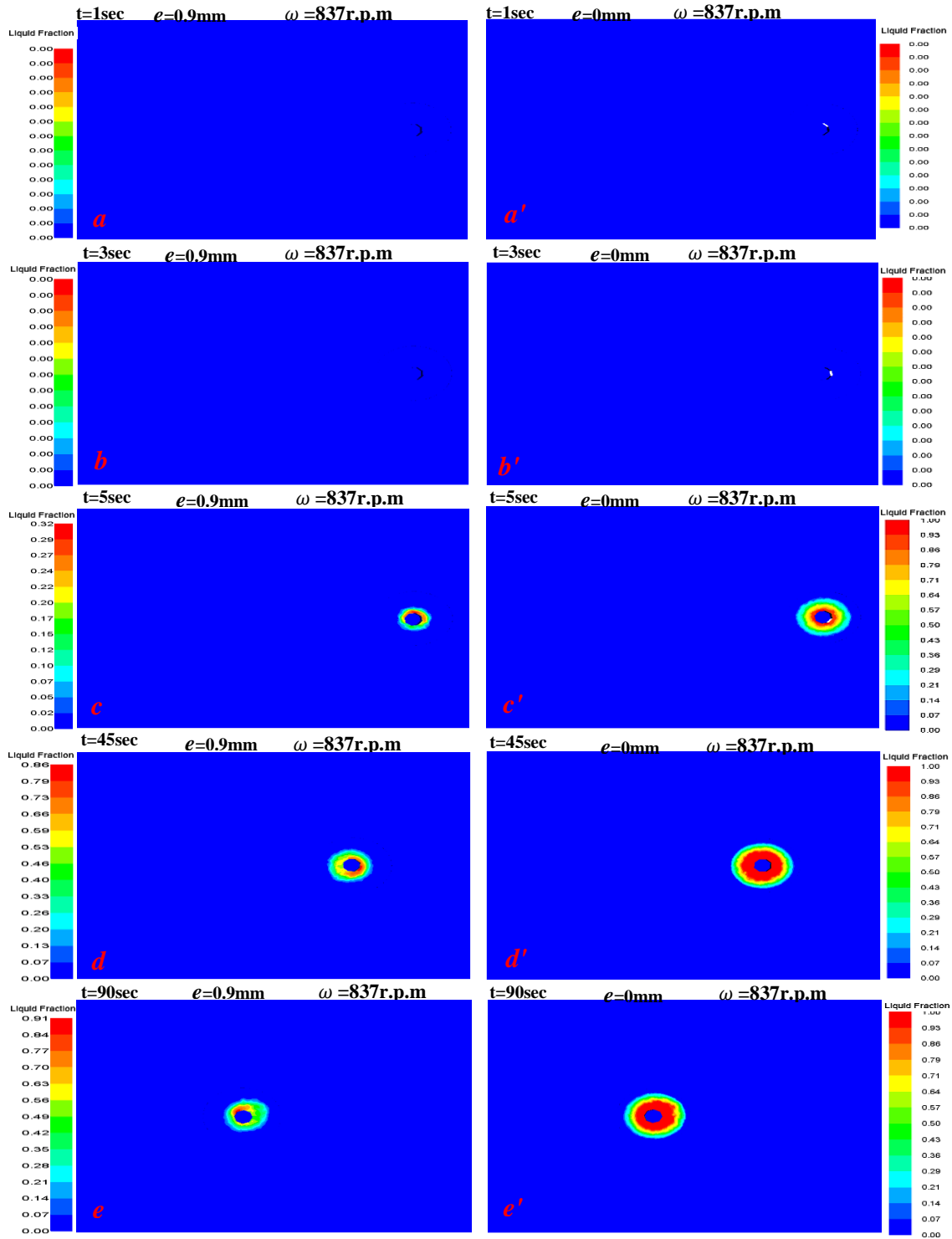


Figure 5.47 Comparison between the evolution in the liquid fraction when welding with and without pin eccentricity at high rotational speed.

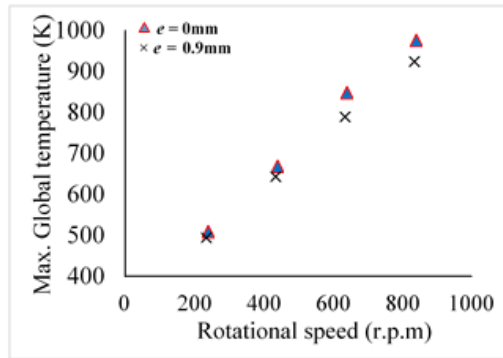


Figure 5.48 Global peak temperature for different rotational speeds with and without eccentricity

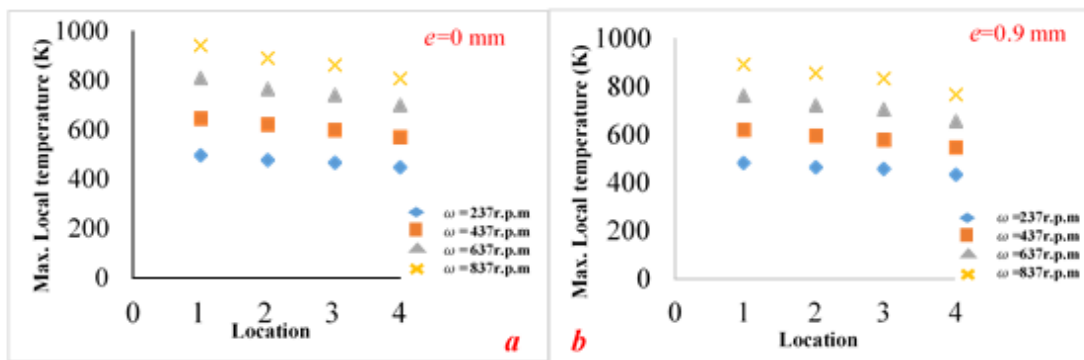


Figure 5.49 Local peak temperature for different rotational speeds with and without eccentricity at different locations

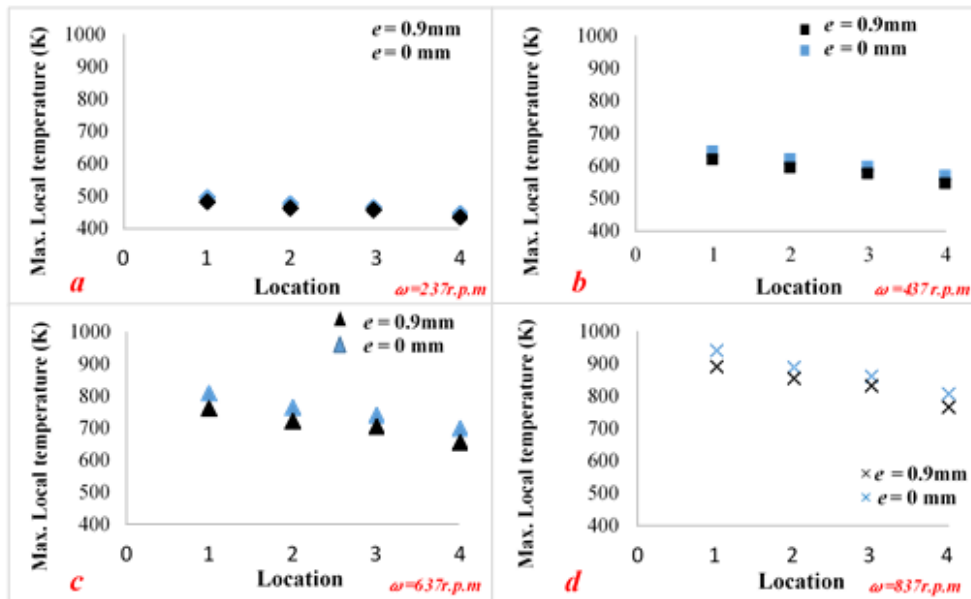


Figure 5.50 A comparison between the local peak temperatures for different rotational speeds with and without eccentricity at different locations

Figure 5.51 shows the variation of the maximum shear stress along the thermal cycle for different welding rotational speeds and eccentricities. For $e=0.9\text{mm}$, it can be seen that the stress values have witnessed an elevating when the values of eccentricity moved from 0mm to 0.9mm . i.e. at the onset of the thermal cycle, 821.7MPa was achieved for $e=0.9\text{mm}$ compared with 727MPa when $e=0\text{mm}$. However, the values of shear stress have generally and orderly kept their trend against the change in the rotational speed where the highest and the lowest were attained when $\omega = 237\text{r.p.m}$ and $\omega = 837\text{r.p.m}$ respectively.

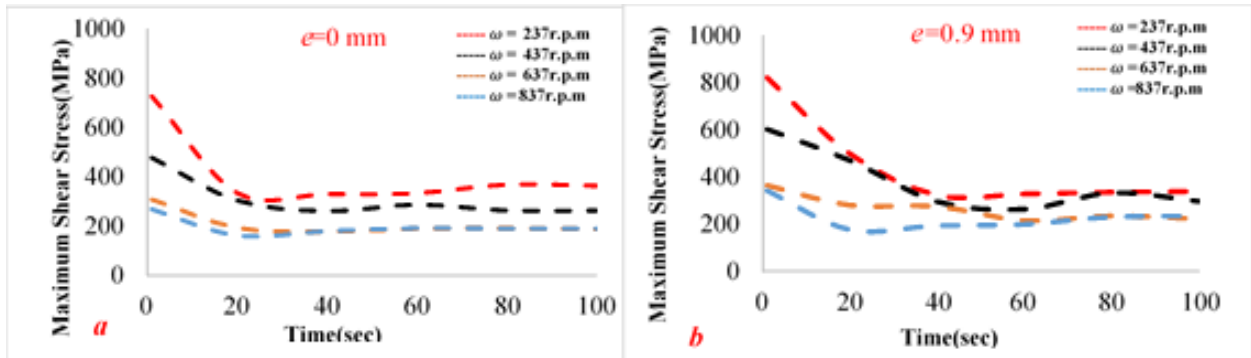


Figure 5.51 a comparison between the maximum shear stress values when using different rotational speeds and pin eccentricities

5.3.3 The effect of axial load on the Thermal Field of FSW

Snapshots of the temperature distribution at different moments from the thermal cycle were taken and listed in figure 5.52 to show its transient progression corresponding to the variation in the axial loads. By keeping in mind that this investigation has been conducted in presence of the pin eccentricity, it can be observed that the behaviour of the temperature profile was generally as the same as that noted for welding with the same tool without eccentricity. i.e. the temperature level is experiencing an elevating against the increase in the axial load values whereas the heating rate increases from 62.65K/sec to 79.25K/sec at $t=3\text{sec}$ when the axial load moves up from 9.7MPa to 12.7MPa . Likewise, the same trend was observed in figure 5.53(a,b,c,d) which depicts the spatial progression in the thermal field at the same time and corresponding to welding processes with several axial loads. Tracking the line of 500K would vividly give an indication as the hottest areas are growing up according to the increase in the axial load. From another point of view, the temperature level has fallen down as the information given in figure 5.53 compared to those in

figure 4.38 where the highest has not reached the solidus temperature of base metal eventhough the presence of eccentricity helps to rising up the process heat input.

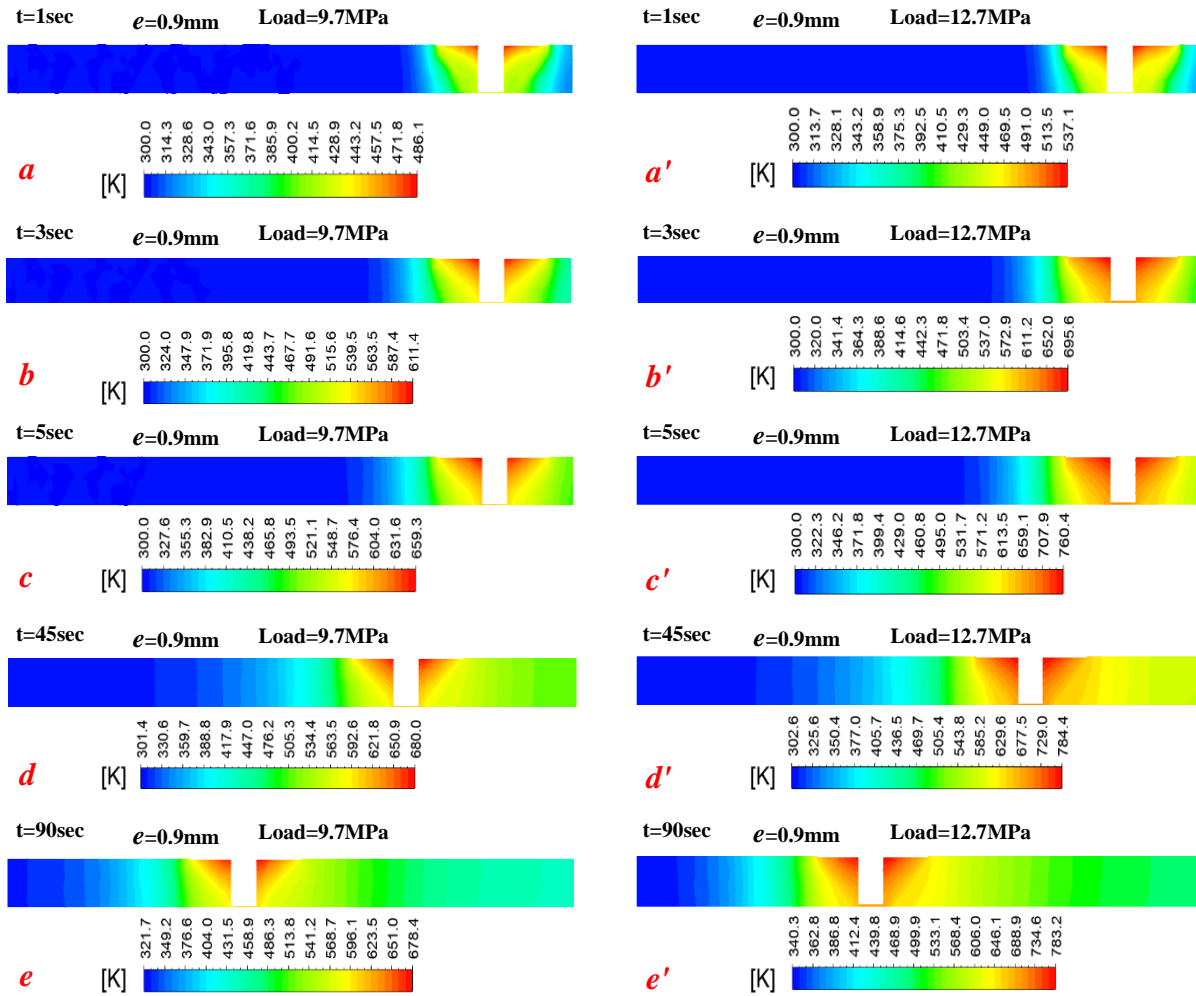


Figure 5.52 temperature distribution for the vertical plane at different time steps calculated for axial loads 9.7MPa and 12.7 MPa in the existence of eccentricity

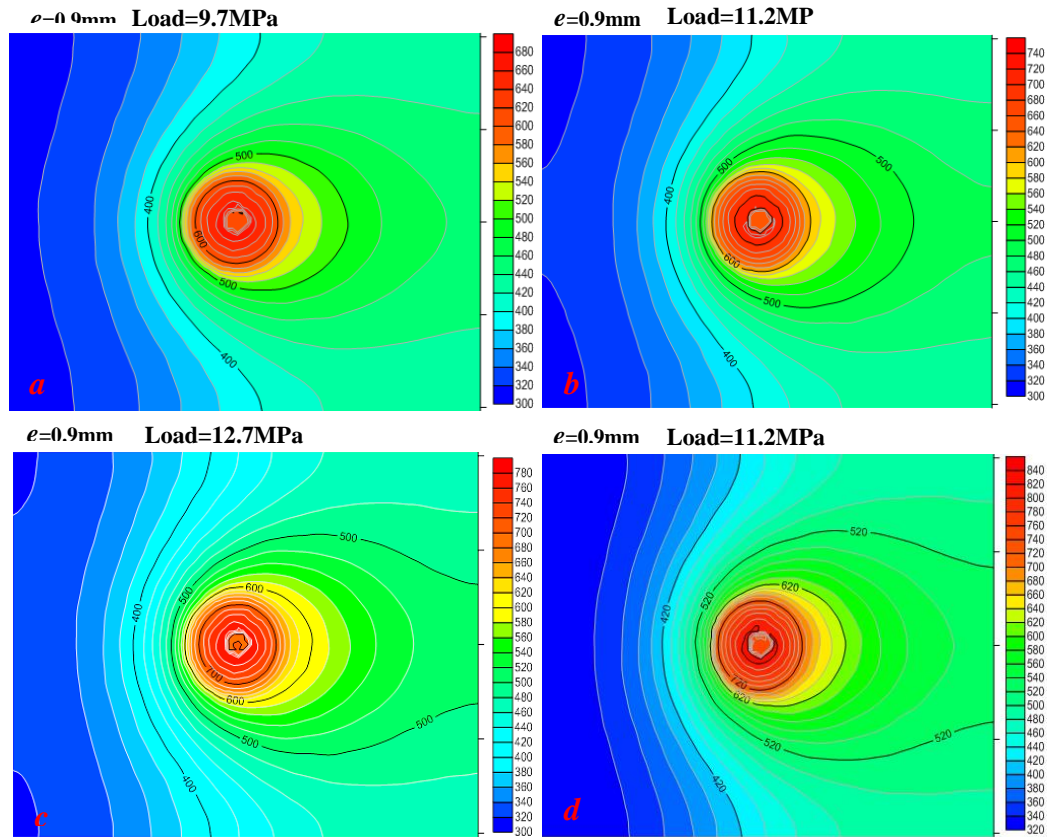


Figure 5.53 Static temperature contours for different axial load $a=9.7\text{MPa}$, $b=11.2\text{MPa}$, $c=12.7\text{MPa}$, $d=14.2\text{MPa}$ in the existence of eccentricities

As observed above, the overall trend of the global peak temperature is similar which can be clearly seen in figure 5.54. For instance, 680K was recorded for 9.7MPa while the temperature has attained 844K for 14.2 MPa which means again the temperature range still lower than the melting point. Besides that, the model has advantageously mimicked the decrease in the temperature as an effect of the eccentricity particularly when the axial load is changed which is difficult in the reality as the plunging depth and the connecting between the workpiece and backing plate are varied. In the same way figures 5.55 and 5.56 reveal that the local peak temperature at several locations is as similar as the global temperature behaves. Interestingly, the percentage of temperature drop is more or less constant where 5.5%, 5.8%, 5.8%, and 5.7% were recorded at point 1 for 9.7MPa, 11.2MPa, 12.7MPa, and 14.2 MPa, respectively. From another point of view, it was observed that the maximum flow velocity under the shoulder recorded for instance 1.73m/s for 14.7 MPa and

$e=0.9\text{mm}$ while it achieved 2.37m/s for the same axial load when $e=0\text{mm}$ which demonstrates how the viscosity affected by the temperature drop due to the role of the eccentricity.

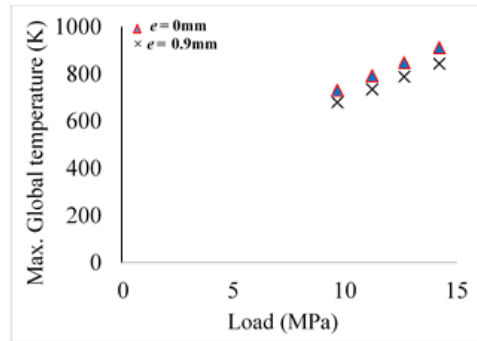


Figure 5.54 Global peak temperature for different axial loads with and without eccentricity

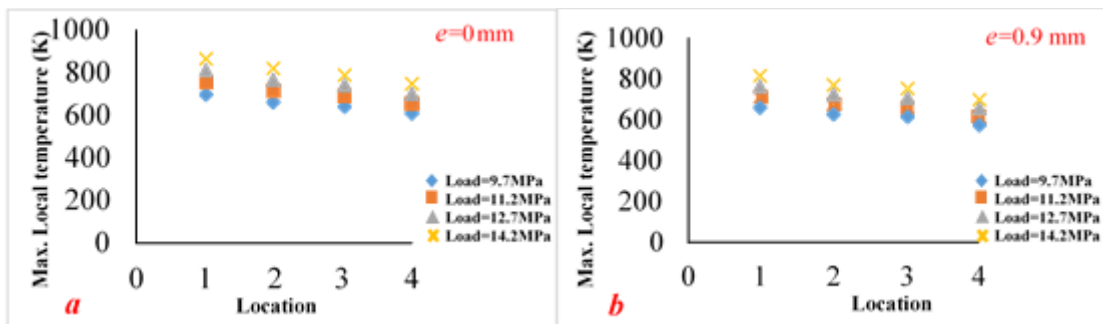


Figure 5.55 Local peak temperature for different axial loads with and without eccentricity at different locations

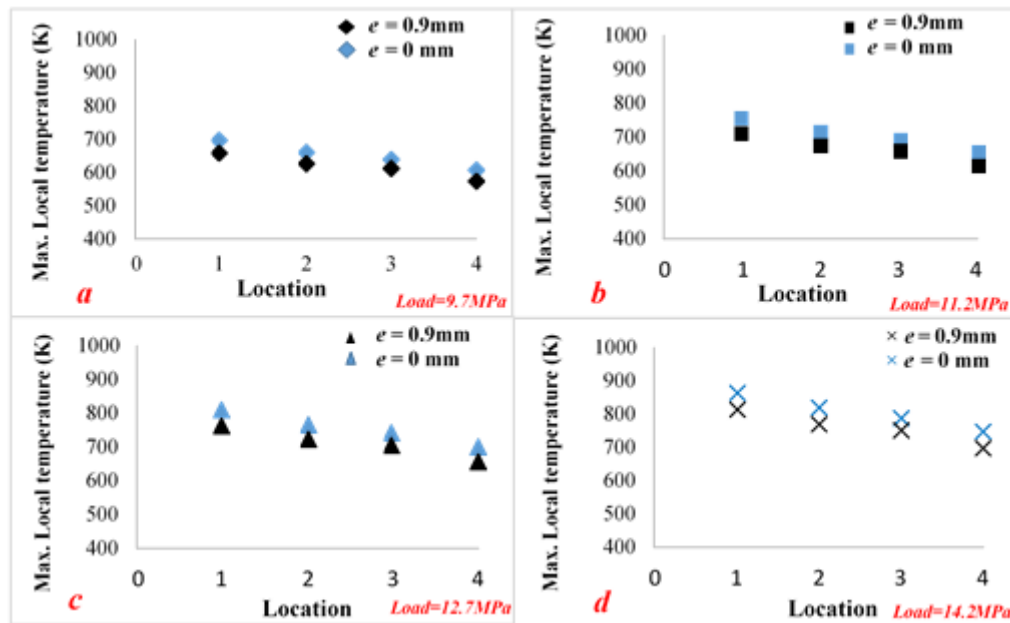


Figure 5.56 A comparison between the local peak temperatures for different axial loads with and without eccentricity at different locations

The findings in figure 5.57 indicate that the maximum shear stress values have orderly kept their trend against the variation in the axial load which is as the same as that obtained when there was no eccentricity. However, for $e=0.9\text{mm}$ the stress has acquired an additional value compared to its values when $e=0\text{mm}$. For example, at $t=1\text{sec}$ and $e=0.9\text{mm}$ 398,380,363.6,347MPa corresponding to axial loads of 9.7,11.2,12.7,14.2 MPa while 350, 334, 308, 305 MPa were registered when $e=0$ at the same moment and axial load variation.

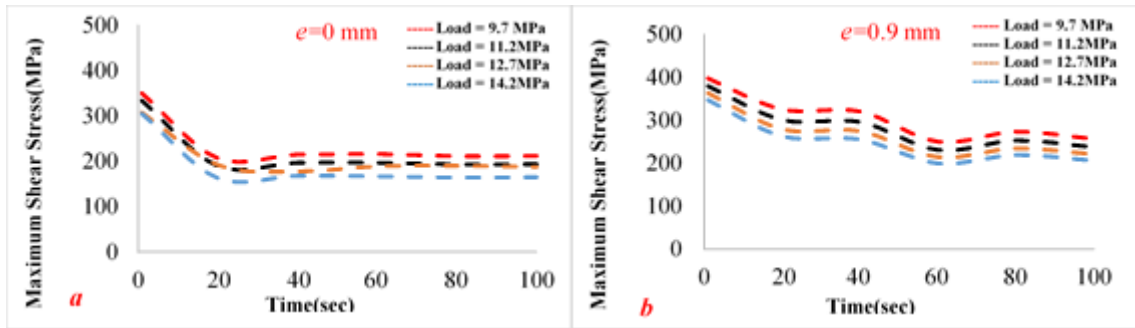


Figure 5.57 a comparison between the maximum shear stress values when using different axial loads and pin eccentricities

5.4 Prediction Model of the Peak Temperature

Based on the data provided and discussed in the previous sections, it was found that the pin eccentricity has shown a significant impact on the thermal field particularly on the maximum temperature that is ever attained during welding. Furthermore, the effect of some parameters under consideration on the peak temperature has more or less changed in presence of the eccentricity. For example, the increase in peak temperature was proportional with the growth in the pin height for $e=0\text{mm}$ while the opposite trend was noted in those welding processes that using the same conditions and tools with eccentricity. This section is therefore presenting a trial to develop a prediction model for the peak temperature which consider the all above mentioned impacts and changes. Consequently, a novel semi-empirical correlation for predicting the peak temperature was developed based on the acquired data from CFD experiments and with the aid of the multiple variable regression analysis. Equation (5.51) provides a correlation between the temperature ratio $T_{max} / (T_s)$ and the considered parameters in the existence of eccentricity.

$$\frac{T_{max}}{T_s} = \frac{0.02703 \left(\frac{P}{P_{max}}\right)^{0.549}}{\left(\frac{V}{\omega R_S}\right)^{0.4983} \left(\frac{N}{R_S} * R_P\right)^{0.01945} \left(\frac{e+t}{R_S}\right)^{0.2377} \left(\frac{e+H}{R_S}\right)^{0.0162}} \quad (5.51)$$

where T_s is the solidus temperature of the material to be welded which is equal to 855K in the current study, V is the tool transverse speed, ω is the tool rotational speed, R_s is the shoulder radius, N is the number of pin side faces, H is the pin height, t is the workpiece thickness, P is the axial load, P_{max} is the maximum axial load and e is the eccentricity value. Then, Eqn. (5.51) can be rearranged to find a direct expression to calculate T_{max} as follows:

$$T_{max} = \left[\frac{0.02703 \left(\frac{P}{P_{max}}\right)^{0.549}}{\left(\frac{V}{\omega R_s}\right)^{0.4983} \left(\frac{N}{R_s} * R_p\right)^{0.01945} \left(\frac{e+t}{R_s}\right)^{0.2377} \left(\frac{e+H}{R_s}\right)^{0.0162}} \right] \times T_s \quad (5.52)$$

It can be seen from the prediction model that (P/P_{max}) , $(v/\omega R_s)$ have the most significant effect on the peak temperature. Moreover, the peak temperature is proportional to (P/P_{max}) and inversely proportional to $(v/\omega R_s, N.R_p /R_s, e+t/R_s, e+H/R_s)$. In equation (5.52), if the fraction in the brackets has a value greater than 1, this means that some parts of the welded material converted to liquid state.

In terms of the adequacy and usefulness of the above developed equation, it was found that the average of differences between the values of T_{max} calculated from eq. (5.52) and T_{max} values obtained from CFD has recorded 1.83% which is very low. A quite strong correlation was acquired as the correlation coefficient achieved 0.99 during the multiple variable regression analysis. Furthermore, it is obvious in figure 5.58. that within errors ranged from 0 to maximum $\pm 5\%$, it would be seen that more than 95% of the data lies in this range. Thus, it can be concluded that the prediction model represents the peak temperature with a high accuracy. Additionally, the above expressed equation is valid for the considered ranges of parameters which shown in table 5-2.

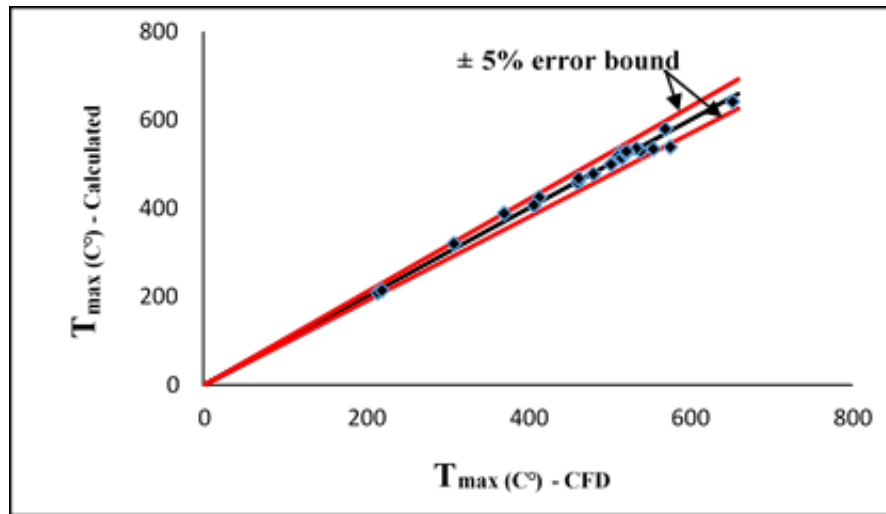


Figure 5.58 prediction model of T_{max} in existence of eccentricity

5.5 Summary of the Thermal Analysis conducted on the FSW using tools with Eccentric Polygonal Pins

The detailed thermal diagnostic of the FSW of thick Aluminium using tools with eccentric pins has revealed the following results:

- Analytically, the increase in the pin eccentricity value faces increases the total amount of heat generated.
- Although, the total amount of heat generated is increased in the presence of eccentricity the thermal field might witness a drop in the temperatures.
- In a comparison to the results that have been attained when using tools with concentric pins, variables such as shoulder diameter, rotational speed, and axial load have kept their impacts on the thermal field where the increase in their values lead to an increase in the temperature. However, lower levels of temperatures have been registered as the eccentricity was obviously influencing.
- In a comparison to the results that have been attained when using tools with concentric pins, the pin height has inversely impacted on the temperature field where the temperature levels have decreased as the pin height was growing up.

To sum-up, an extensive information presented and discussed in this chapter regarding thermal field behaviour during FSW when using tools with eccentric polygonal pin. The corresponding steps of the analytical estimation of the heat generated amount were explained for different cases. Then, a series of CFD simulations were conducted to verify the change in the thermal field through the weldments for different geometrical and operational parameters in the presence of the pin eccentricity. Additionally, a prediction model to estimate the peak temperature was developed and authorised. As it may be possible to use other different pin profiles such as the tapered one which is recommended in the case of thick material, it became significantly studying the accompanying thermal cycles and their changes crossover the time. The next chapter will firstly focus on the concept of pin tapering and how it can be considered during the analytical derivation of the total heat generated amount. That is followed by a detailed thermal diagnostic of the FSW process to see the effect of different parameters under consideration when employment of such a tapered tool.

CHAPTER 6: THERMAL CHARACTERISATION OF FRICTION STIR WELDING USING TOOL WITH TAPERED PINS

This chapter focuses on influence of the tapering of the tool pin on the thermal field of friction stir welding. Firstly, it describes the analytical steps that estimate the heat generation amount in the presence of different tapered pins. Using tapered pins, qualitative and quantitative analysis is then given for the purposes of detecting, diagnosing and assessing the effect of various geometrical and operational parameters on the temperature distribution and the peak temperature. After that, the analysis results were used to develop a semi-empirical relationship for the peak temperature.

6.1 Analytical Modeling of Heat Generation for a tool with Tapered Pin

Taking of pin tapering into consideration means there will be a change in the pin dimensions which affects the frictional heat generated. Therefore, there should be a term represents that change when adopting the analytical approach in estimating of the amount of heat generation. In this section, detailed steps will be presented for the analytical modeling of the heat generation during the FSW process in the presence of the tapered pin. In order to draw comparisons, the concepts of tapering will be studied along with considering the polygonal pins that were chosen in the previous chapters. The analytical models considered have been developed based on analytical models developed by Schmidt et al [13], Gadakh et al [49], A.R.S. Essa et al [57], and V. S. Gadakh et al. [64]. Figure 6.1(a, b, c), depicts the schematic of tools which have tapered and eccentric pins with Heptagonal, Octagonal and Nonagonal profiles, respectively. The main regions that are related to the heat generation are shown, where Q_1 is the heat generated at the shoulder base, Q_2 is the heat generated at the sides of the tool pin and Q_3 represents the heat generated at the pin tip. Summation of these gives the overall heat amount Q_{total} produced due to the friction between the tool surfaces and the workpiece.

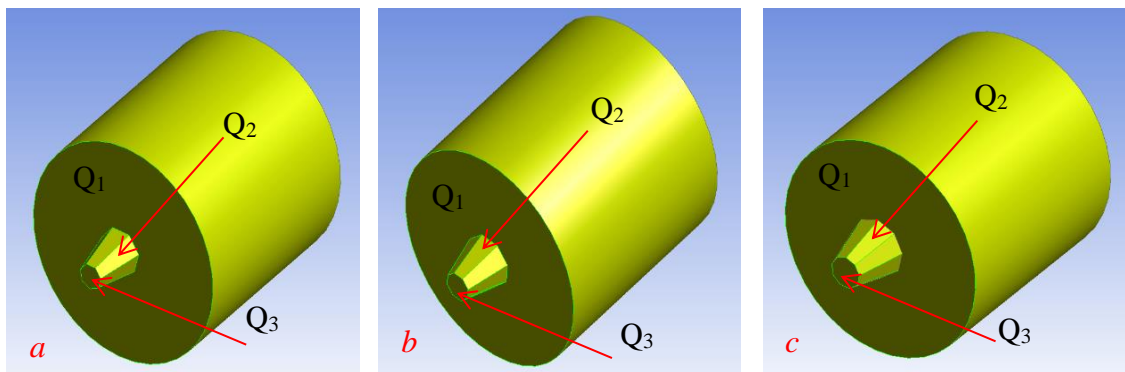


Figure 6.1 Tools with tapered and eccentric pins (a) Heptagon, (b) Octagon, (c) Nonagon

To describe the tapered pin, new trigonometric expressions need to be defined and for more explanation, the simplified tool design is described in figure 6.2, where γ stands to the tapering angle which represents the severity of the tapering. As the tapered pin has two different polygonal bases, R_{pt} and R_{pb} denotes to the radius of the pin top base and bottom base respectively. Similarly, a_{pt} and a_{pb} are the side lengths of the pin top base and bottom base respectively.

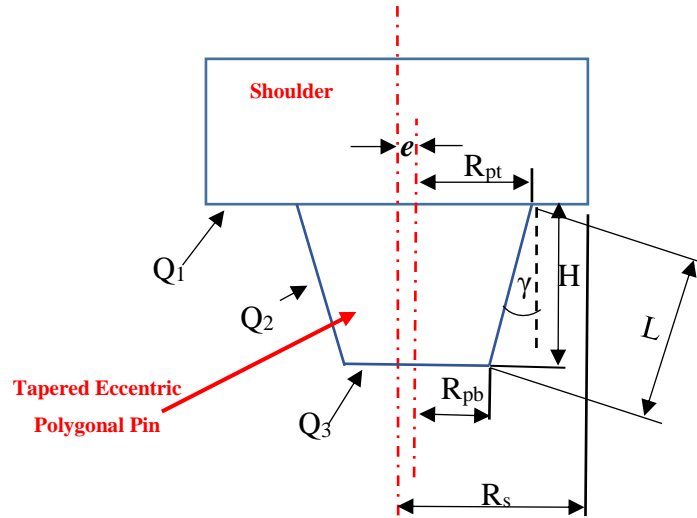


Figure 6.2 schematic drawing of a tool with tapered eccentric polygonal pin

6.2 Heat Generation from a Tool with Tapered Eccentric Heptagonal Pin

6.2.1 Heat Generation from Shoulder Base

As the shoulder still rotating around the original axis and having the same frictional area presented in section 4.1, the heat generated at the shoulder base can be estimated through Eq.(5.1). However, the side length that should be used is the one for the top base (a_{pt})

$$Q_1 = \frac{2}{3}\pi \cdot \omega \cdot \tau_{contact} \cdot R_s^3 - \left[\frac{2 \times 1.53 \pi \cdot \omega \cdot \tau_{contact} \cdot a_{pt}^3}{3} \right] \quad (6.1)$$

$$Q_1 = \frac{2}{3}\pi \cdot \omega \cdot \tau_{contact} (R_s^3 - 1.53a_{pt}^3) \quad (6.2)$$

6.2.2 Heat Generation from Pin Side Surfaces

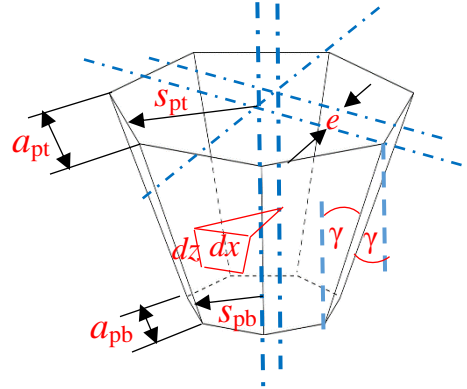


Figure 6.3 Schematic drawing of the frictional zone and the infinitesimal areas related to the Tapered Eccentric Heptagonal pin side

In addition to the trigonometric expressions that were defined in the previous chapters, the expression γ represents the effect of tapering through the following derivation of heat generation equation from the pin side surfaces. Starting from eq. (5.3)

$$dQ = 7(\omega \cdot (s + e) \cdot \tau_{contact} \cdot dx \cdot dz) \quad (5.3)$$

By integration eq. (5.3), over the frictional area from 0 to L

$$Q_2 = 7 \int_0^{\frac{a_{pt}+a_{pb}}{2}} \int_0^L \omega \cdot \tau_{contact} \cdot (s + e) \cdot dx \cdot dz \quad (6.3)$$

$$Q_2 = 7(\omega \cdot (\frac{s_{pt}+s_{pb}}{2} + e) \cdot \tau_{contact} \cdot (\frac{a_{pt}+a_{pb}}{2}) \cdot L) \quad (6.4)$$

Geometrically, L can be substituted by $\frac{H}{\cos \gamma}$

$$Q_2 = 7(\omega \cdot \tau_{contact} \cdot (\frac{s_{pt}+s_{pb}}{2} + e) \cdot (\frac{a_{pt}+a_{pb}}{2}) \cdot \frac{H}{\cos \gamma}) \quad (6.5)$$

From eqn. 4.10, when $n=7$, s_{pt} is equal to $1.0382 a_{pt}$ and s_{pb} is equal to $1.0382 a_{pb}$ as well.

$$Q_2 = 7(\omega \cdot \tau_{contact} \cdot \frac{H}{\cos \gamma} ((0.5191(a_{pt} + a_{pb}) + e) \cdot (\frac{a_{pt}+a_{pb}}{2}))) \quad (6.6)$$

$$Q_2 = 7(\omega \cdot \tau_{contact} \cdot \frac{H}{\cos \gamma} \left(\left((0.5191a_{pt} + 0.5191a_{pb}) + e \right) \cdot \left(\frac{a_{pt} + a_{pb}}{2} \right) \right)) \quad (6.7)$$

$$Q_2 = 7(\omega \cdot \tau_{contact} \cdot \frac{H}{\cos \gamma} \left(\left(\left(0.5191 \frac{a_{pt}^2}{2} + 0.5191 \frac{a_{pt}a_{pb}}{2} + 0.5191 \frac{a_{pb}a_{pt}}{2} + 0.5191 \frac{a_{pb}^2}{2} \right) + \left(\frac{ea_{pt} + ea_{pb}}{2} \right) \right) \right)) \quad (6.8)$$

$$Q_2 = 7(\omega \cdot \tau_{contact} \cdot \frac{H}{\cos \gamma} \left(\left(0.2595a_{pt}^2 + 0.5191a_{pt}a_{pb} + 0.2595a_{pb}^2 \right) + e \left(\frac{a_{pt} + a_{pb}}{2} \right) \right)) \quad (6.9)$$

6.2.3 Heat Generation from the Pin Tip

The heat generated at the pin tip in this case can be estimated as similar as that in chapter five for the eccentric heptagonal pin. Nonetheless the dimensions of heptagon bottom base should be considered. Starting from Eq. (5.9)

$$Q_3 = 14 \int_0^{\theta=\frac{\pi}{7}} \int_0^{Rp} \omega \cdot (r + e)^2 \cdot \tau_{contact} \cdot d\theta \cdot dr \quad (5.9)$$

Here, $R_p = R_{pb}$

$$Q_3 = 14 \int_0^{\theta=\frac{\pi}{7}} \int_0^{Rpb} \omega \cdot (r + e)^2 \cdot \tau_{contact} \cdot d\theta \cdot dr \quad (6.10)$$

From eq. 4.8, R_{pb} is equal to $1.1523a_{pb}$ when $n=7$. Therefore

$$Q_3 = 14 \int_0^{\theta=\frac{\pi}{7}} \int_0^{Rpb=1.1523a_{pb}} \omega \cdot (r + e)^2 \cdot \tau_{contact} \cdot d\theta \cdot dr \quad (6.11)$$

$$Q_3 = 14 \left[\frac{\pi}{7} \cdot \omega \cdot \tau_{contact} \cdot \left(\left(\frac{(1.1523a_{pb} + e)^3}{3} \right) - \frac{e^3}{3} \right) \right] \quad (6.12)$$

$$Q_3 = \frac{2}{3} \pi \cdot \omega \cdot \tau_{contact} \cdot \left((1.1523a_{pb} + e)^3 - e^3 \right) \quad (6.13)$$

6.2.4 Total Heat Generation from the Tool with Tapered Eccentric Heptagonal Pin

Using eqs. (6.2), (6.9) and (6.12), the total heat generation from the tool with tapered eccentric heptagonal pin can be computed as:

$$\begin{aligned}
 Q_{total} = & \frac{2}{3}\pi \cdot \omega \cdot \tau_{contact} (R_s^3 - 1.53a_{pt}^3) + \\
 & 7 \left(\omega \cdot \tau_{contact} \cdot \frac{H}{\cos \gamma} \left((0.2595a_{pt}^2 + 0.5191a_{pt}a_{pb} + \right. \right. \\
 & \left. \left. 0.2595a_{pb}^2) + e \left(\frac{a_{pt} + a_{pb}}{2} \right) \right) \right) + \\
 & \frac{2}{3}\pi \cdot \omega \cdot \tau_{contact} \cdot \left((1.1523a_{pb} + e)^3 - e^3 \right) \quad (6.14)
 \end{aligned}$$

Rearranging eq. (6.14)

$$\begin{aligned}
 Q_{total} = & \frac{2}{3}\pi \cdot \omega \cdot \tau_{contact} \left[(R_s^3 - 1.53a_{pt}^3) + \right. \\
 & \left(\frac{H}{\cos \gamma} (0.8678(a_{pt}^2 + a_{pb}^2) + 1.736a_{pt}a_{pb} + 1.672e(a_{pt} + \right. \\
 & \left. a_{pb})) \right) + \left. \left((1.1523a_{pb} + e)^3 - e^3 \right) \right] \quad (6.15)
 \end{aligned}$$

From Eqn. 4.8, R_{pt} is equal to $1.1523a_{pt}$ and R_{pb} is equal to $1.1523a_{pb}$ when $n=7$, hence Eqn. (6.15) can be written as following:

$$\begin{aligned}
 Q_{total} = & \frac{2}{3}\pi \cdot \omega \cdot \tau_{contact} \left[(R_s^3 - R_{pt}^3) + \right. \\
 & \left(\frac{H}{\cos \gamma} (0.6535(R_{pt}^2 + R_{pb}^2) + 1.3073(R_{pt}R_{pb}) + 1.451e(R_{pt} + \right. \\
 & \left. R_{pb})) \right) + \left. \left((R_{pb} + e)^3 - e^3 \right) \right] \quad (6.16)
 \end{aligned}$$

In the same way, for the other tools with tapered eccentric polygonal pin profiles that have a higher number of side faces; the heat generation expressions have been developed using the same analytical approach. Based on the number of pin faces, the acquired heat generation formulas are listed in tables (6-1) and (6-2)

Table 6-1 heat generation formulas of tools with different tapered eccentric pin profiles (No. of faces from 7to 12)

Pin Profile	No. of faces	Equation
Tapered Eccentric Heptagonal	7	$Q_{total} = \frac{2}{3}\pi \cdot \omega \cdot \tau_{contact} \left[(R_s^3 - R_{pt}^3) + \left(\frac{H}{\cos \gamma} (0.6535(R_{pt}^2 + R_{pb}^2) + 1.3073(R_{pt}R_{pb}) + 1.451e(R_{pt} + R_{pb})) \right) + ((R_{pb} + e)^3 - e^3) \right]$
Tapered Eccentric Octagonal	8	$Q_{total} = \frac{2}{3}\pi \cdot \omega \cdot \tau_{contact} \left[(R_s^3 - R_{pt}^3) + \left(\frac{H}{\cos \gamma} (0.6754(R_{pt}^2 + R_{pb}^2) + 1.3511(R_{pt}R_{pb}) + 1.4625e(R_{pt} + R_{pb})) \right) + ((R_{pb} + e)^3 - e^3) \right]$
Tapered Eccentric Nonagonal	9	$Q_{total} = \frac{2}{3}\pi \cdot \omega \cdot \tau_{contact} \left[(R_s^3 - R_{pt}^3) + \left(\frac{H}{\cos \gamma} (0.6907(R_{pt}^2 + R_{pb}^2) + 1.3815(R_{pt}R_{pb}) + 1.4703e(R_{pt} + R_{pb})) \right) + ((R_{pb} + e)^3 - e^3) \right]$
Tapered Eccentric Decagon	10	$Q_{total} = \frac{2}{3}\pi \cdot \omega \cdot \tau_{contact} \left[(R_s^3 - R_{pt}^3) + \left(\frac{H}{\cos \gamma} (0.7018(R_{pt}^2 + R_{pb}^2) + 1.4037(R_{pt}R_{pb}) + 1.476e(R_{pt} + R_{pb})) \right) + ((R_{pb} + e)^3 - e^3) \right]$
Tapered Eccentric Undecagon	11	$Q_{total} = \frac{2}{3}\pi \cdot \omega \cdot \tau_{contact} \left[(R_s^3 - R_{pt}^3) + \left(\frac{H}{\cos \gamma} (0.71(R_{pt}^2 + R_{pb}^2) + 1.4201(R_{pt}R_{pb}) + 1.4802e(R_{pt} + R_{pb})) \right) + ((R_{pb} + e)^3 - e^3) \right]$
Tapered Eccentric Dodecagon	12	$Q_{total} = \frac{2}{3}\pi \cdot \omega \cdot \tau_{contact} \left[(R_s^3 - R_{pt}^3) + \left(\frac{H}{\cos \gamma} (0.7164(R_{pt}^2 + R_{pb}^2) + 1.4329(R_{pt}R_{pb}) + 1.4836e(R_{pt} + R_{pb})) \right) + ((R_{pb} + e)^3 - e^3) \right]$

Table 6-2 heat generation formulas of tools with different tapered eccentric pin profiles (No. of faces from 13 and upward)

Pin Profile	No. of faces	Equation
Tapered Eccentric 13-gon	13	$Q_{total} = \frac{2}{3}\pi \cdot \omega \cdot \tau_{contact} \left[(R_s^3 - R_{pt}^3) + \left(\frac{H}{\cos \gamma} (0.7212(R_{pt}^2 + R_{pb}^2) + 1.4424(R_{pt}R_{pb}) + 1.486e(R_{pt} + R_{pb})) \right) + ((R_{pb} + e)^3 - e^3) \right]$
Tapered Eccentric 14-gon	14	$Q_{total} = \frac{2}{3}\pi \cdot \omega \cdot \tau_{contact} \left[(R_s^3 - R_{pt}^3) + \left(\frac{H}{\cos \gamma} (0.7252(R_{pt}^2 + R_{pb}^2) + 1.4505(R_{pt}R_{pb}) + 1.4881e(R_{pt} + R_{pb})) \right) + ((R_{pb} + e)^3 - e^3) \right]$
Tapered Eccentric 15-gon	15	$Q_{total} = \frac{2}{3}\pi \cdot \omega \cdot \tau_{contact} \left[(R_s^3 - R_{pt}^3) + \left(\frac{H}{\cos \gamma} (0.7285(R_{pt}^2 + R_{pb}^2) + 1.457(R_{pt}R_{pb}) + 1.4897e(R_{pt} + R_{pb})) \right) + ((R_{pb} + e)^3 - e^3) \right]$
Tapered Eccentric 25-gon	25	$Q_{total} = \frac{2}{3}\pi \cdot \omega \cdot \tau_{contact} \left[(R_s^3 - R_{pt}^3) + \left(\frac{H}{\cos \gamma} (0.742(R_{pt}^2 + R_{pb}^2) + 1.4842(R_{pt}R_{pb}) + 1.4964e(R_{pt} + R_{pb})) \right) + ((R_{pb} + e)^3 - e^3) \right]$
Tapered Eccentric 30-gon	30	$Q_{total} = \frac{2}{3}\pi \cdot \omega \cdot \tau_{contact} \left[(R_s^3 - R_{pt}^3) + \left(\frac{H}{\cos \gamma} (0.7448(R_{pt}^2 + R_{pb}^2) + 1.4896(R_{pt}R_{pb}) + 1.498e(R_{pt} + R_{pb})) \right) + ((R_{pb} + e)^3 - e^3) \right]$
Tapered Eccentric 40-gon	40	$Q_{total} = \frac{2}{3}\pi \cdot \omega \cdot \tau_{contact} \left[(R_s^3 - R_{pt}^3) + \left(\frac{H}{\cos \gamma} (0.747(R_{pt}^2 + R_{pb}^2) + 1.4942(R_{pt}R_{pb}) + 1.499e(R_{pt} + R_{pb})) \right) + ((R_{pb} + e)^3 - e^3) \right]$

By comparing the developed expressions in the table with each other, it can be seen that all the terms in the equations are the same except the numerical coefficients in the term related to the heat generation at the pin side surface. Accordingly, a general equation can be expressed as:

$$Q_{total} = \frac{2}{3}\pi \cdot \omega \cdot \tau_{contact} \left[(R_s^3 - R_{pt}^3) + \left(\frac{H}{\cos\gamma} (C_{t1}(R_{pt}^2 + R_{pb}^2) + C_{t2}(R_{pt}R_{pb}) + C_{t3}e(R_{pt} + R_{pb})) \right) + ((R_{pb} + e)^3 - e^3) \right] \quad (6.17)$$

where C_{t1} , C_{t2} and C_{t3} have different values according to the number of polygon faces.

All above derived heat generation equations were applied for the same aluminium FSW welding process and conditions that have been undertaken in chapter 3. The acquired results were plotted in figure 6.4(a,b,c,d) and compared with the calculated heat generated amount from the tool with cylindrical pin profile. Those results represent the heat amounts from the analytical model for tools with pins having different proposed tapering angles and eccentricity distances ranging from 0° mm to 21° and from 0 to 0.9mm, respectively. It can be seen in the figure that increasing the value of the taper angle caused a decrease of the generated heat, which would be reasoned by reducing of the frictional area [64]. To clarify, the total heat amount in the case of $\gamma=0^\circ$ is ranging from 11858W to 12210W for different eccentricity values while for $\gamma=21^\circ$ it ranged from 11253W to 11396W for the same values of eccentricities. However, the eccentricity has kept its effect on the heat generated by the tool where the values of heat rising up while the eccentricity going up. In the same line, the effect of eccentricity has been affected by the degree of pin tapering which can be clearly seen when comparing the gaps between the heat generated curves for different eccentricity values at different taper angles. In other words, the rate of heat generation that might be added within the increase in the eccentricity decreases as the taper angle increases and the pin frictional area decreases. For instance, the difference between the heat generated for the tool with heptagonal pin when $\gamma=0^\circ$, $e=0$ mm and $\gamma=0^\circ$, $e=0.9$ mm has achieved to 212W while at $\gamma=21^\circ$ and the same range of eccentricity it recorded 94W. Although, the frictional area between the shoulder and the workpiece still the same that can be attributed to the decrease in the frictional areas between the pin and the workpiece as the taper angle is growing up. In comparison to the heat generated from the tool with cylindrical pin (black line), it is obvious that the thermal performance of the tool is greater affected by the taper angle than the eccentricity and the number of side faces.

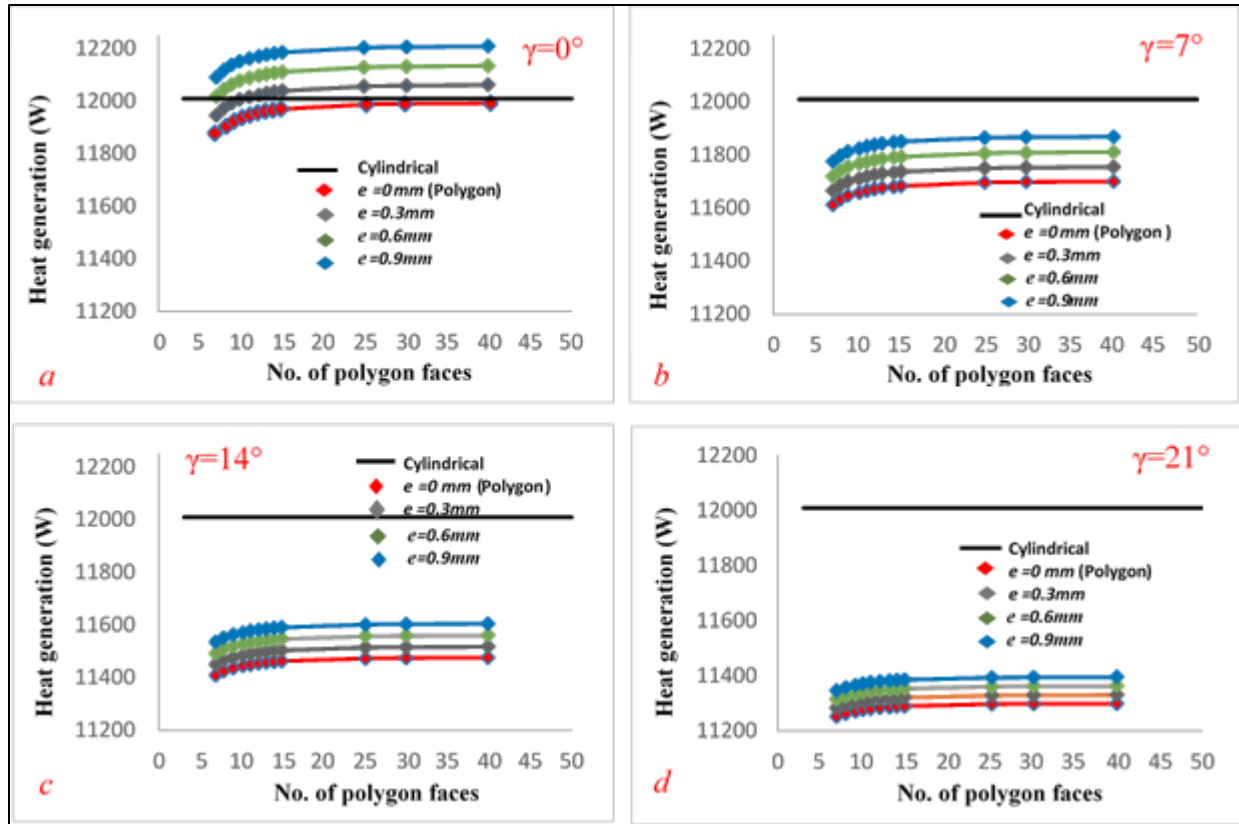


Figure 6.4 heat generation values with No. of polygon faces for different tapering angles and eccentric distances

6.3 Thermal Field Analysis of FSW when using Tapered Eccentric Polygonal Pins

This section of the chapter comprises examining of how the value of the pin tapering might affect the thermal field in FSW especially under several geometrical and operational parameters. The current CFD model will be used along with the new analytical equations that have been developed in the previous sections of this chapter. For the proposed values of taper angle which are 0° , 7° , 14° and 21° , the tool with octagonal pin profile was chosen to conduct this investigation where meaningful comparisons would be drawn up between the thermal characteristics acquired with the pin tapering and without. As presented in tables 6-3 and 6-4, a set of numerical experiments have been proposed to investigate the effects of the selected parameters which are taper angle, eccentricity, shoulder size, pin size, pin height, material thickness, tool rotational speed and axial load. In this set of numerical experiments, the effect of each variable has been addressed by four different values as shown in the table by the yellow shaded cells.

Table 6-3 Details of the designed numerical experiments(from Ex1 to Ex.13)

No.	Taper Angle (°)	Eccentricity Distance(mm)	Shoulder Radius(mm)	Pin -Radius(mm)		Pin Height(mm)	Material Thickness (mm)	Rotational Speed(rpm)	Axial load (MPa)
				Top	Bottom				
EX.1	0	0.9	25	6	6	12	12.7	637	12.7
EX.2	7	0.9	25	6	4.5273	12	12.7	637	12.7
EX.3	14	0.9	25	6	3.0096	12	12.7	637	12.7
EX.4	21	0.9	25	6	1.3962	12	12.7	637	12.7
EX.5	21	0	25	6	1.3962	12	12.7	637	12.7
EX.6	21	0.3	25	6	1.3962	12	12.7	637	12.7
EX.7	21	0.6	25	6	1.3962	12	12.7	637	12.7
EX.8	21	0.9	13	6	1.3962	12	12.7	637	12.7
EX.9	21	0.9	17	6	1.3962	12	12.7	637	12.7
EX.10	21	0.9	21	6	1.3962	12	12.7	637	12.7
EX.11	21	0.9	25	3		12	12.7	637	12.7
EX.12	21	0.9	25	9	4.3962	12	12.7	637	12.7
EX.13	21	0.9	25	12	7.3962	12	12.7	637	12.7

Table 6-4 Details of the designed numerical experiments(from Ex14 to Ex.25)

No.	Taper Angle (°)	Eccentricity Distance(mm)	Shoulder Radius(mm)	Pin -Radius(mm)		Pin Height(mm)	Material Thickness (mm)	Rotational Speed(rpm)	Axial load (MPa)
				Top	Bottom				
EX.14	21	0.9	25	6	1.7798	11	12.7	637	12.7
EX.15	21	0.9	25	6	2.1635	10	12.7	637	12.7
EX.16	21	0.9	25	6	2.5471	9	12.7	637	12.7
EX.17	21	0.9	25	6	1.3962	12	14.7	637	12.7
EX.18	21	0.9	25	6	1.3962	12	16.7	637	12.7
EX.19	21	0.9	24	6	1.3962	12	18.7	637	12.7
EX.20	21	0.9	24	6	1.3962	12	12.7	237	12.7
EX.21	21	0.9	24	6	1.3962	12	12.7	437	12.7
EX.22	21	0.9	24	6	1.3962	12	12.7	837	12.7
EX.23	21	0.9	24	6	1.3962	12	12.7	637	9.7
EX.24	21	0.9	24	6	1.3962	12	12.7	637	11.2
EX.25	21	0.9	24	6	1.3962	12	12.7	637	14.2

6.3.1 Effects of Geometrical Parameters on the Thermal Field of FSW

6.3.1.1 Effect of Pin Tapering on the Thermal Field of FSW

In order to exhibit the transient progress in the temperature distribution during the welding process at different pin taper angles, figure 6.5 presents two different thermal cycles corresponding to FS Welded samples using tools with pin taper angles of $\gamma=0^\circ$ and $\gamma=21^\circ$ at the same eccentricity. In these welding processes, all parameters have been kept constant while the taper angle was the only changed variable. In the figure, it can be clearly seen that the heat affected zone is greater when $\gamma=0^\circ$ than $\gamma=21^\circ$ as well as the temperature degrees. Eventhough, the shoulder keeps delivering the same amount of heat with the change in the pin taper angle, the decrease in the pin size would be the main reason where the decrease in the temperature is a consequence to the contraction in the pin frictional area.

To display the effect of pin taper angle on the temperature distribution when using tools with concentric pin ($e=0\text{mm}$), figure 6.6 lists several contours at different moments over the welding time for two FSW processes using tools with concentric pin and taper angles of $\gamma=0^\circ$ and $\gamma=21^\circ$. The same trend can be observed in the figure where the temperatures decrease along with the increase in the tapering angle. for example, at $t=5\text{sec}$, the temperature drops down by 20 K when γ moves up from 0° to 21° . As presented in figure 6.5 when $e=0.9\text{mm}$ and at the same moment $t=5\text{sec}$, the temperature has interestingly witnessed a decline by 48K for the same increase in the value of taper angle. In this case the role of the pin in heat dissipation becomes higher than that when $e=0$ which readily interprets the change in the temperature drop between the two cases.

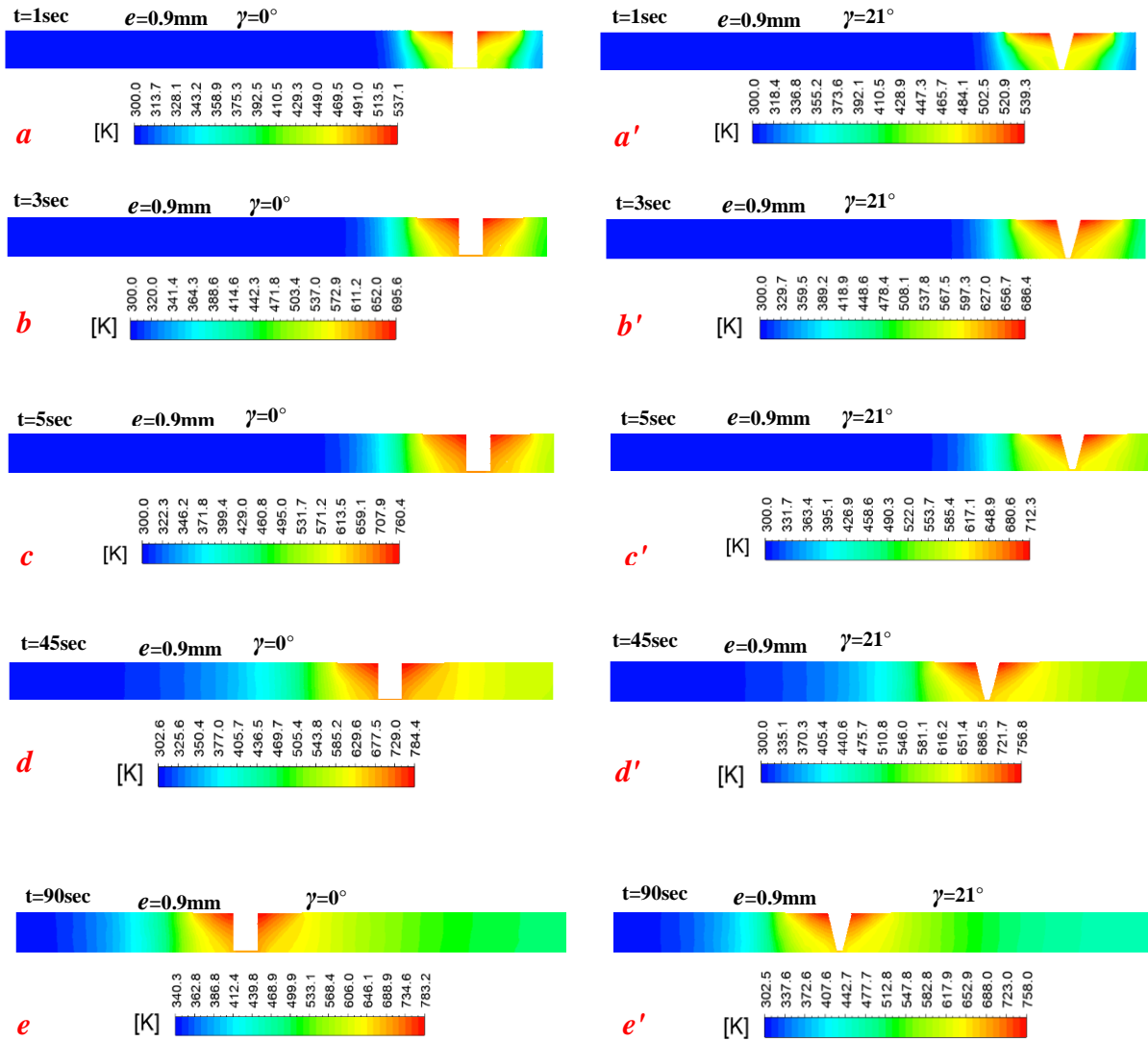


Figure 6.5 temperature distribution for the vertical plane at different time steps calculated for pin taper angles of $\gamma=0^\circ$ and $\gamma=21^\circ$ and $e=0.9\text{mm}$

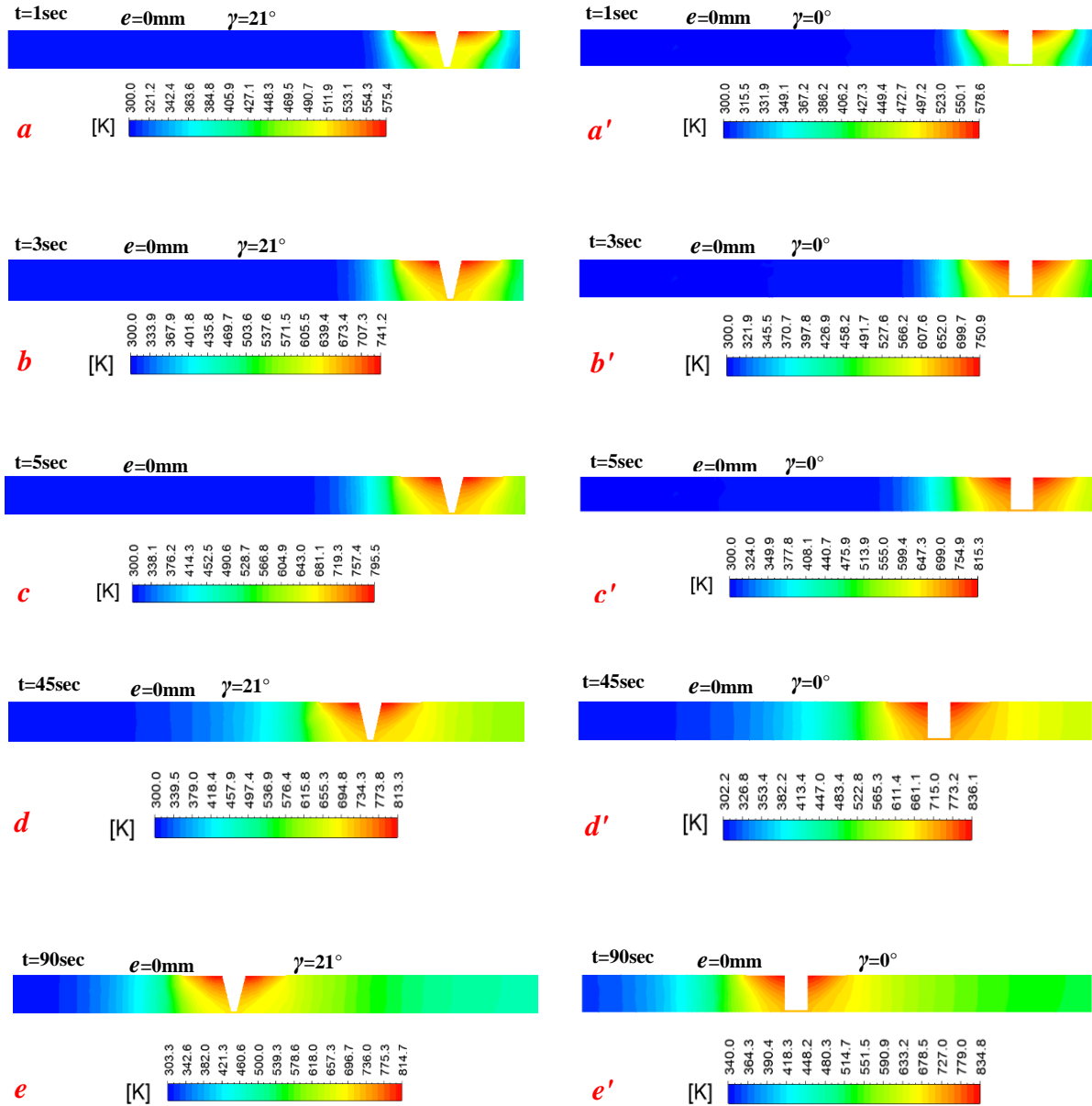


Figure 6.6 Temperature distribution for the vertical plane at different time steps calculated for pin taper angles of $\gamma=0^\circ$ and $\gamma=21^\circ$ and $e=0\text{mm}$

At the same nominated plane in the previous chapters, figure 6.7 (a,b,c,d) illustrates four different snapshots at the same time which depict the influence of the change in the taper angle value on the temperature distribution through the workpiece. Similarly, the temperature degrees tend to fall down as the taper angle increases which can be seen in the scale which indicates ultimately to 780K when of $\gamma=0^\circ$ and 760K at $\gamma=21^\circ$.

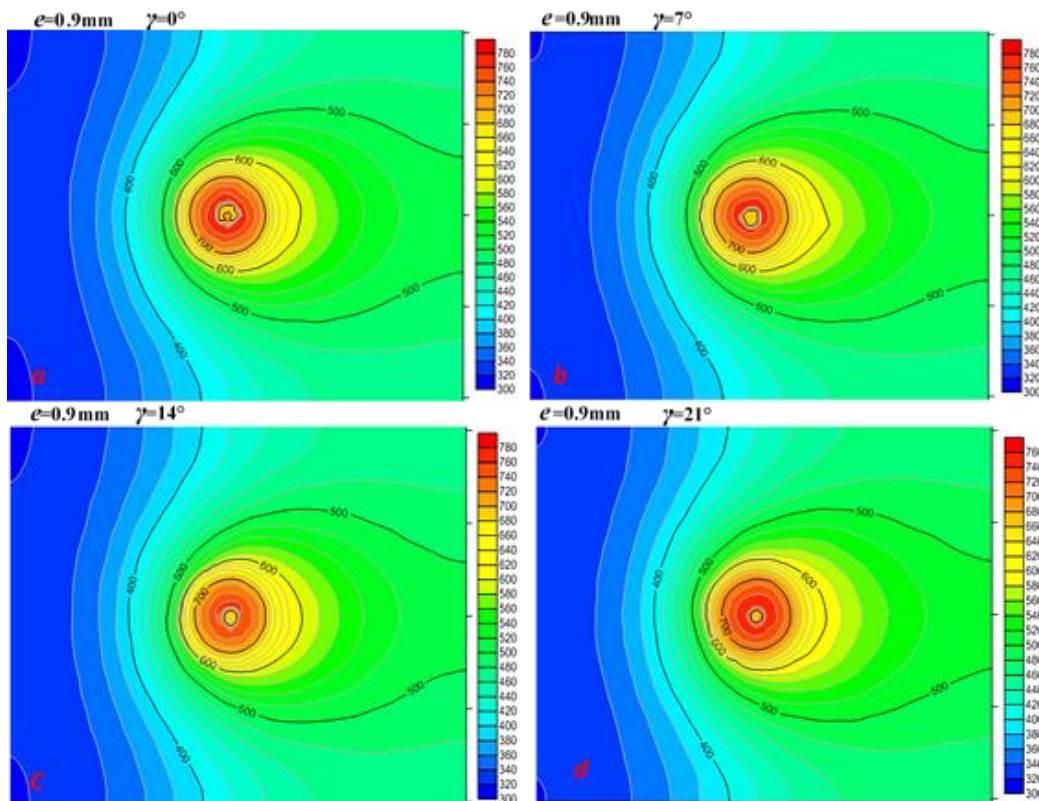


Figure 6.7 Static temperature contours for different pin taper angle $a= \gamma=0^\circ$, $b= \gamma=7^\circ$, $c= \gamma=14^\circ$, $d= \gamma=21^\circ$

To furnish more explanation, the maximum global temperatures were plotted against the angle values in figure 6.10. In the figure, the finding gives a clear indication of how the growing in the taper angle values leads to decline the peak temperature that could ever be achieved in the welding zone. This tendency is fully agreed with the data that have been published by V. S. Gadakh et al. [64] and disagreed with the peak temperature behaviour that acquired by H. Mohanty et al. [35]. That

can be clarified in a view of the original pin size where the change in the taper angle either make the pin size bigger or smaller which means the heat generation rate will be consequently affected.

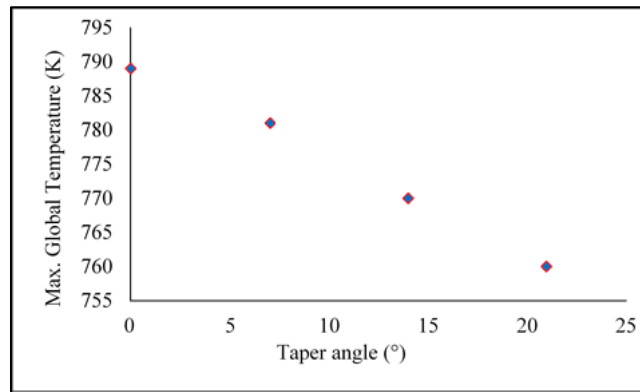


Figure 6.8 Global peak temperature for different pin taper angles

At the same considered points in the previous chapters, the local behaviour of the peak temperature against the alteration in the taper angle values has proved the behaviour of the global one as shown in figure 6.9. For instance, the local maximum temperature at points No. 1 and 2 has recorded 761.7K and 722K when $\gamma=0^\circ$ while the temperatures went down to 734K and 703 when $\gamma=21^\circ$ for the same points, respectively.

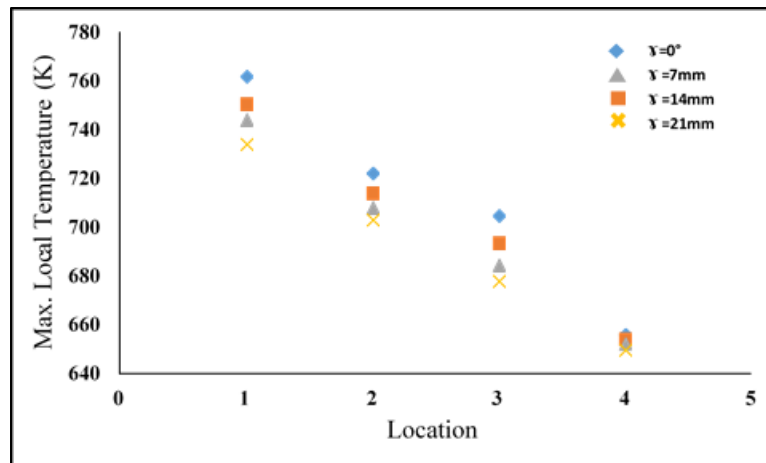


Figure 6.9 Max. Local temperature for different taper angles at different locations

To demonstrate the effect of taper angle on the flow field compared the same with and without eccentricity, velocity vectors were taken at the same plane (under the pin) considered in chapters four figure and five as shown in figure 6.10(a,b,c). The shape and the size of the flow field in existence the taper angle approve what was above mentioned when justifying the thermal behaviour where the volume of the stirring zone and the contact area between the pin and the workpiece have decreased. Both, the heat generated due to the friction activities and the plastic deformation are likely to be affected and decreased. It can be also seen that the flow velocity has recorded a decrease by 0.3m/s under effect of both the eccentricity and the taper angle (c) compared to that under only the effect of eccentricity (b).

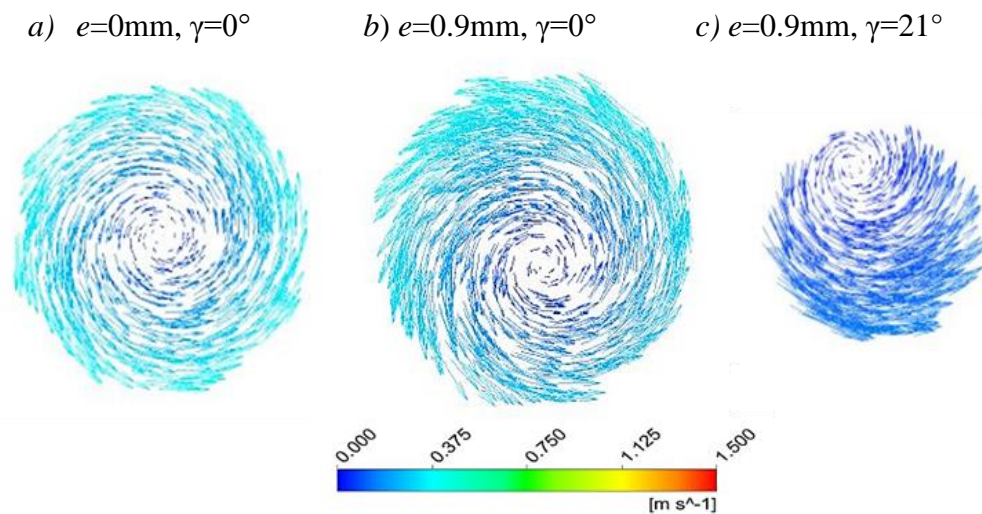


Figure 6.10 a comparison between the flow field under the pin with and without taper angles

Expectedly, the reduction in the temperature degrees corresponding to the increase in the taper angle contributed in growing of the maximum shear stress values on the tool surface as depicted in figure 6.11. Over the welding period, the highest values have been attained when $\gamma=21^\circ$ where 3394MPa was scored at $t=1\text{sec}$. In contrary when the decline in viscous force has taken place, the lowest values were recorded such as 329MPa when $\gamma=0^\circ$ and $t=1\text{sec}$.

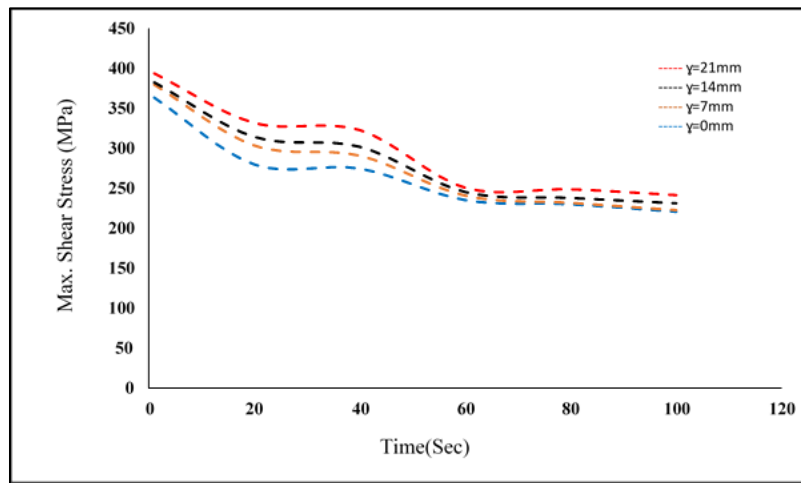


Figure 6.11 variation of the global maximum shear stress along the process time for different taper angles

6.3.1.2 Effect of pin Eccentricity on the Thermal Field of FSW

It is clear to see in figure 6.12 that the effect of the pin eccentricity in case of the tapered pin is as similar as that when the pin is straight. The time dependent contours displayed in the figure represents two different thermal cycles corresponding to FS Welded samples using tools with the same taper angle and eccentricity of 0mm and 0.9mm. Obviously, temperature scales indicate that the temperature degrees that recorded when $e=0.9\text{mm}$ have not interestingly reached those attained for $e=0\text{mm}$ eventhough the heat input increases by increasing the eccentricity.

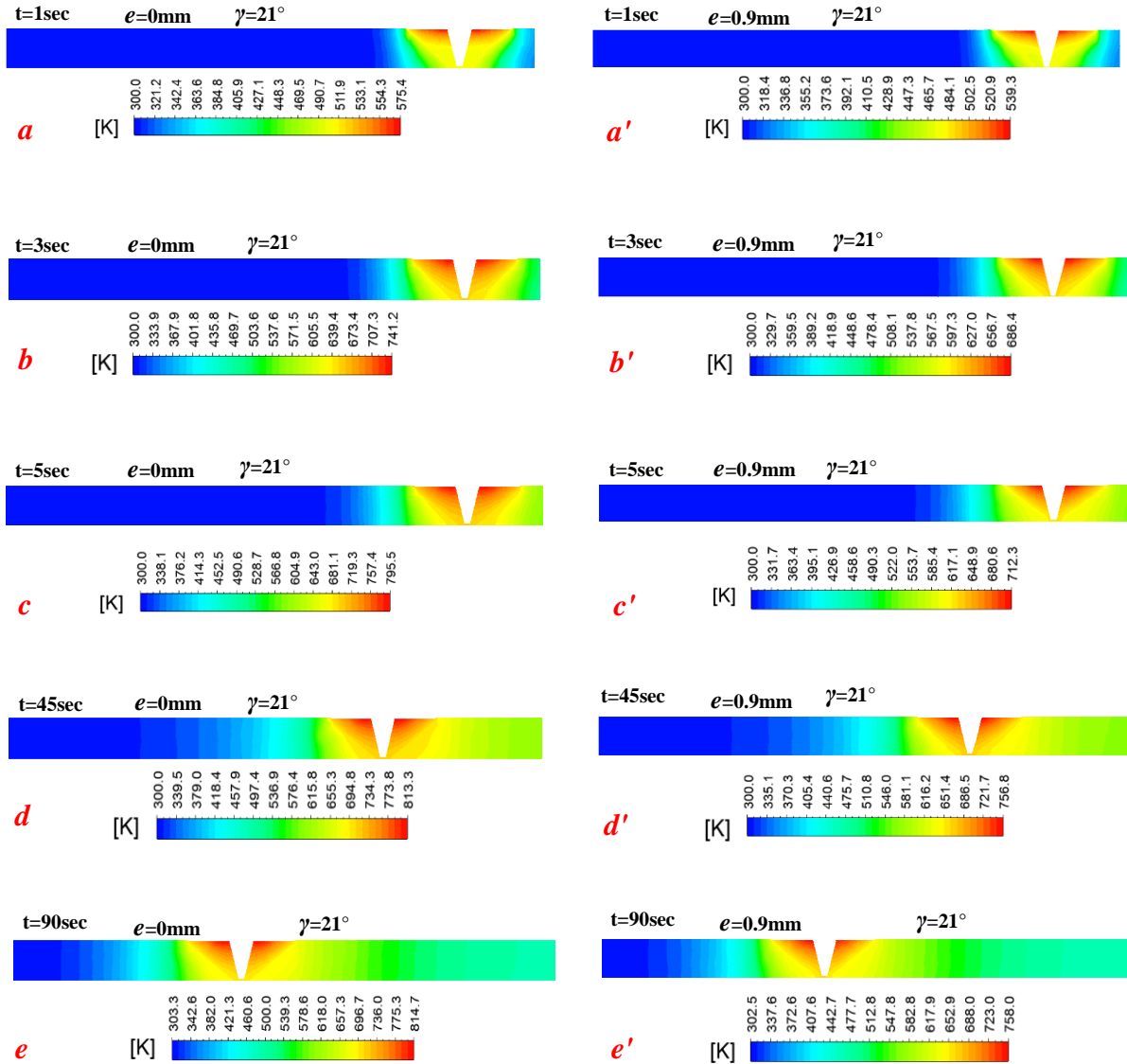


Figure 6.12 temperature distribution for the vertical plane at different time steps calculated at the same taper angle for pin eccentricities of 0mm and 0.9mm

The instantaneous snapshots for the static temperature that are displayed in figure 6.13(a,b,c,d) show the evolution of the thermal field corresponding to the proposed eccentricity values when the pin taper angle is greater than zero. The contraction in the area surrounded by the line of 520K boosts the tendency of the temperatures to dropping down as the eccentricity increases. According to the information presented in this chapter and chapter five, it can be said that the eccentricity keeps the same effect when using an eccentric pin either with or without taper angle particularly in the proposed range which is from $\gamma=0^\circ$ to $\gamma=21^\circ$.

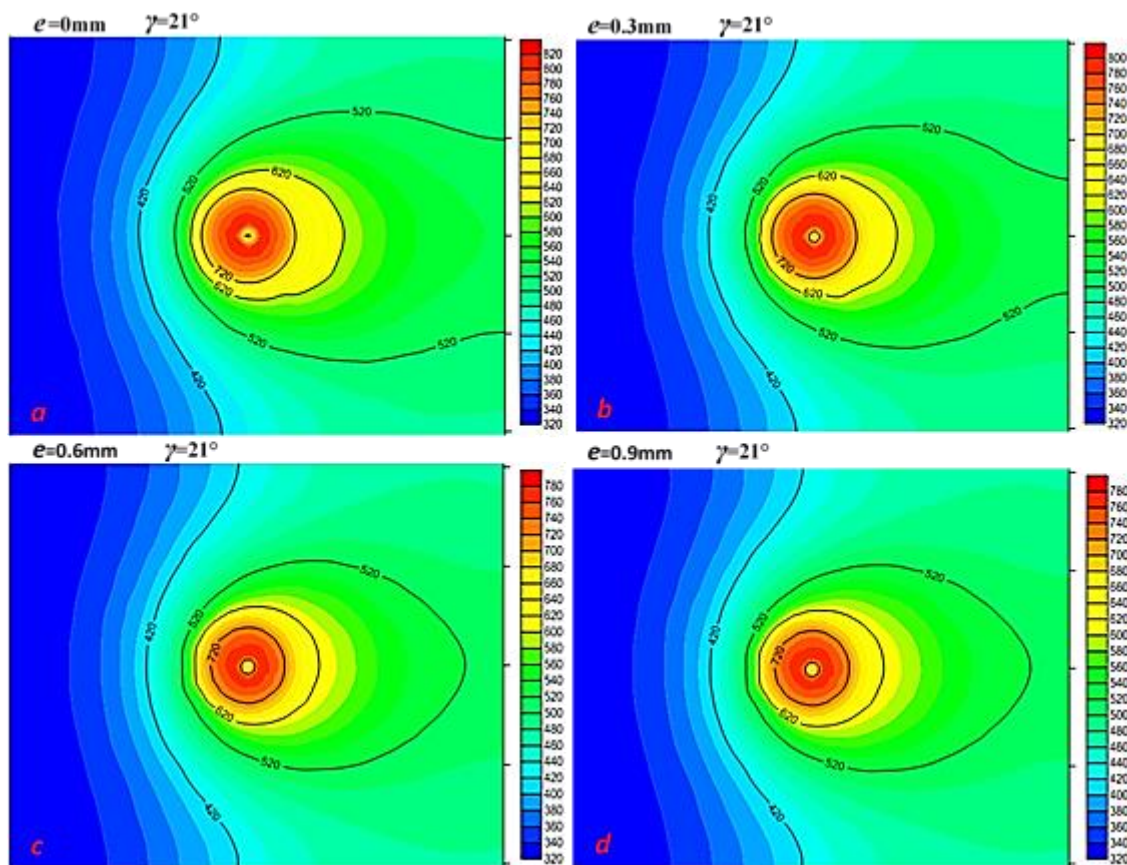


Figure 6.13 static temperature contours for different pin eccentricities $a=0\text{mm}$, $b=0.3\text{mm}$, $c=0.6\text{mm}$, $d=0.9\text{mm}$ in the existence of taper angle

In figure 6.14, it can be seen when $\gamma=21^\circ$ that the global peak temperature showing a quite similar behaviour compared to that recorded when $\gamma=0^\circ$ for the same values of eccentricity. Furthermore, it seems that the effect of eccentricity is mostly proportional as the drop in the peak temperature values due to the change in the eccentricity remains almost the same. To clarify, the peak temperature fell down by 22K when the eccentricity value moved up from 0.6mm to 0.9mm when $\gamma=0^\circ$ which was similar to the temperature drop for the same increase in the eccentricity when $\gamma=21^\circ$.

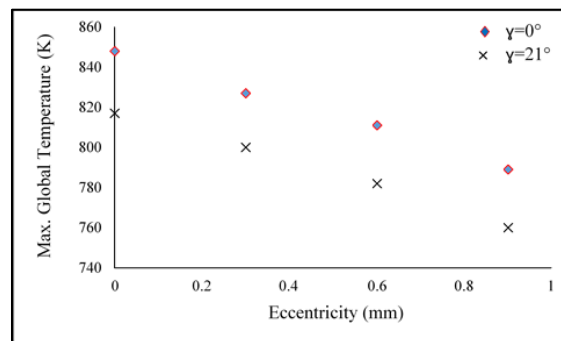


Figure 6.14 Global peak temperature for different pin eccentricities when $\gamma=0^\circ$ and $\gamma=21^\circ$

To investigate the local trend of the peak temperature, figure 6.15 exhibits a comparison between the values of the local peak at the four suggested points when $\gamma=0^\circ$ and $\gamma=21^\circ$. Although, the taper angle has raised it can be generally seen that the effect of the pin eccentricity on the maximum local temperature has not changed within the range of the eccentricity values. In other words, the local temperature decreases with the increase in the eccentricity value.

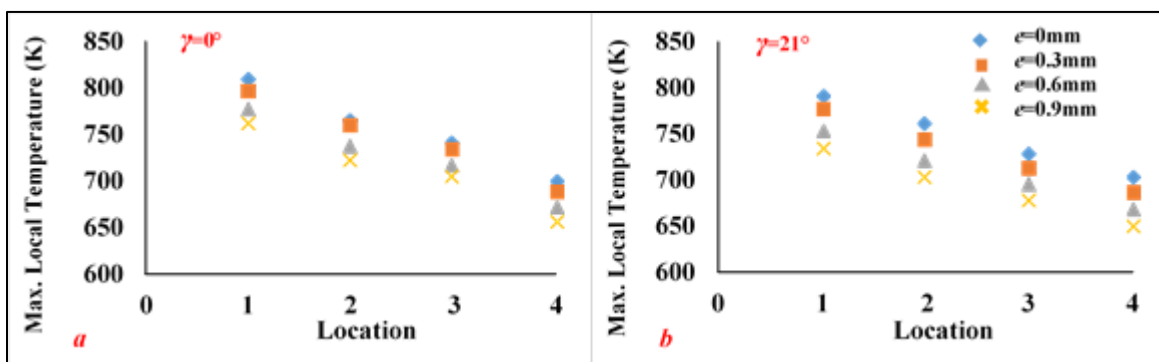


Figure 6.15 Local peak temperature for different pin eccentricities when $\gamma=0^\circ$ and $\gamma=21^\circ$

Figure 6.16, displays the acquired local temperature values in a way allows understanding the combined effect of the eccentricity and taper angle where the increase in both of them leads to dropping in the temperature. For example, the recorded temperatures when $\gamma=0^\circ$ at point no. 1 for $e=0\text{mm}$, $e=0.3\text{mm}$, $e=0.6\text{mm}$ and $e=0.9\text{mm}$ were 809K, 796.5K, 777K and 761.7K, respectively. At the same point and same eccentricity values when $\gamma=21^\circ$, the recorded temperature values were 791K, 777K, 753K and 734K, respectively.

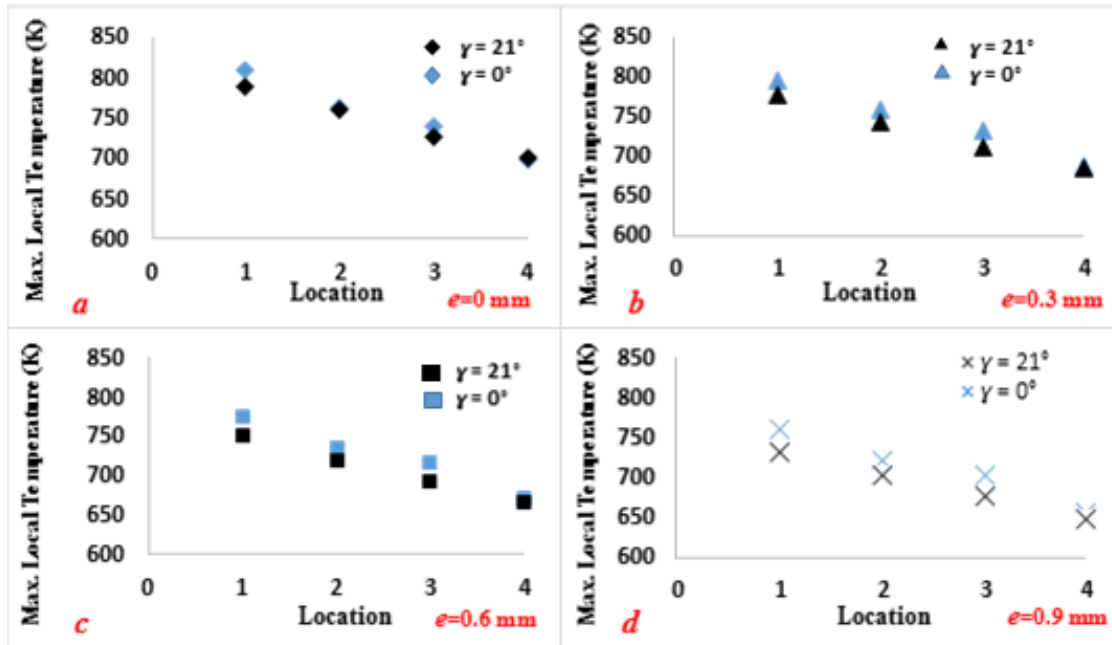


Figure 6.16 A comparison between the local peak temperatures for different pin eccentricities with taper angle and without at different locations

Regarding the effect of eccentricity on the material flow field in existence of the taper angle, no change has been generally recorded as the eccentricity helped to enlarge the size of the flow field and its role in the heat dissipation still dominant compared to that in heat generation which led to increase the material viscosity and decrease the flow velocity.

Figure 6.17, presents a comparison between the trend of the shear stress values against different pin eccentricities in case of $\gamma=0^\circ$ and $\gamma=21^\circ$. Obvious, the maximum shear stress values increase as the eccentricity increase even in the existence of the tapering angle. however, it can be seen that all dashed lines when $\gamma=21^\circ$ shifted upward compared to those when $\gamma=0^\circ$. Here, it is worth

mentioning that the reduction in the pin surface area plays a role in the enhancement of stresses beside the increase in the viscous force due to the change the temperature levels.

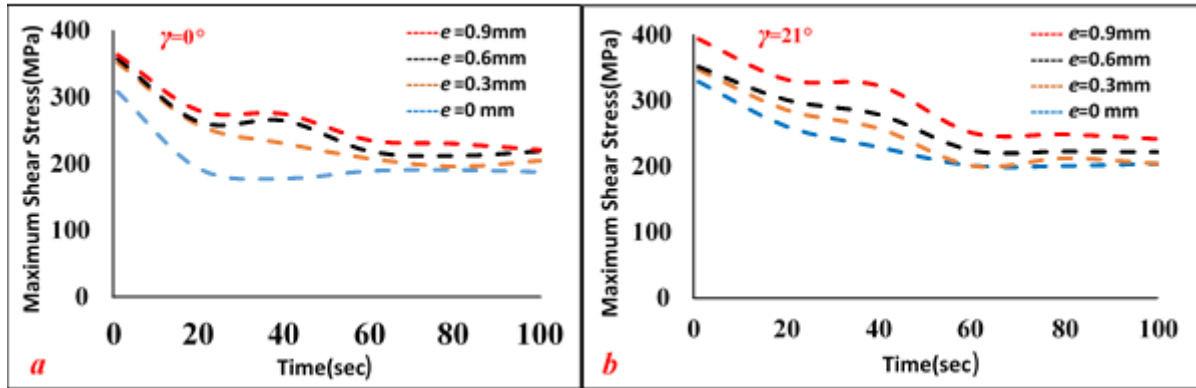


Figure 6.17 a comparison between the shear stress values when using pin eccentricities and pin taper angles

6.3.1.3 Effect of Shoulder Diameter on the Thermal Field of FSW

Figure 6.18, depicts the evolution in the temperature distribution throughout the thermal cycle for two FSW processes with different shoulder diameters under the effect of pin taper angle and eccentricity. Generally, the presented contours indicated that the temperature profile is highly affected by the variation in the shoulder size which is quite manifested in expanding of the heat affected zone according to the increase in the shoulder diameter. Although, the same trend was recorded in chapter five for those thermal cycles which were only under the effect of eccentricity the heating rate has changed. To clarify, for $\gamma = 0^\circ$ and $e = 0.9\text{ mm}$ the average heating rate in the first five seconds from the thermal cycle has increased by a value of 56 K/sec when the shoulder radius moved up from $R_s = 13\text{ mm}$ to $R_s = 25\text{ mm}$ while the average heating rate was 48.9 K/sec when $\gamma = 21^\circ$ and $e = 0.9\text{ mm}$ for the same value of increase in the shoulder radius and the same period of time. That means, the thermal cycle that is under the effects of both γ and e experienced an average heating rate less than that when the thermal cycle under only the effect of e . Eventhough, the shoulder frictional area is the same in both cases that would be also attributed to the change in the thermal performance of the tool where the frictional area of the pin becomes smaller particularly when $\gamma = 21^\circ$.

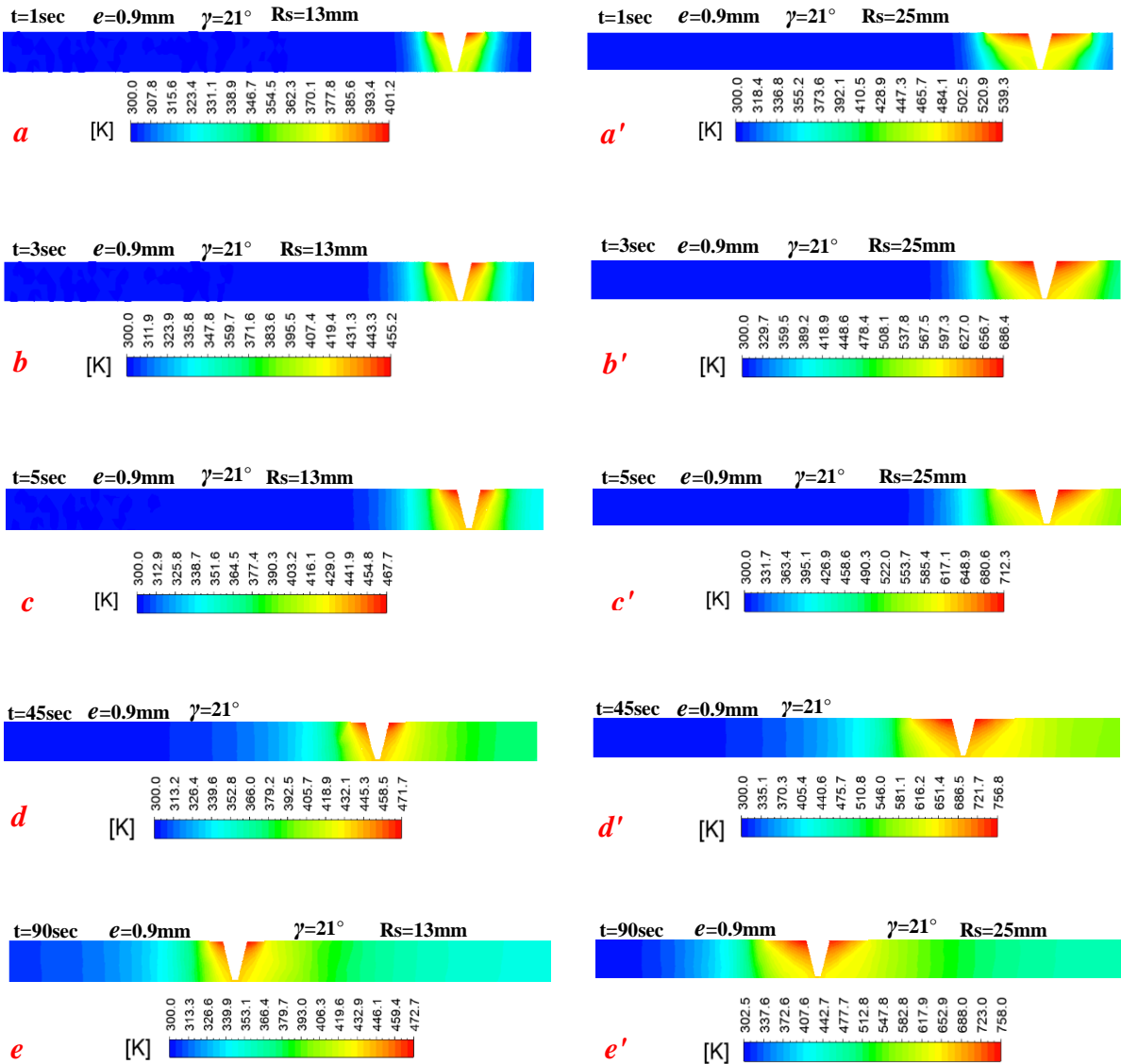


Figure 6.18 temperature distribution for the vertical plane at different time steps calculated for shoulder diameters 26mm and 50mm in the existence of taper angle and eccentricity

For the same shoulder size and eccentricity, figure 6.19(a,b) depicts how the temperature distribution affected by the taper angle. It can be expectedly seen that the temperature goes down as the taper angle increases which leads to eliminate the role of pin in the heat generation process. However, the drop in the temperature scale between a and a' is lower than that between b and b' . the reason here is the enhancement of the heat dissipation whereas the region near to the shoulder becomes much hotter when the shoulder size increases which leads to decrease the viscosity and boosting the material movement. Moreover, the temperature difference between the hot zone and the cold zone in the workpiece becomes higher which activate the heat transfer process.

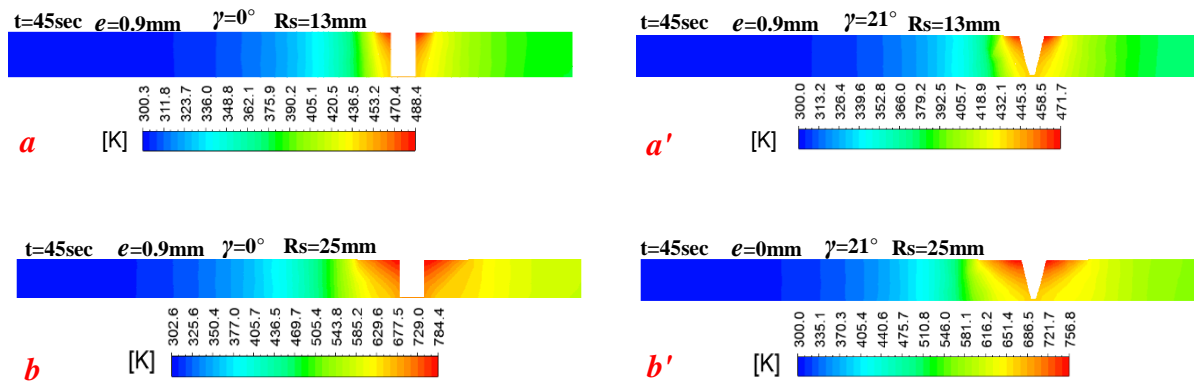


Figure 6.19 Comparison between the temperature distribution when welding with pin taper angle and without when $R_s=13\text{mm}$ and $R_s=25\text{mm}$

Figure 6.20(a,b,c,d), depicts the effect of the change in the shoulder size on the temperature distribution within the workpiece in the existence of taper angle and eccentricity. In the figure, expanding the area surrounded by line 400K has proved that the thermal field experiencing an elevation in the temperature according to the growth in the shoulder dimension and vice versa.

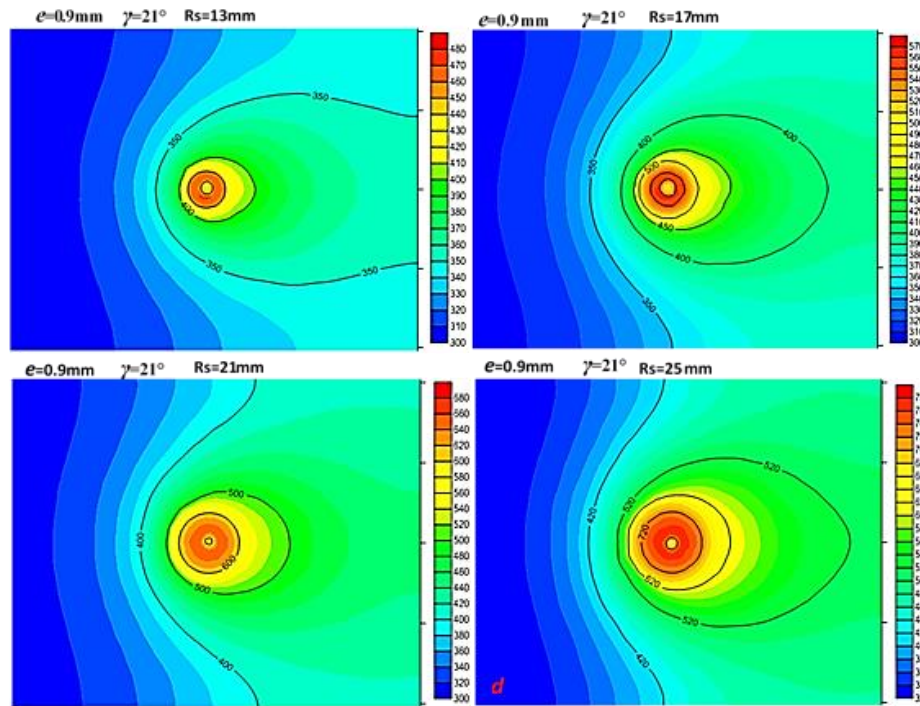


Figure 6.20 static temperature contours for different shoulder diameters $a=26\text{mm}$, $b=34\text{mm}$, $c=42\text{mm}$, $d=50\text{mm}$ under the effect of pin taper angle and eccentricity

Figure 6.21, shows the variations in the maximum global temperature against the considered shoulder diameters under the effect of taper angle as well as a comparison with its values for the same shoulder dimensions when using a concentric pin and eccentric pin without taper angle. noticeably, the change in the temperature along with varied shoulder diameters has followed the same trend in the other two cases.

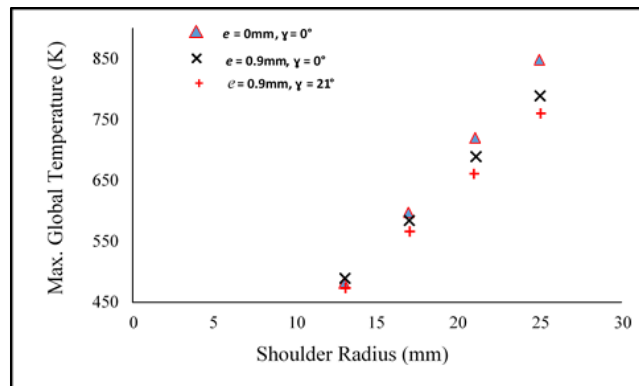


Figure 6.21 Global peak temperature for different shoulder radiuses with taper angle and without

For $\gamma=0^\circ$ and when $\gamma=21^\circ$, figure 6.22 exhibits a comparison between the general behaviour of the local temperature which are agreed where the maximum local temperatures increase according to the increase in the shoulder size. Furthermore, the results have critically plotted in figure 6.24 to display the progress in the local peak temperature corresponding the change in shoulder diameter at all points under consideration. For each point, the drop in the local temperatures due to the increase in the angle value can be seen while they are generally going up when the diameter increases. For example, at point no. 4 and $\gamma=0^\circ$ the temperature values were 418K, 496K, 578K and 655.8 for shoulder radius of 13mm, 17mm, 21mm and 25mm, respectively, while they were 412K, 488K, 571K and 649.5K when $\gamma=21^\circ$ for the same radius respectively.

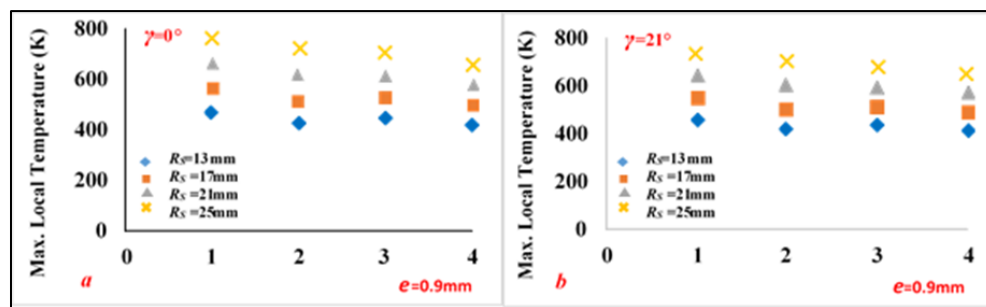


Figure 6.22 Local peak temperature for different shoulder radii with taper angle and without at different location

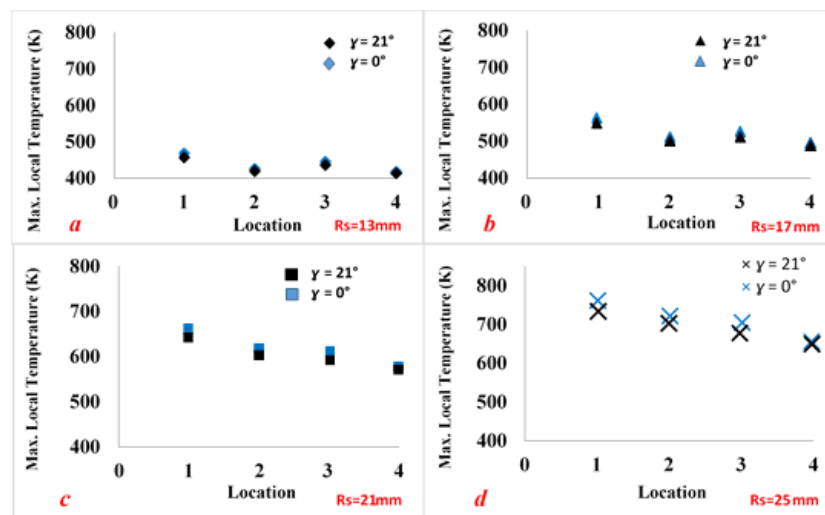


Figure 6.23 A comparison between the local peak temperatures for different shoulder radii with taper angle and without at different locations

According to the above discussed thermal trend, figure 6.24 depicts that the increase in the shoulder size causes an increase in the volume of the stirring zone and material velocity even in existence of the taper angle. That can be understood in the increase in the contact area between the shoulder and the workpiece and the drop in the material viscosity by $0.5 \times 10^5 \text{ Kg.m}^{-1}.\text{s}^{-1}$.

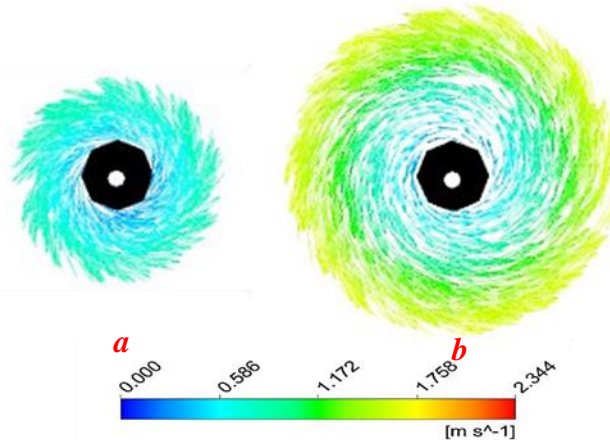


Figure 6.24 Flow velocity field for different shoulder diameters in existence of the taper angle
 $a=26\text{mm}$, $b=50\text{mm}$

Depending on the changes in the thermal field that were discussed above as well as the reduction in the pin area, it is again noticed in figure 6.25 that the values of maximum shear stress for $\gamma=21^\circ$ are higher than for $\gamma=0^\circ$. However, the effect of the variation in the shoulder diameter on the maximum wall shear stress when using tool with tapered pin is evidently agreed with that related to the straight pin at the same value of eccentricity.

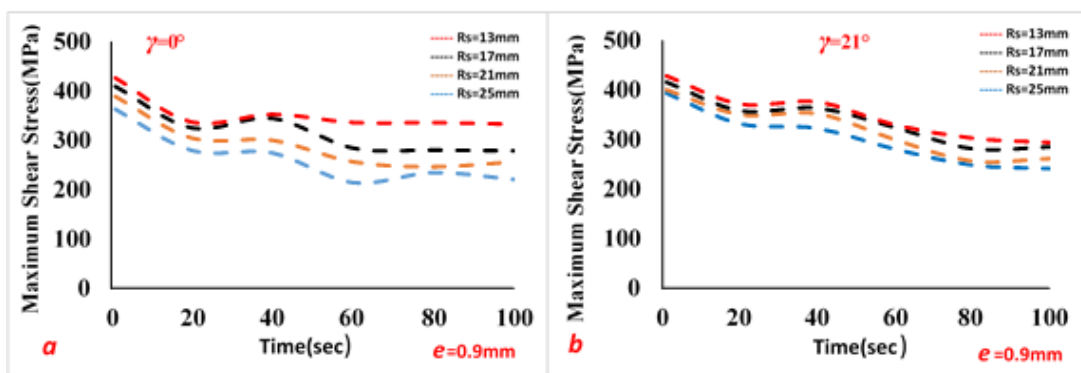


Figure 6.25 a comparison between the shear stress values when using different shoulders and pin taper angles

6.3.1.4 Effect of pin diameter on the Thermal Field of FSW

For $R_{pt}=6\text{mm}$ and $R_{pt}=12\text{mm}$, a comparison between the time dependent temperature profile is depicted in figure 6.26. It can be seen that within the increase in the pin top base size the temperature degrees are witnessing a sort of decrease such that 10K in the third second. However, figure 6.27 shows the role of the taper angle in the temperature drop at the same pin size which can be recognised by the difference in the temperature readings between a and a' as well as b and b' . it also observed when $R_{pt}=6\text{mm}$, the drop in the temperature was 27.6K while 37.3K was recorded when $R_{pt}=12\text{mm}$.

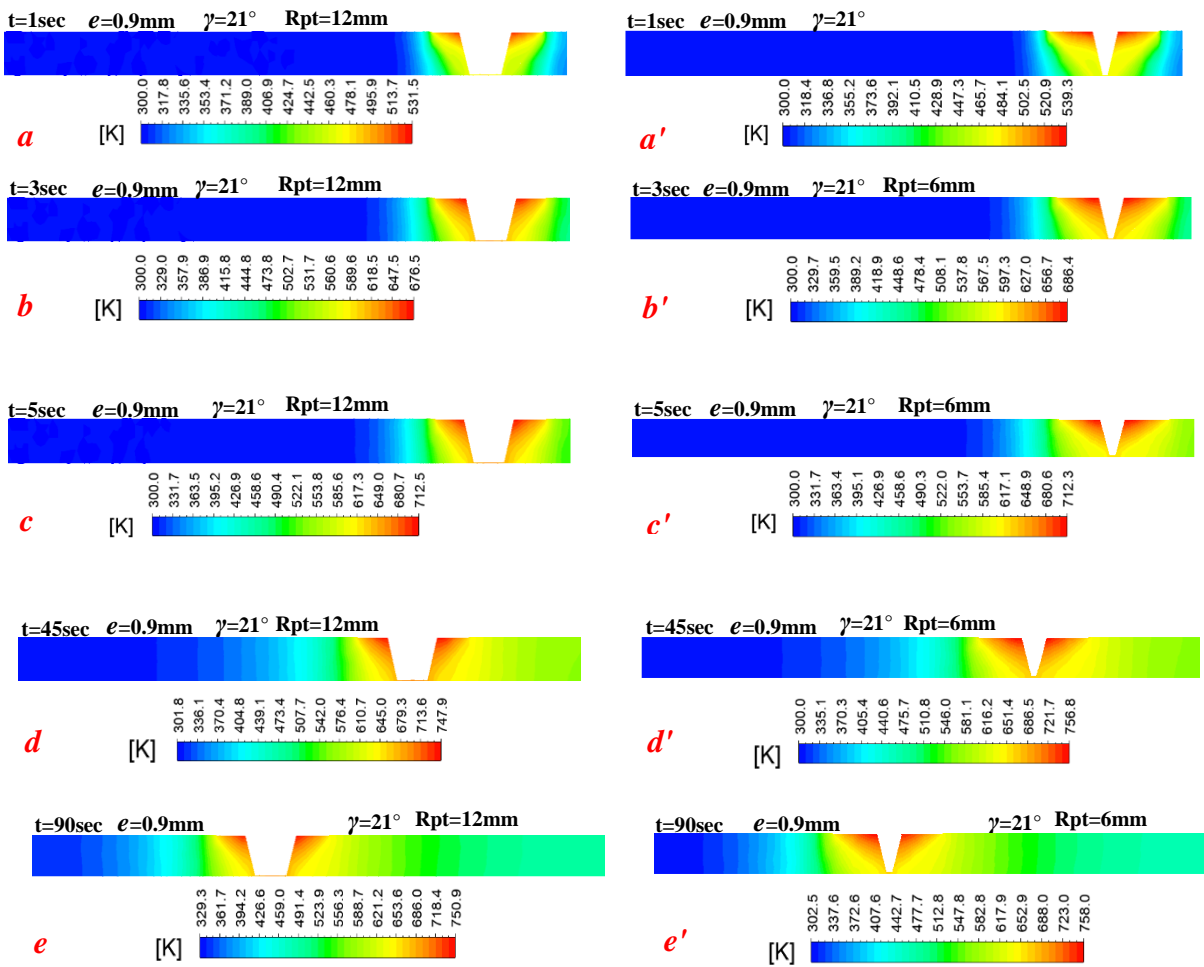


Figure 6.26 temperature distribution for the weld centre lined vertical plane at different time steps calculated for pin top diameters 12mm and 24mm in the existence of pin taper angle and eccentricity

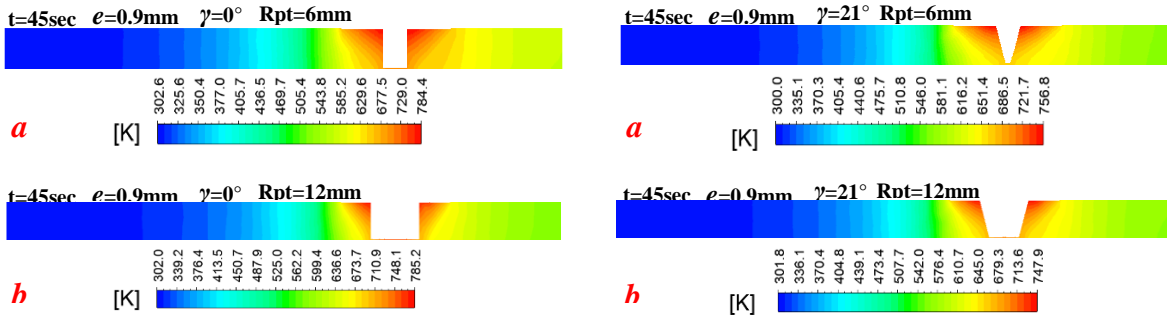


Figure 6.27 Comparison between the temperature distribution when welding with pin taper angle and without for Rpt=6mm and Rpt=12mm

Figure 6.28(a,b,c), depicts the qualitative variation in the temperature distribution for different pin top diameters in existence of taper angle and eccentricity. In the figure, the changes in the profile represent the effect of the varied pin top size where the appearing of line 500K in *b* instead the line of 520K that has taken place in *a* indicating the temperature drop corresponding to the increase in the pin top radius from Rpt=6mm to Rpt=9mm. However, it can be observed that the change in the temperature profile is very marginal between *b* and *c* as the role of the pin in heat generation process becomes greater which would compensate the losses due to the decrease in the shoulder size. That can be also seen for $e=0.9\text{mm}$ and $\gamma=21^\circ$ in figure 6.29 in which the maximum global temperatures are plotted against the pin top size and compared with their values when $e=0\text{mm}$ and $\gamma=0^\circ$ as well as $e=0.9\text{mm}$ and $\gamma=0^\circ$. It is worth mentioning here that the difference in the temperature drop can be reasoned in the light of the balance between the heat generation and heat dissipation due to the change in the pin size and eccentricity. Noticeably, the temperature when Rpt=3mm was not displayed because of the pin bottom base would not have been created in this case.

Regarding the local trend of the peak temperature when $\gamma=21^\circ$, the results in figure 6.30 revealed that the temperature values have recorded a reduction against the pin growth and a variation when compared with those for $\gamma=0^\circ$. This variation can be more clarified in figure 6.31 where the temperature at every single point has witnessed a drop for all proposed pin dimensions. In the same time, the flow field has been influenced by the change in temperature due to the variation in the pin size where the viscosity increased from $0.938 \times 10^5 \text{ Kg.m}^{-1}.\text{s}^{-1}$ to $1.68 \times 10^5 \text{ Kg.m}^{-1}.\text{s}^{-1}$

corresponding to the increase in the pin top radius from $R_{pt}=6\text{mm}$ to $R_{pt}=12\text{mm}$ which means a decrease in the flow velocity.

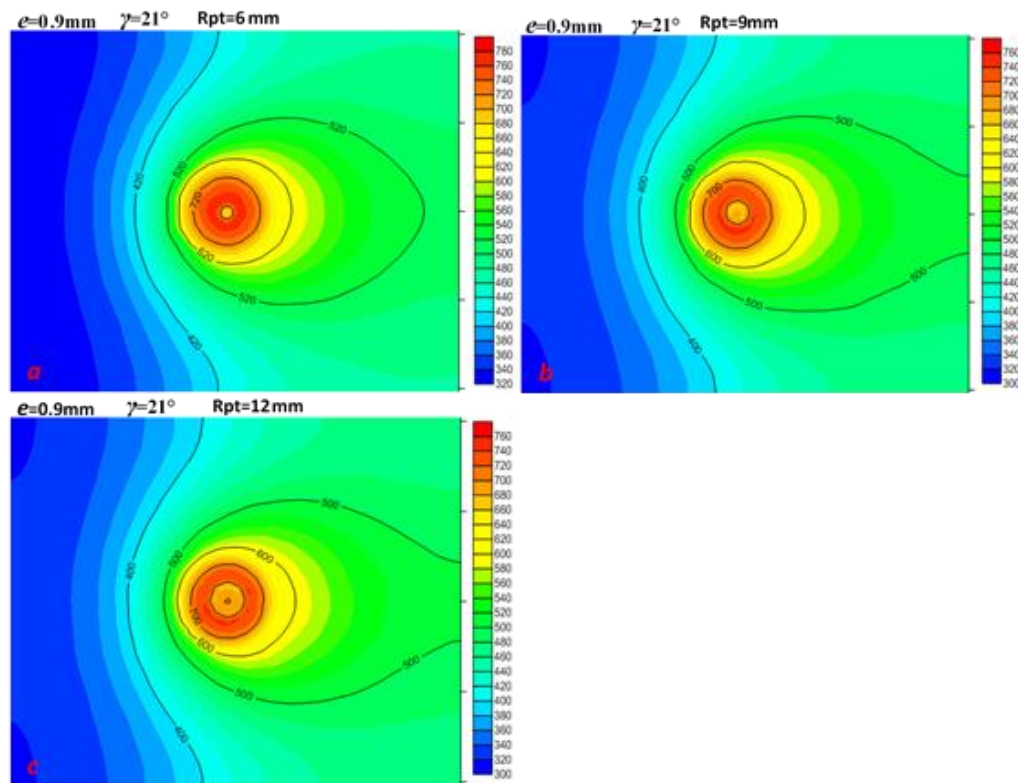


Figure 6.28 static temperature contours for different pin top base diameters $a=12\text{mm}$, $b=18\text{mm}$, $c=24\text{mm}$ in the existence of pin taper angle and eccentricity

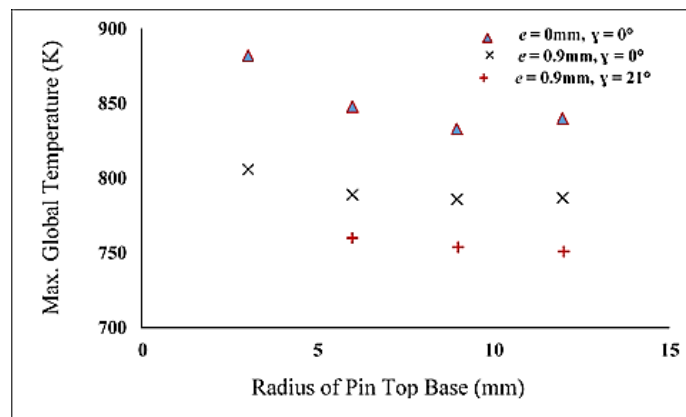


Figure 6.29 Global peak temperature for different pin top base radiuses with taper angle and without

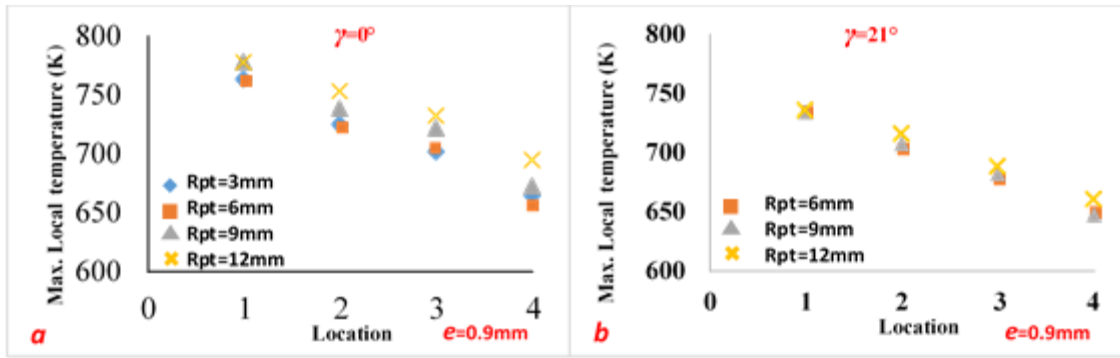


Figure 6.30 Local peak temperature for different pin radii with taper angle and without at different location

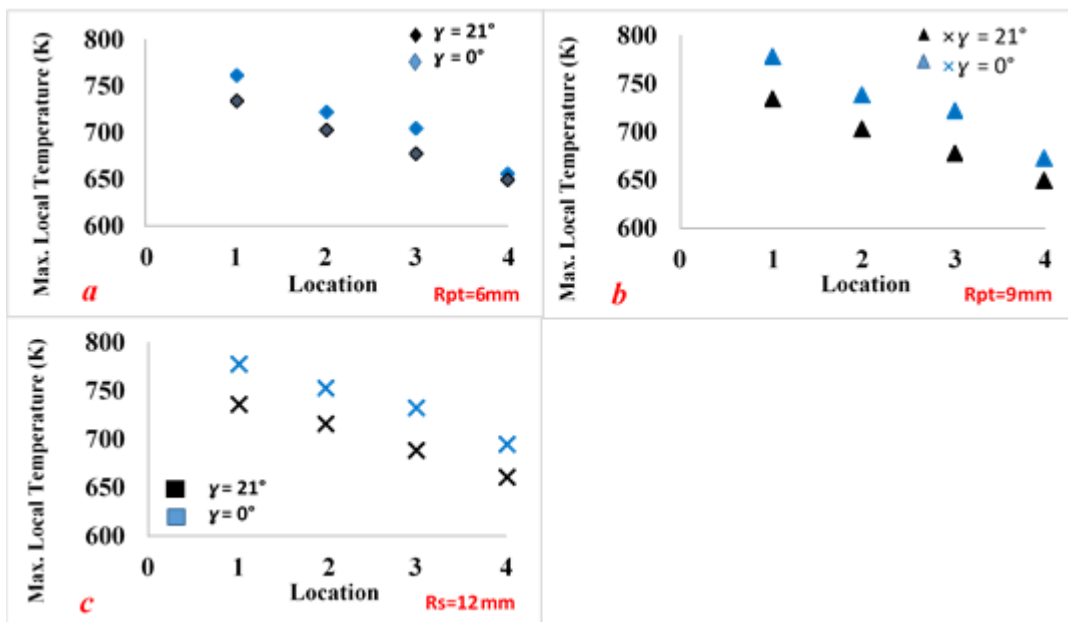


Figure 6.31 comparison between the local peak temperatures for different pin radii with taper angle and without at different locations

The comparison between the values of the maximum shear stress that is held in figure 6.32 permits to estimate the progress in the stress values when the taper angle increases from 0° to 21° for different pin top base sizes. Expectedly, there was a shift upward in the stress level due to the decrease in the temperature and the pin size. However, at $\gamma=21^\circ$ it has orderly kept the general behaviour against the pin radius where the highest values have been registered when $R_{pt}=12\text{mm}$ while the minimum was at $R_{pt}=6\text{mm}$.

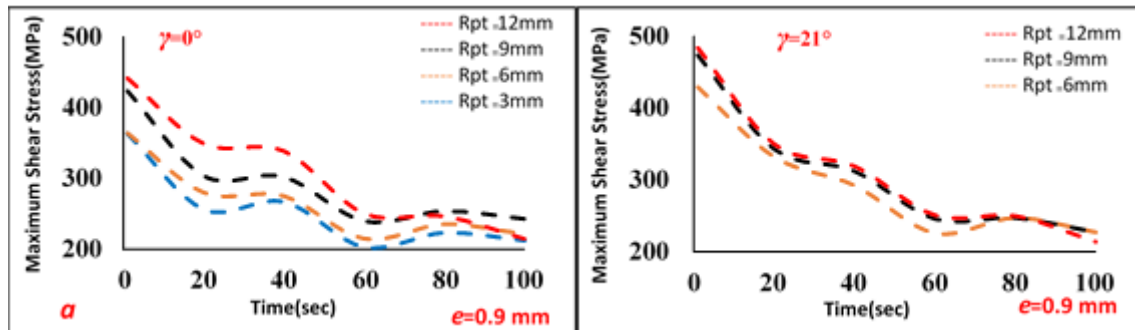


Figure 6.32 a comparison between the shear stress values when using different pin sizes and pin taper angles

6.3.1.5 The effect of pin Height on the Thermal Field of FSW

Figure 6.33, shows the transient evolution in the temperature distribution when the pin height grew from 9mm to 12mm under the effect of pin taper angle and eccentricity. It is apparent that the temperature distribution changes according to the change in the pin height where a decrease in the temperature degrees can be noted. That is what has been observed in the case of eccentric straight pin which was reasoned by the enhancement in the heat dissipation. Although, the eccentricity has been kept similar that can be understood in the amount of the stirred material which become greater when $H_p=12\text{mm}$. For further analysis, figure 6.34(a,b) illustrates the effect of the pin taper angle at the same pin height which can be seen in the temperature drop. At the same moment of the thermal cycle, figure 6.35 displays the variation in the temperature according to the change in the pin height where the drop in temperature has been likewise ascertained with that growing in the pin height. However, the stabilisation in the temperature scale indicates that the range of varying is not that much wide.

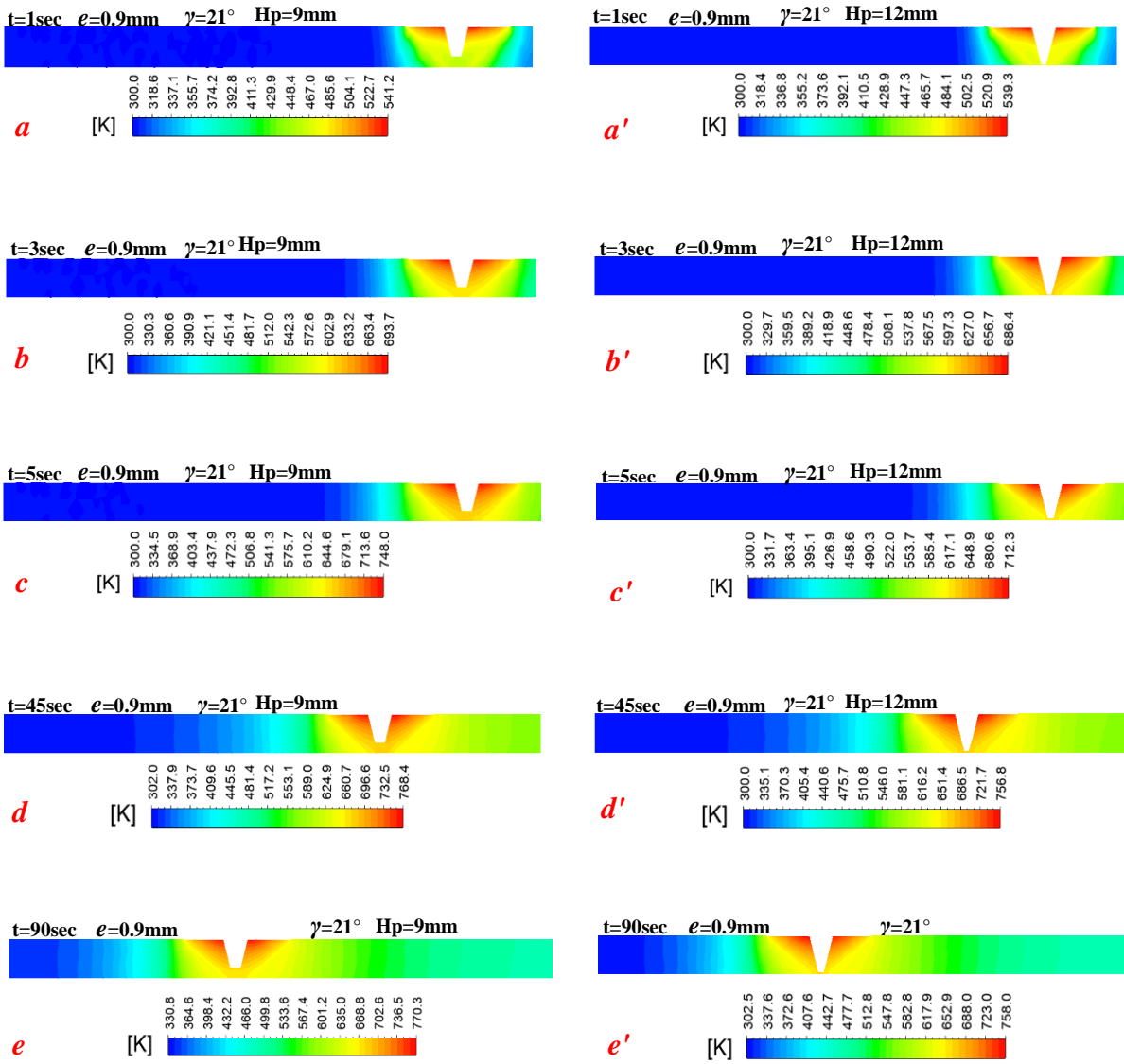


Figure 6.33 temperature distribution for the weld centre lined vertical plane at different time steps calculated for pin heights of 9mm and 12mm in the existence of pin taper angle and eccentricity

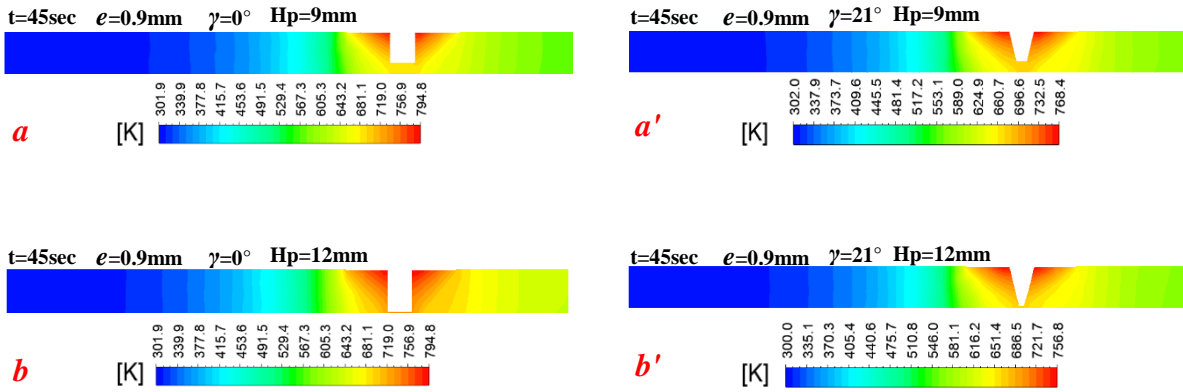


Figure 6.34 Comparison between the temperature distribution when welding with pin taper angle and without and for $H_p=9\text{mm}$ and $H_p=12\text{mm}$

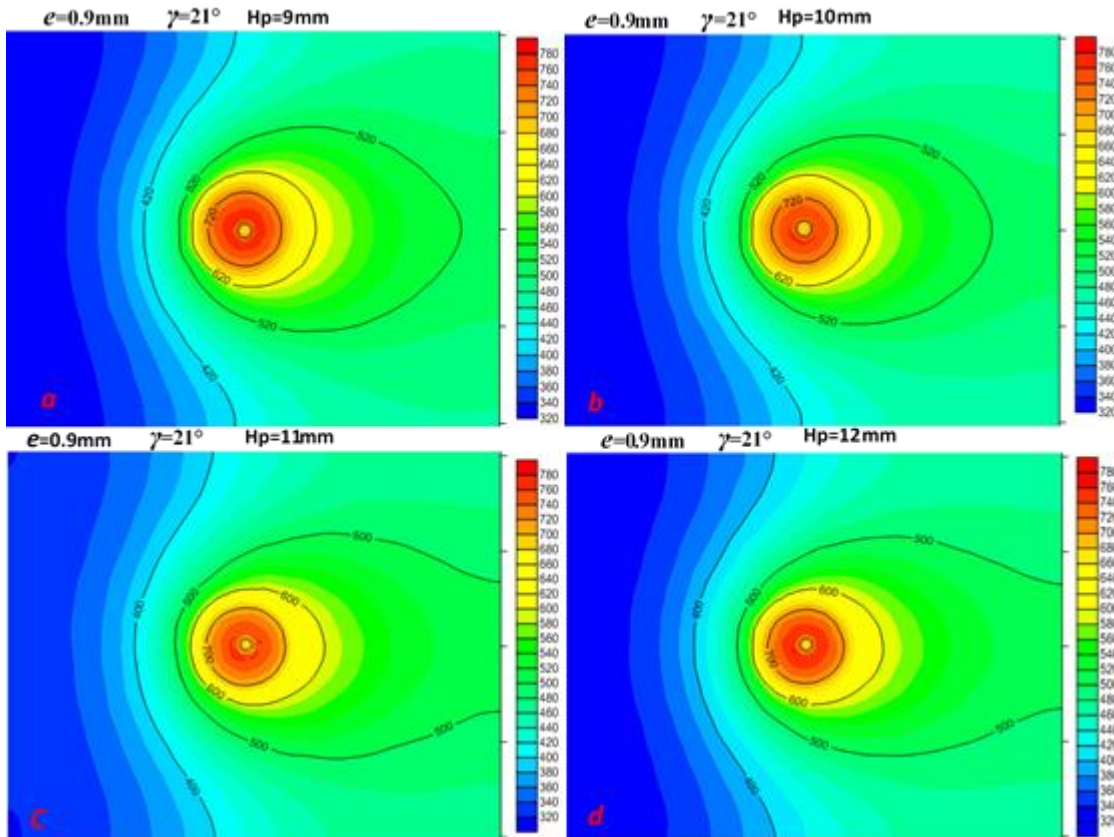


Figure 6.35 static temperature contours for different pin heights a=9mm, b=10mm, c=11mm, d=12mm in the existence of pin taper angle and eccentricity

In figure 6.36, the global peak temperature when $e=0.9\text{mm}$ and $\gamma=21^\circ$ shows a trend which is similar to that recorded for $e=0.9\text{mm}$ and $\gamma=0^\circ$ but opposite to the values acquired when $e=0\text{mm}$ and $\gamma=0^\circ$. Evidently, the peak temperature values went down in existence of the taper angle which is expected as the frictional area decreases. Interestingly, the temperature drop seems to be almost proportional to the pin height under the combined effect of the pin taper angle and eccentricity where it is ranging between 3.2% to 3.6% compared to the temperature values when $e=0.9\text{mm}$ and $\gamma=0^\circ$. Although, The general trend of the material flow field against the change the pin height for the same pin eccentricity was similar to that when $\gamma=0^\circ$, the velocity registered a relative drop corresponding to the increase in the viscosity which was boosted by the temperature decrease as the taper angle increases.

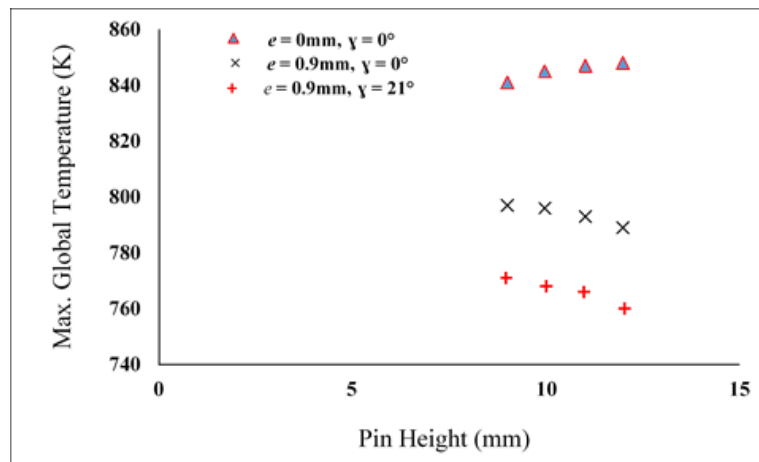


Figure 6.36 Global peak temperature for different pin heights with pin taper angle and without

Figure 6.37, presents a comparison between the local behaviour of the peak temperature when $\gamma=21^\circ$ and $\gamma=0^\circ$. It can be clearly seen that the peak temperature has generally experienced a similar behaviour for both cases at the points under consideration. However, the results depicted in figure 6.38 have effectively given a vivid picture of the drop in the local peak temperature against the increased pin height and the taper angle. For instance, the local peak temperature at point no. 1 has reached 767K when $\gamma=0^\circ$ and $H_p=9\text{mm}$ while 761.7K when $H_p=12\text{mm}$ for the same value of γ . At the same location when $\gamma=21^\circ$, the temperature recorded 745K and 736K for the pin heights of 9mm and 12mm, respectively.

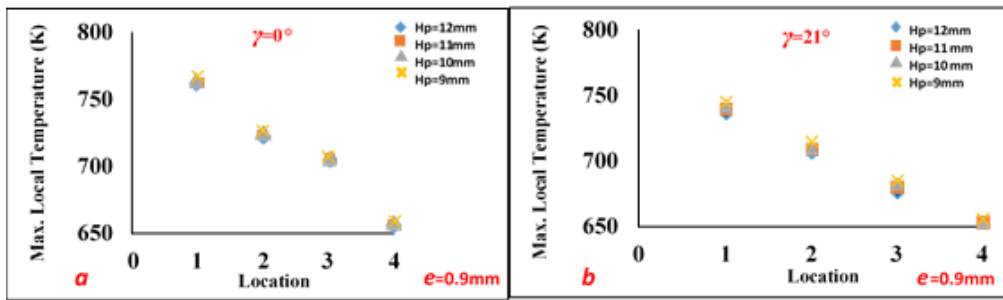


Figure 6.37 Local peak temperature for different pin heights with and without pin taper angle at different locations

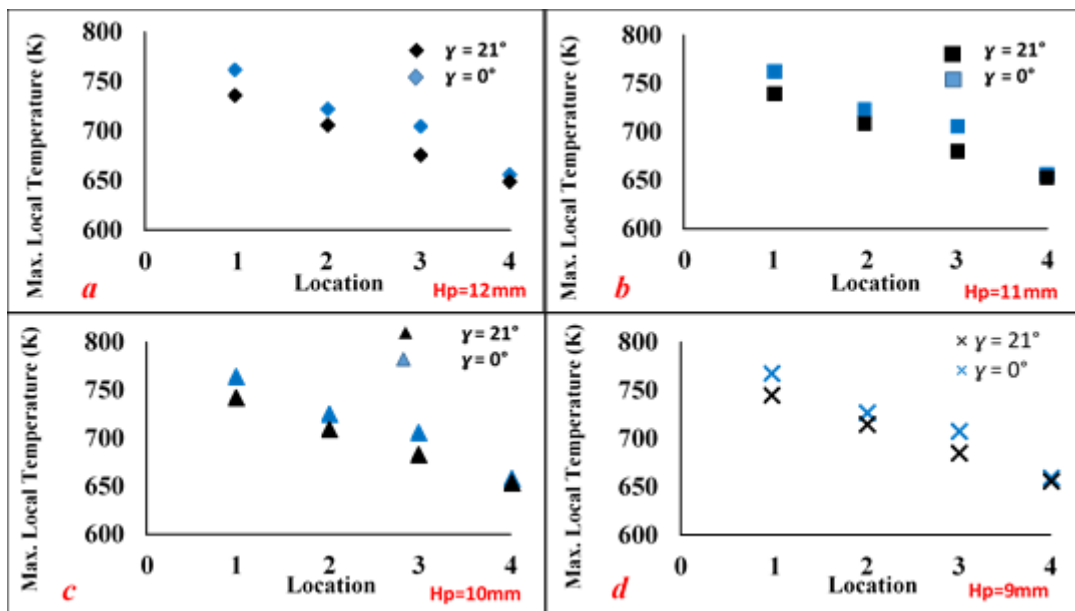


Figure 6.38 A comparison between the local peak temperatures for different pin heights with and without pin taper angle at different locations

Compared to the straight pin, figure 6.39 shows that the tapered pin has scored higher values for the maximum shear stress. Likewise, its values have moved upward with the increase in pin heights. That has remarkably happened as the exposed surface area is increasing which can be

justified as the effect of the viscous force on the stress values is dominant rather than the exposed area.

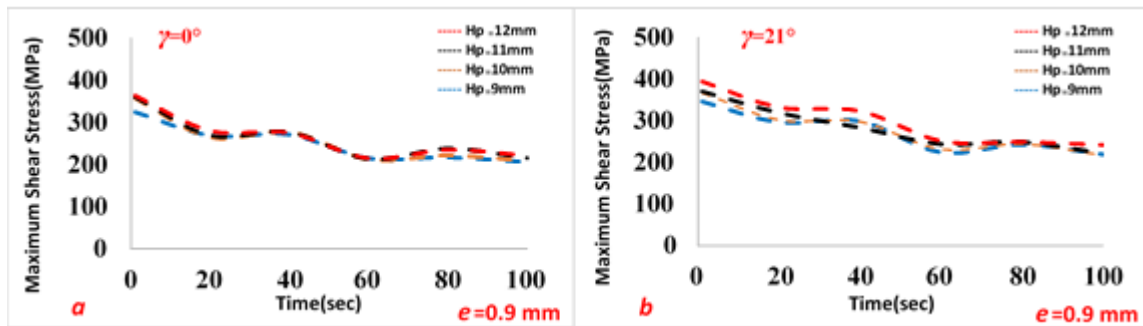


Figure 6.39 a comparison between the shear stress values when using different pin heights and pin taper angles

6.3.1.6 The effect of the workpiece thickness on the Thermal Field of FSW

The two lists of contours depicted in figure 6.40 reflect the time dependent variation in the temperature distribution through FS welded workpieces with different thickness. As can be seen that the hottest zone has become more restricted with the increased workpiece thickness which means a reduction in the temperatures level. This tendency was similarly noted for welding with the tools proposed in chapter four and five where the rate of heat dissipation might be increased due to the increase in the plate thickness. To manifest the influence of the taper angle on the temperature distribution for different workpiece thicknesses, figure 6.41 depicts the change in the thermal field due to the increase in the taper angle from $\gamma = 0^\circ$ to $\gamma = 21^\circ$ for the plate thicknesses of 12.7mm and 18.7mm. It can be seen that the drop in the temperature when thick=12.7mm is about three times of that recorded when thick=18.7mm. In figure 6.42 (a,b,c,d) where an additional investigation can be achieved, the shrinkage in line 500K has proved the reduction of temperature corresponding to the increase in the workpiece thickness.

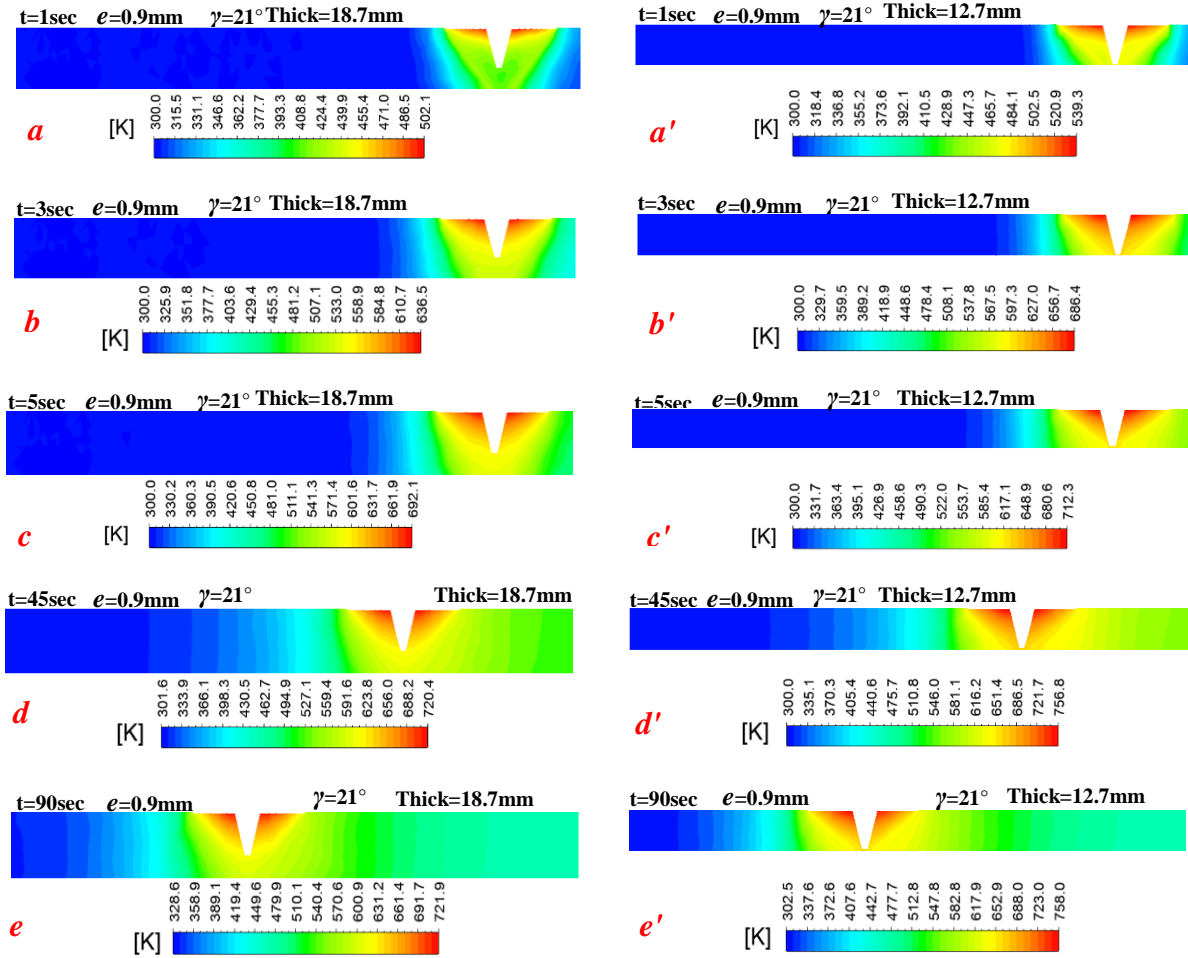


Figure 6.40 temperature distribution for the vertical plane at different time steps calculated for workpiece thickness 18.7mm and 12.7mm in the existence of pin taper angle and eccentricity

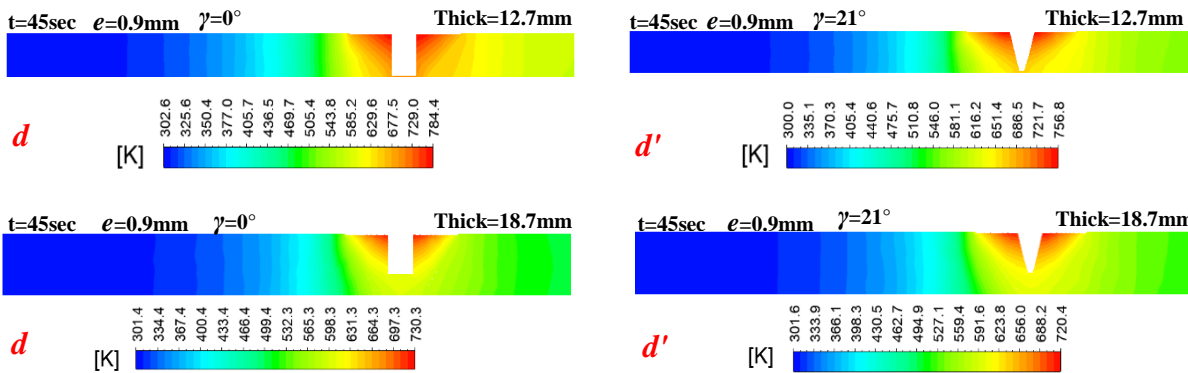


Figure 6.41 Comparison between the temperature distribution when welding with and without pin taper angle for varied workpiece thicknesses

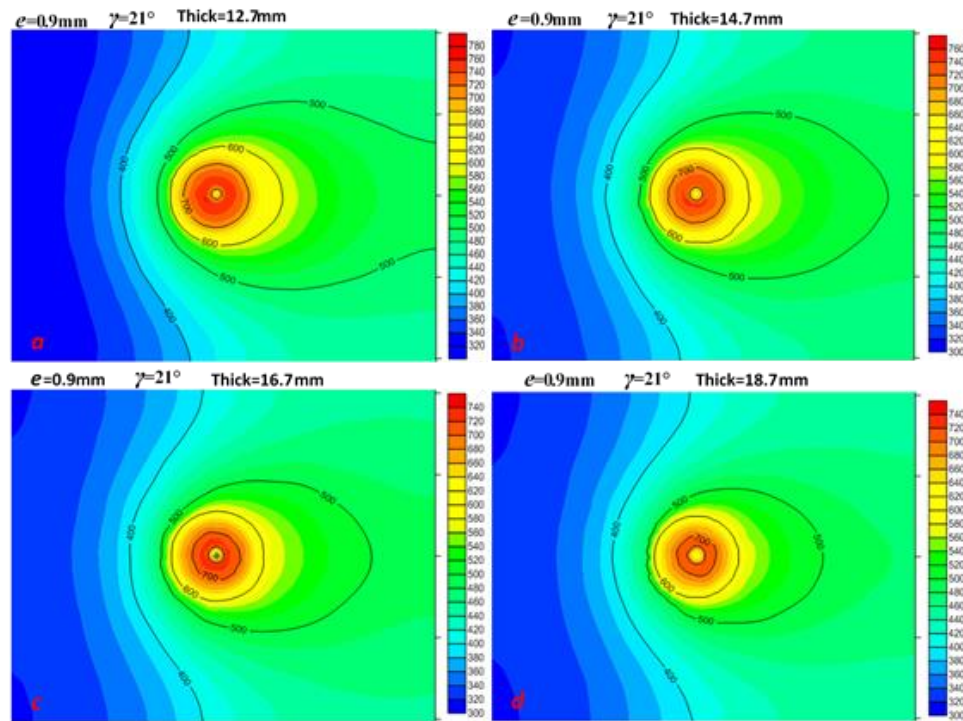


Figure 6.42 static temperature contours for different workpiece thickness $a=12.7\text{mm}$, $b=14.7\text{mm}$, $c=16.7\text{mm}$, $d=18.7\text{mm}$ in the existence of pin taper angle and eccentricity

Figure 6.43, shows the variation in the values of the global peak temperature when using tools with eccentric tapered pin compared with those related to the concentric and eccentric pins. The major difference being that there was a noticeably lower level in the readings when $e=0.9\text{mm}$ and $\gamma=21^\circ$. However, the increased role of the eccentricity in the heat dissipation could justify the steeper inclination in the results when $e=0.9\text{mm}$ and $\gamma=0^\circ$. Figure 6.44, displays that the maximum local temperature for $\gamma=21^\circ$ has generally behaved as similar as those when $\gamma=0^\circ$ where the highest value registered for thick=12.7mm while the lowest has been for thick=18.7mm at all points under consideration. Until the effect of plate thickness at varied values of γ on the local peak temperature tangibly appears, the acquired data was efficiently plotted in figure 6.45.

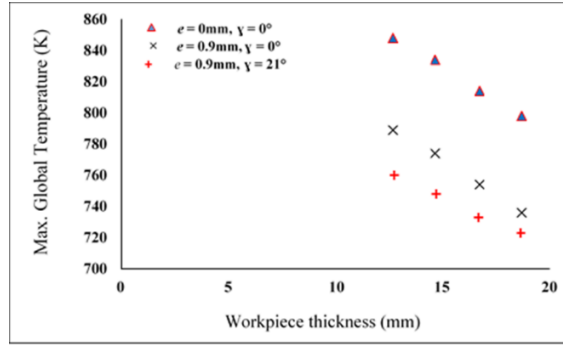


Figure 6.43 Global peak temperature for different workpiece thickness with and without pin taper angle

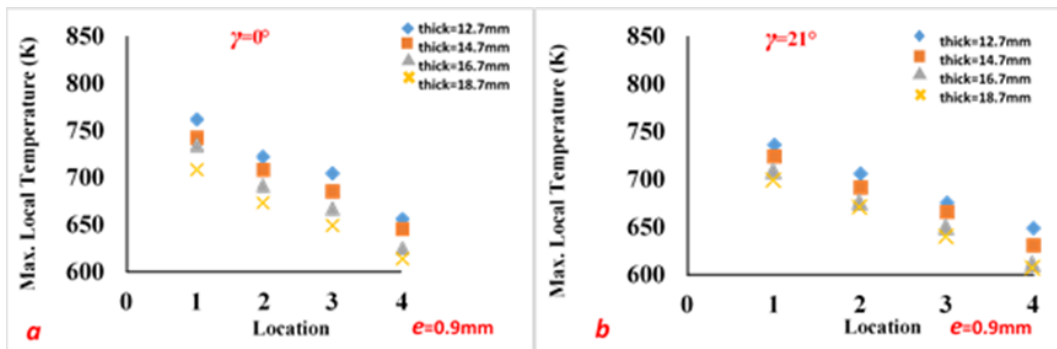


Figure 6.44 Local peak temperature for different workpiece thicknesses with and without taper angle at different locations

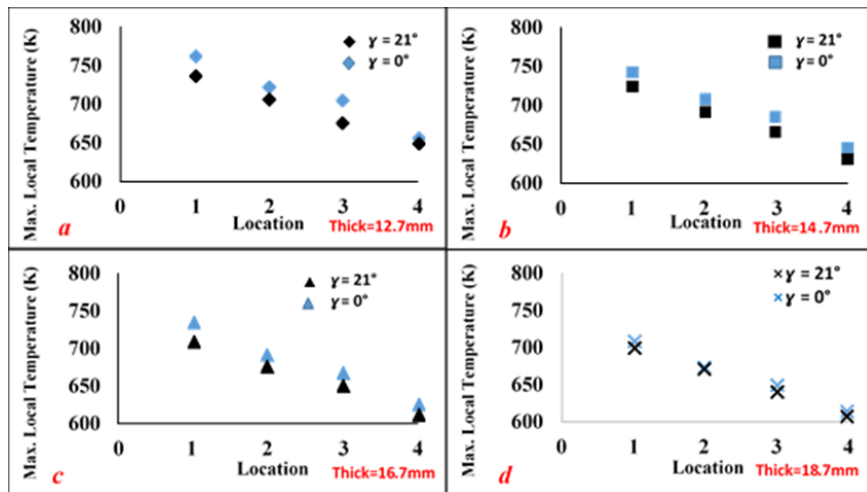


Figure 6.45 A comparison between the local peak temperatures for different workpiece thicknesses with and without taper angle at different locations

The change in the temperature field resulted from the taper angle effect and represented in the temperature drop reflected in the flow velocity. For instance, the decrease in the velocity reached 0.3m/s $\gamma=21^\circ$. However, the flow field has shown a trend against the variation in the plate thickness which is as similar as that when $\gamma=0^\circ$. In addition to that elevation in the shear stress values due to the variation in the taper angle, figure 6.46 has also depicted how those numerical values raising against the increased workpiece thickness. For instance, 363.6MPa and 468MPa have been recorded when $\gamma=0^\circ$ at $t=1$ sec for thicknesses of 12.7mm and 18.7mm, respectively while at the same time and $\gamma=21^\circ$, 394MPa and 481.4Mpa were attained for 12.7mm and 18.7mm, respectively.

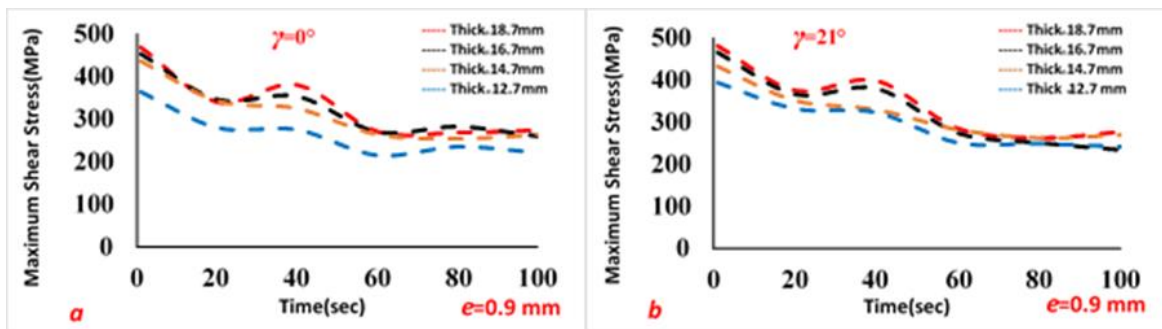


Figure 6.46 a comparison between the maximum shear stress values when using different workpiece thicknesses and pin taper angles

6.3.2 The effect of rotational speed on the Thermal Field of FSW

Usually, the increase in the rotational speed leads to augment the temperature levels. Hence, the current situation in which the tapered pin is considered was not an exception as can be seen in figure 6.47. The snapshots in the figure represent the progress in the thermal field through the weldment due to the variation in the rotational speeds when using tools with tapered pins. When the attention is focused on the line 400K, it is clearly observed the gradual widening in the area surrounded by this line against the increasing in the rotational speed. However, the recorded temperature levels are not as the same as those presented in figure 5.45 which are for a tool with straight pin. In other words, the temperature scale indicates a decline in the temperature degrees which can be a consequence of the taper angle.

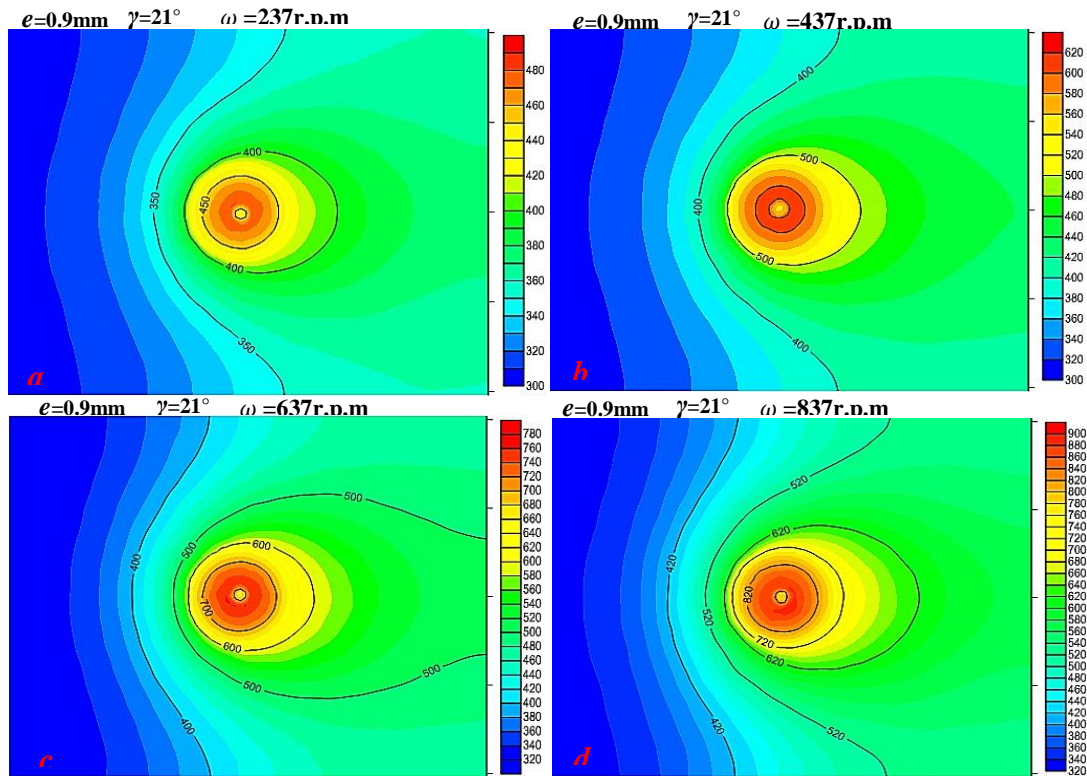


Figure 6.47 static temperature contours for different rotational speed a=237r.p.m, b=437r.p.m, c=637r.p.m, d=837r.p.m in the existence of pin taper angle and eccentricity.

For further investigation, as it can be seen in figure 6.48 a comparison has been transiently drawn to study the thermal field at high value of rotational speed when $\omega = 837\text{r.p.m}$ for $\gamma=0^\circ$ and $\gamma=21^\circ$. According to the temperature scale, hence the temperature difference between the two thermal cycles has reached values greater than 25K particularly at advanced stages of the process. Although, the severity of the thermal cycle varies from $\gamma=0^\circ$ to $\gamma=21^\circ$ the temperature level has exceeded the material solidus temperature after $t=3\text{sec}$ in both cases. Therefore, the current used model has monitored the time dependent evolution of the liquid fraction where another meaningful comparison was beneficially drawn to evaluate the influence of the pin taper angle on the liquid fraction at the same welding conditions. Figure 6.49, shows that the mushy zone has formed where the liquid fraction achieved 0.32 at $t=5\text{sec}$ for $\gamma=0^\circ$ which is more than five times of that for $\gamma=21^\circ$. Because of the variation in the temperatures level, it can be also seen in the figure that the size of mushy zone differs from case to another where it becomes smaller when the temperature dropped down. Additionally, the liquid fraction has not remarkably reached 1 even at advanced stage from the thermal cycles ($t=90\text{sec}$).

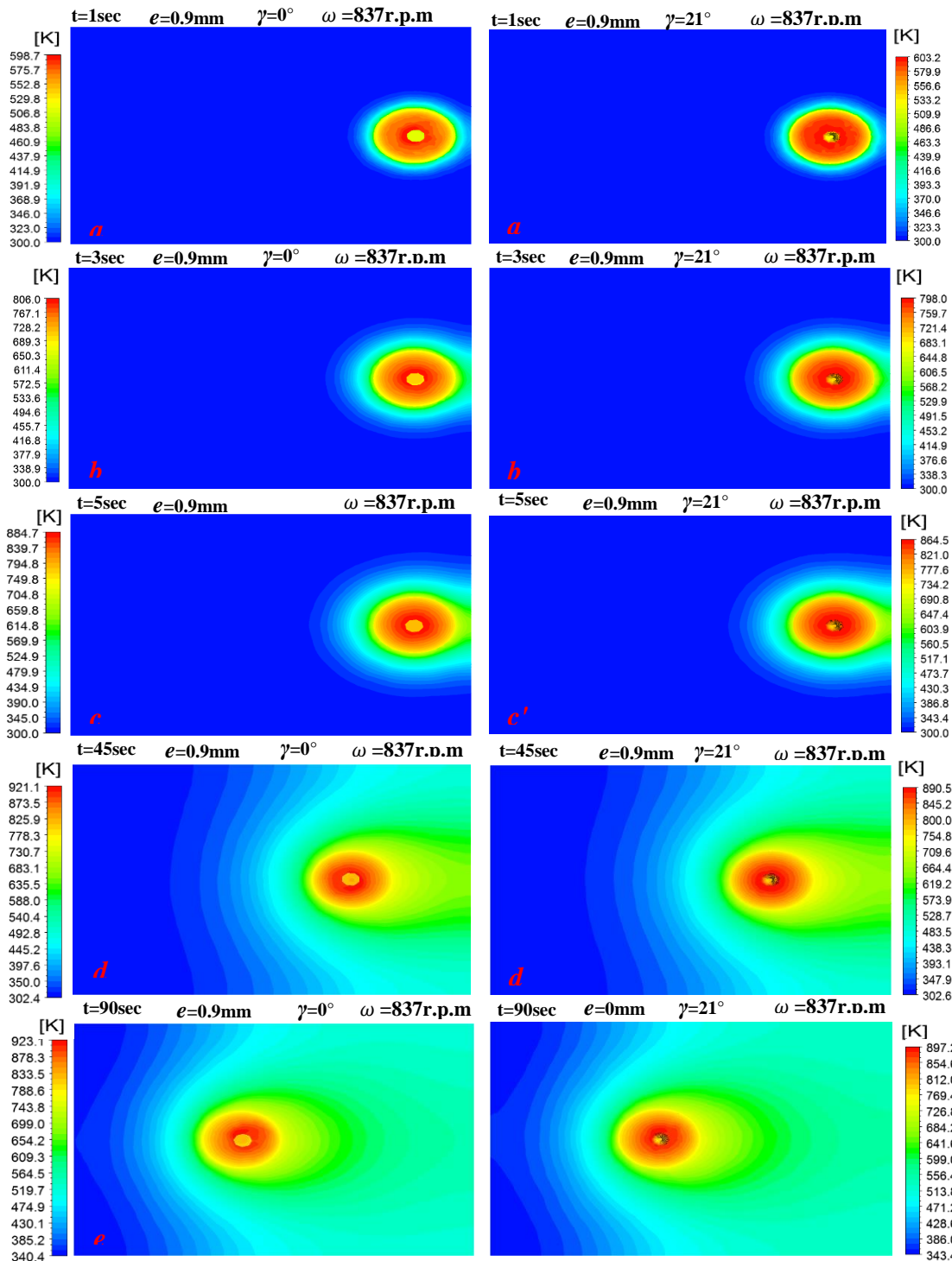


Figure 6.48 Comparison between the temperature distribution when welding with and without pin taper angle at high rotational speed.

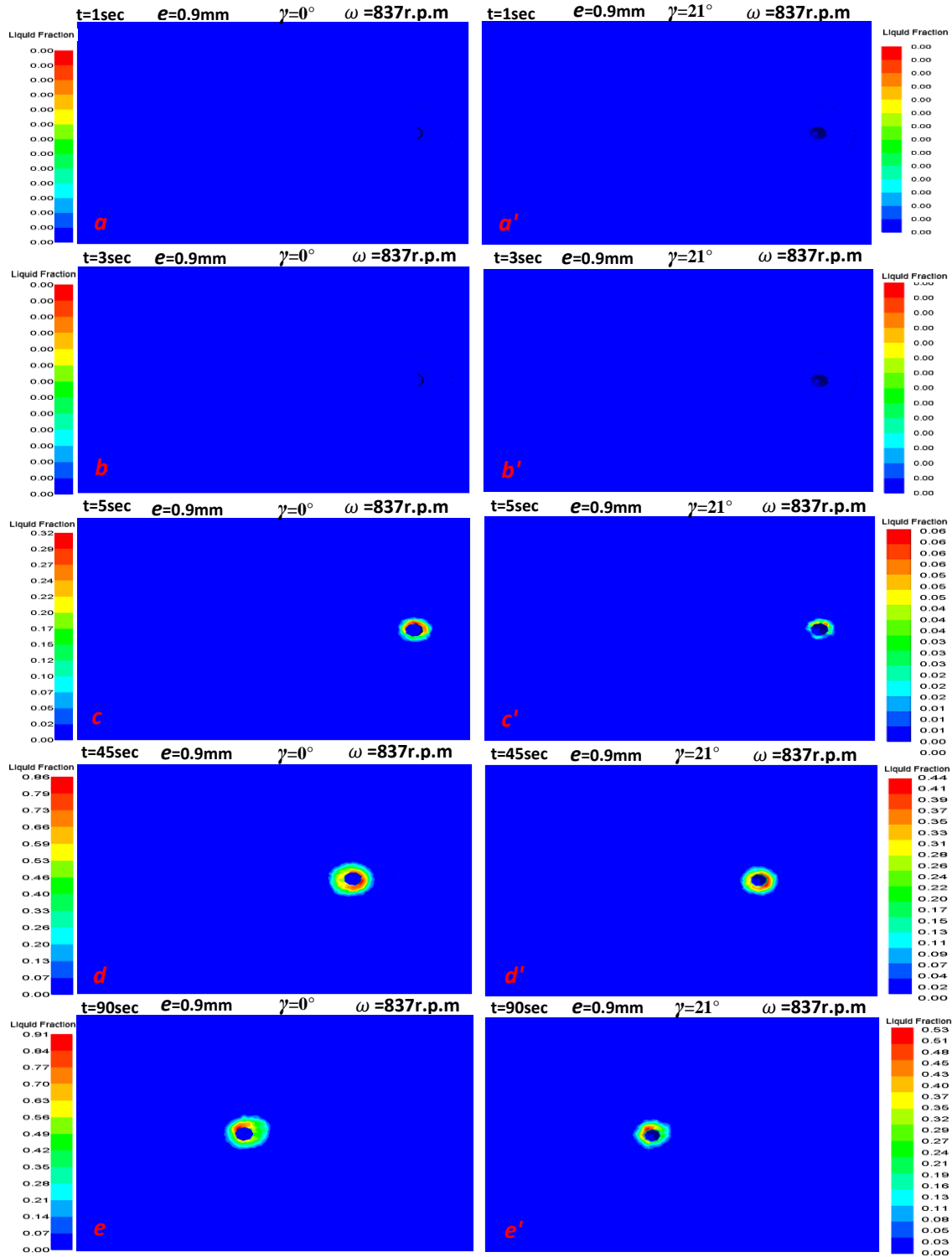


Figure 6.49 Comparison between the evolution in the liquid fraction when welding with and without pin taper angle at high rotational speed.

Figure 6.50, depicts the variation in the values of the global peak temperature when using tools with eccentric tapered pin at different rotational speeds compared with those related to the concentric and eccentric pins. In the figure, the comparison reveals that the temperature scored lower values due to the increase in the taper angle but a significant elevation in the peak temperature still taking a place against the increase in the rotational speed. For example, 975K was recorded for $e=0\text{mm}$, $\gamma=0^\circ$ and it has attained 924K when $e=0.9\text{mm}$, $\gamma=0^\circ$ while 899K for $e=0.9\text{mm}$, $\gamma=21^\circ$. In the same way figures 6.51 and 6.52, reveal that the local peak temperature at several locations is as identical as the global temperature behaves.

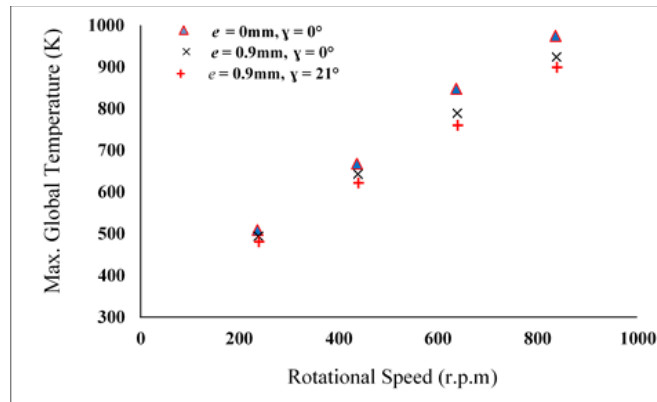


Figure 6.50 Global peak temperature for different rotational speeds with and without taper angle

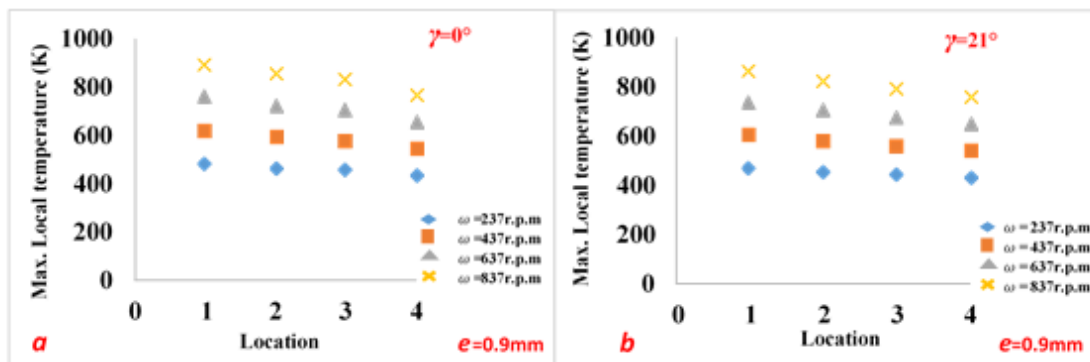


Figure 6.51 Local peak temperature for different rotational speeds with and without taper angle at different locations

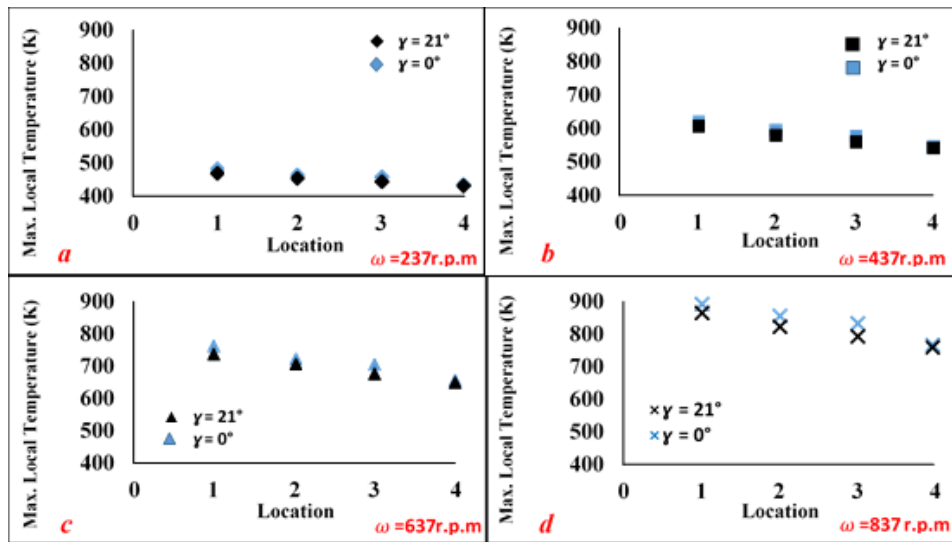


Figure 6.52 A comparison between the local peak temperatures for different rotational speeds with and without pin taper angle at different locations

From the velocity vectors in figure 6.53, it can be vividly seen that the material flow field under the effects of both the eccentricity and the taper angle still witnessing an increase in the velocity magnitudes corresponding to the increase in the tool rotational speed. On the other hand, existence of the taper angle which affects the heat generation has played a role in the increase of the material viscosity values such that under the shoulder by $0.55 \times 10^5 \text{ Kg.m}^{-1}.\text{s}^{-1}$ compared to its value when $\gamma=0^\circ$ for $\omega = 837 \text{ r.p.m}$ which was previously explained in chapter five.

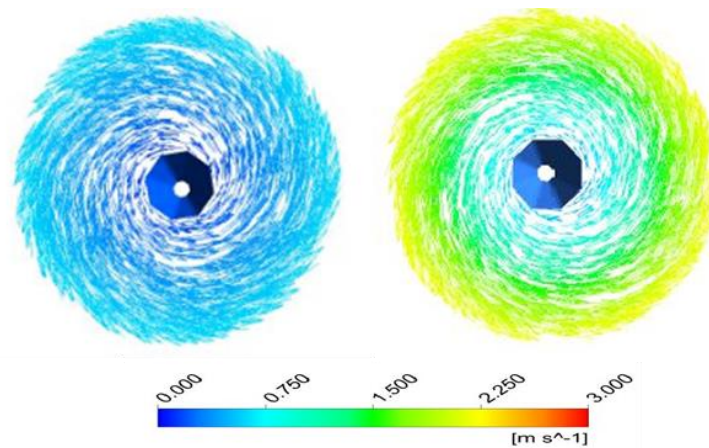


Figure 6.53 Flow velocity field for different rotational speed at underneath the shoulder in existence of the taper angle

Figure 6.54, shows the variation of the maximum shear stress along the thermal cycle for different welding rotational speeds and pin taper angles. It can be seen that the stress values have witnessed an elevating when the taper angle value moved from $\gamma=0^\circ$ to $\gamma=21^\circ$. i.e. at the onset of the thermal cycle, 667MPa was achieved for $\gamma=21^\circ$ compared with 602MPa when $\gamma=0^\circ$ for $\omega =437$ r.p.m. However, the values of shear stress have generally and orderly kept their trend against the change in the rotational speed where the highest and the lowest were attained when $\omega =237$ r.p.m and $\omega =837$ r.p.m respectively.

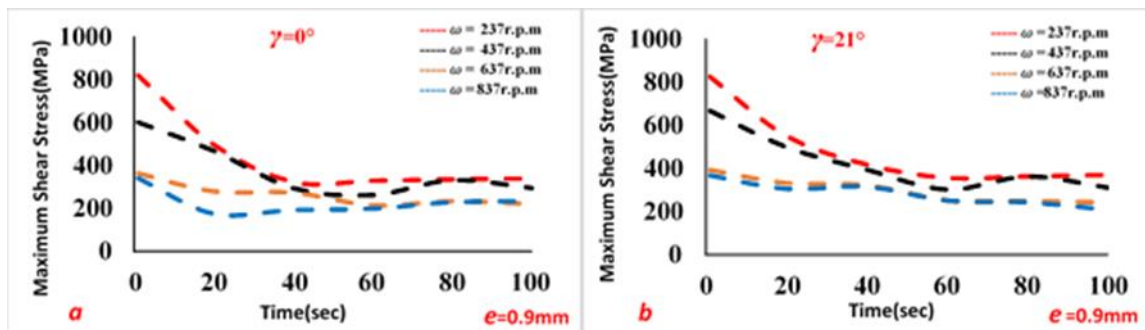


Figure 6.54 a comparison between the maximum shear stress values when using different rotational speeds and pin taper angles

6.3.3 The effect of axial load on the Thermal Field of FSW

Figure 6.55, lists the snapshots of the temperature distribution at different moments from the thermal cycle to show its transient progression corresponding to the variation in the axial loads when using different pin taper angles. It can be observed that the behaviour of the temperature profile was generally as the same as that noted for welding with the same tool without taper angle. i.e. the temperature level is experiencing an elevating against the increase in the axial load values whereas the heating rate increases from 57.85K/sec to 73.5K/sec at $t=3$ sec when the axial load moves up from 9.7MPa to 12.7 MPa. However, these heating rates are less than the ones recorded when welding with the same tool without taper angle by 5K at the same time of the thermal cycle. From another point of view, figure 6.56 depicts how the temperature profile would be changed according to the change in the taper angle and axial load.

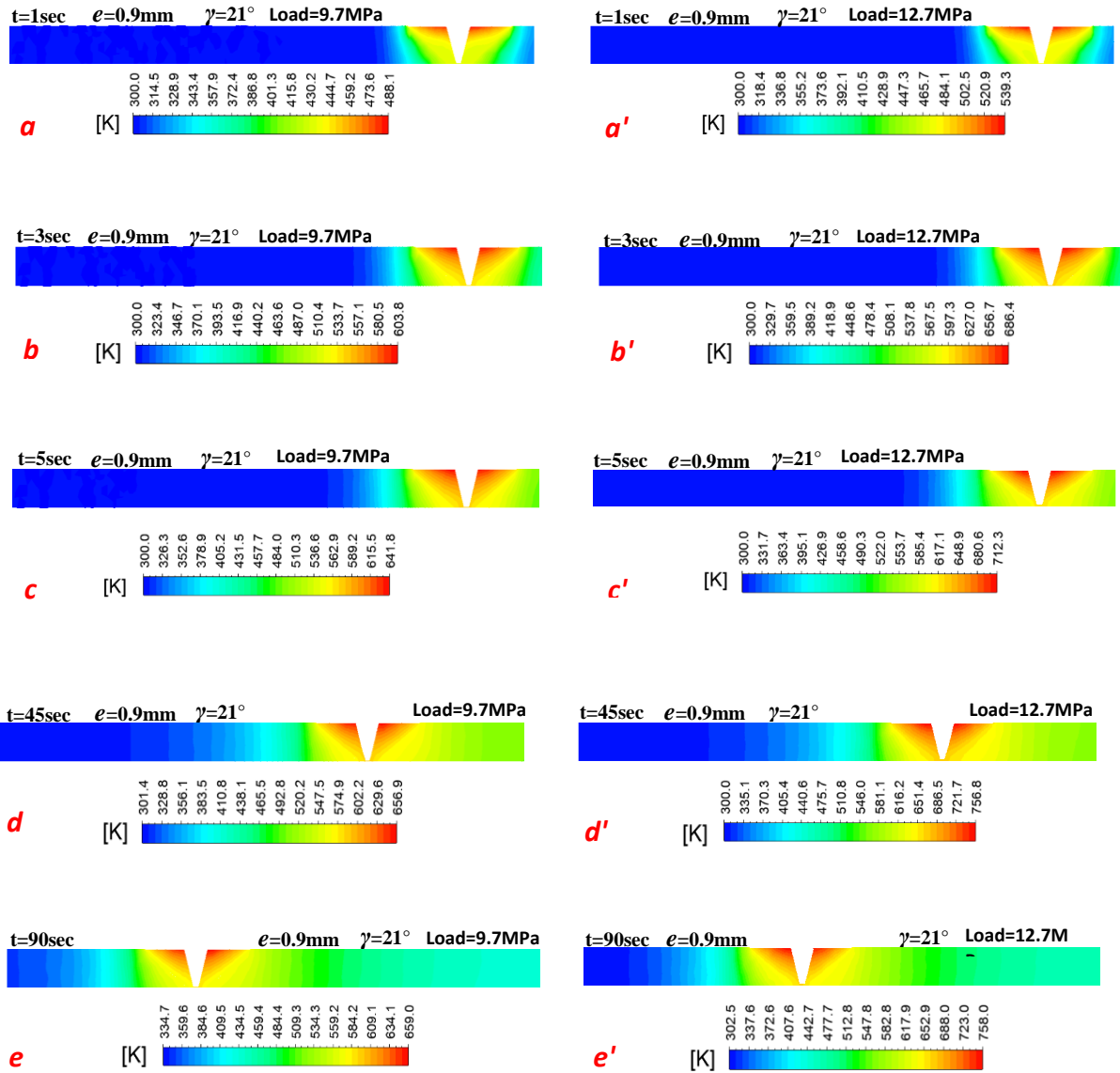


Figure 6.55 temperature distribution for the vertical plane at different time steps calculated for axial loads 9.7MPa and 12.7 MPa in the existence of taper angle

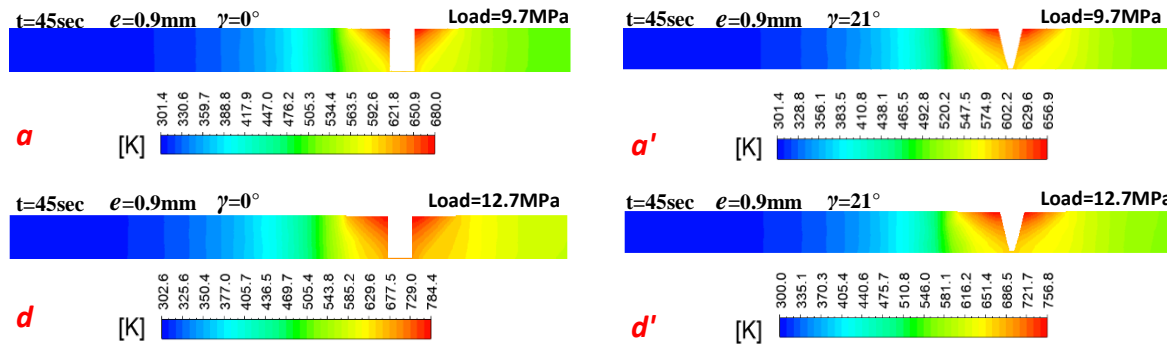


Figure 6.56 Comparison between the temperature distribution when welding with and without pin taper angle for axial loads of 9.7MPa and 12.7MPa

Figure 6.57 6.56, depicts the spatial progression in the thermal field at the same time and corresponding to welding processes with several axial loads. Tracking the line of 500K would vividly give an indication as the hottest areas are growing up according to the increase in the axial load. Nonetheless, the temperatures levels in a, b, c, and d have recorded lower values than those depicted in figure 5.53 which are related to the welding processes that have not used the tapered pin but at the same values of axial load. Consistently, the same trend was detected in figure 6.58 which depicts the increase in global peak temperature corresponding to the increased axial loads. For instance, 659K was recorded for 9.7MPa while the temperature has attained 813K for 14.2 MPa which means again the temperature range still lower than the melting point. Figure 6.59, evidently reveals that the local peak temperature at several locations is as similar as the global temperature behaviour against the axial load variation. Furthermore, the data in figure 6.60 permit recognising the local drop in the temperature due to the variation in the taper angle at different axial loads. Accordingly, the softness of the material has decreased as the taper angle increased which cause a relative decrease in the velocity of the flow field. Nevertheless, as previously reported in chapters four and five the same trend can be observed on the flow field against the change in the axial load.

The findings in figure 6.61 also indicate that the maximum shear stress values have orderly kept their trend against the variation in the axial load which is as the same as that obtained when there was no taper angle. However, higher values can be noticed when $\gamma=21^\circ$ such that recorded at $t=1\text{sec}$ and 9.7MPa where it has increased by 30MPa compared to the one recorded when $\gamma=0^\circ$ for the same time and load.

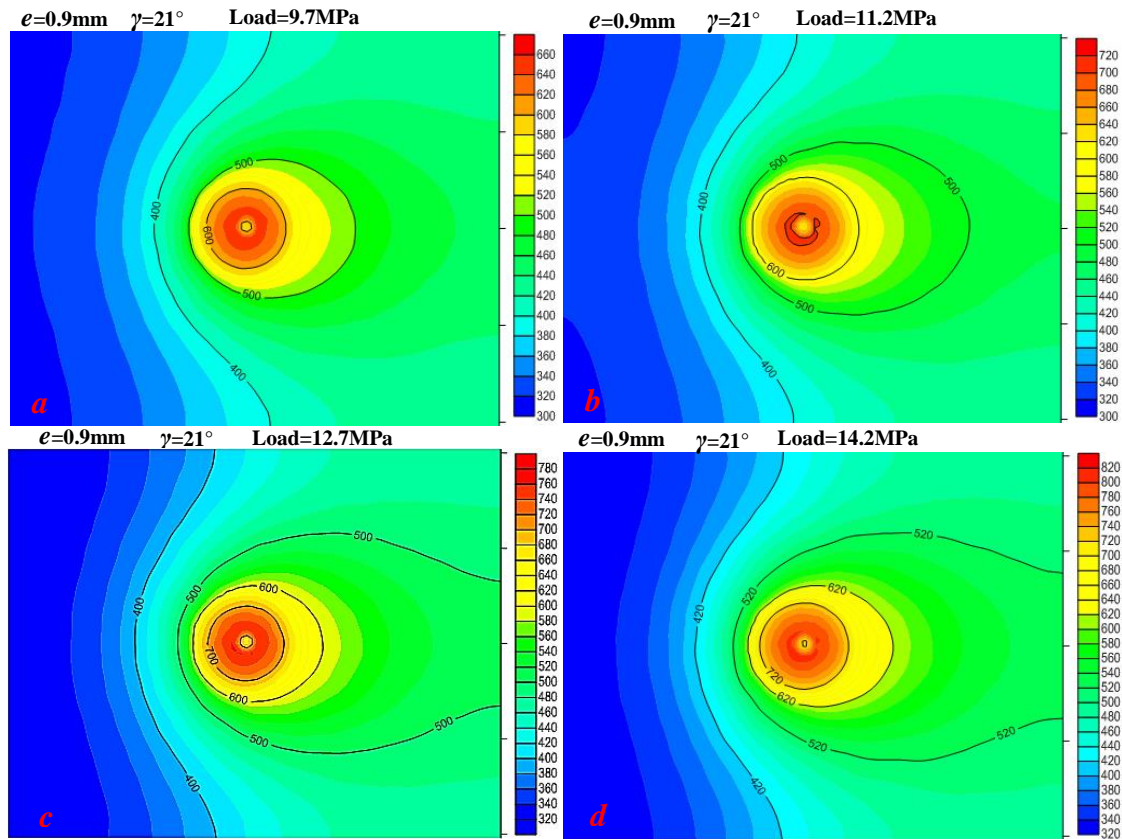


Figure 6.57 static temperature contours for different axial load a=9.7MPa, b=11.2MPa, c=12.7MPa, d=14.2MPa in the existence of pin taper angle

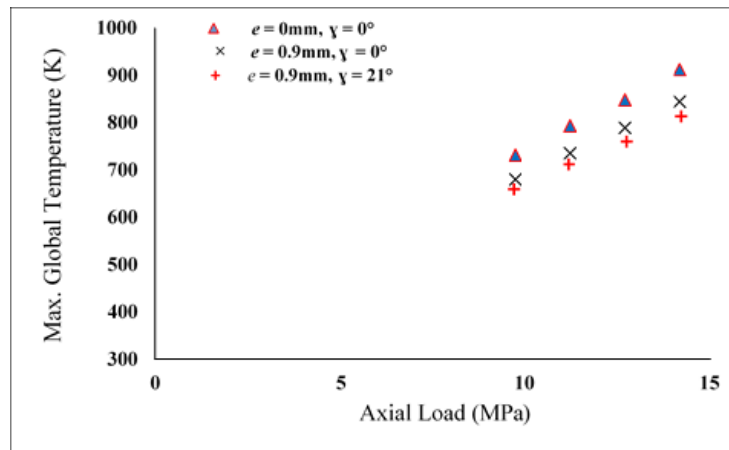


Figure 6.58 Global peak temperature for different axial loads with and without taper angle

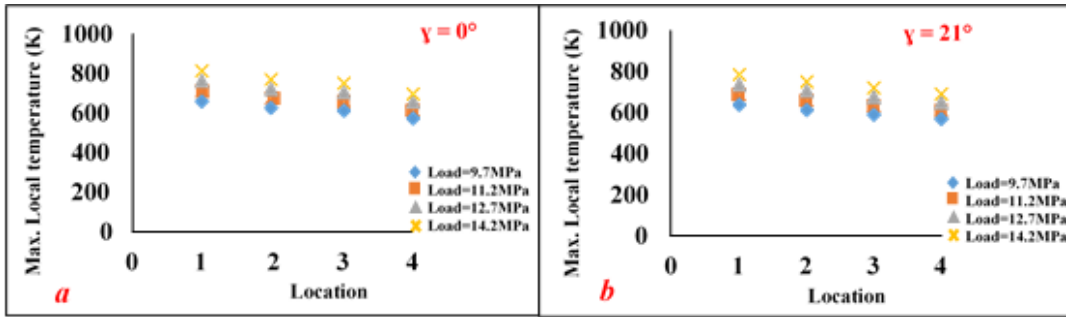


Figure 6.59 Local peak temperature for different axial loads with and without taper angle at different locations

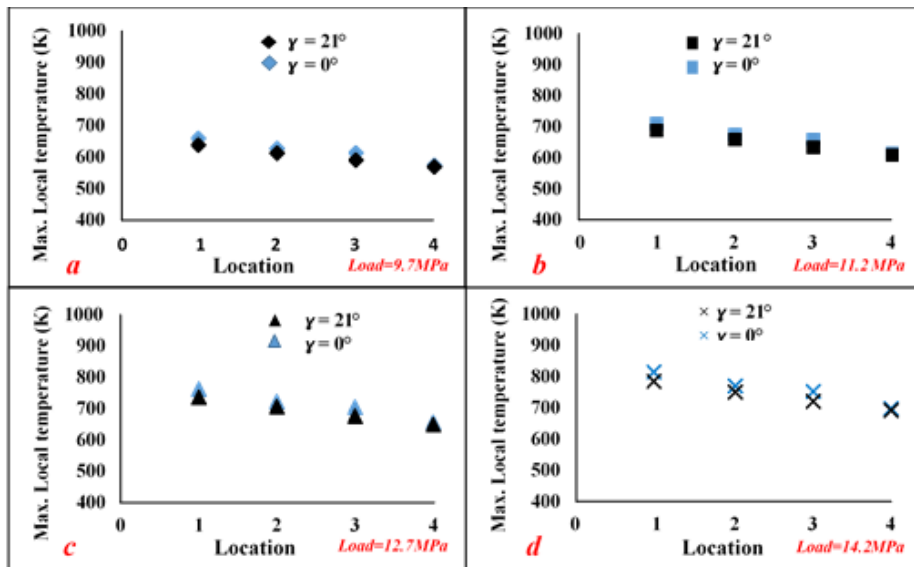


Figure 6.60 A comparison between the local peak temperatures for different axial loads with and without taper angle at different locations

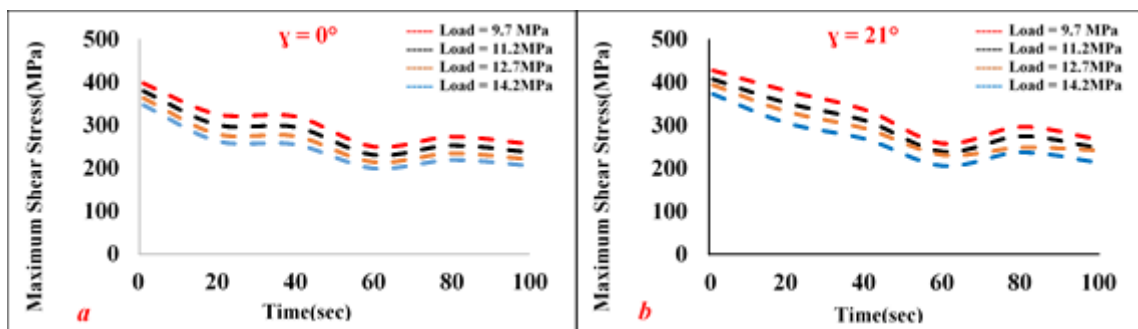


Figure 6.61 a comparison between the maximum shear stress values when using different axial loads and pin taper angles

6.4 Prediction Model of the Peak Temperature in the existence of pin taper angle

In light of the results and the comparisons presented in this chapter, it was found that the pin taper angle has shown a significant impact on the thermal field particularly on the maximum temperature that is ever attained during welding. As discussed in chapters 4 and 5, a prediction model for the peak temperature can be developed which representing all the changes in the effect of the variables under consideration when using tools with tapered pins. Hence, a novel semi-empirical correlation for predicting the peak temperature was developed based on the acquired data from CFD experiments and with the aid of the multiple variable regression analysis. Equation(6.18), provides a correlation between the temperature ratio $T_{max} / (T_s)$ and the considered parameters in presence of taper angle.

$$\frac{T_{max}}{T_s} = \frac{0.02809 \left(\frac{P}{P_{max}}\right)^{0.5793} \left(\frac{\cos \gamma}{\cos \psi}\right)^{0.2209}}{\left(\frac{V}{\omega R_s}\right)^{0.4939} \left(\frac{N}{R_s} * R_{pt}\right)^{0.04327} \left(\frac{e+t}{R_s}\right)^{0.2066} \left(\frac{e+H}{R_s}\right)^{0.02524}} \quad (6.18)$$

where T_s is the solidus temperature of the material to be welded which is equal to 855K in the current study, V is the tool transverse speed, ω is the tool rotational speed, R_s is the shoulder radius, N is the number of pin side faces, H is the pin height, t is the workpiece thickness, P is the axial load, P_{max} is the maximum axial load used in the CFD experiments, e is the eccentricity value, ψ is the tilt angle and γ is the pin taper angle. Then, eq. (6.19) can be rearranged to find a direct expression to calculate T_{max} as follows:

$$T_{max} = \left[\frac{0.02809 \left(\frac{P}{P_{max}}\right)^{0.5793} \left(\frac{\cos \gamma}{\cos \psi}\right)^{0.2209}}{\left(\frac{V}{\omega R_s}\right)^{0.4939} \left(\frac{N}{R_s} * R_{pt}\right)^{0.04327} \left(\frac{e+t}{R_s}\right)^{0.2066} \left(\frac{e+H}{R_s}\right)^{0.02524}} \right] \times T_s \quad (6.19)$$

It can be seen from the prediction model that (P/P_{max}) , $(v/\omega R_s)$ have the most significant effect on the peak temperature. Moreover, the peak temperature is proportional to (P/P_{max}) and $(\cos\gamma/\cos\psi)$ while inversely proportional to $(v/\omega R_s)$, $N.R_p / R_s$, $e+t/R_s$, $e+H/R_s$. In equation (6.19), if the fraction in the brackets has a value greater than 1, this means that some parts of the welded material converted to liquid state.

In view of authorising the usefulness of the current prediction model, the accuracy of the results from this semi-empirical relationship have been quantified where the average of differences

between the values of T_{max} calculated from eq. (6.19) and T_{max} values that obtained from CFD found to be 5.35%. A quite strong correlation was acquired as the correlation coefficient achieved 0.99 during the multiple variable regression analysis. Furthermore, it is obvious in figure 6.62 that within errors ranged from 0 to maximum $\pm 9\%$, it can be seen that more than 90% of the data lies in this range. Thus, it can be concluded that the prediction model represents the peak temperature with reasonable accuracy. Lastly, the above expressed equation is valid for the ranges of parameters under consideration which shown in tables 6-3 and 6-4.

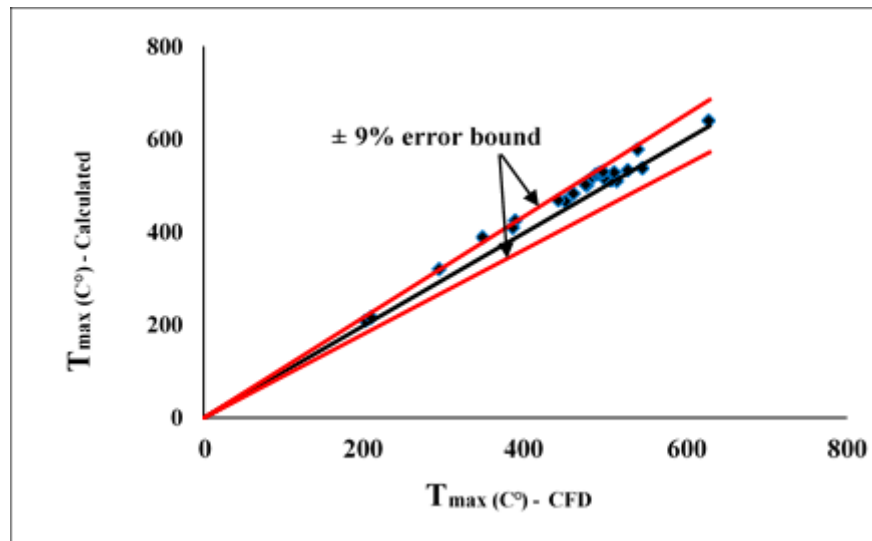


Figure 6.62 prediction model of T_{max} in existence of pin taper angle

6.5 Summary of the Thermal Analysis conducted on the FSW using tools with Tapered Eccentric Polygonal Pins

Both analytical and CFD approaches have aided to achieve a detailed diagnosis of the FSW of thick aluminium using tools with tapered Pins. Accordingly, the following results have been revealed:

- Analytically, the increase in the pin taper angle value leads to a decrease in the total amount of heat generated.
- The total amount of heat generated is conversely impacted by the taper angle compared with eccentricity.

- Although, the total amount of heat generated is decreased in the presence of taper angle the thermal field might witness an elevation in the temperatures against the increased value of some variables such as shoulder diameter, rotational speed and the axial load.
- In a comparison to the results that have been attained when using tools with eccentric pins, all the variables under consideration have generally kept their impacts on the thermal field

In concluding this chapter, a trial was conducted to have a holistic view on the changes that might be experienced by the thermal field of FSW when using tools with tapered eccentric polygonal pin relying on the analytical and CFD approaches. In doing so, the corresponding steps of the analytical estimation of the heat generated amount were explained for different cases. Then, a series of CFD simulations were conducted to verify the change in the thermal field through the weldments for the defined group of parameters in the presence of the pin taper angle. After that, a prediction model to estimate the peak temperature was developed and authorised.

CHAPTER 7: CONCLUSIONS

This chapter concludes the results obtained in the previous chapters regarding the thermal characteristics of FSW using tools with different pin profiles. It also revises the important achievements and contributions of the research work described in this thesis on the basis of the defined aims and objectives. As a final point, after evaluating the works carried out in this study the requirements for the future work in the area of FSW thermal analysis have been suggested.

7.1 Research Problem Synopsis

Friction stir welding is getting more and more popular even though it is still a new process compared to the conventional welding processes. That is because of the benefits that can be offered over those methods, like the lower level of defects, better appearance of the welded joint as well as the lower operational cost after the initial investment. However, different types of defects would accompany this joining process particularly those related to the thermal changes during the process which means influencing the joint quality. Therefore, having a vivid picture of the changes in the welding thermal field particularly due to the variation in the geometrical and operational parameters would allow to control the thermal characteristics of the process and then avoiding some defects.

From an extensive review of the published literature, a number of limitations have been found out regarding the investigation of the thermal field of FSW and its changes especially those related to the shape and position of the tool pin. Therefore, to provide an efficient predicting of the behaviour of thermal field throughout the workpiece particularly in the vicinity of the welded joint, a set of aims and objectives have been identified in this study to reflect and define the scope of this work.

7.2 Research Aims and Major Achievements

Based on the comprehensive literature review of the works that had been carried out in this area, the main aims of this study and the corresponding achievements were identified and summarised as follows:

Research Aim # 1: Thermal characterisation of friction stir welding using tools with polygonal pins.

Achievement # 1: This study has introduced a detailed analytical and CFD based investigation on the thermal field of friction stir welding of thick material using tools with polygonal pins and developed a peak temperature prediction model within the workpiece. A numerical study has been carried out on the temperature distribution in welding processes using tools with heptagonal, octagonal and nonagonal pins. By adopting an innovative modelling techniques, three - dimensional and transient CFD model was developed to represent the physical model of FSW. An analytical approach has been used to estimate the total amount of heat generated due to the friction

between the tool and the workpiece whereas a set of novel mathematical equations were developed for the different cases of tools considered. Hence, it was possible to present a comparison between the heat generated amounts under different numbers of polygon side faces. These resulted values of heat generation were then used as input to the numerical model in form of heat flux. In order to cover a wide range of geometrical and operational conditions, the numerical simulations have been conducted for various (a) No. of polygon faces (b) shoulder diameters (c) pin diameters (d) pin heights (e) material thicknesses (f) rotational speeds (g) axial loads.

On the basis of the detailed numerical investigation of the thermal field, the temperature distribution within the weldments has been critically analysed qualitatively and quantitatively. Qualitative analysis makes use of the time dependent temperature contours in the workpiece while, the quantitative analysis makes use of the local peak temperature within the workpiece. The presented results have given a clear picture of the temporal and the spatial temperature behaviour. The effect of the presence of the polygonal pin on the thermal field along with the variables under consideration has been visualised. Based on the thermal changes, the study also presents the maximum shear stress applied on the tool surface. In the welding applications, specialist use the weld peak temperature to control the final microstructure of the welded joint which allow the undesirable structures and defects to be avoided. Hence, the current study made use of the peak temperature values for various cases under investigation in order to develop a semi-empirical equation predicting the maximum temperature in the weldments.

The major achievement in the present study is represented in establishment of a more realistic CFD model of FSW which succeeded to estimate the amount of liquid metal whereas no single CFD model has done this yet. Development of novel mathematical equations calculating the heat generation when using tools with polygonal pins is also an achievement. Additionally, development of a semi-empirical equation predicting the weld peak temperature which includes the effects of different operational and geometrical parameters is a novelty of this work.

Research Aim # 2: Thermal characterisation of friction stir welding using tools with eccentric pins

Achievement # 2: Extensive analytical and CFD based investigations have been carried out in this study on the thermal field of friction stir welding of thick material using tool with eccentric polygonal pins, and a prediction model of the weld peak temperature has been developed. A numerical study has been carried out on the temperature distribution in welding processes using tools with eccentric pins. For such tools with eccentric pins, an analytical approach has been used to develop equations estimating the total amount of heat generated due to the friction between the tool and the workpiece. To clarify the effect of eccentricity, a comparison was drawn for the heat generated amounts under different values of eccentricities. This value of heat generation was then used as input to the numerical model in form of heat flux. In order to cover a wide range of geometrical and operational conditions, the numerical simulations have been conducted for various (a) eccentricities (b) shoulder diameters (c) pin diameters (d) pin heights (e) material thicknesses (f) rotational speeds (g) axial loads.

Based on Series of numerical investigations of the thermal field behaviour, the temperature distribution within the weldments has been critically analysed both qualitatively and quantitatively. Qualitative analysis makes use of the time dependent temperature contours in the workpiece whereas, the quantitative analysis makes use of the local peak temperature within the workpiece. The obtained results have provided a better understanding of the temporal and spatial changes of the temperature values. The effects of the presence of the eccentric pin on the thermal field along with the variables under consideration have been visualised. Based on the temperature changes, the study has also presented the maximum shear stress applied on the tool surface. In the welding applications, specialist needs to know the weld peak temperature which is very helpful in controlling the final microstructure of the welded joint and then avoiding the undesirable structures and defects. Hence, In the present study, the peak temperature values for various cases have been calculated in order to develop a semi-empirical equation predicting the maximum temperature in the weldments.

The major achievement in the present study is represented in development of novel mathematical equations calculating the heat generation when using tools with eccentric pins. The other achievement is development of a novel semi-empirical equation predicting the weld peak temperature which includes the effects of different operational and geometrical parameters.

Research Aim # 3: Thermal characterisation of friction stir welding using tools with tapered pins.

Achievement # 3: This study provides a detailed analytical and CFD based investigations on the thermal field of friction stir welding using tool with tapered polygonal pins and developing a prediction model to estimate the weld peak temperature. A numerical study has been carried out on the temperature distribution for welding processes using tools with tapered pins. For such tools which consist tapered pins, an analytical approach has been used to calculate the total amount of heat generated due to the friction between the tool and the workpiece. To clarify the effects of taper angle and the coupled effect of the taper angle and eccentricity, comparisons were drawn for the heat generated amounts under different values of taper angle and eccentricities. This value of heat generation was then used as input to the numerical model in form of heat flux. In order to cover a wide range of geometrical and operational conditions, the numerical simulations have been conducted for various (a) pin taper angle (b) eccentricities (c) shoulder diameters (d) pin diameters (e) pin heights (f) material thicknesses (g) rotational speeds (h) axial loads.

Based on the detailed numerical investigations of the thermal field behaviour, the temperature distribution within the weldments has been critically analysed both qualitatively and quantitatively. Qualitative analysis makes use of the time dependent temperature contours in the workpiece whereas, the quantitative analysis makes use of the local peak temperature within the workpiece. The obtained results have provided a better understanding of the temporal and spatial changes of the temperature values. The effects of the presence of the pin taper angle on the thermal field along with the variables under consideration have been visualised. Based on the temperature changes, the study also presents the maximum shear stress applied on the tool surface. In the welding applications, specialist needs to know the weld peak temperature which is very helpful in controlling the final microstructure of the welded joint and then avoiding the undesirable structures and defects. Hence, in the present study, the peak temperature values for various cases have been calculated in order to develop a semi-empirical equation predicting the maximum temperature in the weldments.

The major achievement in the present study is represented in development of novel mathematical equations calculating the heat generation when using tools with tapered pins. The other achievement is development of a novel semi-empirical equation predicting the weld peak

temperature which includes the effects of the taper angle along with different operational and geometrical parameters.

7.3 Thesis Conclusions

An extensive study has been performed to add significant contributions to the existing literature and filling knowledge gaps in the area of friction stir welding using tools with different pin profiles. The major conclusions from each aspect of this research work are given below:

Research Objective # 1: To develop a more realistic CFD model to simulate FSW process.

Conclusion # 1: A three – dimensional transient CFD model has been developed offering a more realistic representation to the physical model of friction stir welding. The adopted new modeling techniques have shown capability in avoiding the unnecessary assumptions. i.e. the dynamic mesh method has been used to specify the translational movement of the welding tool instead of using the fluid flow. Considering the solidification and melting model has also led to minimise the fluid region which is an approximation. A reasonable accuracy was achieved from the developed model as it has shown good agreement with the experimental measurements. The current established CFD model captured the temporal and spatial temperature distribution throughout the weldments during the welding process for a wide range of variation in the geometrical and operational parameters. Furthermore, it has calculated the time dependent values of the maximum shear stress for the proposed welding processes.

Research Objective # 2: To develop analytical equations for determination of the heat generated during FSW process while using tools with polygonal pin profiles.

Conclusion # 2: From the analytical derivations carried out in this study regarding the heat generated in FSW when using polygonal pins, different mathematical expressions have been developed corresponding to the number of the pin faces, to calculate the total amount of heat generated. It can be also concluded that due to the increase in the frictional area, the total heat amount changes with respect to the number of polygon faces, which increases with the increased number of faces. In comparison with the cylindrical pin, the heat generated amount has recorded lower values for the polygonal pin with a low number of side faces. However, for the cases that have a higher number of faces, the heat amount approached to that for the cylindrical pin. The

novel equations presented in this study is of extreme importance for a completion of the CFD simulation of FSW which aid to calculate the process heat input.

Research Objective # 3: To establish the effects of geometrical and operational parameters of FSW with polygonal pins on the temperature distribution and peak temperature within the workpiece.

Conclusion # 3: From the investigations carried out regarding the effect of the geometrical and operational parameters on the time dependent and spatial temperature distribution during FSW using polygonal pin, some significant points can be concluded. First, for thick aluminium plates, the temperature distribution is not mostly impacted by the increased heat value corresponding to the increase in the number of polygon side faces from 7 to 9. Secondly, the increase in the welding parameters such as shoulder diameter, rotational speed and the axial force has obviously caused an increase in the temperatures while a margin increase in the temperature recorded corresponding to the increase in the pin height. Conversely, the increase in the workpiece thickness decreases the temperature. Moreover, for thick weldments, a relative drop in the temperature caused by the increase in the pin diameter is noticed, however, an elevation in the temperature values can be observed when the heat generation from the tool pin can compensate that lost due to the accompanying decrease in the shoulder size.

Research Objective # 4: Development of a semi-empirical relationship for the peak temperature within the workpiece while using polygonal pin profiles.

Conclusion # 4: After the effect of a wide range of process parameters have been analysed based on the acquired numerical data from FSW processes using tools with polygonal pins, a semi-empirical relationship has been developed for the peak temperature within the workpiece. The results and the analysis presented in this study is of great value for the people who work in the welding field as the prediction model developed for the peak temperature can be used in where the welding procedure specifications are of interest.

Research Objective # 5: To develop analytical correlations for determining the heat generation while using tools with eccentric polygonal pin profiles.

Conclusion # 5: From the analytical derivations carried out in this study regarding the heat generated in FSW when using eccentric polygonal pins, different mathematical expressions have been developed to calculate the total amount of heat generation. These equations include a term representing the effect of the eccentricity distance. It can be also concluded that due to the increase in the frictional area, the total heat amount changes with respect to the value of eccentricity where the heat generated increases with the increased eccentricity. In comparison with the generated amount for the cylindrical pin, the heat amounts for the considered eccentric polygonal pins have recorded lower values for some cases and higher for others which can be attributed to the role of eccentricity. Theoretically, as far as the eccentricity value increases all the tools under considerations can generate a heat which exceeds that recorded for the tool with concentric cylindrical pin. The novel equations presented in this study is of extreme importance for a completion of the CFD simulation of FSW which aid to calculate the process heat input.

Research Objective # 6: To determine the effects of geometrical and operational parameters of FSW using eccentric polygonal pins on the temperature distribution and peak temperature within the workpiece

Conclusion # 6: From the investigations carried out regarding the effect of the geometrical and operational parameters on the time dependent and spatial temperature distribution during FSW using eccentric polygonal pins, some significant points can be concluded. First, the thermal field might experience a drop in the temperature degrees such that recorded when the eccentricity and workpiece thickness are increased eventhough the heat generated is increased due to the increased eccentricity distance. Second, the increase in the welding parameters such as shoulder diameter, rotational speed and the axial force has obviously caused an increase in the temperatures while the pin height has adversely affected compared to its trend registered for the concentric pin. However, comparing to the effects of considered parameters on the temperature in the processes using concentric pin, lower levels of temperatures have generally been observed as the eccentricity was obviously influencing.

Research Objective # 7: Development of a semi-empirical correlation for the peak temperature within the workpiece while using tools with eccentric polygonal pin profiles

Conclusion # 7: Set of FSW processes have been simulated which use tools with eccentric polygonal pins and thereafter the effect of a wide range of process parameters were analysed based on the acquired numerical data in this study. Subsequently, a semi-empirical relationship has been developed for the peak temperature within the workpiece. To conclude, the results and the analysis presented in this study is of great value for the people who work in the welding field as the prediction model developed for the peak temperature can be used in where the welding procedure specifications are of interest.

Research Objective # 8: To develop analytical equations for determining the heat generation while using tool with tapered eccentric polygonal pin profiles

Conclusion # 8: With the growing complexity of considering the pin tapering, the same analytical approach has been used in this study to develop expressions calculating the heat generated in FSW when using tapered eccentric polygonal pins. The developed equations include a new term representing the effect of the pin side inclination which is the taper angle. After using those attained equations, it can be also concluded that the increase in taper angle cause a drop in the total heat generated because of the decrease in the frictional area. In comparison with the generated amount for the cylindrical pin, the heat amounts for the considered tapered pins have obviously recorded high rates of descent even at small values of taper angle. The novel equations presented in this study is of extreme importance for a completion of the CFD simulation of FSW which aid to calculate the process heat input.

Research Objective # 9: To analyse the effects of geometrical and operational parameters of FSW with tapered eccentric polygonal pins on the temperature distribution and peak temperature within the workpiece

Conclusion # 9: Based the investigations carried out regarding the effect of the geometrical and operational parameters on the temporal and spatial temperature distribution during FSW using tapered eccentric polygonal pins, some significant points can be concluded. To begin with, the increased values of taper angle cause a decrease in the temperatures. Secondly, under the coupled effect of the taper angle and eccentricity, the temperature degrees still experience an elevation corresponding to the increased values in shoulder diameter, rotational speed and the axial load. The increase in the other variables such as the workpiece thickness and the pin height give also

rise to a decrease in the temperatures. Comparing to the effects of parameters on the temperature in the processes using eccentric and concentric pins, lower levels of temperatures have been generally observed as the taper angle was obviously influencing.

Research Objective # 10: Development of a semi-empirical relationship for the peak temperature within the workpiece while using tools with tapered eccentric polygonal pin profiles

Conclusion # 10: number of suggested FSW processes using tools with tapered eccentric polygonal pins have been simulated and then the effect of a wide range of process parameters were analysed based on the acquired numerical data in this study. Accordingly, a semi-empirical relationship has been developed for the peak temperature within the workpiece. To conclude, the results and the analysis presented in this study is of great value for the people who work in the welding field as the prediction model developed for the peak temperature can be used in where the welding procedure specifications are of interest.

7.4 Thesis Contributions

The summary of major contributions and novelties in the study conducted by the author and described in this thesis are given below:

Contribution # 1: It has been found in literature that the unnecessary assumptions still used in developing of the common CFD codes of FSW particularly those simulate the process in the transient domain. Using the fluid flow to identify the welding tool translational movement and the fluid region itself in the CFD model are counted to be among those assumptions. Therefore, the first contribution in this study is the successful using of the dynamic mesh technique and solidification and melting model in developing a more realistic transient CFD model of FSW in which the above-mentioned assumptions have been avoided. The current improved CFD model has capability to mimic the real motion of the welding tool and the advantage of a very limited fluid zone. Furthermore, calculating liquid fraction that might be formed at very high temperature.

Contribution # 2: The published literature provides very limited information on the thermal field analysis of FSW of thicker workpiece using tools with polygonal pins. Therefore, the second significant contribution of this study bridges this gap in the knowledge base where detailed

investigations on local and global thermal field characteristics throughout the workpiece in FSW processes using tools with polygonal pins have been provided. In view of that, novel mathematical equations that calculate the total heat generation amount for FSW processes using different polygonal pins have been developed. The availability of the computational fluid dynamics tools which is represented in the current improved model along with the mathematical equations of the heat generation have enabled the author to carry out the aimed investigation. The transient and spatial temperature distribution have been investigated over a wide range of welding conditions. Effects of parameters such as shoulder diameter, pin diameter, pin height, workpiece thickness, tool rotational speed and the axial load on the (local and global) peak temperature and the maximum shear stress at the tool surface have clearly been enumerated. Moreover, based on the data generated from the numerical investigation, a novel peak temperature prediction model has been developed which include the relevant geometrical and operational parameters. The achieved prediction model of the peak temperature is a novel contribution to the knowledge base where it can be beneficial in selection of the welding parameters.

Contribution # 3: The other major contribution of this research work is extensive investigations on the (local and global) thermal field characteristics throughout the workpiece in FSW processes using tools with eccentric pins have been provided. Related to the available literature, an extreme limited information has been provided regarding the effect of the tool pin eccentricity particularly those associated with the thermal field of FSW. Likewise, novel mathematical equations that calculate the total heat generation amount for FSW processes using different eccentric polygonal pins have been developed. The availability of the computational fluid dynamics tools which is represented in the current improved model along with the developed mathematical equations of the heat generation have enabled the author to carry out the aimed investigation. For the welding processes using such eccentric pins, the transient and spatial temperature distribution have been investigated over a wide range of welding conditions. Effects of parameters such as shoulder diameter, pin diameter, pin height, workpiece thickness, tool rotational speed and the axial load on the (local and global) peak temperature and the maximum shear stress have clearly been enumerated. Moreover, based on the data generated from the numerical investigation, a novel peak temperature prediction model has been developed which include the relevant geometrical and operational parameters. The achieved prediction model of the peak temperature is a novel

contribution to the knowledge base where it can be beneficial in selection of the welding parameters.

Contribution # 4: For the FSW that using the tools with tapered pins, the majority of the available published works does not comprise information about the welding thermal field characteristic and their changes during the process. The last significant contribution of this study is extensive investigations on the local and global thermal field characteristics throughout the workpiece in FSW processes using tools with tapered eccentric polygonal pins. In view of this, very complicated and novel mathematical equations that calculate the total heat generation amount for FSW processes using different tapered eccentric polygonal pins have been developed. The availability of the computational fluid dynamics tools which is represented in the current improved model along with the developed mathematical equations of the heat generation have enabled the author to carry out the aimed investigation. For the welding processes using such tapered eccentric pins, the transient and spatial temperature distribution have been investigated over a wide range of welding conditions. Effects of parameters such as the pin eccentricity, shoulder diameter, pin diameter, pin height, workpiece thickness, tool rotational speed and the axial load on the (local and global) peak temperature and the maximum shear stress at the tool surface have clearly been enumerated. Moreover, based on the data generated from the numerical investigation, a novel peak temperature prediction model has been developed which include the relevant geometrical and operational parameters. The achieved prediction model of the peak temperature is a novel contribution to the knowledge base where it can be beneficial in selection of the welding parameters.

7.5 Recommendations for future work

Although friction stir welding has been an area of study over the past few years, it is still an open field of research. Based on the gaps in the knowledge base that have been bridged in this thesis, the author identifies some possible future works which are described below

Recommendation # 1:

As a powerful and advanced modelling technique, using of dynamic mesh would be possible in identifying the rotational motion of the welding tool in order to attain higher degree of reality and accuracy regarding the CFD models of friction stir welding. This task requires a super

computational power which assists to achieving a successful dynamic mesh for the process and making the computational time to be acceptable as the time step needed is quite small.

Recommendation # 2:

The heat generated amount in FSW would be affected under the variation of other geometrical parameters related to the tool design. In order to accommodate the effect of those variables such as further shoulder and pin profiles as well as the tool tilt angle, additional mathematical derivations need to be carried out using the considered analytical approach.

Recommendation # 3:

By considering other welding conditions and expanding their range, more comprehensive numerical studies and investigations can be conducted on the FSW processes. In light of that, it would be possible to consider other material types (material properties), different workpiece initial temperatures, different ambient temperature, different welding positions, different translational speeds. Moreover, estimation of the effects of each single variable from the above mentioned variables on the welding peak temperature will be able to take the prediction models presented in this study to a wide range of application.

Recommendation # 4:

Friction stir welding is one of various engineering applications in which the calculation of temperature field in the solid is classified as problem of heat conduction including a moving heat source. The welding peak temperature is also vitally significant for those specialist who are interested in controlling the final properties of the welded joint. Therefore, the use of inverse analysis would be possible for estimating the required heat flux at the interface between the tool and workpiece to attain the aimed and optimum welding peak temperature. Knowing such a surface condition would be beneficial in selecting of the best possible welding parameters that are required to produce proper thermal cycle and peak temperature. This task requires a complete knowledge regarding the inverse heat conduction problems and the varied solving techniques that have been proposed to solve them.

References

1. Mishra, R.S., P.S. De, and N. Kumar, Friction Stir Welding and Processing. Science and Engineering. 2014, Dordrecht: Springer International Publishing.
2. Mishra, R.S. and Z. Ma, Friction stir welding and processing. Materials Science and Engineering: R: Reports, 2005. **50**(1): p. 1-78.
3. INTERNATIONAL, A., Welding Brazing and Soldering - ASM Hand Book. 1993.
4. Davari, H., et al., Experimental and numerical thermomechanical analysis of hybrid friction welding of commercially pure copper bars. Materials and Manufacturing Processes, 2011. **26**(5): p. 694-702.
5. Friction Stir Welding Benefits and Advantages. 2014; Available from: <http://www.twi-global.com/capabilities/joining-technologies/friction-processes/friction-stir-welding/benefits-and-advantages/>.
6. Neto, D.M. and P. Neto, Numerical modeling of friction stir welding process: a literature review. The International Journal of Advanced Manufacturing Technology, 2013. **65**(1): p. 115-126.
7. Lohwasser, D. and Z. Chen. Friction stir welding : from basics to applications. 2010; Available from: <http://site.ebrary.com/id/10833095>.
8. Mishra, R.S., P.S. De, and N. Kumar, Fundamentals of the Friction Stir Process, in Friction Stir Welding and Processing. 2014, Springer. p. 13-58.
9. Friction Stir Welding – Working Principle, Advantages, Disadvantages with Application 2017; Available from: <http://www.theweldingmaster.com/friction-stir-welding/>.
10. Li, H., Coupled Thermo-Mechanical Modelling of Friction Stir Welding, in Department of Mechanical Engineering. 2008, Strathclyde.
11. Gibson, B.T., et al., Friction stir welding: Process, automation, and control. Journal of Manufacturing Processes, 2014. **16**(1): p. 56-73.
12. Engineering, M., A New Look at Aircraft Assembly/Friction stir welding is the answer, R.B. Aronson, Editor. 2004.

13. Schmidt, H., J. Hattel, and J. Wert, An analytical model for the heat generation in friction stir welding. *Modelling and Simulation in Materials Science and Engineering*, 2003. **12**(1): p. 143.
14. N Zhang, Y., et al., Review of tools for friction stir welding and processing. Vol. 51. 2012.
15. Rai, R., et al., Review: friction stir welding tools. *Science and Technology of Welding and Joining*, 2011. **16**(4): p. 325-342.
16. Mehta, M., et al., Numerical modeling of friction stir welding using the tools with polygonal pins. *Defence Technology*, 2015. **11**(3): p. 229-236.
17. Elangovan, K. and V. Balasubramanian, Influences of tool pin profile and tool shoulder diameter on the formation of friction stir processing zone in AA6061 aluminium alloy. *Materials & Design*, 2008. **29**(2): p. 362-373.
18. Blondeau, R., *Metallurgy and mechanics of welding*. 2013: John Wiley & Sons.
19. Elangovan, K. and V. Balasubramanian, Influences of pin profile and rotational speed of the tool on the formation of friction stir processing zone in AA2219 aluminium alloy. *Materials Science and Engineering: A*, 2007. **459**(1): p. 7-18.
20. Schneider, J. and A. Nunes Jr, Characterization of plastic flow and resulting microtextures in a friction stir weld. *Metallurgical and materials transactions B*, 2004. **35**(4): p. 777-783.
21. Zhang, Z.H., et al., Effective predictions of ultimate tensile strength, peak temperature and grain size of friction stir welded AA2024 alloy joints. *The International Journal of Advanced Manufacturing Technology*, 2014. **73**(9): p. 1213-1218.
22. Mehta, M., A. De, and T. Debroy, Material adhesion and stresses on friction stir welding tool pins. Vol. 19. 2014. 534-540.
23. Ulysse, P., Three-dimensional modeling of the friction stir-welding process. *International Journal of Machine Tools and Manufacture*, 2002. **42**(14): p. 1549-1557.
24. Colegrove, P.A. and H.R. Shercliff, 3-Dimensional CFD modelling of flow round a threaded friction stir welding tool profile. *Journal of Materials Processing Technology*, 2005. **169**(2): p. 320-327.
25. Crawford, R., et al., Modelling of friction stir welding for robotic implementation. Vol. 1. 2006. 101-106.

26. Kang, S.-W., B.-S. Jang, and J.-W. Kim, A study on heat-flow analysis of friction stir welding on a rotation affected zone. *Journal of Mechanical Science and Technology*, 2014. **28**(9): p. 3873-3883.
27. Kadian, A.K. and P. Biswas, A comparative study of material flow behavior in friction stir welding using laminar and turbulent models. *Journal of Materials Engineering and Performance*, 2015. **24**(10): p. 4119-4127.
28. Nandan, R., G. Roy, and T. Debroy, Numerical simulation of three-dimensional heat transfer and plastic flow during friction stir welding. *Metallurgical and materials transactions A*, 2006. **37**(4): p. 1247-1259.
29. WU, C.-s., et al., Visualization and simulation of plastic material flow in friction stir welding of 2024 aluminium alloy plates. *Transactions of Nonferrous Metals Society of China*, 2012. **22**(6): p. 1445-1451.
30. Nandan, R., et al., Numerical modelling of 3D plastic flow and heat transfer during friction stir welding of stainless steel. *Science and Technology of Welding and Joining*, 2006. **11**(5): p. 526-537.
31. Atharifar, H., D. Lin, and R. Kovacevic, Numerical and experimental investigations on the loads carried by the tool during friction stir welding. *Journal of Materials Engineering and Performance*, 2009. **18**(4): p. 339-350.
32. Aljoaba, S., et al., Modeling of friction stir processing using 3D CFD analysis. *International journal of material forming*, 2009. **2**(1): p. 315-318.
33. Lin, S.-B., et al., Modeling of friction stir welding process for tools design. *Frontiers of Materials Science*, 2011. **5**(2): p. 236-245.
34. Yu, Z., et al., Transient heat and material flow modeling of friction stir processing of magnesium alloy using threaded tool. *Metallurgical and Materials Transactions A*, 2012. **43**(2): p. 724-737.
35. Mohanty, H., et al., Study on the effect of tool profiles on temperature distribution and material flow characteristics in friction stir welding. *Proceedings of the Institution of Mechanical Engineers, Part B: Journal of Engineering Manufacture*, 2012: p. 0954405412451811.

36. Schmidt, H.B. and J.H. Hattel, Thermal modelling of friction stir welding. *Scripta Materialia*, 2008. **58**(5): p. 332-337.
37. Chen, G.-q., et al., Computational fluid dynamics studies on heat generation during friction stir welding of aluminum alloy. *Computational Materials Science*, 2013. **79**: p. 540-546.
38. Ji, S., et al., Design of friction stir welding tool for avoiding root flaws. *Materials*, 2013. **6**(12): p. 5870-5877.
39. Cho, H.-H., et al., Three-dimensional numerical and experimental investigation on friction stir welding processes of ferritic stainless steel. *Acta Materialia*, 2013. **61**(7): p. 2649-2661.
40. Chen, G., et al., Simulation of metal flow during friction stir welding based on the model of interactive force between tool and material. *Journal of materials engineering and performance*, 2014. **23**(4): p. 1321-1328.
41. Zhang, Z. and Q. Wu, Analytical and numerical studies of fatigue stresses in friction stir welding. *The International Journal of Advanced Manufacturing Technology*, 2015. **78**(9-12): p. 1371-1380.
42. Fujii, H., et al., Effect of tool shape on mechanical properties and microstructure of friction stir welded aluminum alloys. *Materials Science and Engineering: A*, 2006. **419**(1): p. 25-31.
43. Elangovan, K., V. Balasubramanian, and M. Valliappan, Influences of tool pin profile and axial force on the formation of friction stir processing zone in AA6061 aluminium alloy. *The International Journal of Advanced Manufacturing Technology*, 2008. **38**(3): p. 285-295.
44. Vijay, S.J. and N. Murugan, Influence of tool pin profile on the metallurgical and mechanical properties of friction stir welded Al-10wt.% TiB₂ metal matrix composite. *Materials & Design*, 2010. **31**(7): p. 3585-3589.
45. Biswas, P., D. Anil Kumar, and N. Mandal, Friction stir welding of aluminum alloy with varying tool geometry and process parameters. Vol. 226. 2011. 641-648.
46. Gopalakrishnan, S. and N. Murugan, Prediction of tensile strength of friction stir welded aluminium matrix TiCp particulate reinforced composite. *Materials & Design*, 2011. **32**(1): p. 462-467.

47. Palanivel, R., et al., Effect of tool rotational speed and pin profile on microstructure and tensile strength of dissimilar friction stir welded AA5083-H111 and AA6351-T6 aluminum alloys. *Materials & Design*, 2012. **40**: p. 7-16.
48. Dharanendran, V. and V. Rao, A Multi Response Optimization of Tool Pin Profile on the Tensile Behavior of Age-hardenable Aluminum Alloys during Friction Stir Welding. Vol. 7. 2014. 4503-4518.
49. Gadakh, V., A. Kumar, and G.V. Patil, Analytical modeling of the friction stir welding process using different pin profiles. *Welding Journal*, 2015.
50. Gharaibeh, N., Effect of Pin Profile on Mechanical Properties of 6061 Al Alloy Welded Joints Prepared by Friction Stir Welding. Vol. 6. 2016. 39-42.
51. Firouzdor, V. and S. Kou, Al-to-Mg Friction Stir Welding: Effect of Positions of Al and Mg with Respect to the Welding Tool. Vol. 88. 2009. 213S-224S.
52. Gratecap, F., et al., Exploring material flow in friction stir welding: Tool eccentricity and formation of banded structures. *International Journal of Material Forming*, 2012. **5**(2): p. 99-107.
53. Liang, Z., et al., Effect of Tool Offset and Tool Rotational Speed on Enhancing Mechanical Property of Al/Mg Dissimilar FSW Joints. *Metallurgical and Materials Transactions A*, 2013. **44**(8): p. 3721-3731.
54. Tingey, C., et al., Effect of tool centreline deviation on the mechanical properties of friction stir welded DH36 steel. *Materials & Design (1980-2015)*, 2015. **65**: p. 896-906.
55. Mao, Y., et al., Effect of tool pin eccentricity on microstructure and mechanical properties in friction stir welded 7075 aluminum alloy thick plate. *Materials & Design (1980-2015)*, 2014. **62**: p. 334-343.
56. Guo, N., et al., Effect of tool eccentricity on surface periodic banded structures in friction stir welding. Vol. 103. 2015. 012020.
57. Essa, A.R.S., et al., An analytical model of heat generation for eccentric cylindrical pin in friction stir welding. *Journal of Materials Research and Technology*, 2016.
58. Azizieh, M., et al., Mechanical properties and microstructural evaluation of AA1100 to AZ31 dissimilar friction stir welds. *Materials Chemistry and Physics*, 2016. **170**: p. 251-260.

59. Shah, L.H., et al., Effect of tool eccentricity on the properties of friction stir welded AA6061 aluminum alloys. *Manufacturing Letters*, 2018. **15**: p. 14-17.
60. Shanmuga Sundaram, N. and N. Murugan, Tensile behavior of dissimilar friction stir welded joints of aluminium alloys. *Materials & Design*, 2010. **31**(9): p. 4184-4193.
61. Lorrain, O., et al., Understanding the material flow path of friction stir welding process using unthreaded tools. *Journal of Materials Processing Technology*, 2010. **210**(4): p. 603-609.
62. Suresha, C.N., B.M. Rajaprakash, and S. Upadhya, A Study of the Effect of Tool Pin Profiles on Tensile Strength of Welded Joints Produced Using Friction Stir Welding Process. *Materials and Manufacturing Processes*, 2011. **26**(9): p. 1111-1116.
63. Ji, S.D., et al., Numerical simulation of material flow behavior of friction stir welding influenced by rotational tool geometry. *Computational Materials Science*, 2012. **63**: p. 218-226.
64. Gadakh, V.S. and K. Adepu, Heat generation model for taper cylindrical pin profile in FSW. *Journal of Materials Research and Technology*, 2013. **2**(4): p. 370-375.
65. Ramanjaneyulu, K., et al., Structure-Property Correlation of AA2014 Friction Stir Welds: Role of Tool Pin Profile. *Journal of Materials Engineering and Performance*, 2013. **22**(8): p. 2224-2240.
66. Othman, N., et al., Effect of Taper Pin Ratio on Microstructure and Mechanical Property of Friction Stir Welded AZ31 Magnesium Alloy. Vol. 10. 2016. 619-622.
67. Al-moussawi, M., et al., Modelling of friction stir welding of DH36 steel. *The International Journal of Advanced Manufacturing Technology*, 2017. **92**(1): p. 341-360.
68. FLUENT online manual. Available from: <http://www.ansys.com/products/fluidynamics/>.
69. Blazek, J., *Computational Fluid Dynamics: Principles and Applications*. 2005.
70. D. Anderson Jr, J., *Computational fluid dynamics - An engineering tool*. 1976.
71. Jayanti, S., *Computational Fluid Dynamics for Engineers and Scientists*. 2018.
72. Patankar, S.V., *Numerical Heat Transfer and Fluid Flow*. 1980: Hemisphere Publishing Corporation.
73. Pozrikidis, C. and D. Gartling, *Fluid Dynamics: Theory, Computation, and Numerical Simulation*. Vol. 55. 2002. 55.

74. Versteeg, H. and H.K. and Malalasekera, An Introduction to Computational Fluid Dynamics. 1995.
75. E. Hamza, T.A., R. Mishra, Computational Fluid Dynamics based Transient Thermal Analysis of Friction Stir Welding, in 6th International and 43rd National Conference on Fluid Mechanics and Fluid Power (FMFP-2016). 2016.
76. Ansys 13.0.0 User Guide
77. Mijajlović, M., Experimental studies of parameters affecting the heat generation in friction stir welding process. Vol. 16. 2012. 351-362.
78. Al-abidi, A.A., et al., CFD applications for latent heat thermal energy storage: a review. Renewable and Sustainable Energy Reviews, 2013. **20**: p. 353-363.
79. Muhieddine, M., E. Canot, and R. March, Various approaches for solving problems in heat conduction with phase change. International Journal on Finite Volumes, 2009: p. 19.
80. Kang, S.-W. and B.-S. Jang, Comparison of friction stir welding heat transfer analysis methods and parametric study on unspecified input variables. Journal of Mechanical Science and Technology, 2014. **28**(10): p. 4233-4246.
81. Versteeg, H.K. and W. Malalasekera, An introduction to computational fluid dynamics: the finite volume method. Vol. 2nd. 2007, Harlow: Pearson Prentice Hall.
82. Asim, T., Computational Fluid Dynamics Based Diagnostics and Optimal Design of Hydraulic Capsule Pipelines. 2013.
83. Dudley, J. Selecting a Target Transient Time Step in a CFD Analysis. 2015 27 Mach; Available from: <https://caesai.com/blog/selecting-target-transient-time-step-cfd-analysis>.
84. Dynamic Mesh Update Methods. Available from: FLUENT 6.3 User's Guide - 11.3.2.
85. Radius of a regular polygon. Available from: <http://www.mathopenref.com/polygonradius.html>.
86. NAGAPPAN, K.W.P., Transient Temperature Distribution in Inertia Welding of Steels. 1970.
87. Albakri, A., et al., Thermo-mechanical and metallurgical aspects in friction stir processing of AZ31 Mg alloy—a numerical and experimental investigation. Journal of Materials Processing Technology, 2013. **213**(2): p. 279-290.

88. Zhang, Y.N., et al., Review of tools for friction stir welding and processing. *Canadian Metallurgical Quarterly*, 2012. **51**(3): p. 250-261.
89. Hernández, C.A., et al., Three-dimensional numerical modeling of the friction stir welding of dissimilar steels. *The International Journal of Advanced Manufacturing Technology*, 2017. **93**(5): p. 1567-1581.
90. Nakamura, T., et al., Tool Temperature and Process Modeling of Friction Stir Welding. Vol. 08. 2018. 78-94.
91. Colegrove, P.A., H.R. Shercliff, and R. Zettler, Model for predicting heat generation and temperature in friction stir welding from the material properties. *Science and Technology of Welding and Joining*, 2007. **12**(4): p. 284-297.
92. Ramasamy, P., V. Balusamy, and R.K. Velamati, Effect of Axial Pressure and Tool Rotation Speed on Temperature Distribution during Dissimilar Friction Stir Welding. Vol. 418-420. 2011. 1934-1938.
93. CROFT, D.N., HEAT TREATMENT OF WELDED STEEL STRUCTURES. 2003.

Appendix A:

A-1: User Defined Function (UDF) subroutine to estimate the values of viscosity

```

#include"udf.h"

DEFINE_PROPERTY(cell_viscosity_Zener, cell, thread)

{

real mu_lam;

real temp = C_T(cell, thread);

real defRateMag = C_STRAIN_RATE_MAG(cell, thread);

real AA=1652000;

real alpha=0.0000000164;

real nn=5.33;

real QQ=191000;

real RR=8.314;

real effective_strain_rate;

effective_strain_rate = pow(2*defRateMag*defRateMag/3,0.5);

if (defRateMag <= 0.0000000001)

{

mu_lam = 17292961.17;

}

```

```

else
{
mu_lam =
1/(((pow(3,0.5))*alpha*effective_strain_rate)*log((pow(((effective_strain_rate*exp(QQ/(RR*temp
p)))/AA),1/nn))+pow(pow((effective_strain_rate*exp(QQ/(RR*temp)))/AA,2/nn)+1,0.5)));
}
return mu_lam;
}

```

A-2: User Defined Function (UDF) subroutine to define the translational speed of the welding tool

```

#include"udf.h"

DEFINE_CG_MOTION(MZ,dt,vel,omega,time,dtime)
{
    omega[2]= 66.7;
    vel[0]= - 0.00159;
}

DEFINE_CG_MOTION(WallP,dt,vel,omega,time,dtime)
{
    Thread *t;
    face_t f;
    t = DT_THREAD(dt);

```

```
begin_f_loop(f,t)
{
    vel[0]= - 0.00159;
}
end_f_loop(f,t)
```

Appendix B:

B-1: Peak Temperature Values of FSW when Using Tools with Polygonal Pins

Table B-1.1. Global Peak Temperature for Different Shoulder Diameters

Shoulder Diameter	Global Peak Temperature
26mm	481K
34mm	597K
42mm	720K
50mm	848K

Table B-1.2. Local Peak Temperature for Different Shoulder Diameters

Shoulder Diameter	Local Peak Temperature			
	Point 1	Point 2	Point 3	Point 4
26mm	461.57K	413.4K	436K	409.25K
34mm	571.6K	522K	530K	504.25K
42mm	690.7K	645.5K	635.75K	601K
50mm	809.27K	764.9K	741K	699.5K

Table B-1.3. Global Peak Temperature for Different Pin Diameters

Pin Diameter	Global Peak Temperature
6mm	882K
12mm	848K
18mm	833K
24mm	840K

Table B-1.4. Local Peak Temperature for Different Pin Diameters

Pin Diameter	Local Peak Temperature			
	Point 1	Point 2	Point 3	Point 4
6mm	832K	784.8K	755.5K	723.5K
12mm	809.3K	765K	741K	699.5K
18mm	804.6K	762K	732K	696.7K
24mm	807K	764K	736.5K	701.3K

Table B-1.5. Global Peak Temperature for Different Pin Heights

Pin Height	Global Peak Temperature
12mm	848K
11mm	847K
10mm	845K
9mm	841K

Table B-1.6. Local Peak Temperature for Different Pin Heights

Pin Height	Local Peak Temperature			
	Point 1	Point 2	Point 3	Point 4
12mm	809.3K	765K	741K	699.5K
11mm	807K	762K	736K	697.7K
10mm	798.3K	758K	730K	693K
9mm	796K	753.5K	726.5K	690K

Table B-1.7. Global Peak Temperature for Different Workpiece Thicknesses

Workpiece Thickness	Global Peak Temperature
12.7mm	848K
14.7mm	834K
16.7mm	814K
18.7mm	798K

Table B-1.8. Local Peak Temperature for Different Workpiece Thicknesses

Workpiece Thickness	Local Peak Temperature			
	Point 1	Point 2	Point 3	Point 4
12.7mm	809.3K	765K	741K	699.5K
14.7mm	793.6K	746K	721K	678.5K
16.7mm	772K	727K	699.6K	659K
18.7mm	749.6K	708K	678.6K	642K

Table B-1.9. Global Peak Temperature for Different Tool Rotational Speeds

Tool Rotational Speed	Global Peak Temperature
237r.p.m	509K
437r.p.m	668K
637r.p.m	699.5K
837r.p.m	975K

Table B-1.10. Local Peak Temperature for Different Tool Rotational Speeds

Tool Rotational Speed	Local Peak Temperature			
	Point 1	Point 2	Point 3	Point 4
237r.p.m	496K	477K	466K	447K
437r.p.m	645K	621K	598.5K	570.5K
637r.p.m	809.3K	765K	741K	699.5K
837r.p.m	941K	890K	862K	807K

Table B-1.11. Global Peak Temperature for Different Axial Loads

Axial Load	Global Peak Temperature
9.7MPa	731K
11.2MPa	793K
12.7MPa	848K
14.7MPa	912K

Table B-1.12. Local Peak Temperature for Different Axial Loads

Axial Load	Local Peak Temperature			
	Point 1	Point 2	Point 3	Point 4
9.7MPa	697K	660.3K	639.4K	607.7K
11.2MPa	754.5K	714K	690.2K	654.7K
12.7MPa	809.3K	765K	741K	699.5K
14.7MPa	863.5K	819K	788K	747K

B-2: Peak Temperature Values of FSW when Using Tools with Eccentric Polygonal Pins

Table B-2.1. Global Peak Temperature for Different Pin Eccentricities

Eccentricity	Global Peak Temperature
0mm	848K
0.3mm	827K
0.6mm	811K
0.9mm	789K

Table B-2.2. Local Peak Temperature for Different Pin Eccentricities

Eccentricity	Local Peak Temperature			
	Point 1	Point 2	Point 3	Point 4
0mm	809.3K	765K	741K	699.5K
0.3mm	796.5K	759.7K	733.8K	688.2K
0.6mm	776.9K	737.2K	716.6K	671.6K
0.9mm	761.76K	722K	704.6K	655.8K

Table B-2.3. Global Peak Temperature for Different Shoulder Diameters

Shoulder Diameter	Eccentricity	Global Peak Temperature
26mm	0.9mm	489K
34mm	0.9mm	584K
42mm	0.9mm	689K
50mm	0.9mm	789K

Table B-2.4. Local Peak Temperature for Different Shoulder Diameters

Shoulder Diameter	Eccentricity	Local Peak Temperature			
		Point 1	Point 2	Point 3	Point 4
26mm	0.9mm	468.2K	425.9K	445.4K	418K
34mm	0.9mm	563.6K	511.75K	525.76K	496.5K
42mm	0.9mm	662.3K	618.35K	612.6K	578K
50mm	0.9mm	761.76K	722K	704.6K	656K

Table B-2.5. Global Peak Temperature for Different Pin Diameters

Pin Diameter	Eccentricity	Global Peak Temperature
6mm	0.9mm	608K
12mm	0.9mm	789K
18mm	0.9mm	786K
24mm	0.9mm	787K

Table B-2.6. Local Peak Temperature for Different Pin Diameters

Pin Diameter	Eccentricity	Local Peak Temperature			
		Point 1	Point 2	Point 3	Point 4
6mm	0.9mm	763.2K	725K	702K	664.5K
12mm	0.9mm	761.76K	722K	704.6K	655.8K
18mm	0.9mm	778.2K	738.6K	721.9K	672.7K
24mm	0.9mm	777.5K	753K	732.25K	694.8K

Table B-2.7. Global Peak Temperature for Different Pin Heights

Pin Height	Eccentricity	Global Peak Temperature
12mm	0.9mm	789K
11mm	0.9mm	793K
10mm	0.9mm	796K
9mm	0.9mm	797K

Table B-2.8. Local Peak Temperature for Different Pin Heights

Pin Height	Eccentricity	Local Peak Temperature			
		Point 1	Point 2	Point 3	Point 4
12mm	0.9mm	761.76K	722K	704.6K	655.8K
11mm	0.9mm	762.3K	723.3K	705.6K	656.5K
10mm	0.9mm	763.9K	725K	706K	657.7K
9mm	0.9mm	767.6K	726.4K	707.5K	659K

Table B-2.9. Global Peak Temperature for Different Workpiece Thicknesses

Workpiece Thickness	Eccentricity	Global Peak Temperature
12.7mm	0.9mm	789K
14.7mm	0.9mm	774K
16.7mm	0.9mm	754K
18.7mm	0.9mm	736K

Table B-2.10. Local Peak Temperature for Different Workpiece Thicknesses

Workpiece Thickness	Eccentricity	Local Peak Temperature			
		Point 1	Point 2	Point 3	Point 4
12.7mm	0.9mm	761.76K	722K	704.6K	655.8K
14.7mm	0.9mm	742.35K	708K	685.2K	645.3K
16.7mm	0.9mm	734.5K	691.4K	667K	625K
18.7mm	0.9mm	708.3K	673.2K	649K	613.6K

Table B-2.11. Global Peak Temperature for Different Tool Rotational Speeds

Tool Rotational Speed	Eccentricity	Global Peak Temperature
237r.p.m	0.9mm	494K
437r.p.m	0.9mm	643K
637r.p.m	0.9mm	789K
837r.p.m	0.9mm	924K

Table B-2.12. Local Peak Temperature for Different Tool Rotational Speeds

Tool Rotational Speed	Eccentricity	Local Peak Temperature			
		Point 1	Point 2	Point 3	Point 4
237r.p.m	0.9mm	482K	463.2K	457.5K	434K
437r.p.m	0.9mm	619.3K	594.4K	576.85K	545.9K
637r.p.m	0.9mm	761.8K	722K	704.6K	655.8K
837r.p.m	0.9mm	892K	855.2K	832.5K	766K

Table B-2.13. Local Peak Temperature for Different Axial Loads

Axial Load	Eccentricity	Global Peak Temperature
9.7MPa	0.9mm	680K
11.2MPa	0.9mm	735K
12.7MPa	0.9mm	789K
14.7MPa	0.9mm	844K

Table B-2.14. Global Peak Temperature for Different Axial Loads

Axial Load	Eccentricity	Local Peak Temperature			
		Point 1	Point 2	Point 3	Point 4
9.7MPa	0.9mm	658.7K	626.2K	612.5K	573.2K
11.2MPa	0.9mm	710.3K	674.85K	658.6K	614.85K
12.7MPa	0.9mm	761.8K	722K	704.6K	655.8K
14.7MPa	0.9mm	814K	769.7K	751.5K	697.4K

B-3: Peak Temperature Values of FSW when Using Tools with Tapered Eccentric Polygonal Pins

Table B-3.1. Global Peak Temperature for Different Pin Taper Angles

Taper Angle	Eccentricity	Global Peak Temperature
0°	0.9mm	789K
7°	0.9mm	781K
14°	0.9mm	770K
21°	0.9mm	760K

Table B-3.2. Local Peak Temperature for Different Pin Taper Angles

Taper Angle	Eccentricity	Local Peak Temperature			
		Point 1	Point 2	Point 3	Point 4
0°	0.9mm	761.76 K	722 K	704.62 K	655.84 K
7°	0.9mm	750.45 K	713.9 K	693.4 K	654 K
14°	0.9mm	743.85 K	707.8 K	684.2 K	652 K
21°	0.9mm	734 K	702.95 K	677.7 K	649.5 K

Table B-3.3. Global Peak Temperature for Different Pin Eccentricities

Eccentricity	Taper Angle	Global Peak Temperature
0mm	21°	817K
0.3mm	21°	800K
0.6mm	21°	782K
0.9mm	21°	760K

Table B-3.4. Local Peak Temperature for Different Pin Eccentricities

Eccentricity	Taper Angle	Local Peak Temperature			
		Point 1	Point 2	Point 3	Point 4
0mm	21°	790.8 K	760.9 K	728 K	702.9 K
0.3mm	21°	777 K	743.85 K	712.6 K	686.14 K
0.6mm	21°	753 K	720.77 K	695.2 K	667.8 K
0.9mm	21°	734 K	702.95 K	677.7 K	649.5 K

Table B-3.5. Global Peak Temperature for Different Shoulder Diameters

Shoulder Diameter	Taper Angle	Eccentricity	Global Peak Temperature
26mm	21°	0.9mm	473K
34mm	21°	0.9mm	566K
42mm	21°	0.9mm	661K
50mm	21°	0.9mm	760K

Table B-3.6. Local Peak Temperature for Different Shoulder Diameters

Shoulder Diameter	Taper Angle	Eccentricity	Local Peak Temperature			
			Point 1	Point 2	Point 3	Point 4
26mm	21°	0.9mm	456.8K	419.2 K	435.7K	412.7K
34mm	21°	0.9mm	548.4K	501K	511K	488.2K
42mm	21°	0.9mm	642.35K	602.9K	592.44K	570.95K
50mm	21°	0.9mm	734K	702.95K	677.7K	649.5K

Table B-3.7. Global Peak Temperature for Different Pin Diameters

Pin Diameter	Taper Angle	Eccentricity	Global Peak Temperature
6mm	21°	0.9mm	
12mm	21°	0.9mm	760K
18mm	21°	0.9mm	754 K
24mm	21°	0.9mm	751 K

Table B-3.8. Local Peak Temperature for Different Pin Diameters

Pin Diameter	Taper Angle	Eccentricity	Local Peak Temperature			
			Point 1	Point 2	Point 3	Point 4
6mm	21°	0.9mm				
12mm	21°	0.9mm	734 K	702.95 K	677.7 K	649.5 K
18mm	21°	0.9mm	734.25 K	707.5 K	682.2 K	647.6 K
24mm	21°	0.9mm	736 K	716 K	688.5 K	660.8 K

Table B-3.9. Global Peak Temperature for Different Pin Heights

Pin Height	Taper Angle	Eccentricity	Global Peak Temperature
12mm	21°	0.9mm	760 K
11mm	21°	0.9mm	766 K
10mm	21°	0.9mm	768 K
9mm	21°	0.9mm	771 K

Table B-3.10. Local Peak Temperature for Different Pin Heights

Pin Height	Taper Angle	Eccentricity	Local Peak Temperature			
			Point 1	Point 2	Point 3	Point 4
12mm	21°	0.9mm	736 K	706 K	675.5 K	648.8 K
11mm	21°	0.9mm	739.4 K	708.75 K	679.88 K	652.9 K
10mm	21°	0.9mm	741.8 K	709 K	682.6 K	653.3 K
9mm	21°	0.9mm	744.9 K	714.7 K	684.9 K	655.6 K

Table B-3.11. Global Peak Temperature for Different Workpiece Thicknesses

Workpiece Thickness	Taper Angle	Eccentricity	Global Peak Temperature
12.7mm	21°	0.9mm	760 K
14.7mm	21°	0.9mm	748 K
16.7mm	21°	0.9mm	733 K
18.7mm	21°	0.9mm	723 K

Table B-3.12. Local Peak Temperature for Different Workpiece Thicknesses

Workpiece Thickness	Taper Angle	Eccentricity	Local Peak Temperature			
			Point 1	Point 2	Point 3	Point 4
12.7mm	21°	0.9mm	736 K	706 K	675.5 K	648.8 K
14.7mm	21°	0.9mm	724 K	691.5 K	665.8 K	630.8 K
16.7mm	21°	0.9mm	708.75 K	676 K	650 K	611.4 K
18.7mm	21°	0.9mm	699.3 K	670.9 K	640 K	607.3 K

Table B-3.13. Global Peak Temperature for Different Tool Rotational Speeds

Tool Rotational Speed	Taper Angle	Eccentricity	Global Peak Temperature
237r.p.m	21°	0.9mm	481 K
437r.p.m	21°	0.9mm	622 K
637r.p.m	21°	0.9mm	760 K
837r.p.m	21°	0.9mm	899 K

Table B-3.14. Local Peak Temperature for Different Tool Rotational Speeds

Tool Rotational Speed	Taper Angle	Eccentricity	Local Peak Temperature			
			Point 1	Point 2	Point 3	Point 4
237r.p.m	21°	0.9mm	468.8 K	453.3 K	443.8 K	431 K
437r.p.m	21°	0.9mm	606 K	579.25 K	559.4 K	541 K
637r.p.m	21°	0.9mm	736 K	706 K	675.5 K	648.8 K
837r.p.m	21°	0.9mm	864.2 K	822.3 K	792.4 K	758.5 K

Table B-3.15. Global Peak Temperature for Different Axial Loads

Axial Load	Eccentricity	Global Peak Temperature
9.7MPa	0.9mm	659 K
11.2MPa	0.9mm	712 K
12.7MPa	0.9mm	760 K
14.7MPa	0.9mm	813 K

Table B-3.16. Local Peak Temperature for Different Axial Loads

Axial Load	Taper Angle	Eccentricity	Local Peak Temperature			
			Point 1	Point 2	Point 3	Point 4
9.7MPa	21°	0.9mm	637.7 K	612 K	589.8 K	568.2 K
11.2MPa	21°	0.9mm	687.3 K	658.5 K	633.6 K	609.25 K
12.7MPa	21°	0.9mm	736 K	706 K	675.5 K	648.8 K
14.7MPa	21°	0.9mm	784.2 K	750.4 K	720.2 K	691 K

PUBLICATIONS

- Hamza, E., “A review of using Computational Fluid Dynamic in simulating of Friction Stir Welding and Parametric studies”, in 11th International Symposium on FSW (11ISFSW) 2016: TWI Ltd, Cambridge, UK.

- Hamza, E. Asim, T. and Mishra, R. “Computational Fluid Dynamics based Transient Thermal Analysis of Friction Stir Welding”, in 6th International and 43rd National Conference on Fluid Mechanics and Fluid Power (FMFP-2016). December 2016: Allahabad, India